



## **University of Huddersfield Repository**

Li, Duo

DEVELOPMENT AND APPLICATION OF ON-MACHINE SURFACE MEASUREMENT FOR ULTRA-PRECISION TURNING PROCESS

### **Original Citation**

Li, Duo (2018) DEVELOPMENT AND APPLICATION OF ON-MACHINE SURFACE MEASUREMENT FOR ULTRA-PRECISION TURNING PROCESS. Doctoral thesis, University of Huddersfield.

This version is available at <http://eprints.hud.ac.uk/id/eprint/34816/>

The University Repository is a digital collection of the research output of the University, available on Open Access. Copyright and Moral Rights for the items on this site are retained by the individual author and/or other copyright owners. Users may access full items free of charge; copies of full text items generally can be reproduced, displayed or performed and given to third parties in any format or medium for personal research or study, educational or not-for-profit purposes without prior permission or charge, provided:

- The authors, title and full bibliographic details is credited in any copy;
- A hyperlink and/or URL is included for the original metadata page; and
- The content is not changed in any way.

For more information, including our policy and submission procedure, please contact the Repository Team at: [E.mailbox@hud.ac.uk](mailto:E.mailbox@hud.ac.uk).

<http://eprints.hud.ac.uk/>

**DEVELOPMENT AND APPLICATION OF ON-MACHINE  
SURFACE MEASUREMENT FOR ULTRA-PRECISION  
TURNING PROCESS**

**DUO LI**

A thesis submitted to the University of Huddersfield in partial fulfilment of the requirements for  
the degree of Doctor of Philosophy

The University of Huddersfield

July 2018

## **Copyright statement**

- i. The author of this thesis (including any appendices and/or schedules to this thesis) owns any copyright in it (the “Copyright”) and he has given The University of Huddersfield the right to use such copyright for any administrative, promotional, educational and/or teaching purposes.
- ii. Copies of this thesis, either in full or in extracts, may be made only in accordance with the regulations of the University Library. Details of these regulations may be obtained from the Librarian. This page must form part of any such copies made.
- iii. The ownership of any patents, designs, trademarks and any and all other intellectual property rights except for the Copyright (the “Intellectual Property Rights”) and any reproductions of copyright works, for example graphs and tables (“Reproductions”), which may be described in this thesis, may not be owned by the author and may be owned by third parties. Such Intellectual Property Rights and Reproductions cannot and must not be made available for use without the prior written permission of the owner(s) of the relevant Intellectual Property Rights and/or Reproductions

## Acknowledgements

It would be impossible to complete my PhD study without the support from many great people who have been always willing to give help through the years.

First and foremost, I would like to express my deepest gratitude to my supervisor Professor Dame Xiangqian Jiang for offering me the opportunity to carry out research work in the field of on-machine metrology. Her guidance, caring, encouragement and valuable advices are of great help for my academic journey and personal growth.

I would also like to express my sincere appreciation to my co-supervisor Professor Liam Blunt for the inspiring discussions and suggestions on the research project. He guided me to join into the field of precision engineering. His humour and wisdom always encourage me to move forward.

Special thanks go to Dr Zhen Tong. His diligence on the development of the ultra-precision machining group gives continuous support to my research work. Group members including Mr Chris Dawson, Mr Christian Young and Mr Zavid Mohammed have also provided me with much assistance in the experimental work. I am deeply grateful to their devotion and efforts.

I would like to thank all other colleagues in the EPSRC centre for Innovative Manufacturing in Advanced Metrology, including Dr Feng Gao, Dr Wenhan Zeng, Dr Shan Lou, Dr Karl Walton, Dr James Williamson, Dr Luca Pagani, Dr Prashant Kumar, Dr Hongyu Ren, Dr Dawei Tang, Dr Jian Wang, Dr Hussam Muhamedsalih, Dr Qunfen Qi, Dr Tukun Li, Dr Yuchu Qin, Dr Tianqi Gu, Mr Tao Zhang, Mr Yongjia Xu, Dr Xin Wu, Dr Shujun Huang and other supported staff members. It is amazing and wonderful experience to work with these talented and helpful people. In addition, I appreciate the University of Huddersfield and the China Scholarship Council (CSC) for providing me 100% fee waiver scholarship and maintenance support.

Finally, I would like to give utmost thanks to all my family members for their endless supports and profound love. I dedicate this thesis to my loving parents for enduring my absence while I was studying PhD abroad.

## Abstract

Optical freeform components, featured with high functional performance, are of enormous demand in advanced imaging and illumination applications. However, the geometrical complexity and high accuracy demand impose considerable challenges on the existing ultra-precision freeform machining technologies. Surface measurement and characterisation become the key to further improving machining performance. In order to further increase the metrology availability and efficiency, a shift in the approach of surface metrology from offline lab-based solutions towards the use of metrology upon manufacturing platforms is needed. On-machine surface measurement (OMSM) will not only allow the assessment of manufactured surfaces just-in-time without transportation and repositioning, but also provide feedback for process optimization and post-process correction with consistent coordinate frame.

In the thesis, a single point robust interferometer is integrated onto a diamond turning lathe to establish the metrology-embedded ultra-precision manufacturing platform. To extract a priori information for the subsequent OMSM, a theoretical and experimental study of surface generation was carried out for ultra-precision turning of optical freeform surfaces. With the proposed machining methodology and surface generation simulation, two freeform surfaces (sinusoidal grid and micro-lens arrays) were successfully fabricated using the slow tool servo technique. The machined topography of freeform surfaces was uniformly distributed and in agreement with simulated results. Since it operates in the manufacturing environment, the machine tool effects on the OMSM were comprehensively evaluated, including on-machine vibration test, machine kinematic error mapping and linearity error calibration. A systematic calibration methodology for single point OMSM was proposed. Both theoretical and experimental investigation have been conducted to prove the validity of the proposed calibration methodology and the effectiveness of OMSM.

With the aid of OMSM, potential applications were explored to exploit the integration benefits to further enhance the ultra-precision machining performance. OMSM integration will increase the automation level of the manufacturing. As OMSM preserves the coordinate system between the machining and measurement, the process investigation can be carried out in a more deterministic manner. The effect of process parameters on the surface form errors was investigated for ultra-precision cylindrical turning process. An empirical model based on response surface methodology has been established and validated with the experimental results. Moreover, a corrective machining methodology was proposed to further improve the accuracy of diamond turned surfaces with OMSM. According to different correction tasks, corresponding OMSM data processing methods were presented. Profile and surface correction experiments were performed to validate the proposed corrective machining methodology and 40% improvement of surface accuracy was achieved.

# Table of Contents

## Contents

<b>Copyright statement.....</b>	<b>2</b>
<b>Acknowledgements.....</b>	<b>3</b>
<b>Abstract.....</b>	<b>5</b>
<b>Table of Contents .....</b>	<b>7</b>
<b>List of Tables .....</b>	<b>10</b>
<b>List of Figures.....</b>	<b>11</b>
<b>List of abbreviations .....</b>	<b>16</b>
<b>List of Symbols .....</b>	<b>18</b>
<b>1 Introduction .....</b>	<b>20</b>
1.1 Research background.....	20
1.2 Aims and objectives.....	22
1.3 Research methodology and thesis structure.....	22
1.4 Contributions to knowledge.....	25
1.5 Publications .....	26
<b>2 Review of ultra-precision machining and surface metrology.....</b>	<b>28</b>
2.1 Introduction .....	28
2.2 Optical freeform surfaces and applications .....	28
2.2.1 Imaging applications .....	29
2.2.2 Illumination applications .....	31
2.3 Ultra-precision machining techniques .....	33
2.3.1 Ultra-precision turning .....	33
2.3.2 Ultra-precision raster milling.....	36
2.3.3 Ultra-precision grinding.....	37
2.3.4 Ultra-precision polishing .....	38
2.4 Surface measurement and characterisation.....	39
2.4.1 Instrumentation for surface measurement.....	39
2.4.2 Characterisation .....	47
2.5 Summary.....	51
<b>3 Review and discussion of OMSM .....</b>	<b>54</b>
3.1 Introduction .....	54
3.2 Benefits of OMSM .....	55
3.3 Considerations for OMSM integration .....	56
3.4 Review of OMSM instrumentation and applications .....	57
3.4.1 Contact OMSM and applications.....	58
3.4.2 Non-contact optical OMSM and applications.....	65
3.4.3 Comparison among different OMSM .....	74
3.5 Summary.....	75
<b>4 Theoretical and experimental investigation of STS machining of freeform surfaces... </b>	<b>77</b>

4.1	Introduction .....	77
4.2	Tool path generation.....	77
4.2.1	STS machining principle.....	79
4.2.2	Tool geometries selection .....	81
4.2.3	Tool radius compensation .....	83
4.3	Surface generation simulation and analysis.....	88
4.3.1	Principles.....	88
4.3.2	Simulation analysis .....	91
4.4	Experiments and discussions .....	96
4.4.1	Experimental setup.....	96
4.4.2	Sinusoidal grid surface machining.....	97
4.4.3	MLA surface machining .....	100
4.5	Summary.....	102
<b>5</b>	<b>Development and systematic calibration of OMSM .....</b>	<b>103</b>
5.1	Introduction .....	103
5.2	Overview of the developed OMSM system .....	104
5.2.1	Working principle and system configuration.....	104
5.2.2	Measurement coordinate alignment .....	107
5.2.3	On-machine scanning strategies .....	108
5.3	Calibration of OMSM system.....	110
5.3.1	OMSM calibration scheme .....	110
5.3.2	On-machine vibration analysis .....	111
5.3.3	Machine tool kinematic error mapping.....	114
5.3.4	Amplification coefficient and linearity error correction.....	122
5.4	OMSM experiment .....	125
5.5	Summary.....	129
<b>6</b>	<b>Process investigation and machining error modelling with OMSM .....</b>	<b>131</b>
6.1	Introduction .....	131
6.2	Process investigation methodology .....	132
6.2.1	Response surface methodology.....	134
6.2.2	Design of experiment.....	135
6.3	Experiments and discussions .....	137
6.3.1	Experimental setup.....	137
6.3.2	Comparison between OMSM and Talyrond .....	138
6.3.3	Response surface analysis.....	139
6.3.4	Confirmation test .....	145
6.4	Summary.....	146
<b>7</b>	<b>Corrective machining with OMSM .....</b>	<b>148</b>
7.1	Introduction .....	148
7.2	Corrective machining methodology .....	149
7.3	OMSM processing for corrective machining .....	151
7.3.1	2D profile processing.....	151
7.3.2	Surface processing .....	152
7.4	Experiments and discussions .....	156
7.4.1	Profile corrective machining.....	156
7.4.2	Surface corrective machining .....	159
7.5	Summary.....	164

<b>8 Conclusions and Future work.....</b>	<b>166</b>
8.1    Overall conclusions .....	166
8.2    Future work.....	170
<b>Publications and Awards.....</b>	<b>173</b>
<b>References .....</b>	<b>175</b>
<b>Appendix A Machine tool kinematic error measurement.....</b>	<b>186</b>
A.1 Introduction .....	186
A.2 <i>X</i> axis straightness error .....	188
A.3 <i>C</i> axis axial and tilt errors .....	190
A.4 Squareness error between <i>X</i> and <i>C</i> axis .....	193

## List of Tables

Table 2.1 Areal height parameters [112].....	50
Table 3.1 Contact type of OMSM and applications.....	64
Table 3.2 Non-contact optical type of OMSM and applications.....	72
Table 3.3 Merits and limitations of different types of OMSM .....	74
Table 4.1 Mechanical properties of the sample material (Al6082).....	97
Table 4.2 Machining parameters for sinusoidal grid surface .....	97
Table 4.3 Diamond tool parameters .....	98
Table 4.4 MLA design parameters.....	100
Table 4.5 Surface topography $S_q$ by actual measurement and simulation.....	101
Table 5.1 Vibration test results .....	113
Table 5.2 Step height measurement results .....	124
Table 5.3 Characterisation results of on-machine and offline measurement .....	128
Table 6.1 Factors and levels of process parameters .....	135
Table 6.2 CCD design of experiment.....	136
Table 6.3 Experimental results of form error (OMSM).....	139
Table 6.4 ANOVA table of response surface model for machined surface error .....	140
Table 6.5 Regression model summary .....	141
Table 6.6 Coded coefficients of regression model .....	142
Table 6.7 Confirmation tests .....	146
Table 7.1 Machining parameters.....	156
Table 7.2 Profile error correction results .....	159
Table 7.3 OMSM scanning parameters.....	159
Table 7.4 Individual surface error characterisation.....	164

## List of Figures

Figure 1.1 The overall research framework .....	27
Figure 2.1 Examples of (a) continuous smooth surface; (b) structured surface; (c) conjunct surface .....	29
Figure 2.2 Polaroid SX-70 folding Single Lens Reflex camera [26] .....	30
Figure 2.3 Layout of the see-through HMD with the adoption of freeform prisms [7] .....	31
Figure 2.4 Different design of freeform lens array and corresponding illumination spots [29] ...	31
Figure 2.5 Schematic ray path of the freeform micro-lens optics design for LED illumination [31] .....	32
Figure 2.6 A freeform Köhler integrator for automotive lighting applications [32] .....	33
Figure 2.7 Commercial single crystal diamond cutting tools.....	34
Figure 2.8 Configuration of slow tool servo machining [42].....	35
Figure 2.9 Nanotech fast tool servo device [46] .....	35
Figure 2.10 Raster milling configuration on a five-axis ultra-precision machine tool [49].....	36
Figure 2.11 Wheel-normal ultra-precision grinding of optical moulds [52].....	37
Figure 2.12 The schematic of ELID grinding [53].....	38
Figure 2.13 Ultra-precision bonnet polishing of a freeform optics [63] .....	39
Figure 2.14 Schematic of phase grating interferometer transducer in stylus profilometry [16] ...	41
Figure 2.15 Taylor Hobson profilometer PGI series [78] .....	41
Figure 2.16 Nanometric resolution probing systems developed by (a) NPL [80] and (b) METAS [82] .....	42
Figure 2.17 Isara 400 3D ultra-precision CMM [83] .....	43
Figure 2.18 Schematic principle of a CGH in interferometry.....	44
Figure 2.19 (a) Fibre-based multiple wavelength interferometer and (b) open reference system [90] .....	45
Figure 2.20 Schematic principle of vertical scanning WLI [96].....	46
Figure 2.21 Working principle of phase measuring deflectometry [98] .....	47
Figure 2.22 (a) Original measurement; (b) form; (c) waviness; (d) roughness.....	48
Figure 2.23 Common characterisation parameters for profile measurement [109] .....	49
Figure 2.24 Ambiguity of 2D profile measurement and characterisation [111] .....	49
Figure 3.1 Consideration for OMSM integration.....	57

Figure 3.2 Schematic of (a) on-machine contact probing for optics grinding process; (b) tilted angle probe configuration [133].....	58
Figure 3.3 (a) Mould grinding machine with integrated probing unit; (b) schematic of compensation grinding strategy [134].....	59
Figure 3.4 (a)Workflow of combination of on- and off-machine measurement; (b) Experiment setup of on-machine measurement [20] .....	60
Figure 3.5 Robust AFM based on-machine measuring system [136] .....	61
Figure 3.6 STM based on-machine measuring system with ultra-sharp tips [137].....	61
Figure 3.7 STM on-machine measurement applied in (a) fly-cutting of V grooves [138]; (b) tool servo machining of 3D compound eye structures (b) [139].....	62
Figure 3.8 Micro-lens (a) defect identification and (b) repair process with FS-FTS [142] .....	63
Figure 3.9 Schematic of tool tip position measurement and relay fabrication of micro-structures with FS-FTS [143] .....	63
Figure 3.10 (a) Schematic and (b) experimental setup of on-machine shearing interferometer for diamond turning processes [145] .....	66
Figure 3.11 PSI on-machine measurement of diamond turned MIRI spectrometer mirror [146]	66
Figure 3.12 Principle of the dynamic interferometer [147] .....	67
Figure 3.13 Large telescope optics polishing system with on-machine dynamic interferometer measurement [148] .....	68
Figure 3.14 Schematic diagram of WSI with vibration compensation [149].....	68
Figure 3.15 WSI for on-machine topography measurement [149] .....	69
Figure 3.16 Integration of mini-PMD on a multi-axis ultra-precision machine tool [150] .....	69
Figure 3.17 Chromatic confocal based on-machine measurement for ultra-precision turning processes [151] .....	70
Figure 3.18 Optical slope sensor for on-machine measurement of FTS machined sinusoidal structures [152].....	71
Figure 3.19 Disparity pattern-based autostereoscopic system for in-situ inspection of diamond turned micro-structures [153].....	72
Figure 4.1 Workflow for STS tool path generation .....	78
Figure 4.2 The schematic of STS machining setup.....	79
Figure 4.3 (a) STS ideal tool path and (b) X-Y projection.....	81
Figure 4.4 Geometric parameters of a typical diamond cutting tool.....	81
Figure 4.5 Schematic of tool geometry selection for STS freeform machining .....	82

Figure 4.6 Schematic of overcutting phenomenon caused by a circular tool tip .....	84
Figure 4.7 Tool radius compensation using normal direction method.....	84
Figure 4.8 Normal direction compensation method and tool path analysis .....	86
Figure 4.9 Tool radius compensation using Z direction method.....	87
Figure 4.10 Comparison of two compensation method along a radial profile .....	87
Figure 4.11 Z direction compensation method and tool path analysis .....	88
Figure 4.12 Schematic diagram of profile topography generation.....	89
Figure 4.13 Simulation of topography generation along radial profile.....	90
Figure 4.14 Simulation example of areal surface topography generation.....	91
Figure 4.15 Relationship graphs between processing parameters and surface quality .....	93
Figure 4.16 Simulation analysis of overcutting phenomenon and tool radius compensation (left column: without compensation, right column: with compensation) .....	95
Figure 4.17 Experimental setup of STS machining .....	96
Figure 4.18 (a) Design and (b) STS tool path of sinusoidal grid surface.....	98
Figure 4.19 Photo of STS machined sinusoidal grid surface .....	98
Figure 4.20 Machined sinusoidal grid surface CCI measurement: (a) original; (b) after form removal.....	99
Figure 4.21 Topography distribution of sinusoid grid surface.....	99
Figure 4.22 (a) Design and (b) STS tool path of MLA surface .....	100
Figure 4.23 Photo of STS machined MLA surface .....	101
Figure 4.24 Topography distribution of MLA surface (CCI measurement) .....	101
Figure 5.1 Schematic of the OMSM platform.....	104
Figure 5.2 Schematic diagram of DRI bulk optics interferometer [169] .....	105
Figure 5.3 DRI spectral interferogram [94] .....	106
Figure 5.4 Remote DRI probe setup [170] .....	106
Figure 5.5 (a) Schematic diagram and (b) experiment setup of OMSM probing alignment .....	107
Figure 5.6 (a) Multiple radial, (b) multiple circular, (c) spiral measurement paths and their applicable surfaces .....	109
Figure 5.7 Structure diagram of OMSM calibration .....	110
Figure 5.8 Sampling frequency decision graph.....	112
Figure 5.9 Scanning vibration test: (a) time domain vibration signal and (b) spectrum analysis of vibration signal.....	113
Figure 5.10 Flow chart of kinematic error mapping .....	114

Figure 5.11 Kinematic error chain for on-machine surface measurement system.....	115
Figure 5.12 Configuration of the machine tool coordinate systems .....	115
Figure 5.13 Simulation of kinematic error effect on OMSM results .....	119
Figure 5.14 Machine kinematic error map.....	120
Figure 5.15 (a) DRI measurement, (b) scanning error map and (c) Fisba measurement of optical flat.....	121
Figure 5.16 (a) DRI measurement versus (b) combination of scanning error and Fisba measurement.....	121
Figure 5.17 Schematic of radial distributed step artefact.....	122
Figure 5.18 DRI on-machine measurement of the step artefact.....	123
Figure 5.19 Flow chart of step height characterisation .....	123
Figure 5.20 (a) Uncorrected and (b) corrected error plot of the step height measurement.....	124
Figure 5.21 Experimental setup of the proposed OMSM system .....	125
Figure 5.22 Multiple radial measurement of a cosine curve sample.....	126
Figure 5.23 Measurement results and error analysis of (a) DRI on-machine measurement and (b) PGI offline measurement .....	126
Figure 5.24 Sphere sample (a) DRI on-machine and (b) CCI measurement .....	128
Figure 6.1 Factors influencing surface form error in ultra-precision turning process .....	133
Figure 6.2 Flow chart of process investigation strategy with the aid of OMSM .....	134
Figure 6.3 Experimental setup for process investigation with OMSM.....	137
Figure 6.4 Talyrond offline measurement.....	138
Figure 6.5 Comparison between (a) OMSM and (b) Talyrond measurement .....	138
Figure 6.6 Fitted residual plot in the observation order .....	142
Figure 6.7 Fitted residual plot (versus factors) .....	143
Figure 6.8 Normal probability plot of residuals .....	144
Figure 6.9 3D response surface graphs .....	145
Figure 7.1 Framework of corrective machining with the aid of OMSM .....	150
Figure 7.2 Data processing for profile corrective machining.....	151
Figure 7.3 Data processing for surface corrective machining.....	153
Figure 7.4 Simulated MLA measurement map .....	153
Figure 7.5 Process of MLA individual feature analysis.....	154
Figure 7.6 Symmetric folding of profile error derived from OMSM.....	157
Figure 7.7 Workflow of profile corrective machining experiment .....	158

Figure 7.8 Profile error correction results .....	158
Figure 7.9 (a) OMSM point clouds and (b) the corresponding reconstructed surface.....	160
Figure 7.10 Corrective machining tool path generation.....	161
Figure 7.11 Holistic error (a) before and (b) after corrective machining.....	162
Figure 7.12 Individual error distribution (a) before and (b) after corrective machining .....	163
Figure 7.13 Bar graph of MLA form error.....	164

## List of abbreviations

AFM	Atomic force microscope
ANOVA	Analysis of variance
CAD	Computer aided design
CCD	Central composite design
CGH	Computer generated hologram
CMM	Coordinate measurement machine
DOE	Design of experiment
DPA	disparity pattern autostereoscopic
DRI	Dispersed reference interferometry
ELID	Electrolytic in-process dressing
FTS	Fast tool servo
HMD	Head-mounted display
HTM	Homogeneous transformation matrix
LVDT	Linear variable differential transformer
MIRI	Mid-Infrared Instrument
MLA	Micro-lens array
NPL	National Physics Laboratory
NURBS	Non-uniform rational B-splines
OAI	Off-axis illumination
OMSM	On-machine surface measurement
PAL	Progressive addition lenses
PCC	Pearson's correlation coefficient
PMD	Phase measuring deflectometry
PSI	Phase shifting interferometry
PV	Peak to valley
PZT	Piezoelectric translator
RBF	Radial basis function
RMS	Root mean square
RSM	Response surface methodology
SLD	Superluminescent diode
SPDT	Single point diamond turning

SPM	Scanning probe microscopes
STM	Scanning tunnelling microscope
STS	Slow tool servo
UPG	Ultra-precision grinding
UPP	Ultra-precision polishing
UPR	Undulations per revolution
UPRM	Ultra-precision raster milling
WLI	White light interferometry
WSI	Wavelength scanning interferometry

## List of Symbols

$\rho_i$	Radial distance (Cylindrical coordinate)
$\theta_i$	Polar angle (Cylindrical coordinate)
$(x_i, y_i, z_i)$	Surface points (Cartesian coordinate)
$R_w$	Radius of workpiece
$f$	Feedrate
$S$	$C$ axis rotation speed
$N_\theta$	Number of programmed points per revolution
$F(\cdot)$	Surface function
$A_x$	Sinusoidal grid amplitude in $X$ direction
$A_y$	Sinusoidal grid amplitude in $Y$ direction
$\lambda_x$	Sinusoidal grid wavelength in $X$ direction
$\lambda_y$	Sinusoidal grid wavelength in $Y$ direction
$\varphi_x$	Sinusoidal grid phase in $X$ direction
$\varphi_y$	Sinusoidal grid phase in $Y$ direction
$R_c$	Tool tip radius
$\psi$	Tool tip included angle
$\gamma$	Tool rake angle
$\alpha$	Tool clearance angle
$f_\rho(\rho, \theta)$	Intersection profile in the radial plane
$f'_\rho(\rho, \theta)$	First order derivative of the radial plane intersectional profile
$f''_\rho(\rho, \theta)$	Second order derivative of the radial plane intersectional profile
$g_{y_q}(y_q, \rho, \theta)$	Intersection profile in the normal plane
$g'_{y_q}(y_q, \rho, \theta)$	First order derivative of normal plane intersectional profile
$\varphi_i$	slope angle at $(\rho_i, z_i)$ in the radial plane intersection profile
$(\rho_i^{'}, z_i^{'})$	Compensation position in the radial plane
$\Delta z$	Tool shift value in $Z$ direction
$h_{envelope}$	Profile topography height
$S_q$	Root mean square height
$F_{vibration}$	On-machine vibration frequency

$\lambda_{topo}$	Wavelength of the surface topography of interest
$F_{topo}$	Frequency of the surface topography of interest
${}_k^j T$	Transformation matrix from coordinate $k$ to coordinate $j$
${}_k^j T_l$	Location transformation matrix
${}_k^j T_{le}$	Location error transformation matrix
${}_k^j T_m$	Motion (translation or rotation) transformation matrix
${}_k^j T_{me}$	Motion (translation or rotation) error transformation matrix
$[p_{kx}, p_{ky}, p_{kz}]$	Location vectors from coordinate $k$ to coordinate $j$
$E_{ZX}$	$X$ axis straightness error in the $Z$ direction
$E_{ZC}$	$C$ axis axial motion errors
$E_{BC}$	$C$ axis tilt motion errors
$E_{BOC}$	Squareness error between the $C$ axis and $X$ axis in the $X-Z$ plane
$Y$	Estimated response in response surface model
$X_i$	Input variables in response surface model
$\varepsilon$	Random error in response surface model
$\{\alpha_i, \alpha_{ii}, \alpha_{ij}\}$	Coefficient term in response surface model

# 1 Introduction

## 1.1 Research background

High precision optical freeform surfaces, featuring high functional performance, are playing an increasingly important role in modern imaging and illumination [1-4]. Compared to conventional spherical optics, the use of freeform components is beneficial to simplify the system structure, enhance optical performance, and improve product integrities. Optical freeform surfaces are currently classified into three groups [5], which are respectively continuous freeform surfaces, patterned structured surfaces and conjunct surfaces with steps or stiff edges. Among them, structured surfaces are classified as freeform surfaces since they have the same aspects in regard to fabrication, alignment and measurement. Owing to the optical and physical properties, they are increasingly used in the high-value-added photonics and telecommunication products such as laser beam printers and scanners, head mounted displays, progressive lens moulds, fibre optic connectors, and advanced automotive lighting systems [6-9]. To ensure the functionality of the freeform components, these surfaces are required to have sub-micrometre form accuracy and nanometre surface topography [10]. However, the geometrical complexity and high precision demand imposes considerable challenges on the existing fabrication and measurement technologies.

Owing to the technical evolution in advanced manufacturing, ultra-precision machining technologies have been developed for the deterministic fabrication of high precision freeform surfaces including tool servo turning, ultra-precision raster milling, ultra-precision grinding and polishing [11-14]. Among them, slow tool servo (STS) machining provides an important means for generating non-rotationally symmetric optical freeform surfaces without the need for any subsequent processing. It has the advantages of simpler setup, faster cycle times and better machining accuracy over other techniques. Successful STS machining depends largely on the proper selection of cutting conditions, machine characteristics, and tool path strategies. Besides,

many external factors still induce surface deviations from the design specification, such as machine structural errors, vibration and thermal deformation. Therefore, the measurement and characterisation processes become the key to evaluating the machined surface quality and further improving machining processes [5, 15]. Metrology instrumentation has made great progress with the development of new principles, mathematical algorithms and high novel precision sensors [10, 16, 17].

For some demanding advanced manufacturing, such as large telescope optics polishing [18] and reel to reel thin film fabrication [19], offline or post-process measurement is not desirable in terms of process productivity. In order to increase metrology availability and efficiency, a shift in the approach of metrology from offline lab-based solutions towards the use of metrology upon manufacturing platforms is imperative [10, 11, 15]. Furthermore, the metrology integration preserves the consistency between the machining and measurement coordinates. The errors induced by removal and remounting of workpieces cannot be neglected in high precision applications and would deteriorate the surface quality if re-machining processes need to be carried out [20].

In summary, the development of on-machine surface measurement (OMSM) will enable the reduction of measurement cycle time as well as the potential improvement of surface accuracy for ultra-precision machining processes. However, there are still several technological gaps to be bridged to successfully achieve machining-measurement integration. In terms of surface generation in ultra-precision freeform machining the process needs to be deeply investigated to discover salient measurands for the subsequent OMSM. Since the measurement process is operating in the manufacturing environment, the effects on the OMSM from machine tools should be comprehensively evaluated and the systematic errors must be compensated. Moreover, integrated metrology will not only allow the assessment of machined surfaces just-in-time, but also provide valuable feedback to the process control. Therefore, potential applications

with the assistance of OMSM need to be explored to exploit the integration benefits to further enhance the ultra-precision machining performance.

## 1.2 Aims and objectives

To address the key issues and problems identified in the previous section, this research work aims to prove that the proposed OMSM is suitable for informing deterministic process investigation and corrective machining to improve the performance of ultra-precision turning process.

The objectives of the study are as follows:

- To review state-of-the-art OMSM applications in ultra-precision machining processes and conclude several considerations for effective metrology integration;
- To theoretically and experimentally investigate the surface generation in the ultra-precision turning of optical freeform surfaces;
- To develop and calibrate OMSM in ultra-precision machine tool environment, and validate the performance by comparison with offline measurement;
- To develop a deterministic process investigation with the assistance of OMSM and establish an empirical model to describe the relationship between processing parameters and machined surface form error;
- To explore corrective machining strategies with the assistance of OMSM to further improve the ultra-precision machined surface accuracy.

## 1.3 Research methodology and thesis structure

With the aim of improvement of manufacturing accuracy and efficiency, this research work presents the development and application of OMSM for ultra-precision turning process.

Ultra-precision turning with STS technique provides an important means for generating non-rotationally symmetric surfaces without the need for any subsequent processing. It has the

advantages of simpler setup, faster cycle times and better machining accuracy over other techniques. Surface generation in STS machining will be investigated theoretically and experimentally to achieve successful machining and provide essential measurands for the subsequent OMSM.

Selection and integration of OMSM should meet the requirement of ultra-precision turning process. State-of-the-art OMSM and corresponding applications in ultra-precision machining processes will be reviewed. The advantages and disadvantages of different OMSM types will be analysed. Moreover, since the measurement process operates in the manufacturing environment, the effects on the OMSM from machine tools will be evaluated and the systematic errors will be compensated, such as the machine tool vibration, kinematic error and probe linearity error.

Furthermore, potential applications with the assistance of OMSM need to be explored to exploit the integration benefits to further enhance the ultra-precision turning performance. With OMSM, process investigation aims to establish the relationship between process parameters and machined surface error, while corrective machining can be used to further improve the profile and surface accuracy of freeform components. As OMSM preserves the coordinate system between the machining and measurement, the process investigation and corrective machining will be carried out in a deterministic manner.

The overall research framework is illustrated in Figure 1.1. The thesis is organized into eight chapters.

- Chapter 1 gives a brief introduction of the research background, aims and objectives of the research.
- Chapter 2 reviews the current ultra-precision manufacturing techniques for optical freeform surfaces. The topics include an overview of the applications of optical freeform surfaces, state-of-the-art ultra-precision machining as well as surface measurement and characterisation techniques.

- Chapter 3 shifts the emphasis to the comprehensive review of OMSM and applications in the ultra-precision machining processes. The benefits and considerations on the integration of metrology on the manufacturing platforms are discussed. The merits and limitations among different OMSM types are compared and discussed in detail.
- Chapter 4 presents a theoretical and experimental study of surface generation in ultra-precision machining of optical freeform surfaces using STS technique. The machining methodology and surface generation simulation analysis are respectively presented. Machining experiments of freeform surfaces are carried out to validate the proposed method. The chapter aims to provide an application basis and a priori information for the subsequent OMSM development.
- Chapter 5 describes the development and calibration of the OMSM system. This chapter presents details of the implementation of a single point robust interferometer onto an ultra-precision turning machine. Three aspects of OMSM calibration are taken into consideration, including on-machine vibration tests, machine kinematic error mapping and linearity error calibration. Both theoretical and experimental investigation has been conducted to prove the validity of the proposed calibration methodology and the effectiveness of OMSM.
- Chapter 6 investigates the effect of process parameters on the surface form errors in ultra-precision cylindrical turning processes. With the aid of OMSM, the process investigation can be carried out in a more deterministic manner over the conventional investigation with offline measurement. An empirical model based on response surface methodology has been established and validated with the experimental results.

- Chapter 7 proposes a corrective machining technique with the aid of OMSM to further improve the accuracy of diamond turned surfaces. The integration of OMSM preserves the consistency between the machining and measurement coordinates. In-situ surface error processing, profile and surface correction experiments were investigated to validate the proposed methodology.
- Chapter 8 presents an overall conclusion of this research work and some suggestions for the future work.

## 1.4 Contributions to knowledge

This research work in this thesis includes the following contributions to knowledge:

- The theoretical and experimental investigation of surface generation in freeform machining process using STS technique, which can provide an important means to model surface generation and understand the machining phenomenon
- The establishment of a metrology-integrated ultra-precision manufacturing platform with the development of on-machine scanning strategies and the validation of OMSM performance comparable to offline calibrated instrumentation
- The demonstration of a systematic calibration methodology for single point OMSM to improve the measurement fidelity, including on-machine vibration analysis, selective kinematic error mapping and linearity error correction
- The development and validation of a deterministic process investigation with the assistance of OMSM to empirically model the form error of ultra-precision machined surface
- The investigation and demonstration of profile/surface characterisation and corrective machining methodology with the assistance of OMSM to further improve the ultra-precision machined surface accuracy

## **1.5 Publications**

The work in this thesis has produced 3 peer reviewed journal papers, 11 conference papers and 2 book chapters. A full publication list can be found in the Publications and Awards section at the end of this thesis.

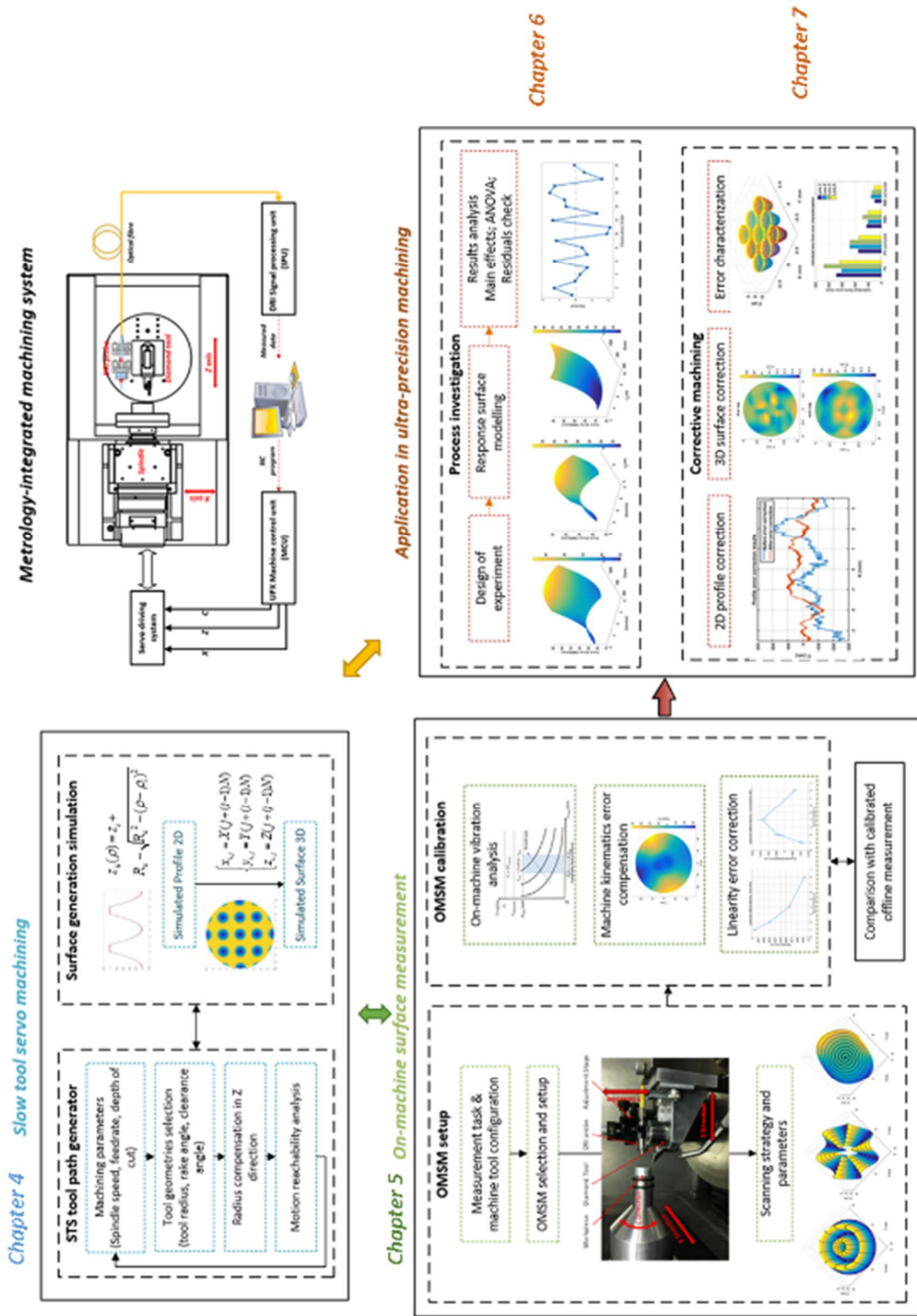


Figure 1.1 The overall research framework

## 2 Review of ultra-precision machining and surface metrology

### 2.1 Introduction

High precision freeform surfaces are gaining more and more interest in numerous optical imaging and illumination systems [2, 11, 21]. According to Jiang's classification, there are three types of freeform surfaces, which are continuous freeform surfaces, patterned structured surfaces and conjunct surfaces with steps or stiff edges [5]. Structured surfaces, such as micro-lens arrays, V-grooves, and pyramid arrays belong to freeform surfaces since they have the same aspects in regard to fabrication, alignment and measurement. Differing from conventional simple surfaces (such as plane, cylinder and sphere), freeform surfaces are more geometrically complex, which normally have no symmetry in rotation or translation [21].

However, due to the geometrical complexity and demanding requirements, there are still many challenges in the machining and measurement of precision optical freeform surfaces with sub-micrometric form accuracy and nanometric surface finish. This chapter will review state-of-the-art ultra-precision machining and surface metrology for highly demanding optical freeform surfaces. Firstly, the demand and application of precision optical freeform surfaces are described. For the comprehensive understanding of how these surfaces are generated, the advanced ultra-precision machining technologies are then reviewed, such as ultra-precision turning using tool servo techniques, ultra-precision milling, ultra-precision grinding and ultra-precision polishing processes. In order to assess the surface quality and functionality, measurement and characterisation techniques for ultra-precision optical freeform surfaces are also presented.

### 2.2 Optical freeform surfaces and applications

Three types of optical freeform surfaces are shown in Figure 2.1, including continuous freeform surfaces, patterned structured surfaces and conjunct surfaces with steps or stiff edges [5].

Continuous smooth surfaces are described by a mathematical formula or modelled in Computer Aided Design (CAD) software [22]. Figure 2.1 (a) shows a mould for freeform lens which is reconstructed from Zernike polynomial functions [23].

Structured surfaces are composed of arrays of features, which are designed for specific functionality. A Fresnel lens (shown in Figure 2.1 (b)) is a typical example and widely used in lighting and solar concentration applications.

Conjunct surfaces are commonly based on a single substrate, containing a set of continuous optical surfaces which are distributed in discrete space. Figure 2.1 (c) shows a Mid-Infrared Instrument (MIRI) spectrometer mirror, which performs the function of light wavelength and spatial splitting in the James Webb Space Telescope [24].



**Figure 2.1 Examples of (a) continuous smooth surface; (b) structured surface; (c) conjunct surface**

Nowadays optical freeform surfaces are increasingly applied in reflective, refractive, and diffractive optical systems [3, 25]. The applications can be mainly categorized into high performance imaging and illumination.

### 2.2.1 Imaging applications

Due to the featured optical performance, freeform optics are able to eliminate the optical aberration, increase the depth of field and expand the field of view. Moreover, the reduction and miniaturization of imaging system is enabled with the application of optical freeform surfaces [1].

The first well-known application of optical freeform surfaces in commercial product was the Polaroid SX-70 folding Single Lens Reflex camera (shown in Figure 2.2), which was introduced in 1972 [26]. Two freeform optical lenses were used for aberration correction in this foldable off-axis viewing system.



**Figure 2.2 Polaroid SX-70 folding Single Lens Reflex camera [26]**

Freeform surfaces can be also commonly found in the eyeglasses. Progressive addition lenses (PAL) is characterised by a gradient of increasing lens power, which starts at the top of the lens and reaches a maximum addition power at the bottom of the lens [27]. The additional lens power required for clear vision can be therefore flexibly adjusted. Wearers can tilt their head to sight through the most appropriate part of the vertical progression for different viewing distances.

Another trending application of high-precision freeform surfaces is head-mounted display (HMD). With the adoption of freeform prisms, the projection system can be configured with a short throw distance and a wide projection angle. Freeform prisms can fold the optical path, making the optics smaller, thinner and lighter than with conventional coaxial optics. The first application of freeform prisms in the HMD products was carried out by Olympus Corporation [28]. As shown in Figure 2.3, researchers also attempted to apply multiple freeform prisms into the HMD design, aiming for a wider field of view and lower f-number while maintaining a compact, lightweight, and non-intrusive form factor [7].

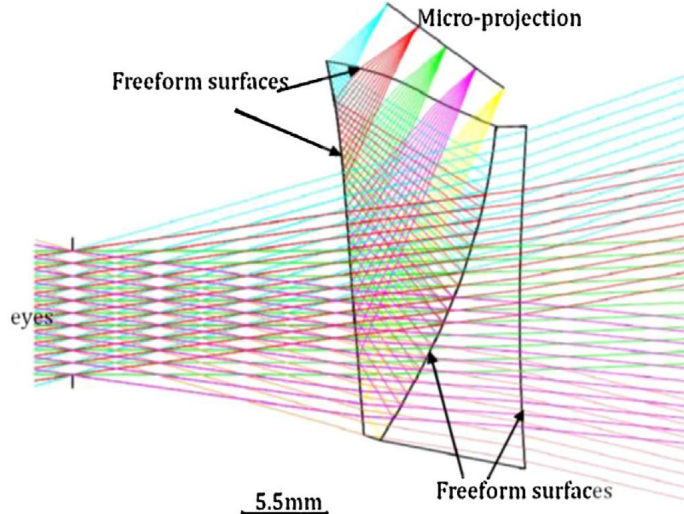


**Figure 2.3 Layout of the see-through HMD with the adoption of freeform prisms [7]**

## 2.2.2 Illumination applications

For off-axis illumination (OAI) in optical lithography, a freeform lens array was used to generate desired OAI patterns and improve the illumination efficiency [29]. The optical design was based on the Snell's law and the conservation law of energy. Through the simulation analysis, the irradiance distribution of OAI patterns can be well controlled with a maximum uniformity of 92.45% and a maximum efficiency of 99.35% while the traditional design can only achieve the efficiency less than 93%. In addition, the use of freeform lens arrays has the benefits of reducing the exposure system complexity and better tolerance to the intensity variations of the input laser beam. Figure 2.4 (a) and Figure 2.4 (b) respectively show different design of freeform lens arrays and corresponding illumination spots.

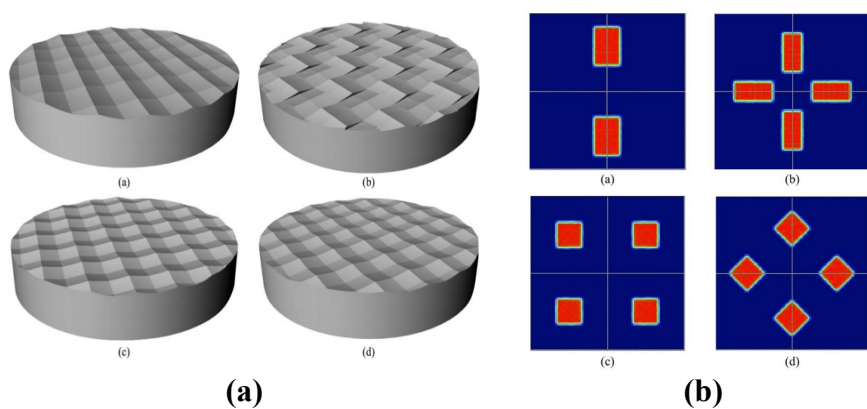


**Figure 2.4 Different design of freeform lens array and corresponding illumination spots**

[29]

The recent emergence of LED illumination has complicated the non-imaging system design due to the variation of source characteristics in different LED designs [30]. Particularly, light intensity distribution must be well controlled to achieve the desirable functionality. Optical freeform surfaces are able to provide uniform and high quality lighting performance for LED illumination application. For example, a freeform micro-lens array was designed to abandon restrictions from the multiple and irregular radiation patterns of existing LED products [31]. Based on Snell's law and the edge-ray principle, the secondary optics can redistribute any type of radiation profile onto the target surfaces to achieve prescribed uniform illuminations. According to specific illumination requirements, the surface shape of the single freeform micro-lens was designed using the ray tracing method and B-spline fitting. Some modules of freeform micro-lens optics were constructed to achieve different styles of illumination. Figure 2.5 illustrates the schematic structure and ray path of the micro-lens optical design for LED illuminations.

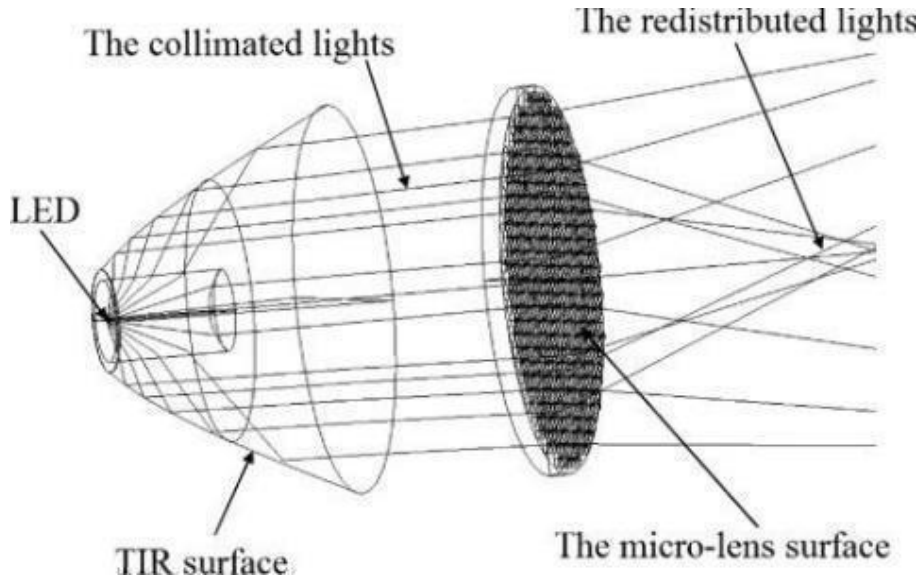


**Figure 2.5 Schematic ray path of the freeform micro-lens optics design for LED illumination [31]**

Freeform optics are also popular in automotive lighting applications. For example, a 3D freeform device with Köhler integration was designed as an LED illuminator (shown in Figure 2.6). The adoption of freeform surfaces was proved to fully control a bundle of rays issuing from

the LED chip corners, which allowed intensity patterns quite insensitive to the LED source positioning errors to be obtained [32].



**Figure 2.6 A freeform Köhler integrator for automotive lighting applications [32]**

With the specific optical functionality and exceptional performance, the application of the optical freeform surfaces has attracted a lot of interest from industry and researchers. However, the geometrically complex design imposes considerable challenges on the existing fabrication and measurement technologies. Current ultra-precision machining and measurement technology for optical freeform surfaces will be reviewed in the following sections.

## 2.3 Ultra-precision machining techniques

Ultra-precision machining is capable of producing optical surfaces with nanometric surface roughness and sub-micrometric form accuracy [33-35]. Differing from traditional simple surfaces, freeform surfaces usually have no symmetry in rotation or translation, which requires multi-axis ultra-precision machining technologies. The current ultra-precision machining methods include ultra-precision turning (with slow tool servo and fast tool servo techniques), ultra-precision raster milling, ultra-precision grinding and ultra-precision polishing.

### 2.3.1 Ultra-precision turning

Ultra-precision turning, also termed as Single Point Diamond Turning (SPDT), has been developed to cut nonferrous metals and plastics since 1960s [36]. Single crystal diamond tools

have the advantages of ultra-high hardness, high wear-resistance and good heat conductivity. Moreover, they can be made with a very sharp cutting edge down to 50 nm edge radius. Figure 2.7 shows examples of commercial single crystal diamond cutting tools. Super smooth finished surfaces (down to several nanometres) can be directly machined on nonferrous metals and plastics by SPDT without the need for subsequent post processing [37-39].

With the development of advanced servo control, two technologies termed as Slow Tool Servo (STS) [40] and Fast Tool Servo (FTS) [41] empower ultra-precision turning to be capable of producing non-rotationally symmetric freeform surfaces. STS technology enables the high speed spindle into the position controlled mode. Arbitrary 3D tool trajectories can be accordingly programmed under cylindrical coordinates to generate freeform shape. Figure 2.8 shows the configuration of a STS machine [42]. The STS machining can be applied to fabricate lens arrays, torics, freeform polynomials, Zernike surfaces, etc. As shown in Figure 2.8, face STS machining is configured when Z axis is used as the oscillation axis. If the tool holder is rotated 90°, cylindrical STS machining can be performed when X axis is used as the oscillation axis.



**Figure 2.7 Commercial single crystal diamond cutting tools**

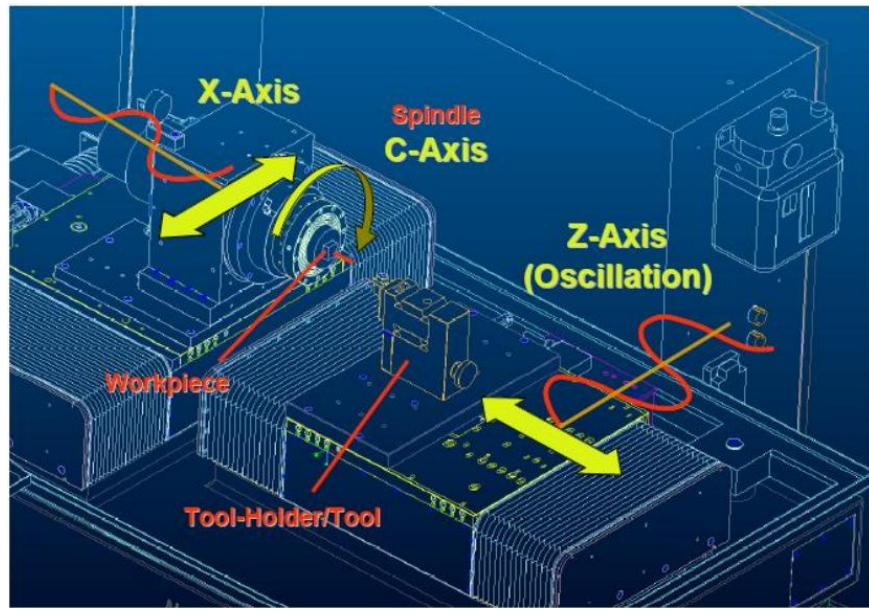


**Figure 2.8 Configuration of slow tool servo machining [42]**

FTS machining is commonly used to fabricate optical micro-structures with short wavelength features [43-45]. It utilizes an additional electro-mechanical device (piezo-actuator or voice coil motor) on the feeding axis of the machine tool. A FTS device can achieve very high motion frequency up to several kHz. Figure 2.9 shows a commercial FTS device [46]. The device comprises a voice coil motor, air bearing with counter balance and linear scale feedback. An external control system drives the FTS device based on high resolution angular position from the work spindle and the linear position of the machine translational slide.

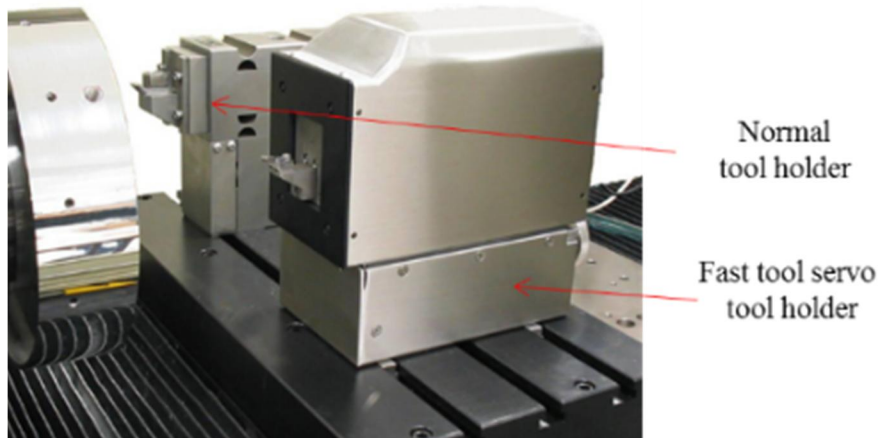


**Figure 2.9 Nanotech fast tool servo device [46]**

From the cutting motion perspective, the working principle of STS and FTS are similar, which is to drive the cutting tool in and out of the workpiece in synchronization with the spindle

rotation and translational slide. The main difference between STS and FTS is the bandwidth of the tool servo motion. STS is more applicable to fabricate freeform surfaces with larger strokes but slow variation while FTS is more suitable for short wavelength structured surfaces. By comparison, the STS can achieve better surface finish and form accuracy. Additionally, it takes full advantage of the existing machine control system without expensive attachment.

### 2.3.2 Ultra-precision raster milling

Ultra-precision raster milling (UPRM) is another method to fabricate freeform surfaces with sub-micrometric surface accuracy[47, 48]. In the UPRM process, a diamond cutting tool is rotated on the main spindle and moved relative to the workpiece along a series of raster scanning lines with defined spacing. The simultaneous motion of multiple axes is required for generation of arbitrary 3D tool paths. Figure 2.10 illustrates the UPRM configuration on a five-axis ultra-precision machine tool. The machine is equipped with three linear axes and two rotational axes. UPRM is an intermittent cutting process, which inevitably imposes cyclic cutting and thermal impact stresses onto the diamond tool. Therefore, it is usually employed for cutting soft and ductile materials such as aluminium and copper. Previous studies related to UPRM mainly focus on spindle vibration effects [49] and tool wear issues [50].



**Figure 2.10 Raster milling configuration on a five-axis ultra-precision machine tool [49]**

### 2.3.3 Ultra-precision grinding

Ultra-precision grinding (UPG) is primarily used for the generation of optical freeform surfaces, which are made from hard and brittle materials [13]. Under the ductile-regime grinding mode, UPG is able to achieve nanometric surface finish and minimal subsurface damage [51]. The development of UPG machine tools has been motivated by demands from freeform optics and semiconductor components. Moore Nanotechnology Systems developed a 4-axis grinding machine tool to produce aspheric and freeform optical moulds [52]. The machine is featured with high dynamic stiffness, ultra-precision motion control, and long term thermal stability. As shown in Figure 2.11, the grinding wheel is set perpendicular to the workpiece surface. The included angle between grinding spindle axis and surface tangent is kept constant over the entire grinding cycle. The normal grinding process ensures the tool geometry errors not to transfer into the surface form.

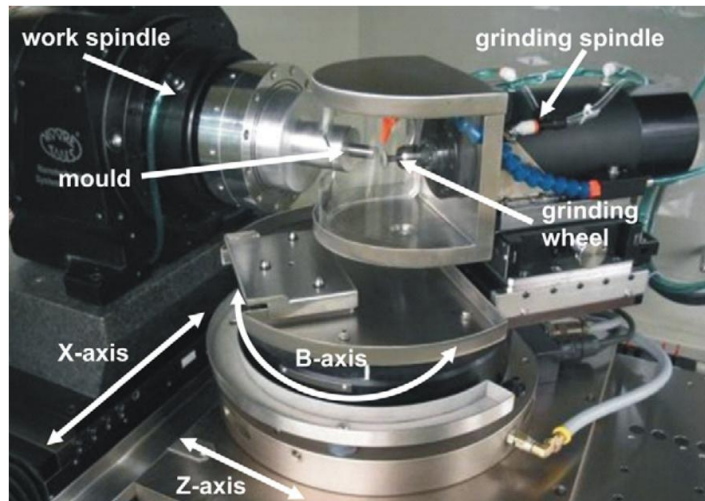


**Figure 2.11 Wheel-normal ultra-precision grinding of optical moulds [52]**

Besides, a stable condition of the grinding wheel over the whole processing cycle is the prerequisite for successful machining. Electrolytic In-process Dressing (ELID) technology, invented by Ohmori [53], is used to generate an oxide layer at the surface of the anode continuously, which prevents excessive grinding wheel wear. With optimal process parameters, a dynamic equilibrium of oxide layer growth and removal can be formed. This will result in stable

dressing conditions and a deterministic grinding process. The schematic of ELID grinding is illustrated in Figure 2.12. ELID technology has successfully been applied to ultra-precision grinding of planar, spherical and freeform optical lenses [54-56]. However, there are still many challenges in UPG, such as the wheel wear for long term grinding processes and form deviation over large scale ground surfaces [13].

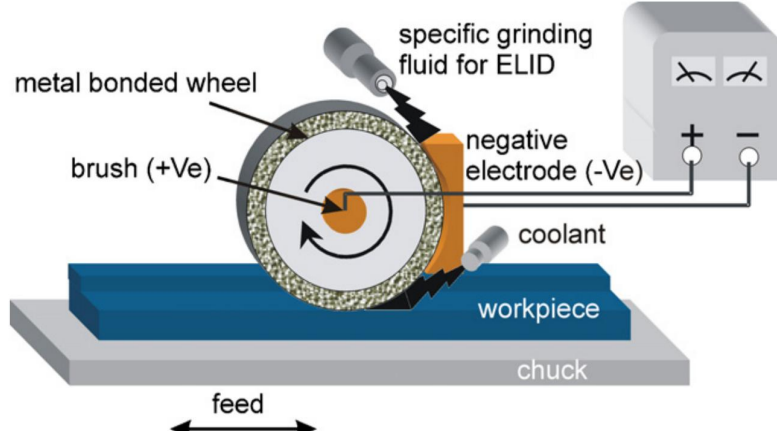


**Figure 2.12 The schematic of ELID grinding [53]**

#### 2.3.4 Ultra-precision polishing

Current ultra-precision polishing (UPP) technologies for optical freeform surfaces include bonnet polishing [57], fluid jet polishing [58, 59], magnetorheological finishing [60, 61] and so forth. As a finishing process, UPP is reported to have the capability to improve surface roughness to nanometre and sub-nanometre levels [62].

Figure 2.13 shows the bonnet polishing of an optical torus surface on a commercial 7-axis UPP machine [63]. With a flexible and conformal bonnet polishing tool and computer controlled precession process [64], uniform nanometric surface roughness as well as high precision local form accuracy can be routinely achieved. Besides optical glasses, UPP has been also successfully applied on variety materials such as CoCr alloy implants material [65] and mould steels [66].



**Figure 2.13 Ultra-precision bonnet polishing of a freeform optics [63]**

Besides the ultra-precision freeform machining technologies reviewed above, other methods such as diamond micro chiselling [67], micro milling [68] and vibration assisted cutting [69] are emerging as the new solutions to the fabrication of complex freeform surfaces.

## 2.4 Surface measurement and characterisation

Although ultra-precision machining is able to fabricate surfaces with high accuracy, many factors still induce surface deviations from design, involving environmental factors, machine structural errors, vibration and tool wear [70-73]. Consequently measurement and characterisation become the key to evaluating the high precision surface quality as well as the ultra-precision machining processes. Due to the geometric complexity, the measurement and characterisation of freeform surfaces is more challenging than the conventional simple surfaces. The state-of-the-art development of the measurement and characterisation of freeform surfaces will now be reviewed.

### 2.4.1 Instrumentation for surface measurement

To meet the demand of measurement for ultra-precision freeform surfaces, metrology instrumentation has made great progress with the development of new principles, mathematical

algorithms and high precision sensors [10, 74]. The techniques can be classified into contact and non-contact optical types depending on the nature of probes.

#### 2.4.1.1 Contact instrument

Contact instruments include stylus profilometers and coordinate measurement machines (CMM). Contact stylus profilometry has been widely used in form and topography measurement of ultra-precision machined surfaces [75]. A stylus with a cone-shaped spherical tip is traversed over the workpiece surface and a transducer measures the vertical displacement with the resolution down to sub-nanometres over a range up to tens of millimetre. Equipped with an extra translational stage, a stylus profilometer is able to measure areal surfaces in a raster scanning mode. The transducer is the decisive part which determines the overall measuring accuracy and dynamic range. The development of the phase grating interferometer transducer, which was independently developed by Taylor Hobson [76] and Jiang [77], significantly improved the dynamic measurement range for stylus profilometry [16]. The schematic of phase grating interferometer transducer in stylus profilometry is shown in Figure 2.14. A laser beam is split into two parts by a beam splitter. When the stylus traverses across the machined surface, the light reflected from the reflector interferes with the light from the reference mirror. The phase of the generated interference stripe is proportional to the displacement of the reflector, and the vertical displacement of the tip of the stylus is accordingly obtained.

One of the typical commercial profilometers is the PGI series provided by Taylor Hobson in UK [78], which is shown in Figure 2.15. In order to solve the nonlinearities in the measurement due to the arcuate movement of the stylus arm, a correction process is carried out automatically with mathematical optimization algorithms after the measurement of a standard certified sphere.

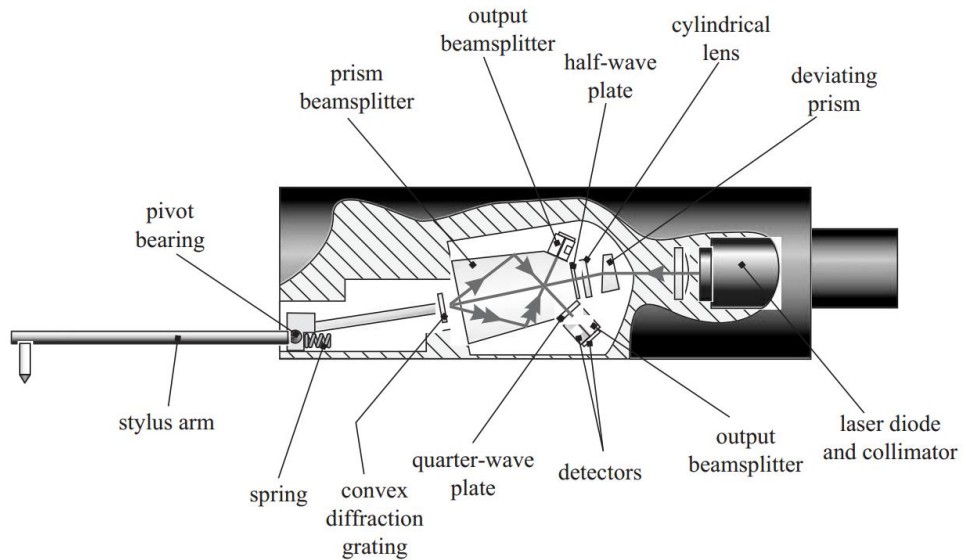


**Figure 2.14 Schematic of phase grating interferometer transducer in stylus profilometry**

[16]



**Figure 2.15 Taylor Hobson profilometer PGI series [78]**

Contact profilometry is preferred for measurement of large deviation freeform surfaces because of its high dynamic range. However, the contact stylus has the potential risk of scratching the ultra-smooth and soft surfaces [75]. Moreover, the measurement speed is relatively slow if areal surface measurement is undertaken.

Coordinate measuring machines (CMMs) are another common type of measurement instruments for freeform surfaces. Most CMMs are based on linear axes arranged under the

Cartesian coordinate system [79]. During the measurement, the linear carriages are moved in the coordinate axes, and the sensing probe acquires spatial coordinates of discrete points to represent the form and geometrical features. The probing system is the most crucial element in CMMs, which accounts for the overall measurement accuracy.

Nanometric resolution probing systems have been developed for measurement of ultra-precision machined surfaces. Two cutting edge examples are respectively shown in Figure 2.16 (a) and Figure 2.16 (b). The National Physics Laboratory (NPL) in UK designed a light-structure probe that has a low probing force of 0.2 mN and a probe tip deflection of 10  $\mu\text{m}$  [80]. The resolution of the probe was stated as 3 nm. The NPL micro-probe is commercially available on the 3D Ultra Precision CMM ‘Isara’ (shown in Figure 2.17) which is offered by IBS Precision Engineering [81].

Swiss Federal Office of Metrology (METAS) developed an innovative touch probe based on a parallel kinematic structure of flexure hinges, which was dedicated to traceable measurement for small parts with nanometre accuracy [82]. With the minimization of the moving mass and isotropic low stiffness, measurement repeatability of about 5 nm was achieved.

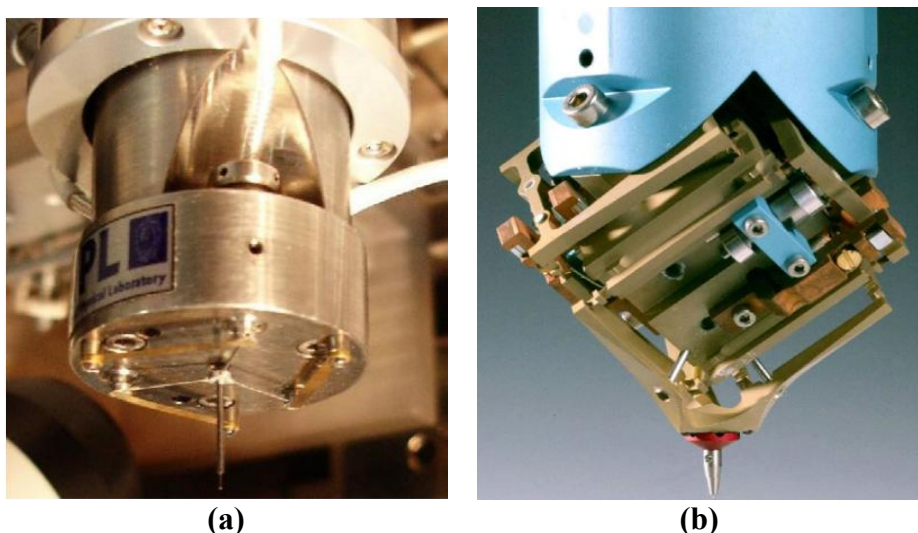


**Figure 2.16 Nanometric resolution probing systems developed by (a) NPL [80] and (b) METAS [82]**

CMMs have similar disadvantages as stylus profilometers. The relative slow scanning speed will cause a long time for the measurement of ultra-precision freeform surfaces that require large amounts of points to represent the surface geometry comprehensively.

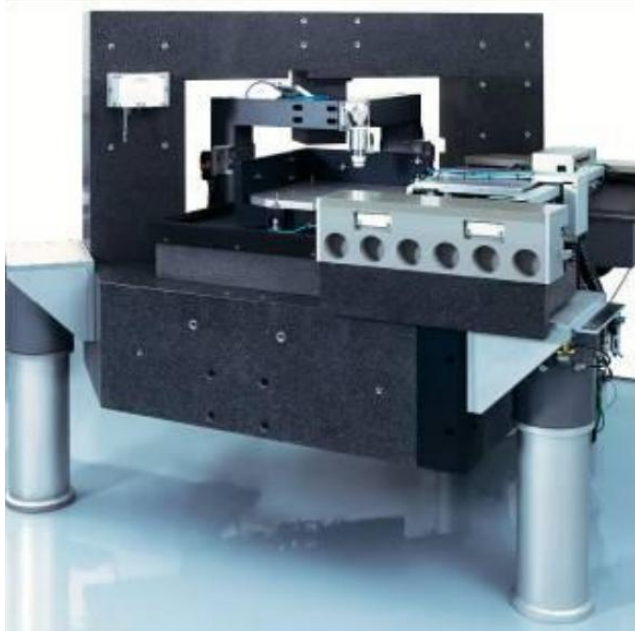


**Figure 2.17 Isara 400 3D ultra-precision CMM [83]**

#### **2.4.1.2 Non-contact optical instrument**

Ultra-precision machined surfaces can be also measured by non-contact optical measurement methods, which are divided into two types, namely interferometric and non-interferometric techniques. Interferometry is well established technique for rapid optical measurement of ultra-precision surfaces [84, 85]. Sub-nanometric resolution is achievable along the direction of beam propagation.

Two typical kinds of commercial interferometers are phase shifting interferometry (PSI) and white light interferometry (WLI). PSI is suitable for measuring super smooth surfaces with angstrom-level resolution [86]. Nevertheless, due to the phase ambiguity problem, it is limited to continuous surfaces measurement and the dynamic range is relatively low. When measuring large departure aspherical or freeform surfaces, correction components such as null lens [87] or Computer Generated Hologram (CGH) elements [88] are required. Figure 2.18 shows the

schematic principle of CGH. Through a CGH element, a spherical wavefront is changed into a specific wavefront according to the diffractive design. However, the fabrication of CGH is costly and difficult. Moreover, the measurement uncertainty tends to be increased due to the manufacturing error and alignment error [89].

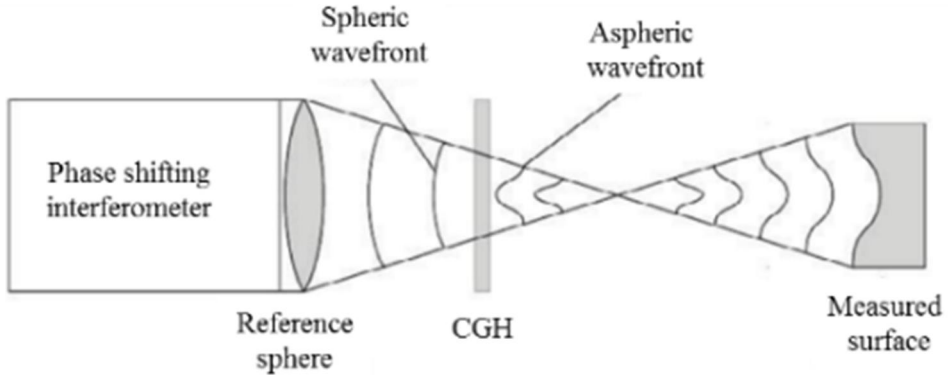


**Figure 2.18 Schematic principle of a CGH in interferometry**

To overcome the phase ambiguity problem of PSI, multiple wavelength interferometry has been developed, which has the same resolution as single wavelength technique while significantly increasing the measurement dynamic range. Luphos Gmbh developed a multiple fibre-based probing system based on multiple wavelength interferometry technique [90]. As shown in Figure 2.19 (a), the light from four independent laser sources is coupled into one fibre and transferred to the probes. After the light is reflected by the object and coupled back into the sensor, interference signals of the four lasers are transferred back to a spectral selection unit. The phase of the four interference signals are analysed individually to evaluate the absolute position of the measured object within the range of half of the synthetic wavelength. An open reference frame concept is proposed to compensate geometrical errors induced by errors of the scanning axes. As shown in Figure 2.19 (b), four fibre-based probes within the reference frame allows real-time calibration of scanning errors as well as determination of the accurate measurement probe position during the scanning.

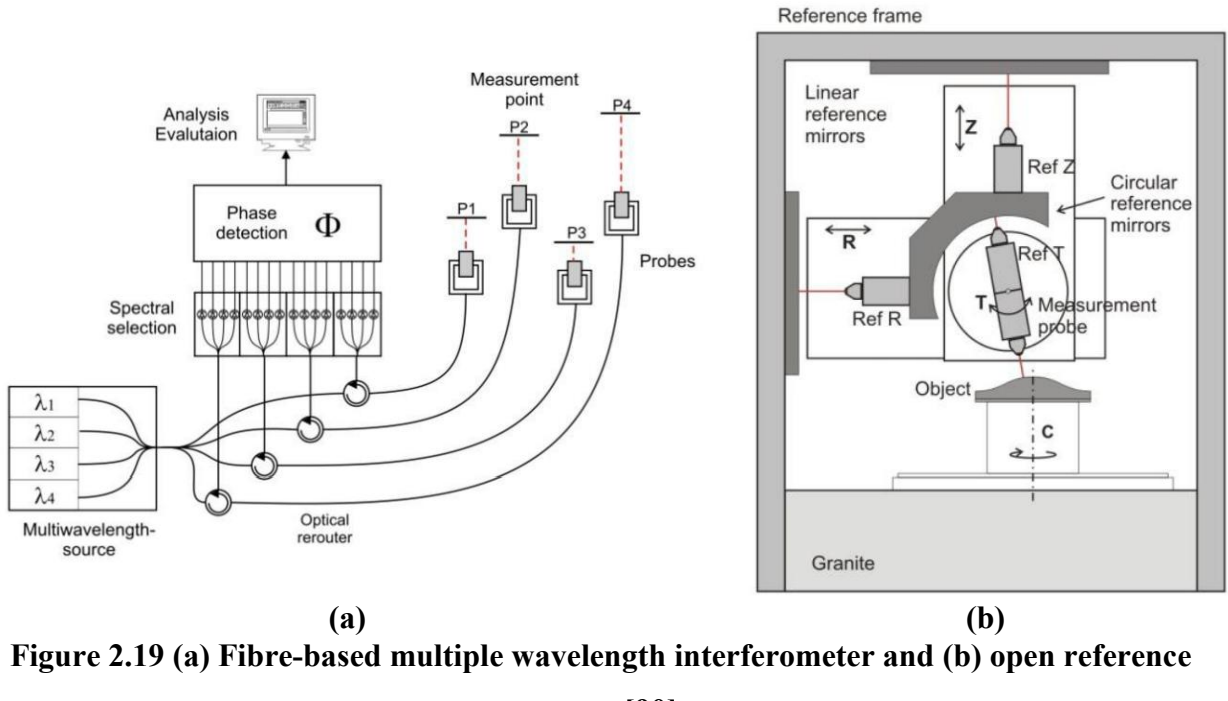


**Figure 2.19 (a) Fibre-based multiple wavelength interferometer and (b) open reference system [90]**

WLI uses broadband illumination such as super-luminescent diodes and halogen lamps. The absolute distance can be determined between the sample and the reference surface without the  $2\pi$  phase ambiguity problem [91]. Depending on the different scanning methods during the measurement, WLI can be classified into three categories, respectively vertical scanning interferometry [92], wavelength scanning interferometry [93] and dispersive interferometry [94, 95]. Figure 2.20 shows the general principle of vertical scanning WLI [96]. A beam of light from halogen lamp source is split into two paths. One path is projected onto the test surface, and the other is directed to the reference mirror. The two sets of light are then recombined together to generate interference fringes within the range of coherence length. A series of sequential interferograms are captured by the image sensor during the vertical scanning. Through the analysis of interferometric fringes, the height data can be reconstructed. Vertical resolution can be down to sub-nanometres while the lateral resolution is several microns, mainly depending upon the objectives used.

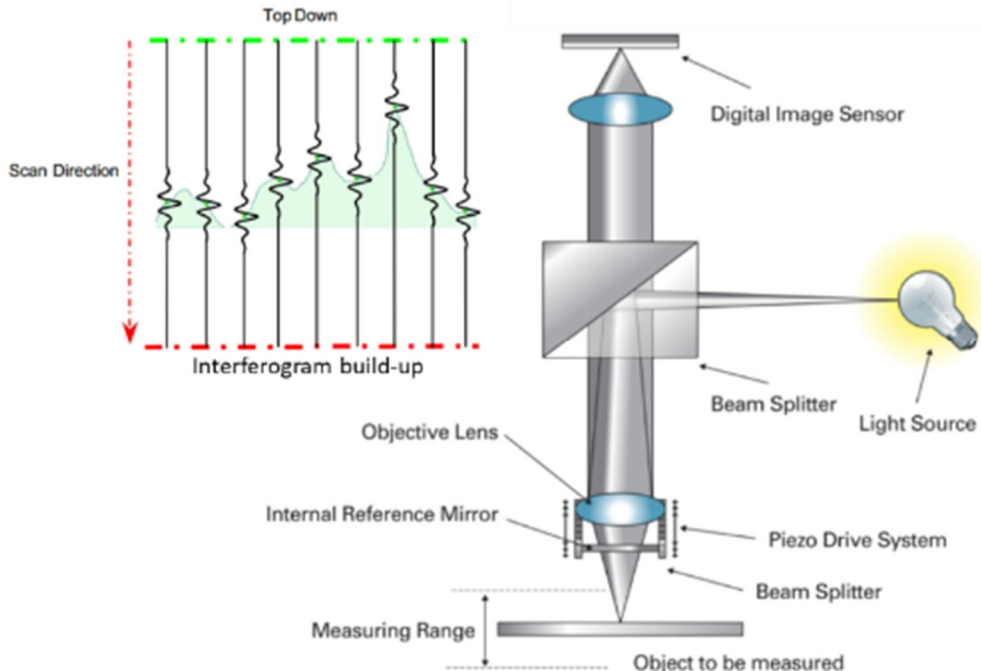


**Figure 2.20 Schematic principle of vertical scanning WLI [96]**

Optical interferometry has a drawback of extreme sensitivity to environmental disturbance such as mechanical vibration, air turbulence and temperature drift [97]. To solve this issue, high speed capturing and single shot method are needed. Although interferometry is considered unbeatable for measuring ultra-precision flat and sphere surfaces, complex freeform surfaces challenges the limits of interferometry. It is costly and difficult to customize the null lens or CGH elements for measuring freeform surfaces.

Phase-measuring deflectometry (PMD) is evolving as a non-interferometric method for freeform surfaces measurement without the need of compensating optics [98]. The working principle of PMD is illustrated in Figure 2.21. A projector generates sinusoidal fringes on a rear projection screen. Depending on the shape of the object, the resulting fringe image is distorted. A set of cameras observe the reflected image of sinusoidal fringes at the surface under testing. After the proper system calibration process, the gradient of measuring field can be derived from the deformed fringes. From the gradient data, the surface height information can be reconstructed by means of numerical integration [99-101].

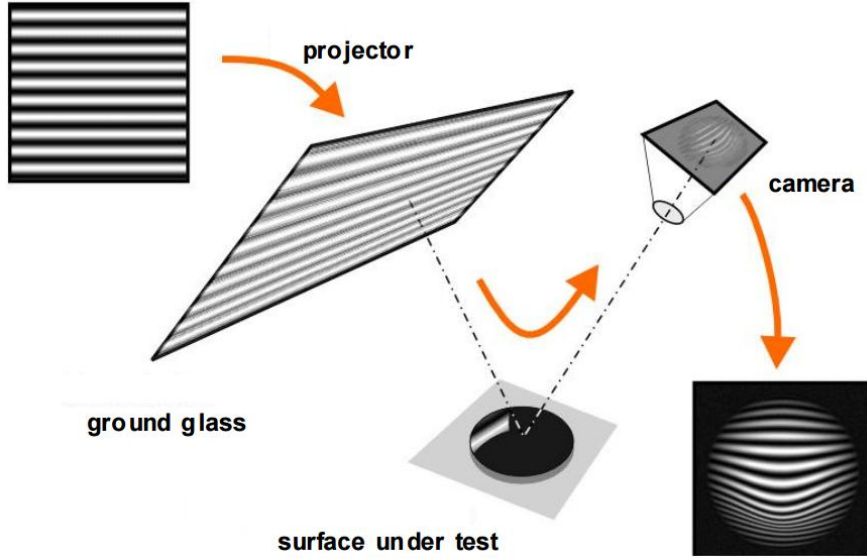


**Figure 2.21 Working principle of phase measuring deflectometry [98]**

With the development of innovative calibration algorithms [102], it has been applied in the measurement of progressive power eyeglasses [103], freeform car body panels [104], and large telescope mirrors [105]. As each derivation process will increase the data noise, the deflectometry methods also have the advantage for the measurement of surface curvature, since only the first derivative needs to be calculated. The major drawback of PMD is that it is limited to continuous surfaces due to the requirement for neighbouring pixels in the calculation of local surface slopes. The global reconstructed height accuracy is still limited to the level of several microns. In addition, parasitic reflections at the rear surface of transparent optics could disturb the measurement result [98, 106].

#### 2.4.2 Characterisation

An essential issue in the manufacturing process is to determine whether machined surfaces meet the requirements of the design specifications [107]. Surface features are generally characterised along the vertical direction by height parameters and along the horizontal direction by spatial parameters. According to the spatial wavelength, the surface features are divided into three types, namely form, waviness and roughness [108]. Form is the long wavelength of surface features while the fine irregularities on the surface, roughness, has a small scale. Waviness is a

periodic component at the intermediate scale. Figure 2.22 illustrates the surface features of a diamond turned optic sample.

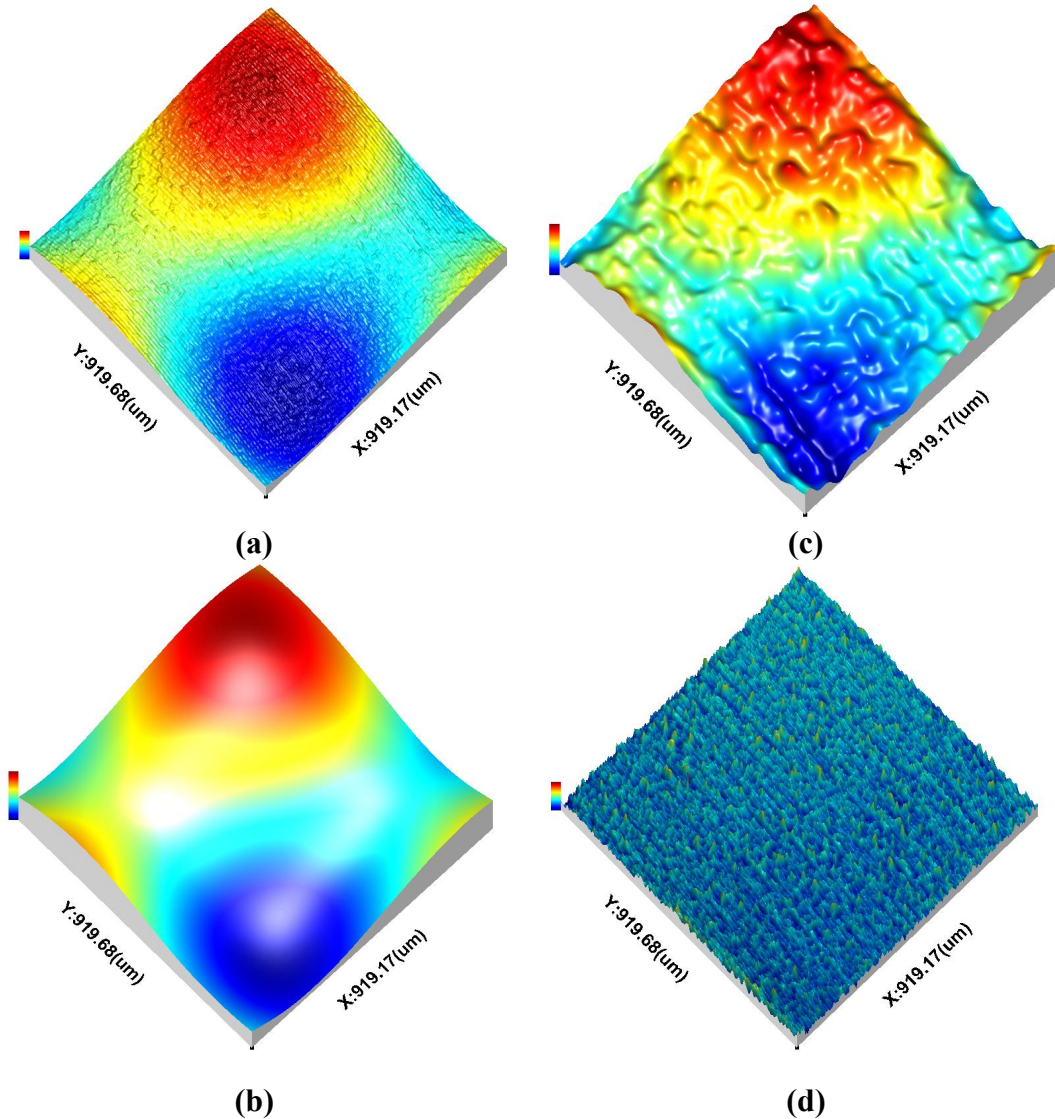


**Figure 2.22 (a) Original measurement; (b) form; (c) waviness; (d) roughness**

The separation and characterisation of the surface features in different wavelengths allow a direct assessment of the machining processes and prediction of the functional performance of the surfaces as well [10]. With the development of novel and robust mathematical tools, characterisation interests have shifted from profile to areal, from stochastic to tessellated, from simple geometries to complex freeform surfaces.

Profile measurement is carried out by measuring a line across the surface and representing that line as height information with lateral position. As shown in Figure 2.23, examples of

common profile parameters are amplitude parameters  $R_a$  (average value) and  $R_q$  (root mean square). And the spatial parameter  $S_m$  is the mean spacing between profile peaks at the mean line.

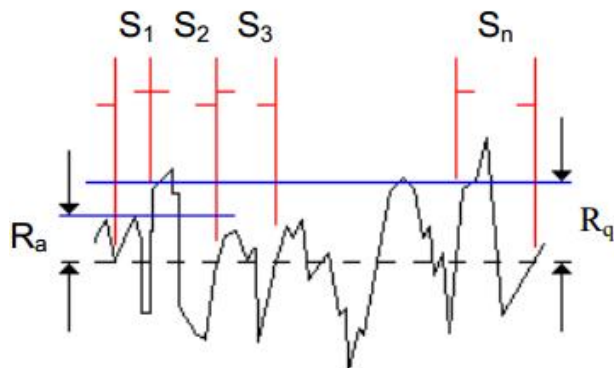


**Figure 2.23 Common characterisation parameters for profile measurement [109]**

However, profile measurement and characterisation do not often illustrate the exact nature of topographic features [110]. Figure 2.24 shows an areal surface measurement and extracted profile from the same workpiece. It can be difficult to distinguish if the selected feature is a pit or scratch only with the 2D profile.

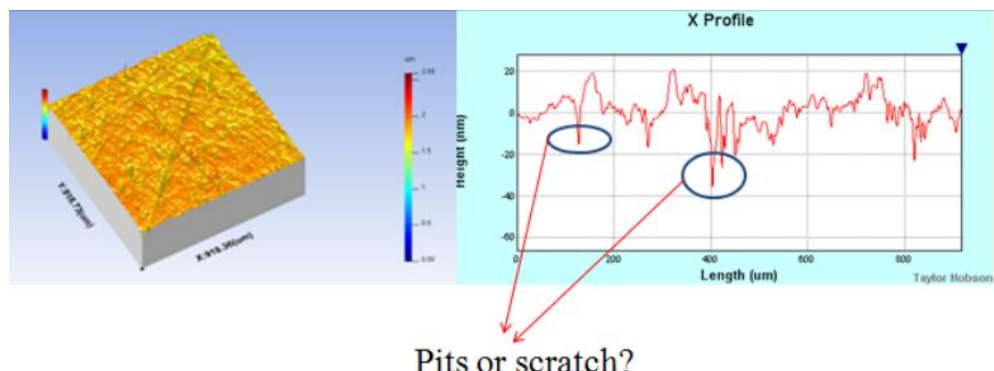


**Figure 2.24 Ambiguity of 2D profile measurement and characterisation [111]**

Areal surface parameters have been developed for the extension of profile characterisation to areal characterisation, which provides more valuable information concerning the surface features. In 2002, a working group in ISO/TC 213 was set up for the development of areal surface texture standards, which came to be the ISO 25178 series later. According to ISO 25178 series, the areal surface parameters are classified into six groups, including height parameters, spatial parameters, hybrid parameters, miscellaneous parameters, functional parameters and feature parameters [112]. Height parameters are defined with respect to a mean plane by means

of levelling the mean square plane of the measured surfaces. Table 2.1 lists the definition and mathematical expression of height parameters. According to ISO 10110-7 (preparation of drawings for optical elements and systems) [113], root mean square (RMS) value is used for optic form accuracy specification. In the thesis, the height parameters are adopted for characterising the form errors of the ultra-precision machined surfaces.

**Table 2.1 Areal height parameters [112]**

Areal height parameters	Definitions	Mathematical expression
$S_a$ (arithmetical mean height)	arithmetic mean of the absolute of the ordinate values within a definition area ( $A$ )	$S_a = \frac{1}{A} \iint_A  z(x, y)  dx dy$
$S_q$ (root mean square height)	root mean square value of the ordinate values within a definition area ( $A$ )	$S_q = \sqrt{\frac{1}{A} \iint_A z^2(x, y) dx dy}$
$S_{ssk}$ (skewness)	quotient of the mean cube value of the ordinate values and the cube of $S_q$ within a definition area ( $A$ )	$S_{ssk} = \frac{1}{S_q^3} \sqrt{\frac{1}{A} \iint_A z^3(x, y) dx dy}$
$S_{ku}$ (kurtosis)	quotient of the mean quartic value of the ordinate values and the fourth power of $S_q$ within a definition area ( $A$ )	$S_{ku} = \frac{1}{S_q^4} \sqrt{\frac{1}{A} \iint_A z^4(x, y) dx dy}$
$S_p$ (maximum peak height)	largest peak height value within a definition area ( $A$ )	
$S_v$ (maximum pit height)	minus the smallest pit height value within a definition area ( $A$ )	
$S_z$ (maximum height)	sum of the maximum peak height value and the maximum pit height value within a definition area ( $A$ )	$S_z = S_p + S_v$

Moreover, the form accuracy characterisation of a freeform surface depends on the fitting accuracy of the measured surface and a reference template [114]. In order to reach a high fitting

accuracy, a two-stage fitting methodology is commonly adopted. An initial fitting procedure is performed to estimate a rough matching position. Different initial fitting techniques have been developed for automation of the alignment process, such as structured region signature method [115], Gaussian curvature method [116] and salient points method [117].

After the rough position is obtained, the fitting result will be subsequently refined for higher accuracy. An iterative closed point method [118] is widely adopted to iteratively refine the transformation (combination of translation and rotation) if the reference template is defined as a set of point cloud. Otherwise, Levenberg–Marquardt algorithm [119] can be applied to a continuous template function which is reconstructed from the point cloud using Radial Basis Function (RBF) or Non-Uniform Rational B-Splines (NURBS). The fitting process [120] is generally formulated as an optimization problem, involving the search for transformation parameters that minimize an error metric, which is in this case, the squares distance between the measurement data and the design model,

$$\varepsilon = \min \sum_{i=1}^N \|R \cdot m_i + t - d_i\|^2 \quad (2.1)$$

where  $d_i$  is the corresponding design point of the measurement point  $m_i$ ,  $R$  is the optimal rotational matrix and  $t$  is the translation vector. The disadvantage of the matching process is that it often involves manual operations for initial data alignment and time-consuming computation [114, 121].

## 2.5 Summary

Differing from conventional simple surfaces, freeform surfaces are more geometrically complex, which normally have no symmetry in rotation or translation. Owing to the featured optical and physical properties of freeform surfaces, they are an important catalyst in the development of the high-value-added photonics and telecommunication products. Ultra-precision

machining and surface measurement technologies for highly demanding optical freeform surfaces have been reviewed in this chapter.

Ultra-precision machining provides an important means for generation of non-rotational symmetric freeform surfaces with sub-micrometric form accuracy and nanometric surface finish without the need for any subsequent processing. Among them, ultra-precision STS machining has the advantages of faster and easier setup, faster cycle times, better surface accuracy over other machining techniques. Successful STS machining depends largely on the selection of cutting conditions, machine characteristics, tool path and cutting strategies. A trial-and-error cutting approach is not efficient because it is time consuming and costly. Hence, a theoretical and experimental study needs to be carried out to understand STS machining. In this work, STS technique will be adopted to fabricate optical freeform surfaces and surface generation will be investigated theoretically and experimentally to achieve the successful machining process.

Many factors still induce machined surface deviations from the design, including environmental factors, machine structural errors, vibration, thermal distortion in part and machine tool and tool wear. Consequently measurement and characterisation become the key to evaluating the machined surface quality and controlling the ultra-precision machining process. Due to the geometric complexity, freeform surface measurement and characterisation are more challenging than the conventional simple geometries. To meet the demand, metrology instrumentation has made great progress with the development of new principles, mathematical algorithms and high precision sensors. The contact stylus instrumentation is preferred for measurement of large deviation freeform surfaces because of its high dynamic range. However, the contact methods have the potential risk of scratching the ultra-smooth and soft surfaces and the measurement speed is relatively slow if areal surface measurement is undertaken. In contrast, optical methods, particularly interferometry methods, are promising for the measurement of high precision freeform surfaces owing to its non-destructive nature, fast capturing and high accuracy.

Therefore, optical interferometry is the promising tool for measurement of ultra-precision turned freeform surfaces.

Although there has been significant advancement for the measurement and characterisation for ultra-precision freeform surfaces, most modern instrumentations are based in environmental controlled laboratories. For some demanding advanced manufacturing, such as large telescope optics polishing and reel to reel thin film fabrication, offline measurement in laboratories is difficult. Furthermore, the errors induced by transportation of workpieces cannot be neglected in the ultra-precision manufacturing [20], which prevents the deterministic process investigation and corrective machining. Therefore, in order to increase the measurement availability and efficiency, a shift in the approach of metrology from offline lab-based solutions towards the use of metrology upon manufacturing platforms is needed.

### **3 Review and discussion of OMSM**

#### **3.1 Introduction**

To further enhance accuracy and efficiency of ultra-precision machining process, surface measurement and effective feedback are essential. With the continuing evolution of intelligent manufacturing, the next generation of measurement instruments will require accessibility into the manufacturing environment [122]. Metrology on manufacturing platforms would allow large improvement of production efficiency and accuracy by means of the elimination of repositioning and alignment operations and their associated errors. Furthermore, the application of integrated measurement will significantly contribute to ultra-precision manufacturing in a cost-effective and environmentally sustainable manner [15, 123], which not only allows the assessment of manufactured surfaces just-in-time, but also provides valuable feedback to the process control for compensation and optimization.

Vacharanukul and Mekid [124] provided a nomenclature classification for the act of measurement during the manufacturing process in three groups, namely in-process, in-situ and post-process.

In-process measurement refers to the act of measurement performed while the manufacturing process continues. It can be fully integrated into the process control system to provide timely information for the manufacturing process. A typical example of in-process measurement can be found in the monitoring and measurement of fast moving films in the flexible electronics roll-to-roll manufacturing process [125]. However, many challenges for in-process measurement have to be overcome, such as speed of measurement, the effect of machining vibrations, heat flux and presence of lubricants and swarf. These challenges greatly limit the application of in-process measurement into ultra-precision machining processes.

In-situ measurement, also known as on-machine measurement, is defined as measuring the surfaces without the removal of the workpiece from the machine tool. The machining process is

usually paused before the measurement process is initiated. Compared with in-process measurement, on-machine or in-situ measurement operates in a relatively mild and static environment without cutting forces and reduced thermal effects, which significantly relaxes the stringent requirements for implementation. Although the machining efficiency is decreased to some degree, the automation level will be increased with the integration of on-machine measurement. In this work, on-machine surface measurement (OMSM) is used as opposed to on-machine measurement of other physical quantities (such as forces, temperature and power consumption). OMSM will be investigated for the improvement of ultra-precision machining performance.

Post-process measurement, also called offline measurement, is a standard inspection at the end of or at defined stages of the production process. The workpieces need to be removed from machine tools and transported to the offline measurement instruments, which are usually located in a temperature controlled and anti-vibration environment. Post-process measurement is time-consuming and the transportation process is risky particularly for large scale precision components. Furthermore, at the ultra-precision level, the errors induced by removal and remounting of workpieces cannot be neglected [20].

### **3.2 Benefits of OMSM**

As discussed above, the obvious benefit of OMSM is that there is no need to transport workpieces between the machining environment and measurement platforms. Also, the machine tool axes are utilized to accommodate the measuring range, which means the machined components can be always measured within the machine tool volume. Therefore, from the production perspective, metrology integration increases the inspection efficiency, production throughput and reduces the cost associated with transportation labour and tools.

Secondly, the automation level of manufacturing is greatly elevated with the application of OMSM. The intimate knowledge of measurement strategy and other operation experiences can

be effectively integrated into the manufacturing control system. Moreover, the machined surface can be inspected in-situ and the extracted information is promptly fed back to the process control system for further decisions. OMSM is considered indispensable for autonomous and intelligent manufacturing.

Thirdly, with the integration of OMSM, the coordinate system between the machining and the measurement process is consistent through the whole manufacturing process. This is particularly important for the ultra-precision freeform machining processes. As the form tolerance is within the sub-micrometre and even nanometre range, the errors induced by removal and remounting are considerable. The realignment operation would inhibit re-machining processes for defect repair and deterministic compensation.

However, there are also some issues or disadvantages emerging with the integration of surface measurement on the machine tool. On-machine inspection will cause the loss of machining availability, which reduce the production throughput in large scale manufacturing. Also, the measurement coordinate frame is integrated in the machine tool. The machine axis kinematic error and thermal effect will deteriorate the measurement result to some extent.

### **3.3 Considerations for OMSM integration**

In order to apply OMSM successfully, there are several technological gaps to be bridged for the shift from laboratory-based measurement systems to the integrated metrology. First of all, the precision and dynamic range of the selected measurement instrument should meet the specific requirement for the corresponding machining process. Since operating in the machine tool environment, the instrument needs to be robust to the presence of vibrations, temperature and other environmental disturbance. These factors should not adversely affect the quality of measurement result. High measurement rate is also preferable, which helps alleviate vibration effects and increase the inspection efficiency. In addition, compact design tends to increase the robustness of the system and is required if the working volume is limited. To promote the

OMSM application in advanced manufacturing, the cost of the additional functionality needs to be taken into account as well. Besides the considerations from the instrumentation perspective, the integration process into the manufacturing environment will lead to further challenges, such as the establishment of the measurement coordinate frame, scanning strategies, calibration methodology and task-oriented surface characterisation. For example, machine tool factors such as vibration and machine tool errors would have a significant effect on the overall measurement performance. Vibration during the measurement is detrimental to the measurement results. Moreover, as surface measurement is actuated by the machine tool stages, kinematic error must be compensated to acquire reliable surface information. The considerations for OMSM integration are summarized in Figure 3.1.

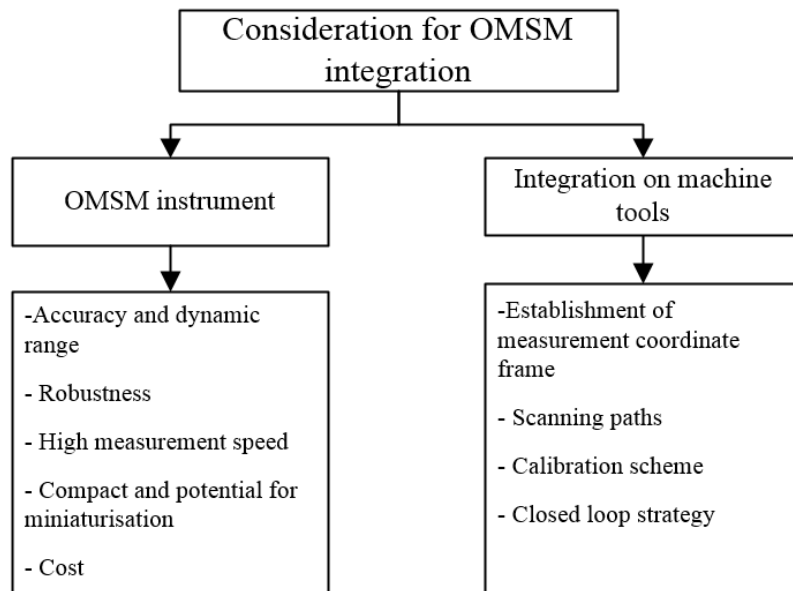


**Figure 3.1 Consideration for OMSM integration**

### 3.4 Review of OMSM instrumentation and applications

Because of the growing complexity and stringent requirement for products, it is necessary to form a closed-loop control of the manufacturing process. OMSM has gained increasing attention from both industry and academia. Knowledge from standard CMMs' probing system has been widely used for OMSM in modern multi-axis machine tools for precision machining. The integrated sensors include basic touch-trigger probes [126, 127], scanning probes [128],

triangular laser [129, 130] and fringe projection systems [131, 132]. In modern numerical control systems, built-in routines with a CAD interface can simplify the integration of probing cycles into machining operations. OMSM will allow automated workpiece set-up, in-cycle gauging and verification of workpieces, which increases inspection automation and reduce scrap rate. The integrated measurement should meet the requirement of machining specification and be targeted to the applications. The review in this section mainly emphasizes OMSM instrumentation and their applications for ultra-precision machining processes.

### 3.4.1 Contact OMSM and applications

Contact probing has been used for OMSM because of its technological maturity and the ease of integration. However, for on-machine application, several modifications and specific setups are often adopted to ensure the performance of measurement system, which makes the contact OMSM different from offline contact measurement. In ultra-precision machining fields, Suzuki et al. [133] integrated a contact probing system to measure steep-angle aspheric optical parts on an ultra-precision grinding machine (shown in Figure 3.2 (a)). A ceramic air slider and high accuracy glass scale were adopted in the probing unit for its low thermal expansion coefficient, high rigidity and light weight. The special tilted angle configuration made the contact probe keep the contact angle with the ground aspheric surface during the measurement process, in order to reduce the variation in the probing friction force (shown in Figure 3.2 (b)).

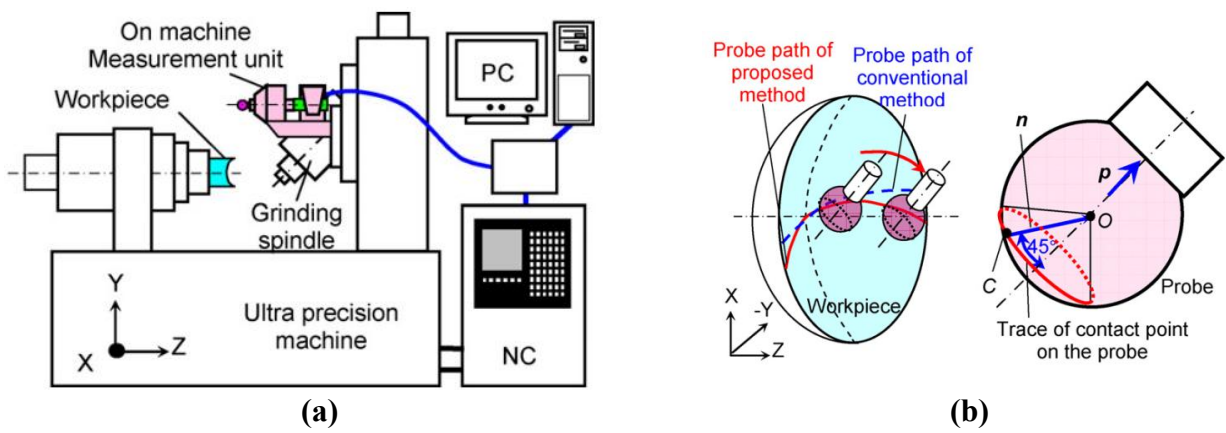


**Figure 3.2 Schematic of (a) on-machine contact probing for optics grinding process; (b) tilted angle probe configuration [133]**

Chen et al. [134] employed a similar contact probe for the ultra-precision grinding of tungsten carbide aspheric moulds (shown in Figure 3.3 (a)). After the reconstruction of actual ground profile based on the measured data, on-machine measurement (PV value of 177 nm) was in good agreement with the off-machine measurements (PV value of 185 nm) obtained by commercially available precision profilometers (Talysurf, Taylor Hobson). The measurement result was then used to establish a new grinding tool path for error correction along the surface normal direction (shown in Figure 3.3 (b)). The proposed compensation grinding process achieved profile accuracy of 177 nm (PV) with a roughness of 1.7 nm (Ra).

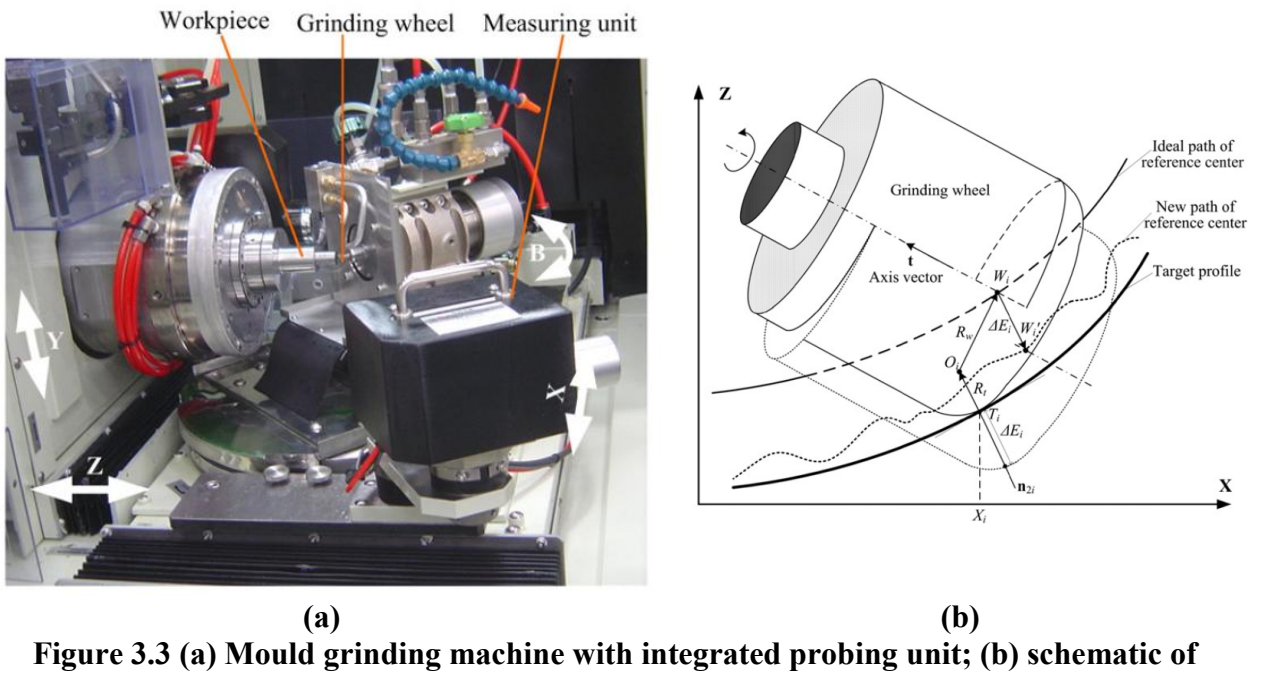


**Figure 3.3 (a) Mould grinding machine with integrated probing unit; (b) schematic of compensation grinding strategy [134]**

Contact probing systems are nowadays provided as accessories in some commercial ultra-precision machining tools. For example, Moore Nanotech provides an on-machine measuring probing system, which is composed of a Linear Variable Differential Transformer (LVDT) sensor and air bearings [135]. Zhang et al. [20] combined this kind of on-machine and off-machine measurement results to increase the diamond machining accuracy for freeform optical surfaces. The on-machine contact measurement was utilized to align the remounting workpiece into the modified machining coordinate while surface error derived from offline measurement

was used for compensation machining. The workflow and experimental setup are respectively shown in Figure 3.4 (a) and Figure 3.4 (b).

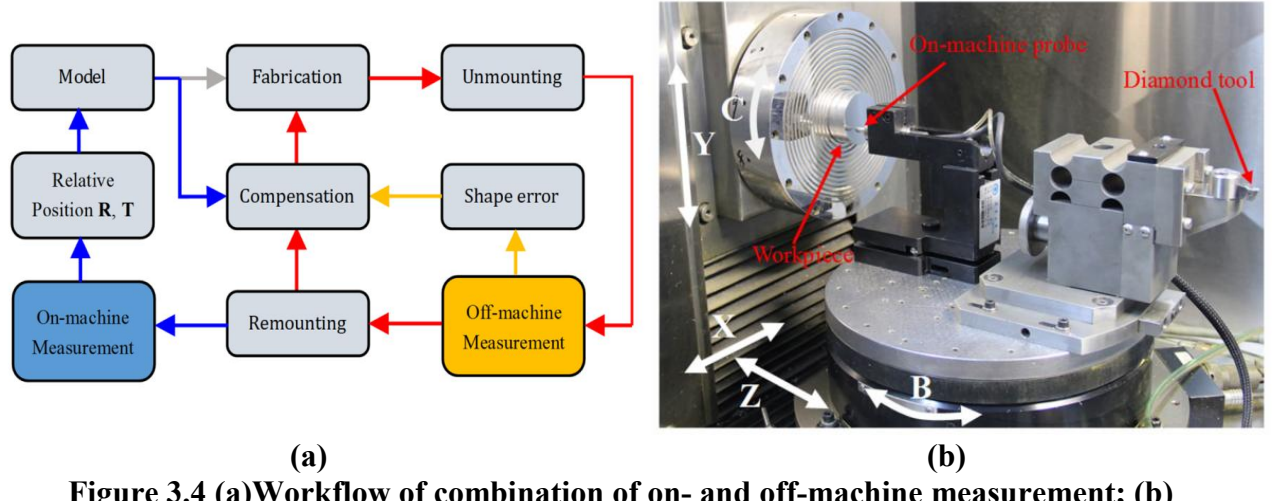


**Figure 3.4 (a)Workflow of combination of on- and off-machine measurement; (b) Experiment setup of on-machine measurement [20]**

The conventional contact probing utilizes a ruby ball. The probe radius often lies in the millimetre range, which greatly limits the measurement lateral resolution. Scanning Probe Microscopes (SPMs) with finer tips are developed to measure ultra-precision machined micro-structures on the machine tool. For instance, Gao et al. [136] specially designed an Atomic Force Microscope (AFM) head to measure diamond turned sinusoidal microstructures. A robust linear encoder was adopted in the AFM-head for accurate measurement of profile height in the presence of electromagnetic noise. The OMSM system was able to measure micro-structured surfaces with 0.5 nm resolution in a spiral path.

Ju et al. [137] developed a Scanning Tunnelling Microscope (STM) probing system and applied it in the ultra-precision fly-cutting process. An ultra-sharp tip with a high aspect ratio 450:1 was used. The working principle of the developed measuring system is illustrated in Figure 3.6. The probe tip follows the surface variations of the machined micro-structure at a constant distance, by means of minimizing the difference between detected current and the set-point value. The capacitance sensor is used to record the displacement of the driven piezoelectric

translator (PZT) which corresponds to the measured surface profile. A step motion test proved that vertical resolution of 5 nm for the served scanning head was realized.

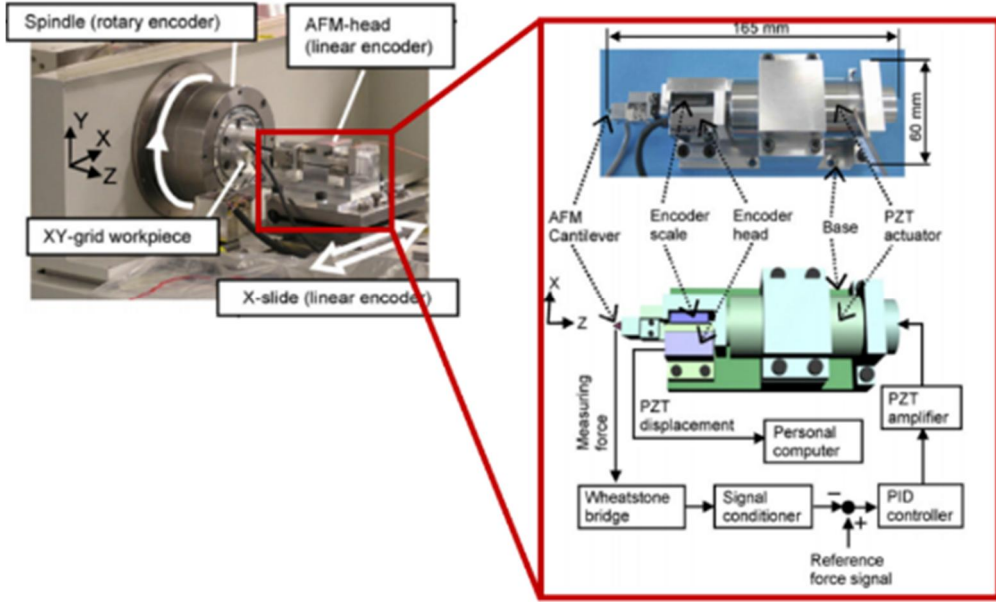


**Figure 3.5 Robust AFM based on-machine measuring system [136]**

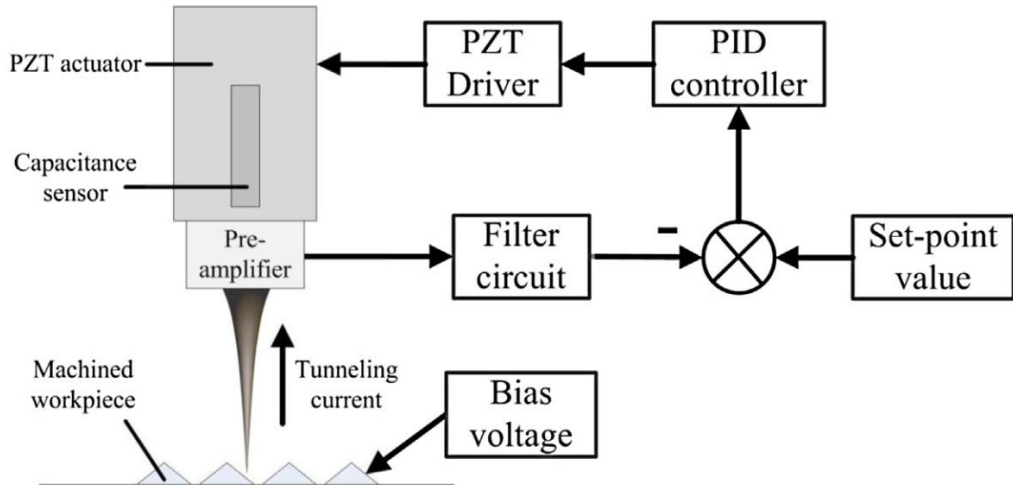


**Figure 3.6 STM based on-machine measuring system with ultra-sharp tips [137]**

The STM based probing system was mounted on the main spindle of an ultra-precision turning machine and employed to assist the precision fabrication of rectangular pyramid arrays (shown in Figure 3.7 (a)). Resulting from the feedback of on-machine measurement, the form accuracy of high slope micro-structures was significantly improved by cutting depth compensation [138].

The same probing system was also employed to measure 3D curved compound eye surfaces machined by STS technique [139]. In this case, the measurement unit was mounted in the *B* axis, as illustrated in Figure 3.7 (b). A tip-tracking strategy was proposed to extend the measuring ranges with more flexibility. Distortion related to the centring error was analysed based on the characterised points. Through the evaluation of OMSM results, the main machining errors were identified as inaccuracy of tool radius and uncompensated region around the inflection points.

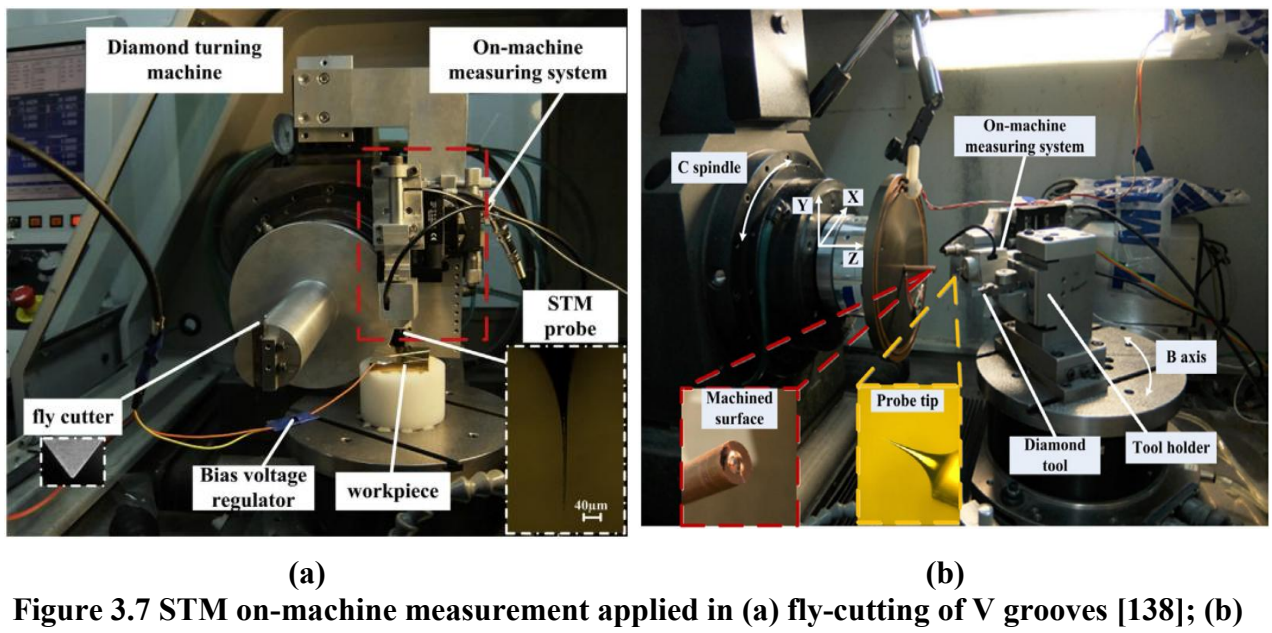


**Figure 3.7 STM on-machine measurement applied in (a) fly-cutting of V grooves [138]; (b) tool servo machining of 3D compound eye structures (b) [139]**

Noh et al. [140] and Lee et al. [141] innovatively integrated a piezoelectric force sensor into the FTS device, which constituted a force-displacement servo unit termed as FS-FTS. FS-FTS acted as a cutting tool and force sensor during the machining, while it was employed as a contact probe after the machining. The particular characteristic enabled the unit to perform structured surface machining, profile measurement, defect identification, and cutting tool reposition.

With the assistance of FS-FTS, Chen et al. [142] proposed an in-process identification and repair of diamond turned micro-lens arrays on the roll mould. Thrust force was monitored during the machining process of the micro-structures, in order to indicate the cutting status and map

singular forces with respect to the cutting tool position. After the defects were identified by FS-FTS scanning, the repair process was subsequently carried out, as illustrated in Figure 3.8.

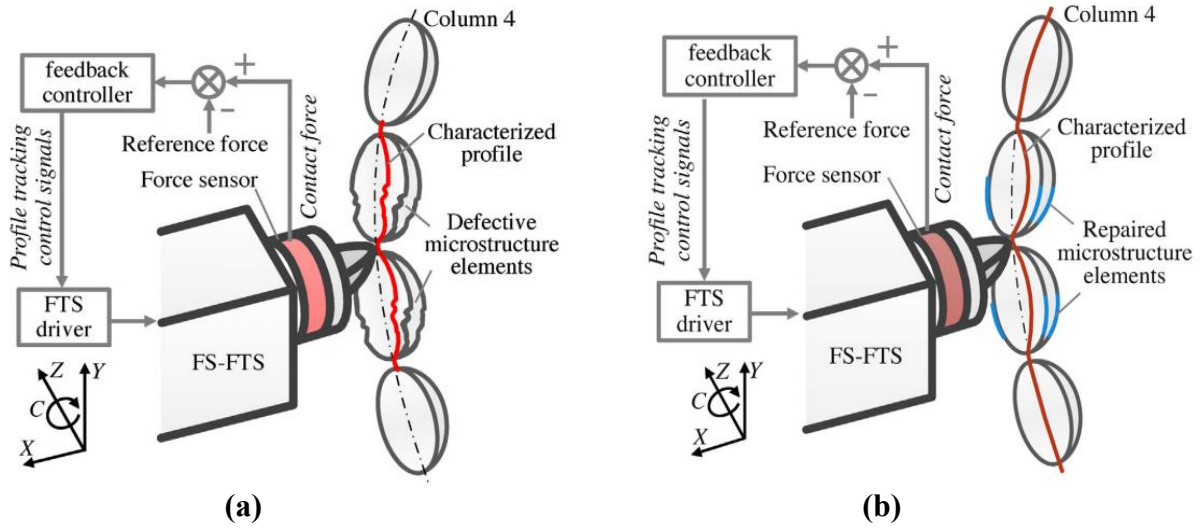


**Figure 3.8 Micro-lens (a) defect identification and (b) repair process with FS-FTS [142]**

Furthermore, the concept of relay fabrication [143] was realized with the capability of repositioning a new tool to former cutting spot after the replacement of the worn tool. The schematic of such process is illustrated in Figure 3.9. A bidirectional scanning strategy was employed to increase the positioning accuracy due to the delay of the feedback control loop. Stitching fabrication of a micro-groove line array and filling fabrication of a micro-lens lattice pattern demonstrated the feasibility of the tool position measurement method.

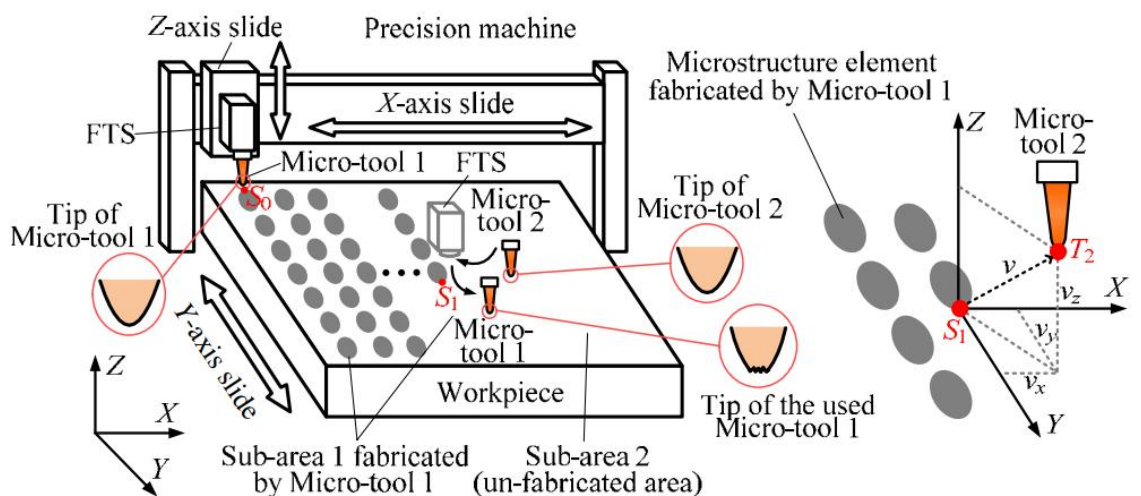


**Figure 3.9 Schematic of tool tip position measurement and relay fabrication of micro-structures with FS-FTS [143]**

Table 3.1 summarizes state-of-the-art researches on the contact type of OMSM and corresponding applications in ultra-precision machining processes.

**Table 3.1 Contact type of OMSM and applications**

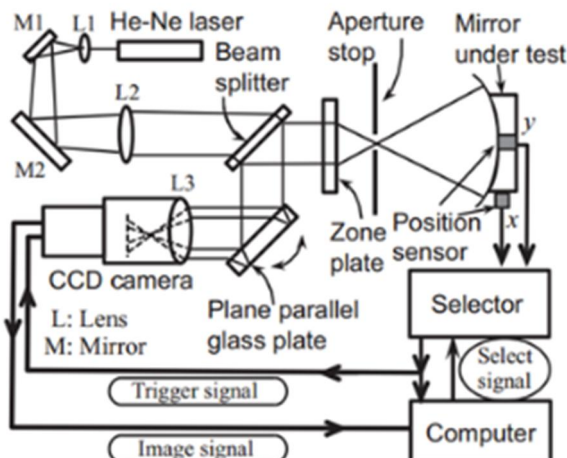
No	Author/year	Principle	Instrument	Performance	Applications	Remarks
1	Suzuki et al. [133]	Contact ball	A high accuracy glass scale with a ceramic air slider	Contact force < 0.3 mN; 0.14 nm scale resolution	Steep optical mould grinding	The tilted angle configuration reduced the variation in the probe friction force
2	Chen et al. [144]	Contact ball	N.A.	Similar to offline profilometer in terms of form deviation	Aspheric mould grinding	Normal-compensation tool path was generated according to the reconstructed profile from OMSM
3	Zhang et al. [20]	Contact ball	A LVDT sensor with an air bearing slide	20nm resolution; measurement standard deviation 10nm	Freeform diamond turning	A novel compensation method was proposed using a combination of on-machine and off-machine measurement
4	Gao et al. [136]	SPM	AFM head with a robust linear encoder	0.5 nm resolution	Micro-structured surface FTS machining	The use of linear encoder increased the robustness of AFM head and alignment issue was investigated for accurate measurement.
5	Zhu et al. [138] and	SPM	Position-servo STM with ultra-sharp stylus	5 nm vertical resolution	Fly-cutting and STS machining	A tip-tracking strategy was proposed to extend the measuring ranges. It is capable of

	Zhu et al. [139]					scanning steep micro-structured surfaces (V grooves and compound eyes)
6	Chen et al. [142] and Chen et al. [143]	Piezo-force sensing	FS-FTS	sub-mN contact force; 30nm resolution	Micro-structured surface machining	Defect repair and relay fabrication of micro-lens arrays were achieved with FS-FTS

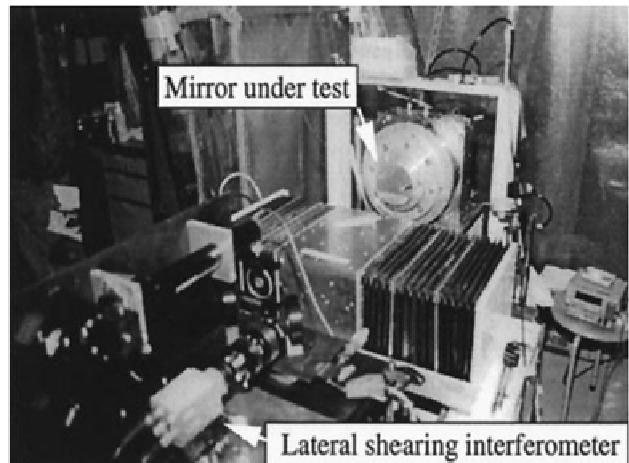
### 3.4.2 Non-contact optical OMSM and applications

As discussed in section 2.4.1, non-contact optical measurement techniques are non-destructive and fast, which makes them suitable for on-machine and in-process applications. Particularly for ultra-precision machining processes, on-machine interferometry has received a lot of attention from researchers for its nanometric precision and high speed acquisition.

Nomura et al. [145] developed a common path lateral-shearing interferometer with a minimum number of optical components. Because the kind of interferometer was minimally affected by mechanical vibrations and air turbulence, it was integrated on the machine to measure the form deviation of diamond turned surfaces. A plane parallel glass plate was used to shear the wavefront under test in the interferometer. In order to measure spherical and aspherical surfaces, zone plates that were computer-generated holograms were added in the system. The schematic and the experimental setup of on-machine shearing interferometer is respectively illustrated in Figure 3.10 (a) and Figure 3.10 (b). Experimental results showed the interferometer was sufficiently stable to be applied in diamond turning process with an accuracy of  $0.06 \mu\text{m PV}$ , even when the machine tool spindle was running at 1000 rpm.



(a)



(b)

**Figure 3.10 (a) Schematic and (b) experimental setup of on-machine shearing interferometer for diamond turning processes [145]**

Shore et al. [146] investigated on-machine measurement for the diamond turned MIRI spectrometer mirror, in order to avoid error prone replacement and alignment of the workpiece. Form accuracy of individual mirrors was measured by a Twyman-Green PSI, which was mounted on a 3-axis machine with sub-micron positioning ability. The measurement setup is illustrated in Figure 3.11. This measurement repeatability was characterised as 1.9 nm (normally distributed). As the MIRI mirror was comprised of several discrete surfaces, the interferometer head was additionally moved in three axes relative to the mirror to establish the confocal position for each mirror segment. The centres of curvature and relative location for the mirrors were subsequently derived.

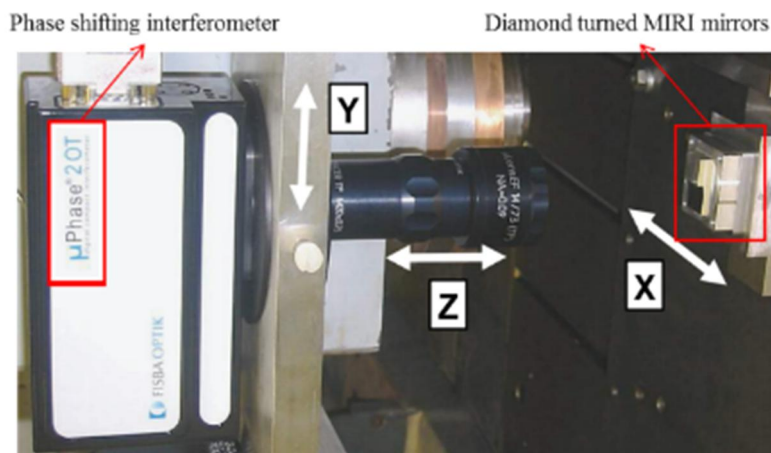


**Figure 3.11 PSI on-machine measurement of diamond turned MIRI spectrometer mirror**

As a variation of traditional PSI, dynamic interferometry was developed as a single shot spatial phase shifting method [147]. Four phase shifted interferograms were simultaneously generated through the use of a quarter wave plate and a pixelated birefringent mask in front of a single detector. The principle is shown in Figure 3.12. The single-shot nature of the dynamic interferometry allows fast surface measurement without sensitivity to vibration or air flow through interferometer paths.

With such preferable characteristics, King et al. [148] proposed an integrated solution for polishing and on-machine measurement of large scale optics up to 1 m in diameter. As shown in Figure 3.13, it consisted of a Zeeko IRP 1000 polishing machine and a 5-axis motorized stage housing 4D dynamic interferometer. The large optics were measured in-situ without the need of risky transportation to offline metrology platforms and corrective polishing was subsequently carried out. The measurement system was also equipped with different CGH elements to measure aspheric and freeform optics. In addition a white light interferometer for texture measurement and a laser tracker for radius measurement were integrated as optional accessories.

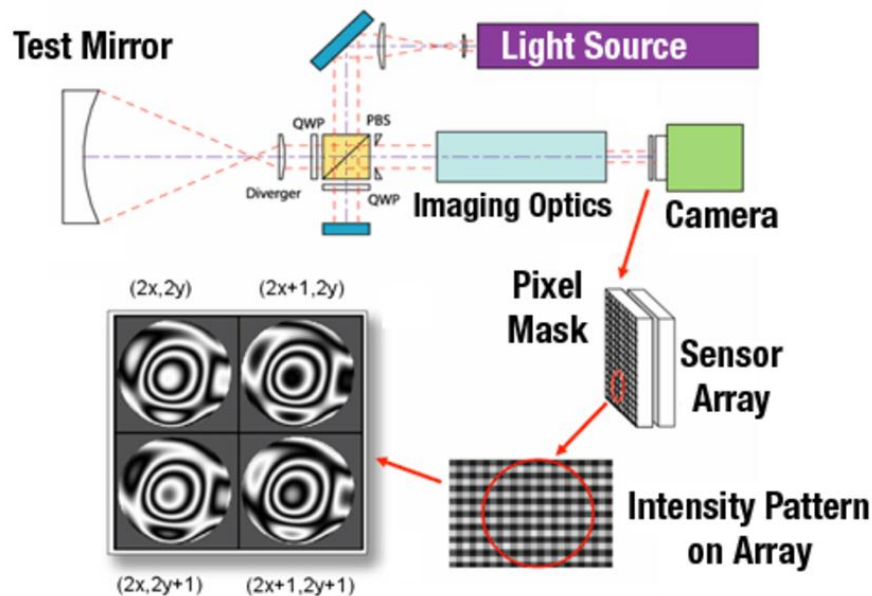


**Figure 3.12 Principle of the dynamic interferometer [147]**

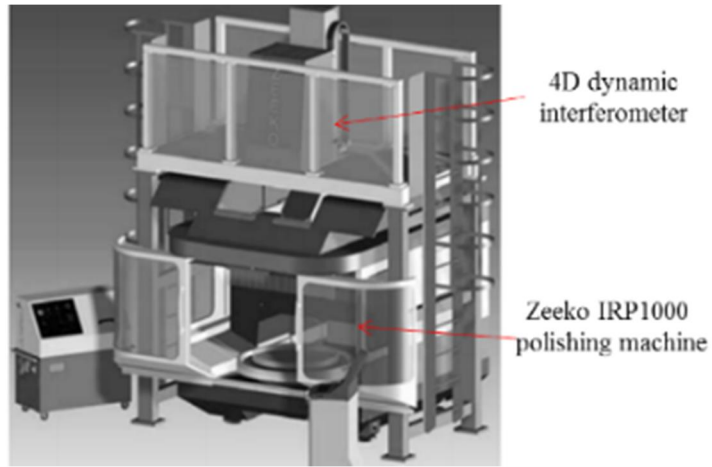


**Figure 3.13 Large telescope optics polishing system with on-machine dynamic interferometer measurement [148]**

In terms of micro-scale topography measurement, a wavelength scanning interferometer (WSI) based on wavelength division multiplexing has been developed for measurement of diamond machined-structured surfaces on a large drum turning machine [149]. For the integration in a noisy manufacturing environment, the vibration sensitivity issue was attenuated by the use of a reference interferometer multiplexed into the measurement paths. The attenuation level obtained was approximately at 27.3 dB for frequencies of up to 40 Hz. Figure 3.14 illustrates a reference interferometer for closed-loop control of a reference mirror mounted on a PZT where the mirror actuates to compensate for the vibration of the measurement samples and stabilize the data capture process. In the application for roll turning a more usual stylus measurement is replaced by the WSI (shown in Figure 3.15).

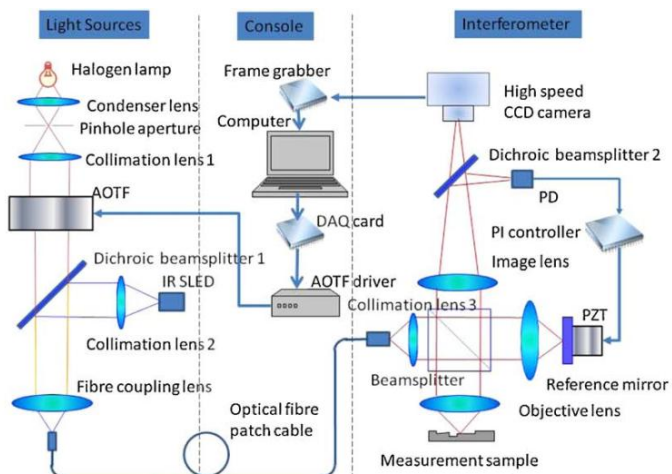


**Figure 3.14 Schematic diagram of WSI with vibration compensation [149]**

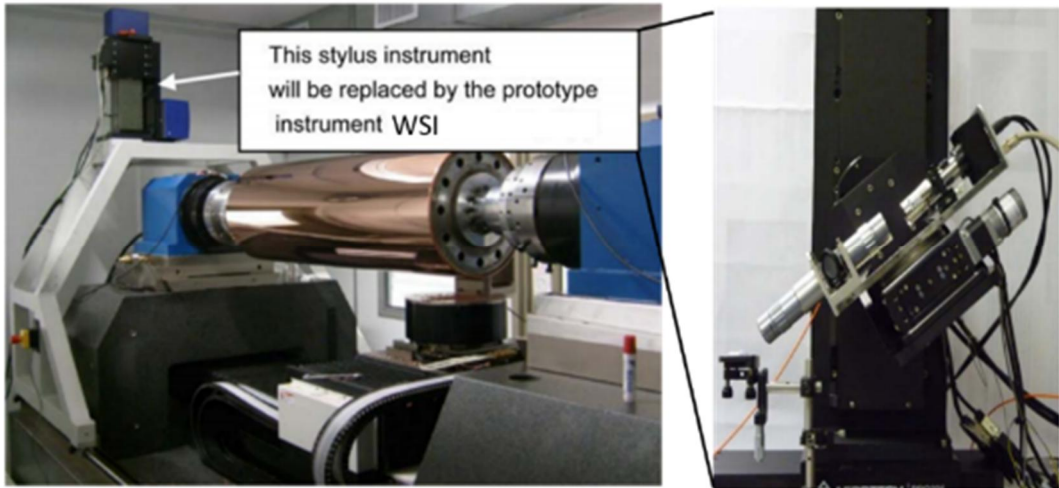


**Figure 3.15 WSI for on-machine topography measurement [149]**

Due to the sensitivity to environmental disturbances and complex system configuration of interferometric instruments, non-interferometric OMSM have been also investigated. Röttinger et al. [150] presented a setup of miniaturized deflectometry on a diamond turning machine and measured high-precision specular surfaces without re-chucking operations (shown in Figure 3.16). The development of global calibration and parasitic reflections reduction will boost the usage of deflectometry. The advantages of on-machine deflectometry include the environmental robustness and the capability of measuring arbitrary freeform surfaces within micron accuracy without additional null testing. By rotating the object with the machine's rotational axis, the field of measurement was easily increased to cover the large aperture and steep mirrors.

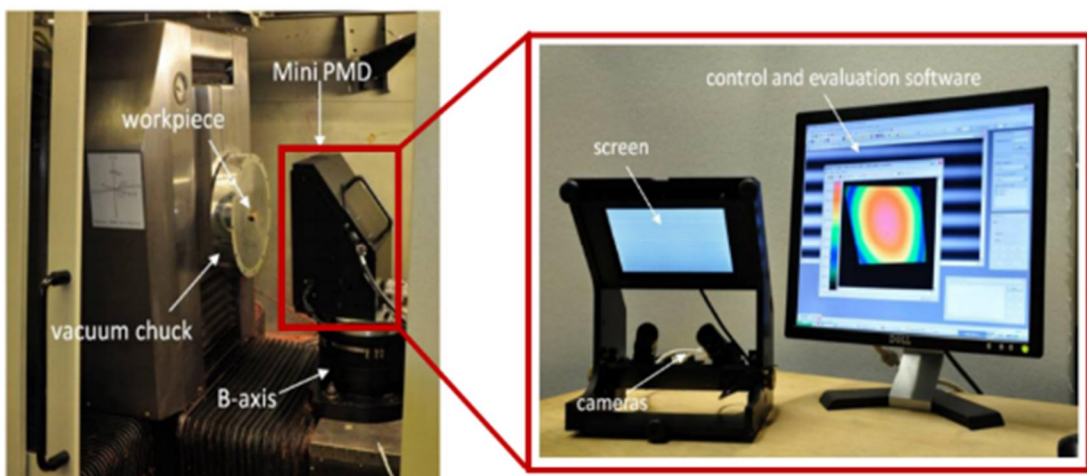


**Figure 3.16 Integration of mini-PMD on a multi-axis ultra-precision machine tool [150]**

Confocal microscopy is an effective tool for surface measurement at the micro scale. Compared with other optical methods, the maximum detectable slope can be as large as 75 degrees with enough scattered light enhanced by software and hardware [74]. All these characteristics make it applicable to measure complex and high slope structured surfaces in the manufacturing environment. Zou et al. [151] integrated a chromatic confocal sensor on a self-developed ultra-precision turning lathe for 3D measurement of diamond turned aspheric surfaces. As shown in Figure 3.17, the sensor was mounted perpendicular to the vacuum chuck plane and aligned with a reference sphere. The combined standard uncertainty of the measurement system was estimated to be 83.3 nm, which mainly resulted from the flatness uncertainty of the scanning hydrostatic slide.

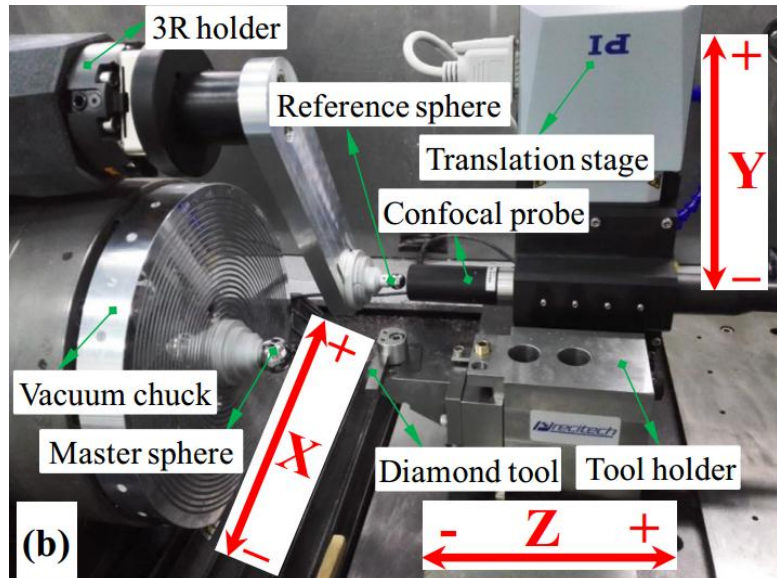


**Figure 3.17 Chromatic confocal based on-machine measurement for ultra-precision turning processes [151]**

Moreover, several researchers developed special OMSM systems for corresponding applications in order to characterise the functional related geometric properties. For instance, Gao et al. [152] developed a two-dimensional optical slope sensor with a multi-spot light beam, for on-machine measurement of local slopes of the FTS turned sinusoidal surface. As illustrated in Figure 3.18, the sensor unit was mounted opposite to the cutting tool on the feeding slide. A

cylindrical lens was integrated in the sensor so that slopes of the sinusoidal structures could be detected without the influence of curvature of the cylindrical workpiece. The on-machine metrology enabled the inspection of machining quality without removal of the master drum from the spindle and assisted to effectively reduce surface slope errors, which were caused by the round nose geometry of the cutting tool.

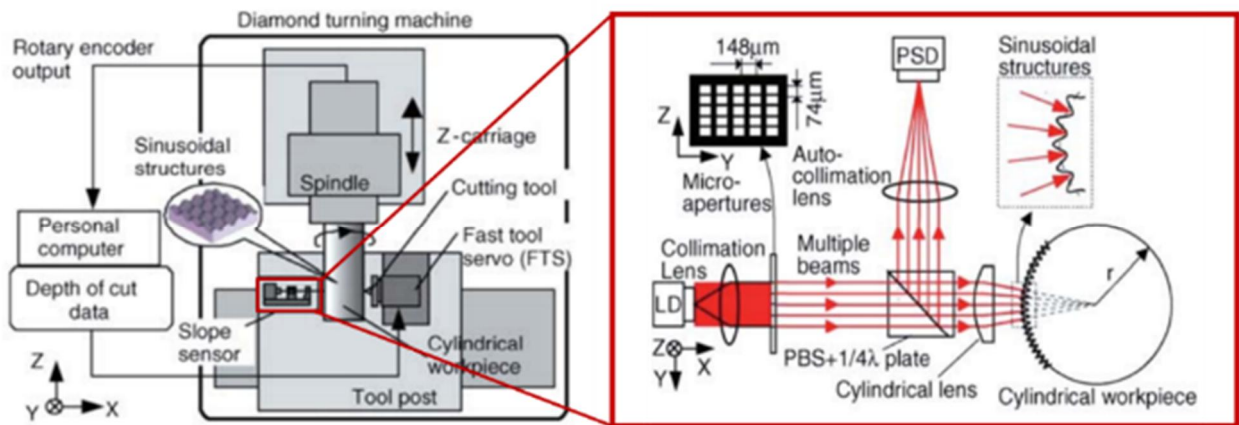


**Figure 3.18 Optical slope sensor for on-machine measurement of FTS machined sinusoidal structures [152]**

To overcome the rigorous environmental requirements for on-machine optical measurement system, Li et al. [153] presented an in-situ 3D metrology system based on a disparity pattern autostereoscopic (DPA) principle to measure micro-structured surfaces on an ultra-precision machine (shown in Figure 3.19). The system made use of a micro-lens array to capture raw 3D information and a 3D digital model of the target surface to directly extract disparity information. The system setup was simple and compact. Under different measuring environments, it was capable of fast data acquisition and high accuracy in 3D computational reconstruction of complex surfaces. Sub micrometres measurement repeatability was achieved by means of an error-elimination process based on statistical analysis.

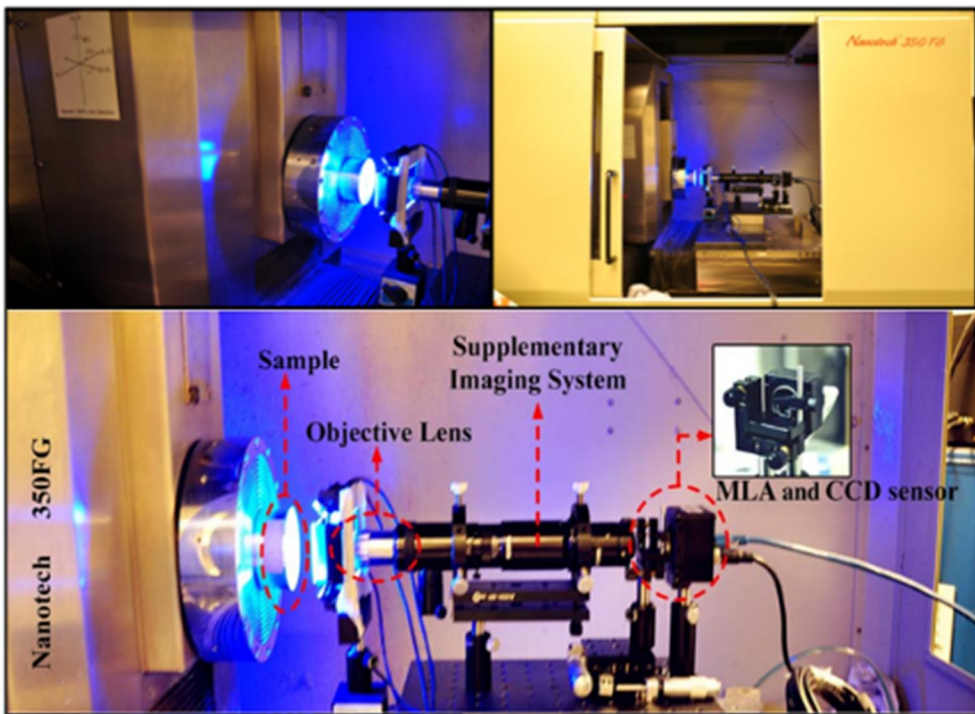


**Figure 3.19 Disparity pattern-based autostereoscopic system for in-situ inspection of diamond turned micro-structures [153]**

Table 3.2 summarizes state-of-the-art researches on non-contact types of on-machine surface measurement and corresponding applications in ultra-precision machining processes.

**Table 3.2 Non-contact optical type of OMSM and applications**

No	Author/year	Principle	Instrument	Performance	Applications	Remarks
1	Shore et al. [146]	Interferometry	Trioptics μphase PSI	1.9nm repeatability	MIRI mirror diamond turning	Relative locations of confocal positions were evaluated with the aid of OMSM
2	Nomura et al. [145]	Interferometry	Lateral shearing interferometer	Good agreement with results measured by Fizeau type interferometer	Diamond turning	Interference fringes were little affected by air turbulence in the optical paths and machine vibrations
3	King et	Interfero-	4D dynamics	30 μsec	Large-scale	Single shot and

	al. [148]	metry	interferometry	acquisition time; $0.002\lambda$ wavelength precision	optics polishing	vibration insensitive measurement
4	X. Jiang [149]	Interferometry	Wavelength scanning interferometer	15 nm vertical resolution; anti-vibration <300 Hz	Micro-structures diamond turning on drum rolls	Real-time vibration compensation with a monitoring interferometer
5	Röttinger et al. [150]	Deflectometry	mini-PMD	Sub-micron accuracy	Freeform ultra-precision machining	Environmentally insensitive and able to measure arbitrary freeform without null testing
6	Zou et al.[151]	Chromatic confocal	STIL confocal point sensor	Relative measurement error 0.022%; combined standard uncertainty 83.3nm	Diamond turning	Measurement uncertainty mainly resulted from the flatness of the scanning slide
7	Gao et al. 2006 [152]	Auto-collimation	Optical slope sensor with a cylinder lens	N.A.	FTS machining of cylindrical sinusoidal structures	The surface slope errors caused by the tool nose geometry were corrected with the integrated slope sensor.
8	Li et al. [153]	Auto-stereoscopy	Disparity pattern-based auto-stereoscopic 3D system	Sub-micrometer measuring repeatability	Pyramid structured surfaces machining	Compact, fast capturing and environmental robust

### 3.4.3 Comparison among different OMSM

To sum up, contact methods have been commonly used for on-machine metrology due to its technological maturity. Compared with optical methods, contact methods are applicable to measure high-slope surface geometries. However, the contact methods normally operate at a low scanning speed and the contact nature makes them unsuitable to measure the soft and delicate surfaces. Some SPMs have also been developed for a few ultra-precision machining applications. However, the tip wear and measurement time is still a big challenge for large area measurement.

Optical techniques are considered more suitable for measurement on manufacturing platforms because of their fast response and non-destructive nature. With the development of calibration and processing algorithms, non-interferometric methods such as deflectometry and confocal sensing are receiving more attention in specific measurement conditions. For ultra-precision machining applications, robust interferometry is still the best choice because of its high measurement resolution (nanometre and even sub-nanometre). According to the discussion above, the merits and limitations of different OMSM types are compared and summarized in Table 3.3.

**Table 3.3 Merits and limitations of different types of OMSM**

Measurement nature	OMSM type	Merits	Limitations
Contact	Probing ball	Ease of integration, technical maturity	Slow scanning; damage on the soft surfaces; limited lateral resolution
	SPM	Nanometric resolution	Slow scanning; tip wear; limited vertical range
Non-contact optical	Interferometry	Nanometric resolution and fast acquisition	Vulnerable to environmental disturbances; slope

			limitation
	Deflectometry	Arbitrary shape measurement and simple setup	Limited global accuracy and complex calibration processes
	Confocal	High measurement angle	Limited measurement precision

From the data acquisition perspective, the OMSM type can be classified into single point methods and areal methods. Areal methods allow full-field acquisition of surface height data at a static position, while single point methods need additional scanning mechanisms to cover the areal surface. In this sense, areal methods are more efficient for surface measurement compared with single point methods. However, single-point methods are able to physically separate imaging optics from the interrogation apparatus, which greatly reduces the influence from machine tool environment on the measurement results. The use of fibre-linked objectives in single point OMSM allows further miniaturization of the measurement apparatus in the volume limited machine environment.

### 3.5 Summary

On-machine metrology would allow large improvements in production efficiency and accuracy by means of elimination of repositioning and alignment operations. The application of integrated measurement will significantly contribute to ultra-precision manufacturing which not only allows the assessment of manufactured surfaces just-in-time, but also provides valuable feedback for process control for optimization and post-process correction.

However, there are several technological gaps to be bridged for the shift from laboratory-based measurement systems to the OMSM application. Since operating in the machine tool environment, the OMSM instruments have to be robust to the presence of vibrations, temperature and other issues. High measurement rate helps to alleviate vibration effects and compact design is preferable if the working volume is limited. Besides, the integration of surface metrology into the manufacturing environment will lead to further challenges, including the establishment of the measurement coordinates, calibration methodology and task-oriented surface characterisation.

This chapter has presented a summary of state-of-the-art OMSM and corresponding applications in ultra-precision machining processes. The merits and limitations of different OMSM types are then analysed. The contact methods are limited by low speed capture, possible damage to the delicate machined surface and the long-term tip wear. Non-contact optical types are preferred for their non-destructive nature and fast acquisition. Particularly for ultra-precision machining applications, robust interferometry is considered as the best choice for its unbeatable measurement resolution. Moreover, single point methods are preferred over areal methods for OMSM applications due to the ability of miniature fibre probes to relay distance and surface information to remote interrogation apparatus.

Therefore, a single point robust interferometer is adopted as the OMSM instrument in this work. To successfully achieve the machining-measurement integration, there are still several issues to be studied. For example, the machining process has to be firstly investigated to find out the measurands of OMSM. Since operating in the manufacturing environment, the machine tool effects on the OMSM should be evaluated and compensated. Moreover, potential applications with the assistance of OMSM need to be explored to exploit the integration benefits for further enhancement of the ultra-precision machining performance.

## **4 Theoretical and experimental investigation of STS machining of freeform surfaces**

### **4.1 Introduction**

STS machining is an enabling technology to fabricate optical freeform surfaces with sub-micrometric form accuracy and nanometric surface finish without the need for any subsequent processing. Compared with other ultra-precision machining technologies, it has the advantages of faster and easier setup, faster cycle times, better surface finishes, and better form accuracy.

Various types of freeform surfaces have been fabricated using STS techniques, including off-axis aspheric mirrors [154], progressive addition lenses [155], micro-lens arrays [12], diffractive optical elements [156], etc. However, little systematic work has been reported about surface generation in the STS machining of freeform surfaces. A successful STS machining depends largely on the selection of machining parameters, tool parameters and machining trajectories. A trial-and-error cutting approach is not economic because it is time consuming and costly [157]. This chapter presents a theoretical and experimental study of STS machining of freeform surfaces. Several key machining issues including tool path planning, selection of cutting tool geometries and tool radius compensation method, are discussed in details. Moreover, surface generation simulation is proposed to investigate the theoretical topography generation during machining process. Finally, machining and measurement experiments of typical freeform surfaces are carried out to validate the effectiveness of proposed machining methodology.

### **4.2 Tool path generation**

The workflow of STS machining of freeform surfaces is proposed as illustrated in Figure 4.1. According to the design and specification of freeform surfaces, the first task is to generate a cutting tool path. In the initial stage, machining parameters are selected to meet the targeted production requirement. Next, tool interference analysis is conducted to check if the diamond cutting tool can fully access the proposed machined features. To eliminate any overcutting

phenomenon, tool radius compensation needs to be performed on the ideal tool path. Subsequently, the motion of machine tool axes is analysed for its reachability of the modified tool path. In the second stage, numerical modelling is carried out which provides an important means to predict theoretical surface generation without the need for costly trial and error tests. Profile topography is generated by the intersection of tool tip profile along the feeding direction and surface topography is formulated by a combination of all the radial sectional profiles along each angle. The simulated surface error is used as feedback information to guide the tool path generation processes. If it is less than the pre-defined value, the machining operation will be carried out.

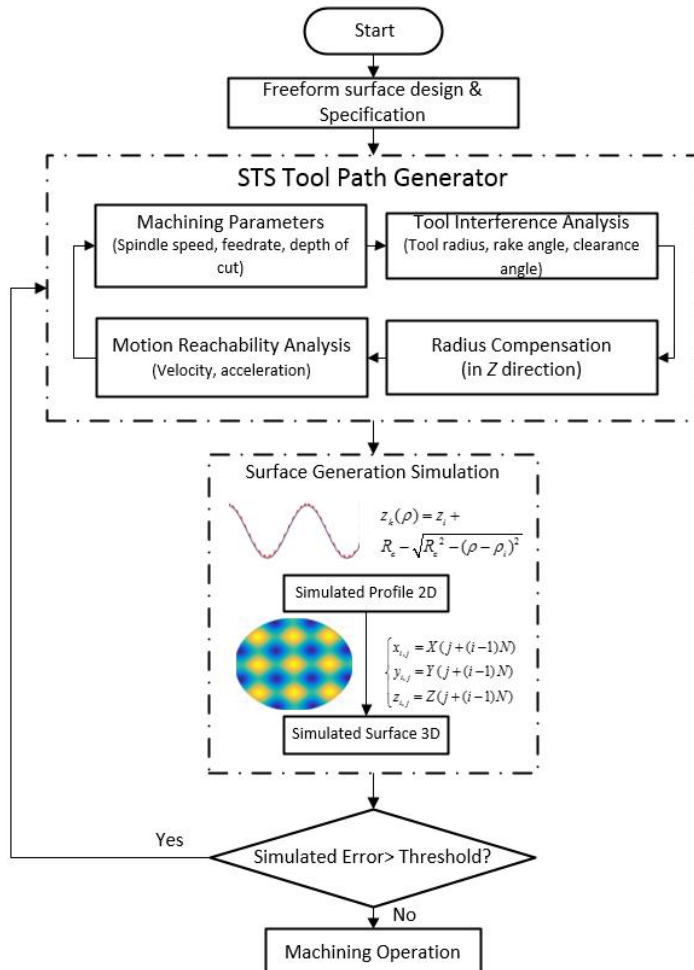


**Figure 4.1 Workflow for STS tool path generation**

#### 4.2.1 STS machining principle

Conventional SPDT process utilizes two linear axes for contouring motion with a velocity controlled spindle. Therefore, only rotational symmetric surfaces can be fabricated. As an adaption of conventional SPDT, STS technique enables the spindle to actuate in a position controlled mode (also called *C* axis mode). The schematic of STS machining setup is shown in Figure 4.2. An arbitrary 3D tool path for non-rotationally symmetric freeform surfaces can be achieved when *X* axis, *Z* axis and *C* axis move simultaneously following a given set of numerical motion commands. In most applications, the workpiece is mounted on the *C* axis while a diamond tool is installed on *Z* axis, which needs to oscillates forward and reverse in servo-synchronization with the angular position of the *C* axis and translational position of *X* axis.

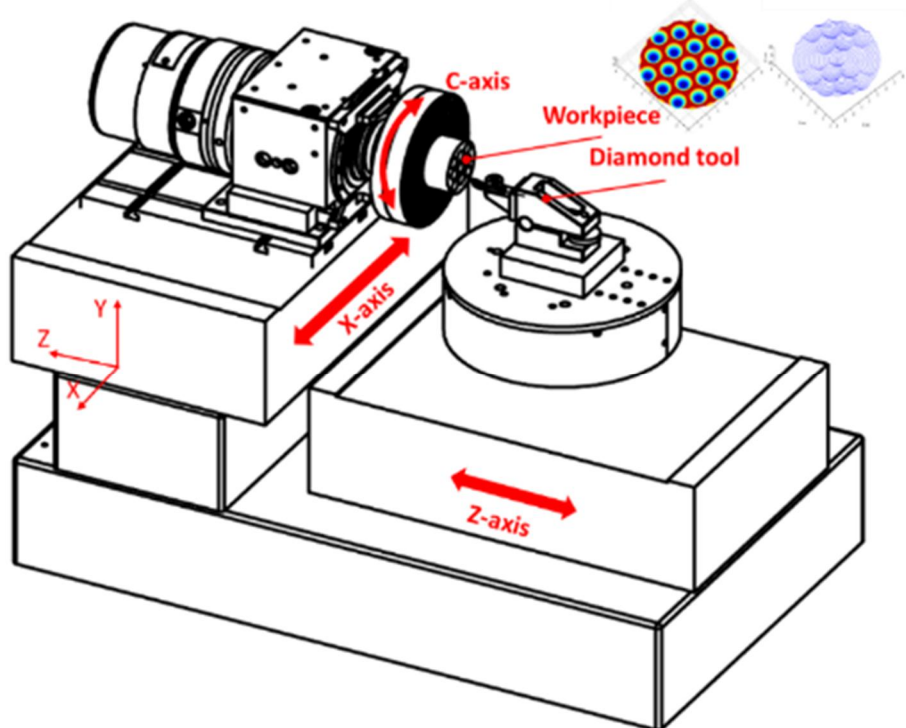


**Figure 4.2 The schematic of STS machining setup**

In STS machining mode, the coordinate system is described as a cylindrical coordinate. The tool path projection on *X-Y* plane is an equivalent spiral curve no matter how complex the surface is (as shown in Figure 4.3 (b)). The discrete points are equal-angle spaced for simple computation and control.

In  $X$ - $Y$  plane, the spiral curve can be described mathematically as follows:

$$\begin{cases} \rho_i = R_w - (i-1) \frac{f}{S \cdot N_\theta} \\ \theta_i = (i-1) \frac{2\pi}{N_\theta} \\ i = 1, 2, \dots, \frac{R_w \cdot S \cdot N_\theta}{f} + 1 \end{cases} \quad (4.1)$$

where  $\rho_i$  is the radial distance (cylindrical coordinate) in mm,  $\theta_i$  is the polar angle (cylindrical coordinate) in radians,  $R_w$  is the radius of workpiece in mm,  $i$  is the number of control points,  $f$  is the feedrate in mm/min,  $S$  is the  $C$  axis rotational speed in revolution per minute (rpm), and  $N_\theta$  is the number of programmed points per revolution. However, the surface model to be fabricated is often expressed in a Cartesian coordinate  $(x_i, y_i, z_i)$  system. Under right-hand coordinate convention, the transformation between the two coordinate systems is as follows:

$$\begin{cases} x_i = \rho_i \cos(\theta_i) \\ y_i = \rho_i \sin(\theta_i) \\ z_i = F(x_i, y_i) = F(\rho_i \cos(\theta_i), \rho_i \sin(\theta_i)) \end{cases} \quad (4.2)$$

where  $(x_i, y_i, z_i)$  is the surface model points and  $F(\bullet)$  is the surface description. To illustrate the tool path generation principle, an STS ideal tool path  $(\rho_i, \theta_i, z_i)$  for a typical freeform surface (sinusoidal grid) can be generated. The surface is mathematically expressed as,

$$z = A_x \cos\left(\frac{2\pi}{\lambda_x} x + \varphi_x\right) + A_y \cos\left(\frac{2\pi}{\lambda_y} y + \varphi_y\right) \quad (4.3)$$

where  $A_x$  and  $A_y$  are the amplitudes in  $X$  and  $Y$  direction.  $\lambda_x$  and  $\lambda_y$  are the wavelength in  $X$  and  $Y$  direction.  $\varphi_x$  and  $\varphi_y$  are the phase in  $X$  and  $Y$  direction. Figure 4.3 shows the generated tool path and its spiral  $X$ - $Y$  projection.

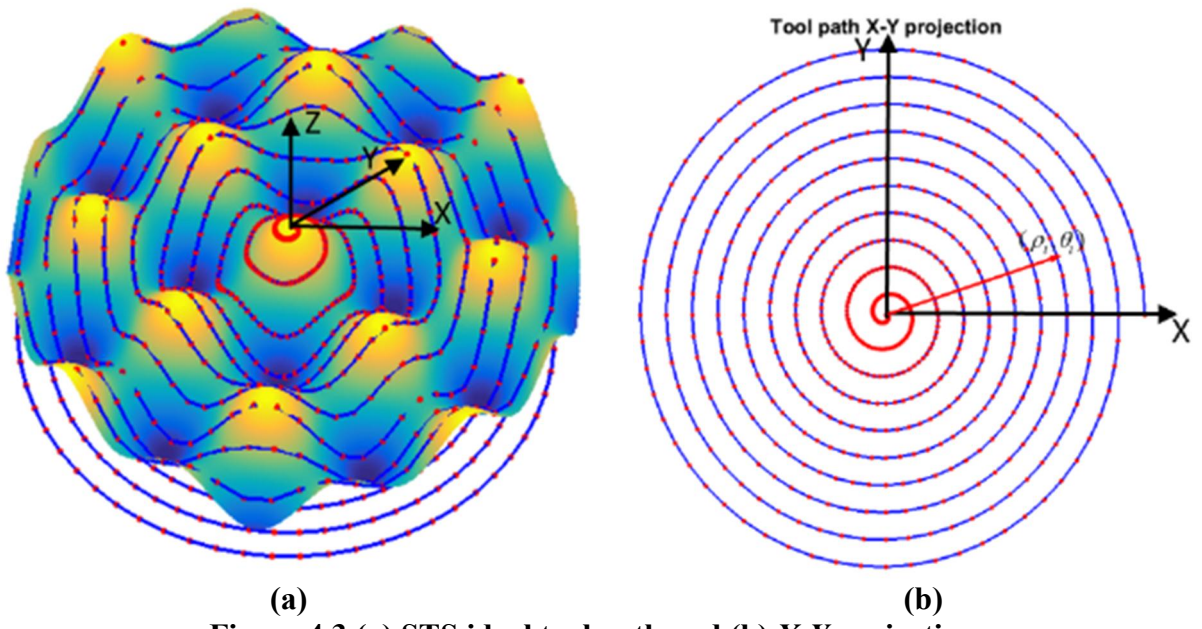


**Figure 4.3 (a) STS ideal tool path and (b) X-Y projection**

#### 4.2.2 Tool geometries selection

Tool geometries should be carefully selected to guarantee the accessibility to the features of the proposed freeform surfaces. As shown in Figure 4.4, geometric parameters of a typical diamond cutting tool include the tool radius  $R_c$ , the included angle  $\psi$ , the rake angle  $\gamma$  and the clearance angle  $\alpha$ .

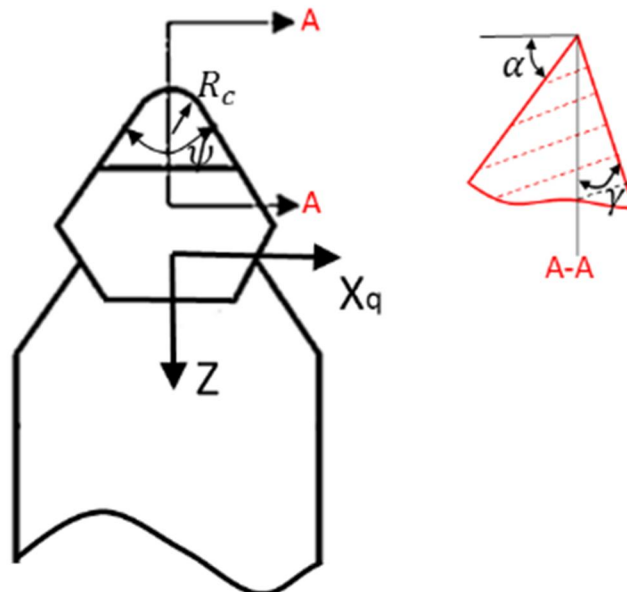


**Figure 4.4 Geometric parameters of a typical diamond cutting tool**

The schematic for tool geometry selection in STS freeform machining is illustrated in Figure 4.5. For every cutting point (red dot in the plot), a radial cutting plane is determined by

the  $Z$  axis and the cutting point while a normal plane is perpendicular to the radial plane and crosses the cutting point (shown in Figure 4.5 (a)). Proper tool parameters should be selected to avoid interference with the machining surfaces in both planes.  $R_c$  and  $\psi$  are calculated in the radial cutting plane, whereas  $\gamma$  and  $\alpha$  are calculated in the normal plane.

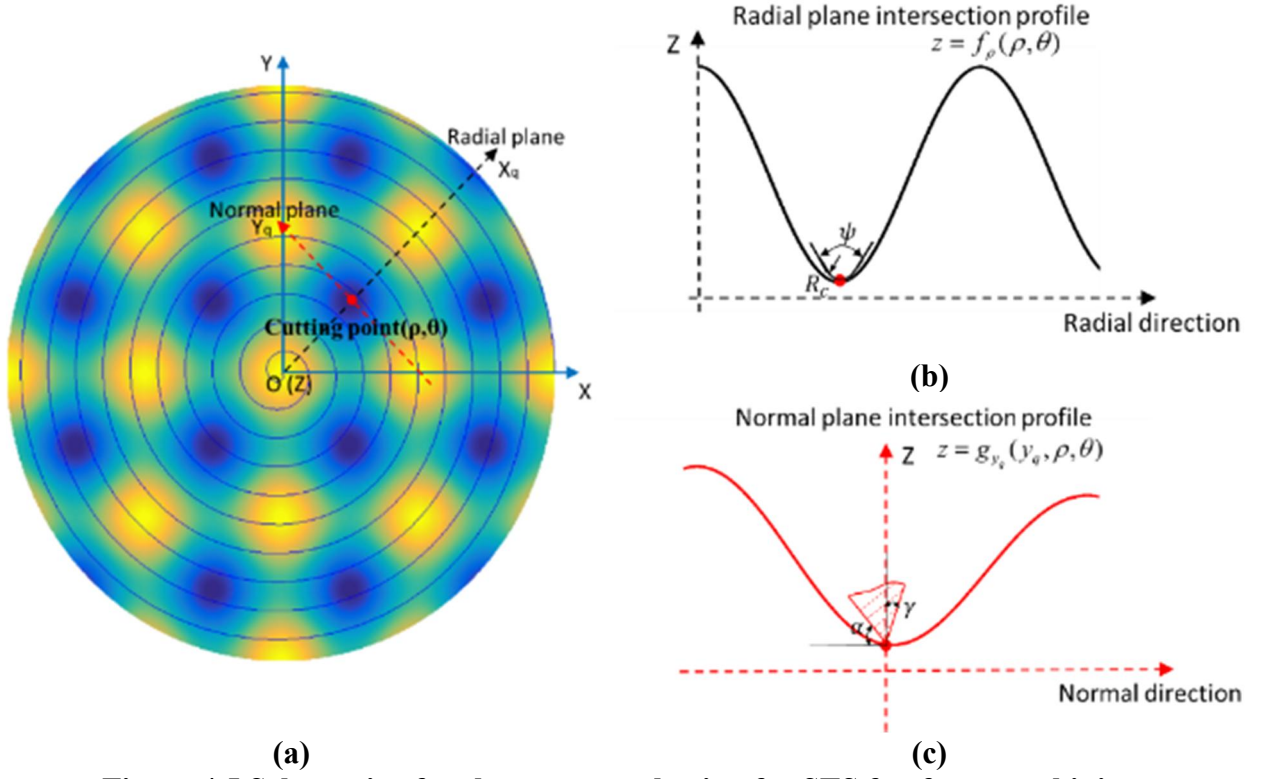


**Figure 4.5 Schematic of tool geometry selection for STS freeform machining**

As shown in Figure 4.5 (b), along each sectional profile  $f_p(\rho, \theta)$  in the radial plane, tool tip nose radius  $R_c$  should be small enough so that the tool is accessible to all the profile features and its critical value is determined by the minimum radius of curvature for all the cutting points. The included angle  $\psi$  should be large enough to make sure the cutting edge always keeps in contact with the machining surface and its critical value is determined by the maximum value of the angle of inclination along the radial intersection profiles. The two conditions can be mathematically expressed as the follows:

$$\begin{cases} R_c \leq \min \left\{ \frac{\left(1 + (f'_\rho(\rho, \theta))^2\right)^{\frac{3}{2}}}{f''_\rho(\rho, \theta)} \right\} & 0 < \rho \leq R \\ \psi \geq 2 \max \left\{ \arctan(f'_\rho(\rho, \theta)) \right\} & 0 < \theta \leq 2\pi \end{cases} \quad (4.4)$$

where  $f'_\rho(\rho, \theta)$  and  $f''_\rho(\rho, \theta)$  are respectively the first derivative and second order derivative of radial intersectional profile  $f_\rho(\rho, \theta)$ . To calculate the limit of the tool rake angle and the clearance angle, the intersection profile  $g_{y_q}(y_q, \rho, \theta)$  in the normal plane is obtained in the normal plane perpendicular to the radial plane (the red curve shown in Figure 4.5 (c)). The tool rake face and flank should not interfere with the machined surface. Thus, the following conditions must be met:

$$\begin{cases} \gamma \geq \max \left\{ \arctan(g'_{y_q}(y_q, \rho, \theta)) - \frac{\pi}{2} \right\} \\ \alpha \geq \max \left\{ -\arctan(g'_{y_q}(y_q, \rho, \theta)) \right\} \end{cases} \quad (4.5)$$

where  $g'_{y_q}(y_q, \rho, \theta)$  is the first derivative of normal plane intersectional profile. Besides the accessibility issue, the effect of the tool tip on the surface generation needs to be considered, which is discussed in the following section.

#### 4.2.3 Tool radius compensation

Due to the circular geometry of the diamond tool tip, the cutting edge will cause overcut on the machined surface if the tool path is programmed based on the ideal infinitely sharp profile. Such an effect is illustrated in Figure 4.6. The red area shows the overcutting phenomenon, which would deteriorate the surface accuracy.

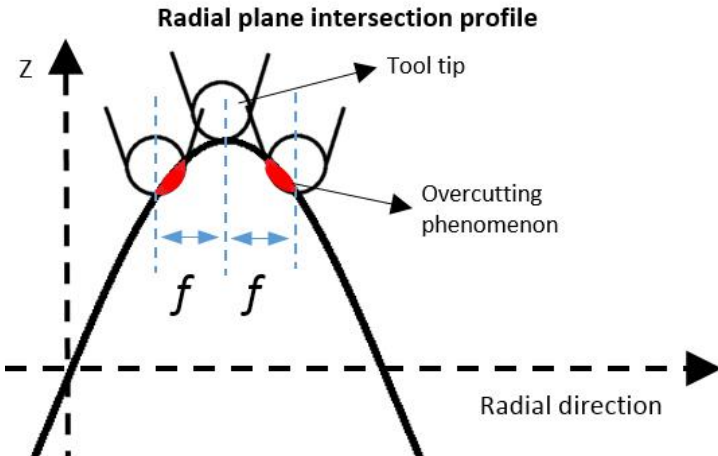


**Figure 4.6 Schematic of overcutting phenomenon caused by a circular tool tip**

To avoid overcut on a machined surface, tool radius compensation is performed so that the circular tool edge should always be tangent to the intersection profile in each radial plane. Conventionally, tool radius compensation is performed in the normal direction on the cutting points [158]. The normal method is illustrated in Figure 4.7. The black tool tip shows the original programmed position. To compensate the overcut, the cutting position (red dot) is shifted so that the tool edge profile contacts tangential to the surface profile as indicated by the orange tool tip. The centre of the circular tool edge is along the normal direction of the cutting point.

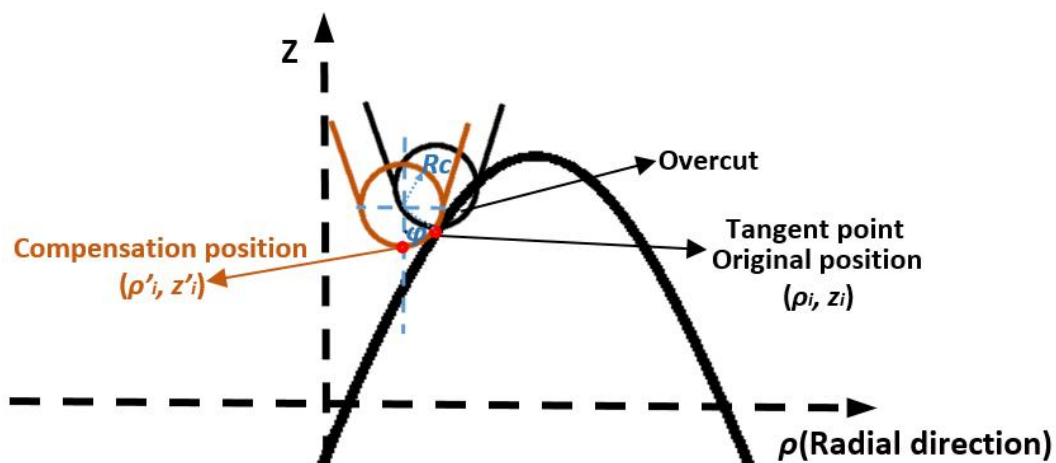


**Figure 4.7 Tool radius compensation using normal direction method**

For a given radial intersection profile  $f_\rho(\rho, \theta)$ , the relationship between the original cutting point  $(\rho_i, z_i)$  and the compensation position  $(\rho'_i, z'_i)$  can be expressed as follows:

$$\begin{cases} \dot{\rho_i} = \rho_i - R_c \sin(\varphi_i) \\ \dot{z_i} = z_i + R_c \cos(\varphi_i) - R_c \\ \tan(\varphi_i) = \frac{df_\rho(\rho)}{d\rho} \Big|_{\rho=\rho_i} \end{cases} \quad (4.6)$$

where  $\varphi_i$  is the slope angle at  $(\rho_i, z_i)$  in the intersection profile. Calculation of slope angle is required at every cutting point as the slope of freeform surfaces varies along the radial direction as well as different angles.

To illustrate the tool radius compensation process, tool path generation was performed for a sinusoidal grid surface described by Equation 4.3. The surface design parameters were set to be  $A_x = A_y = 1 \mu\text{m}$ ,  $\lambda_x = \lambda_y = 0.5 \text{ mm}$ ,  $\varphi_x = \varphi_y = 0$ . The machining parameters were selected to be  $f = 5 \text{ mm/min}$ ,  $S = 100 \text{ rpm}$ ,  $R_c = 0.5 \text{ mm}$ . The compensated and uncompensated 3D tool path are shown in Figure 4.8 (a). Figure 4.8 (b) indicates the  $X$ - $Y$  projection of the compensated tool path and how it deviates from original spiral trajectories. The motion analysis, illustrated in Figure 4.8 (c) and Figure 4.8 (d), shows additional motion components appearing on both  $X$  and  $Z$  axis after the radius compensation in the normal direction. The disadvantage of the normal compensation method is that the tool tip shift is required to be performed in both  $X$  and  $Z$  direction. Moreover, the shift value is not constant as the slope angle varies at different cutting points on freeform surfaces. Therefore, high frequency motion of both  $X$  and  $Z$  axis is required for tool radius compensation in the normal direction. For the configuration of the machine tool used in this work, the heavy working spindle is mounted on the  $X$  axis and its dynamic response is thus limited.

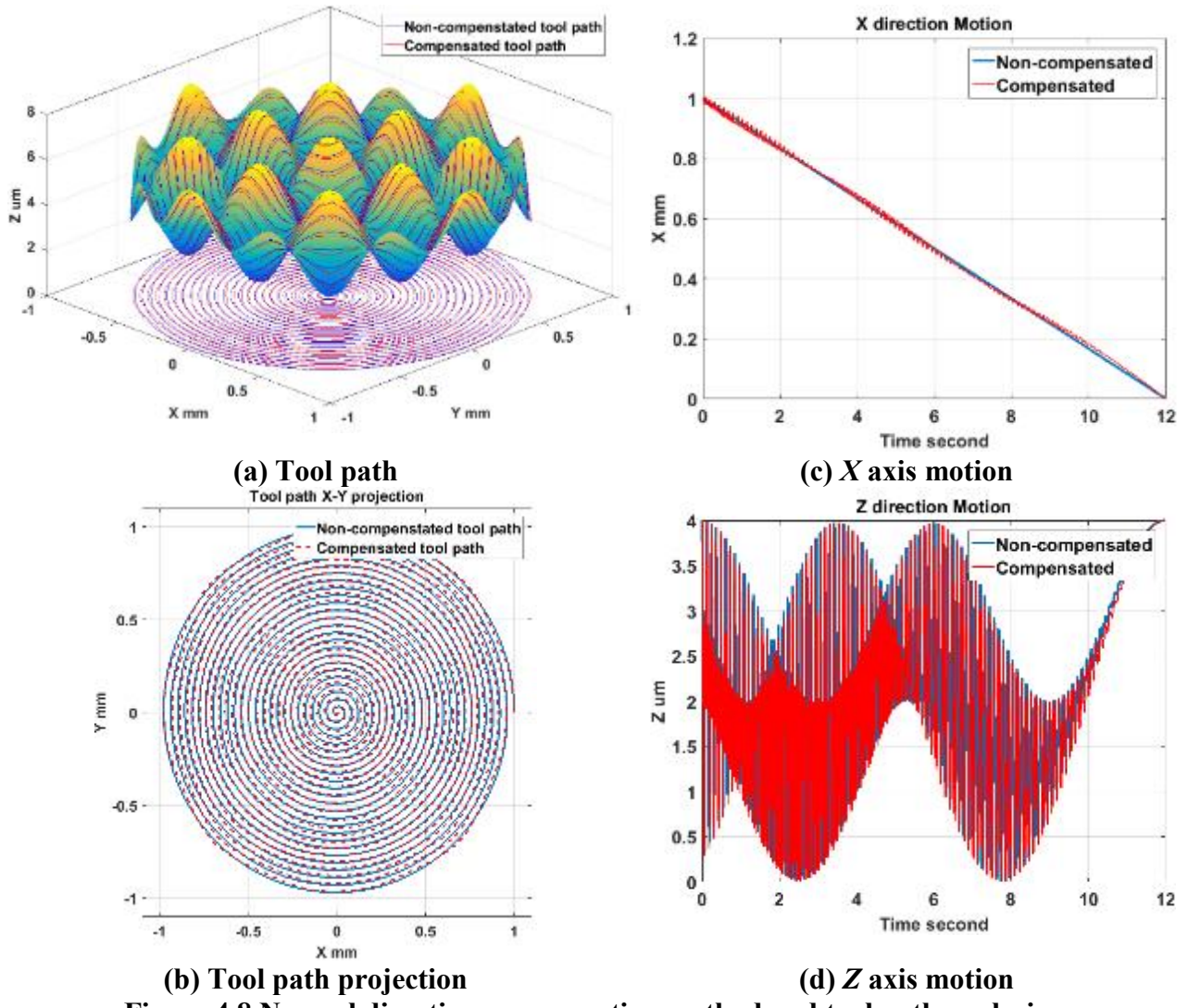


Figure 4.8 Normal direction compensation method and tool path analysis

Therefore, a modified tool radius compensation method is developed in this work as shown in Figure 4.9. In Z direction compensation method, the tool tip only needs to shift along Z direction until the cutting edge is tangential to the surface. The relationship between the original cutting point  $(\rho_i, z_i)$  and the compensation position  $(\rho'_i, z'_i)$  can be expressed as follows:

$$\begin{cases} \rho'_i = \rho_i \\ z'_i = z_i + \Delta z \end{cases} \quad (4.7)$$

$$\begin{cases} \Delta z = \frac{R_c}{\cos \varphi} - R_c \\ \tan(\varphi') = f'_\rho(\rho_i + R_c \sin(\varphi_i)) \end{cases} \quad (4.8)$$

where  $\Delta z$  is the tool shift value in Z direction and  $\phi'$  is the slope angle of the new tangential point.  $\phi'$  is in an implicit equation and solved using Newton's iterative algorithm [159].

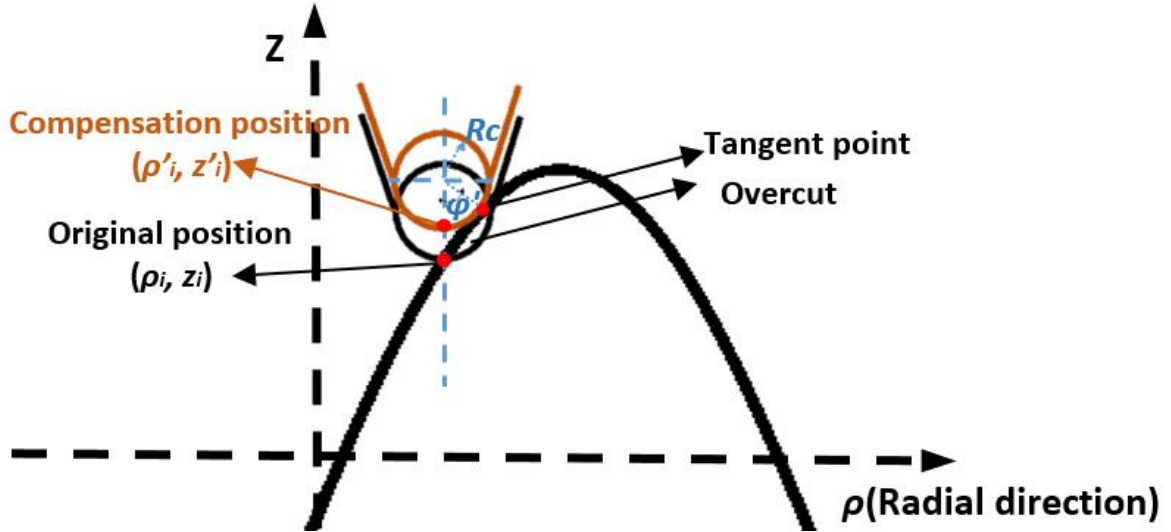


**Figure 4.9 Tool radius compensation using Z direction method**

The difference between the two compensation methods is simulated along a cosine radial profile and illustrated in Figure 4.10. The red dots show the tool position using Z compensation method whereas the black dots represent the tool position using normal compensation method.

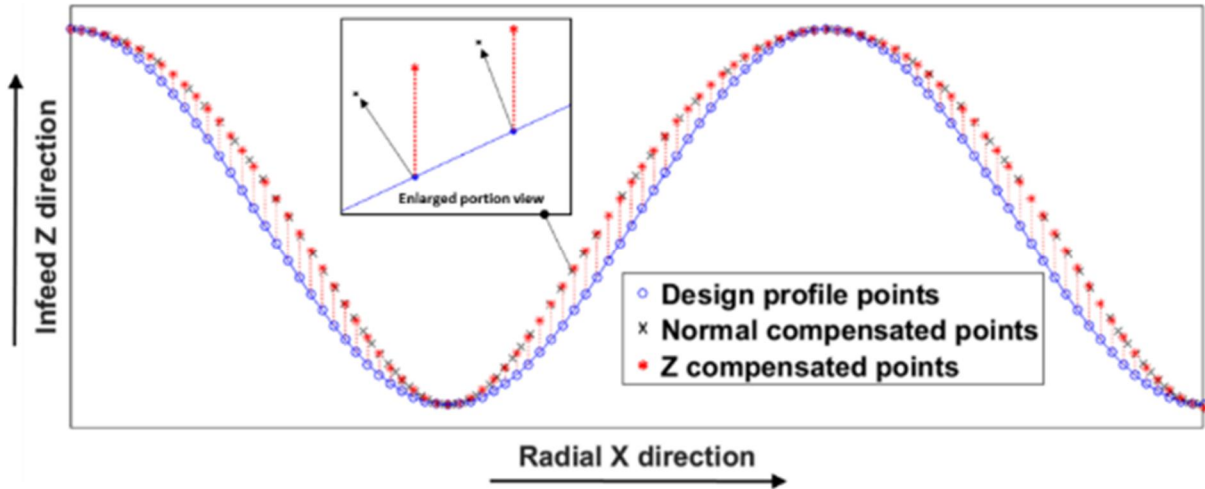
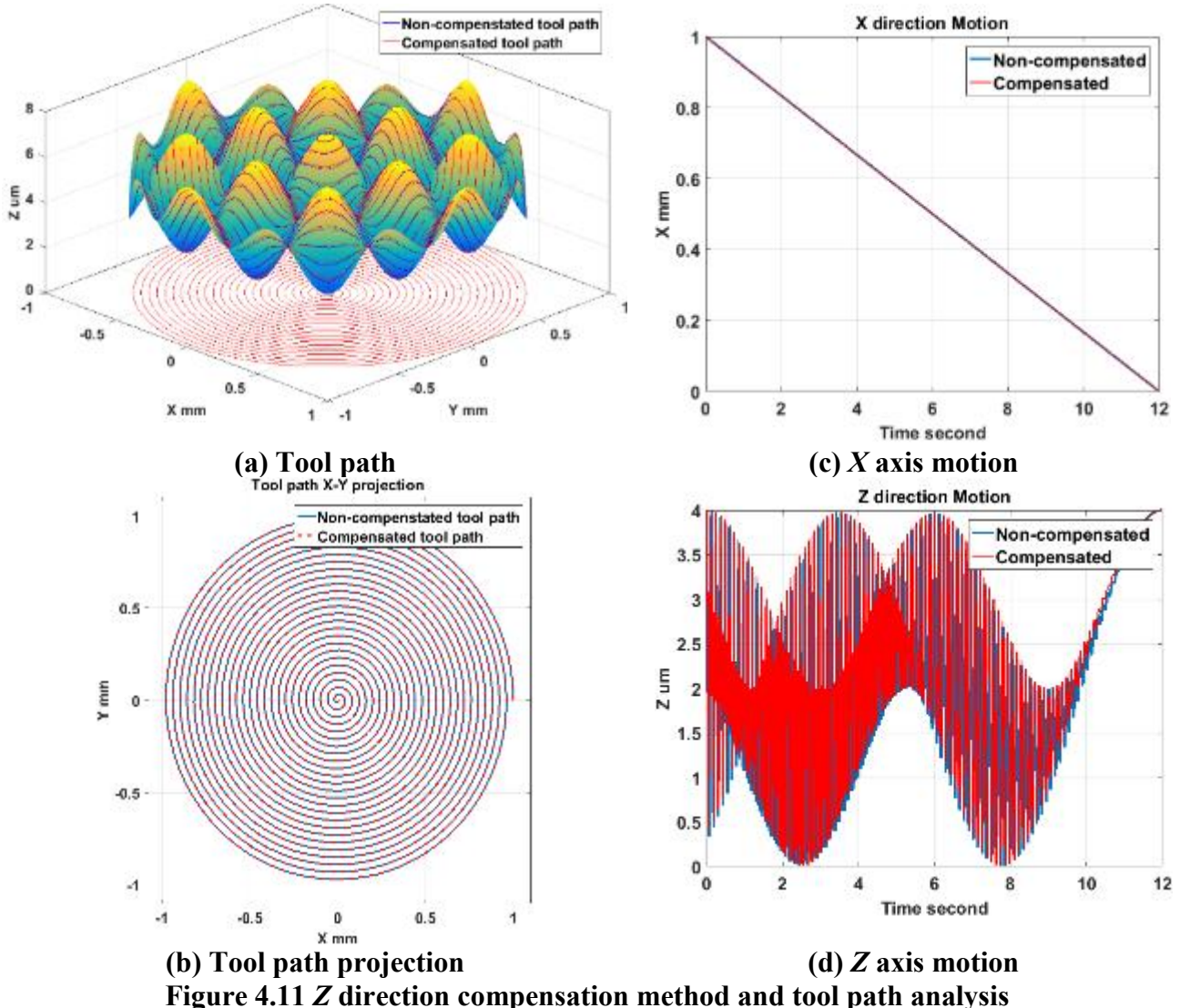


**Figure 4.10 Comparison of two compensation method along a radial profile**

In addition, tool path simulation using Z direction compensation method was carried out for the same sinusoidal grid surface presented above. As shown in Figure 4.11 (b), the  $X-Y$  projection of the compensated tool path coincides with the uncompensated one, which means the tool shift is only performed in Z direction. The motion analysis in Figure 4.11 (c) and Figure

4.11 (d) also validates additional high frequency motion is avoided for the low-dynamic  $X$  axis. Therefore, the  $Z$  direction compensation method is considered more stable for STS machining of freeform surfaces.



### 4.3 Surface generation simulation and analysis

#### 4.3.1 Principles

Surface generation simulation offers a cost effective solution to select optimal cutting conditions, to predict the surface quality and to understand the machining phenomenon without the need for costly trial and error machining tests. As illustrated in Figure 4.12, the successive tool positions are distributed at the interval of feedrate along each radial intersection profile

curve. Once the tool path is derived (the dashed line), the theoretical surface topography can be formed as the envelope of consecutive tool tip profiles along the feeding trajectory. Between the intersection points, the theoretical surface profile is a section of circular tool tip profile (shown as black solid line).

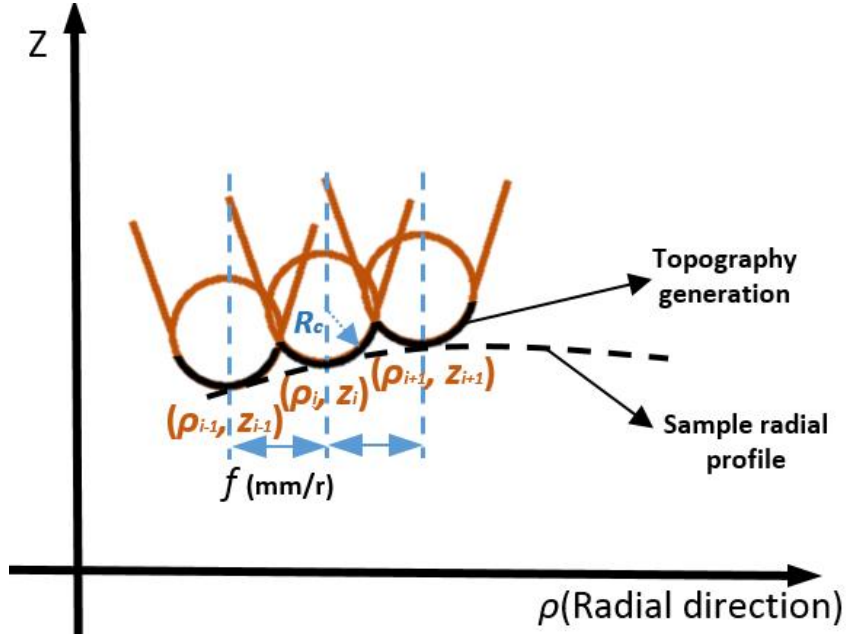


**Figure 4.12 Schematic diagram of profile topography generation**

Assuming the tool tip radius is  $R_c$  and tool tip location is  $(\rho_i, z_i)$ , the cutting profile can be expressed as:

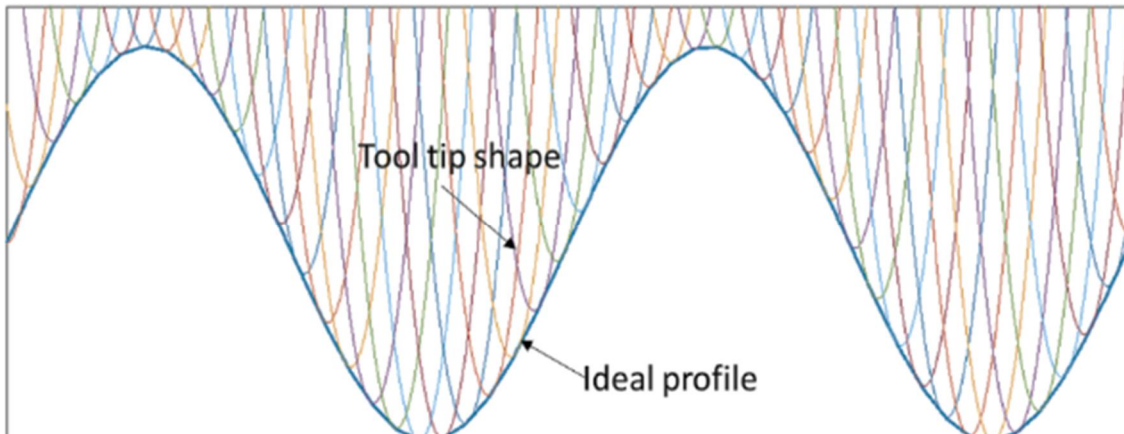
$$z(\rho) = z_i + R_c - \sqrt{R_c^2 - (\rho - \rho_i)^2} \quad (4.9)$$

Thus, the profile topography height  $h_{envelope}$  at radial position  $\rho$  can be calculated as the minimum value of all the cutting profiles:

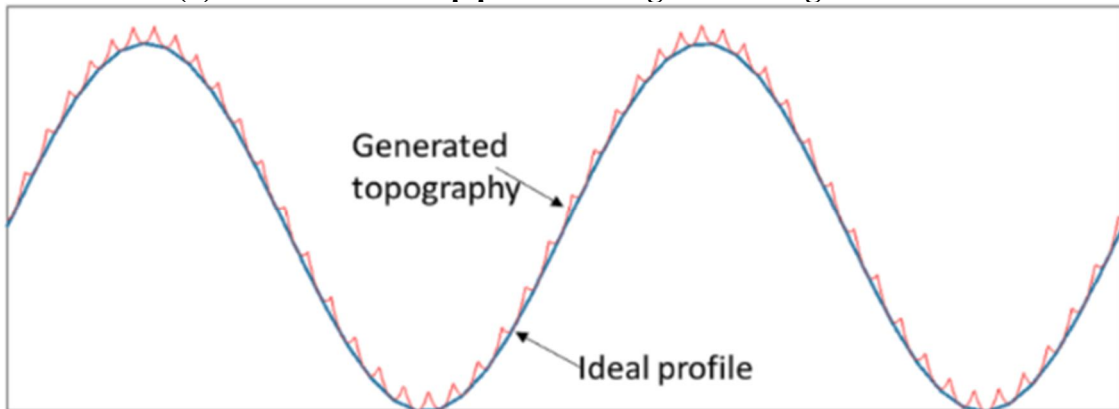
$$h_{envelope}(\rho) = \min \{z_k(\rho)\}, \quad k : i-1 \text{ to } i+1 \quad (4.10)$$

Take a cosine radial profile as an example to validate the topography generation method. The result in Figure 4.13 clearly shows the successive tool tip profiles along the feeding direction and the resulting topography generation. The areal surface topography can be formulated by combination of all the radial intersection profile topography at each angle. With the above proposed method, generation simulation of a sinusoidal grid surface (described by

Equation 4.3) is performed. The surface parameters are the same as those in section 4.2.3. For illustration purpose, the machining parameters are selected to be  $f = 2$  mm/min,  $S = 100$  rpm,  $R_c = 0.05$  mm. Figure 4.14 (a) and Figure 4.14 (b) respectively show the simulated areal surface topography and extracted profile topography at 0 degree. The theoretical turning marks can be clearly seen on the simulated surface.

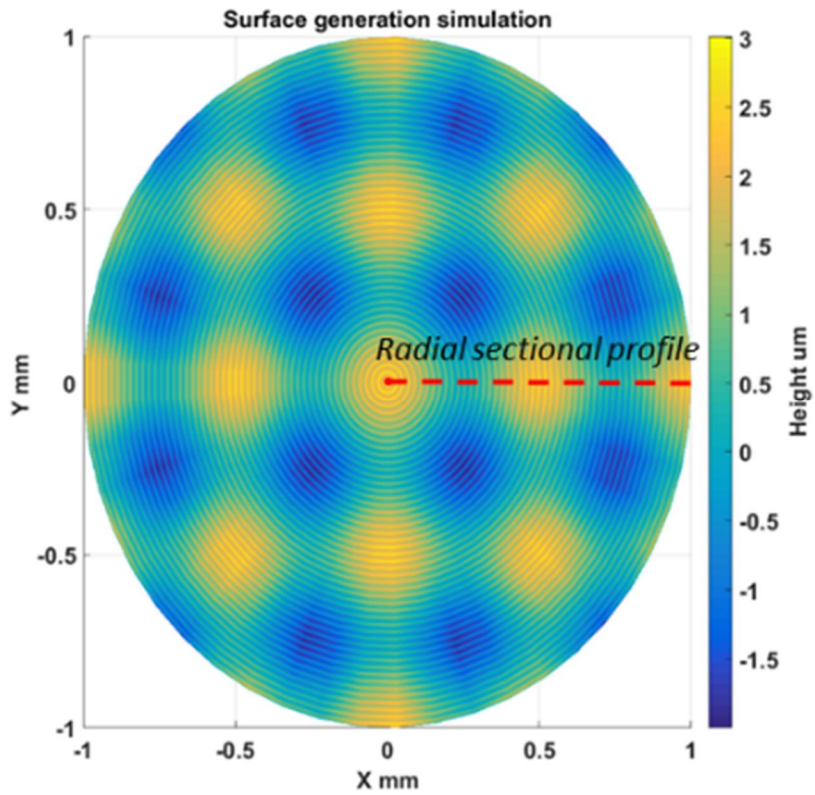


(a) Successive tool tip profiles along the feeding direction

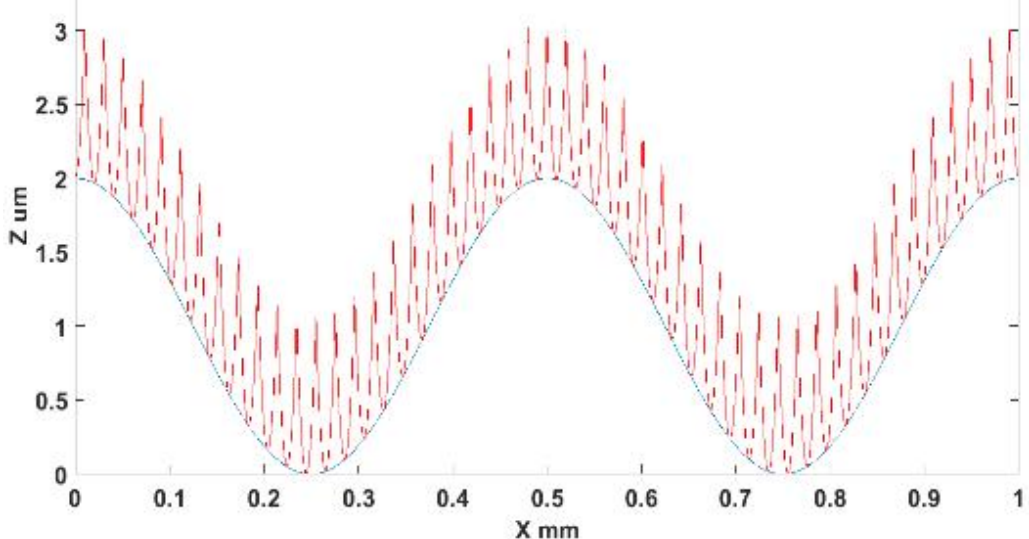


(b) Resulting topography generation

**Figure 4.13 Simulation of topography generation along radial profile**



(a) Surface generation simulation



(b) Radial section profile topography (0 degree)

Figure 4.14 Simulation example of areal surface topography generation

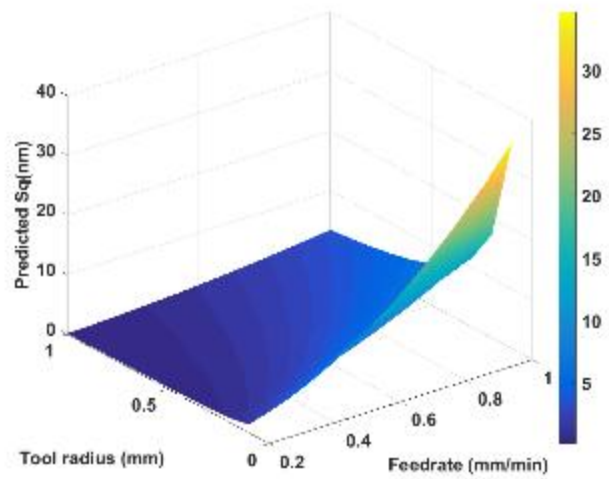
#### 4.3.2 Simulation analysis

With the established surface generation model, simulation analysis is carried out in this section. The analysis is used to guide the selection of cutting parameters to achieve the targeted surface quality and better understand the machining processes as well.

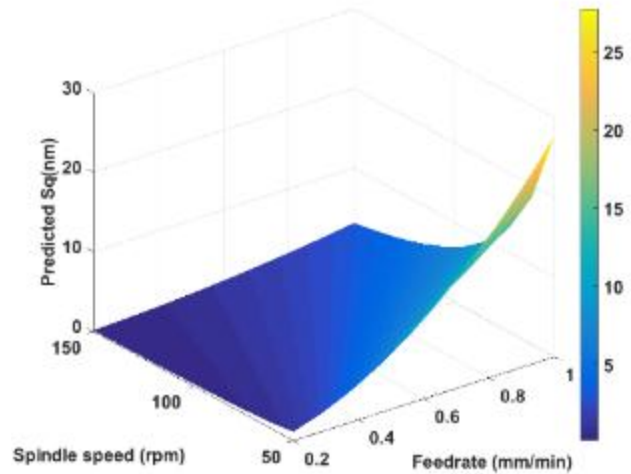
Without consideration of material effects, there are three processing parameters that influence the theoretical surface generation, which are tool radius  $R_c$  (mm), feedrate  $f$  (mm/min), and spindle speed  $S$  (rpm). The relationship between processing parameters and surface quality is investigated with the aid of surface generation simulation developed in this work. The investigation range is set as:  $R_c$  0.1–1 mm;  $f$  0.2–1 mm/min;  $S$  50–150 rpm. The root mean square height  $S_q$  value (described in section 2.4.2) is adopted to quantitatively describe the simulated surface quality.

Figure 4.15 illustrates the relationship graphs between processing parameters and surface quality using the surface generation simulation. From the simulation results, it can be concluded that better surface finish (lower  $S_q$  value) can be obtained under a higher spindle speed, a smaller feedrate and larger tool radius. In practice, it is better to choose higher spindle speed rather than decreasing the feedrate. A lower feedrate would increase the machining time, decrease the tool life and make the machining process vulnerable to the environmental variations. However, higher spindle speed in STS machining requires a higher motion frequency and servo bandwidth, which is limited by the machine tool configuration and control strategy. The increase of tool radius results in the decrease of the  $S_q$  value, the tool tip accessibility should be taken into consideration, which is discussed in section 4.2.2. The relationship graphs are generated with the aid of surface generation simulation without the costly trial and error experiments, which are useful to select optimised processing parameters to obtain a targeted surface quality.

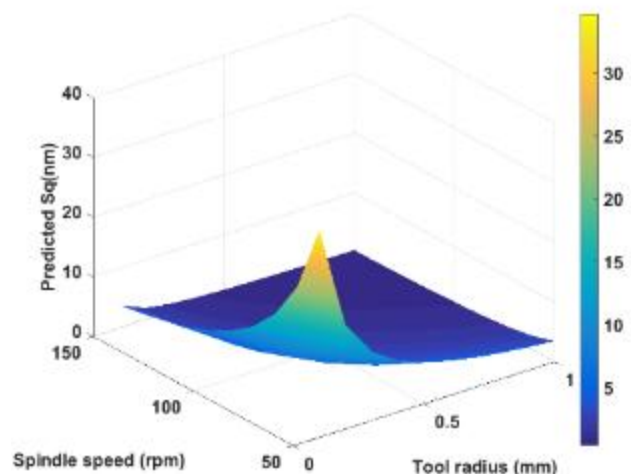
Surface generation simulation also provides an important means for understanding the cutting phenomenon. In the following section, simulation analysis is performed to study the overcutting phenomenon and the effectiveness of tool radius compensation.



(a)  $R_c$  and  $f$  vs.  $S_q$  ( $S=100$  rpm)



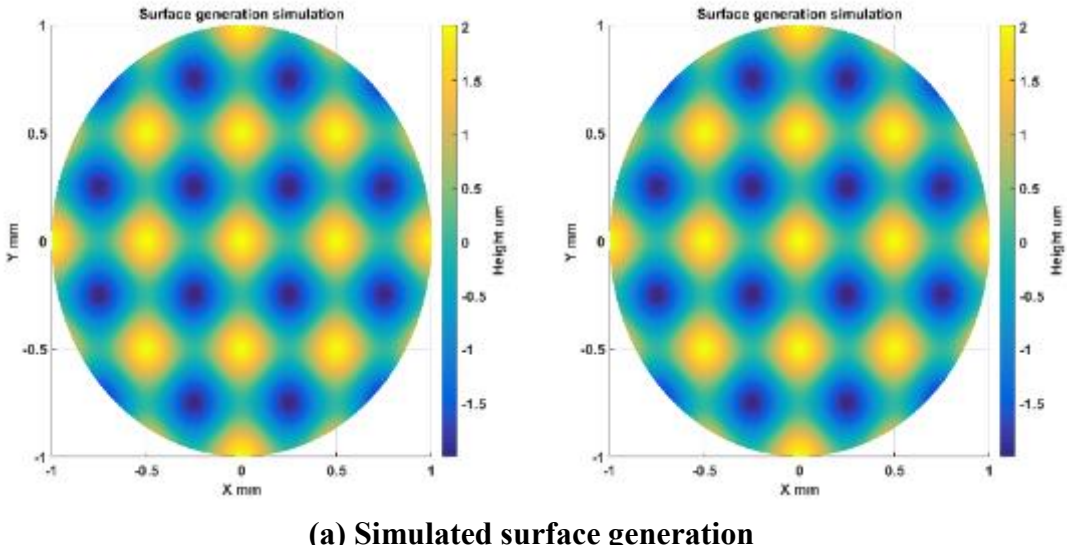
(b)  $S$  and  $f$  vs.  $S_q$  ( $R_c = 0.5$  mm)



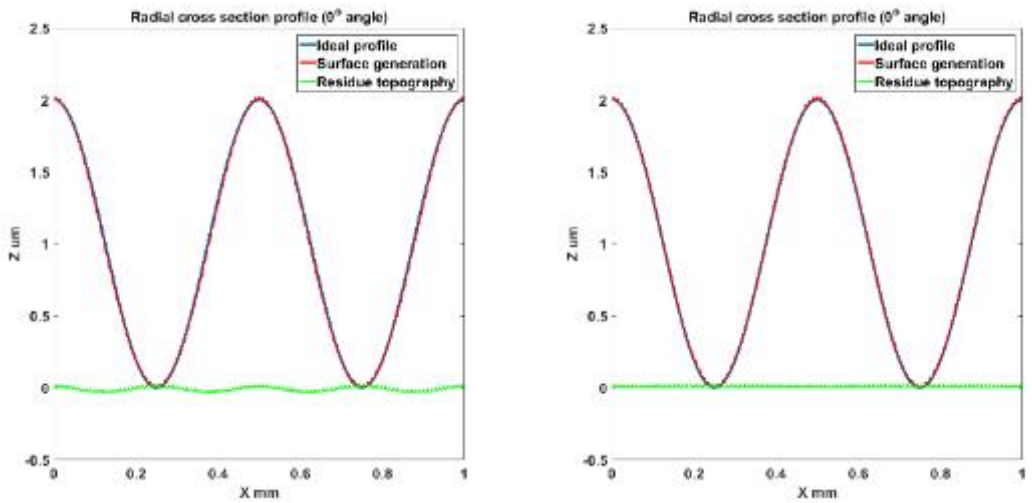
(c)  $S$  and  $R_c$  vs.  $S_q$  ( $f=0.6$  mm/min)

**Figure 4.15 Relationship graphs between processing parameters and surface quality**

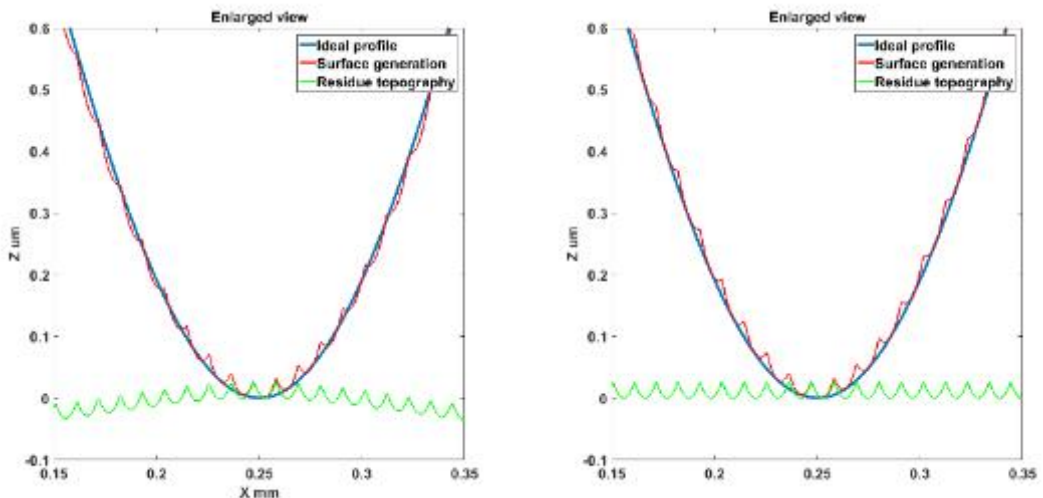
The sinusoidal grid surface described by Equation 4.3 is used in the simulation. The surface design parameters are kept the same as those in section 4.2.3. The machining parameters are selected to be  $f = 5$  mm/min,  $S = 50$  rpm,  $R_c = 0.5$  mm. The simulation results are shown in Figure 4.16. Plots in the right and left show the simulation analysis of surface generation with and without tool radius compensation respectively. As shown in the left plot of Figure 4.16 (b) and Figure 4.16 (c), the overcutting phenomenon can be clearly observed and waviness error components are induced on the machined surface due to the tool tip overcut. In contrast, the overcutting phenomenon is avoided with the proposed tool radius compensation and waviness error components are eliminated, as shown in right plot of Figure 4.16 (b) and Figure 4.16 (c). Figure 4.16 (d) illustrates areal surface topography residual after form removal. The result also indicates that the pattern of induced waviness errors varies with intersection angles. The study has validated the proposed tool radius compensation method and effectiveness of simulation analysis to investigate the cutting phenomenon.



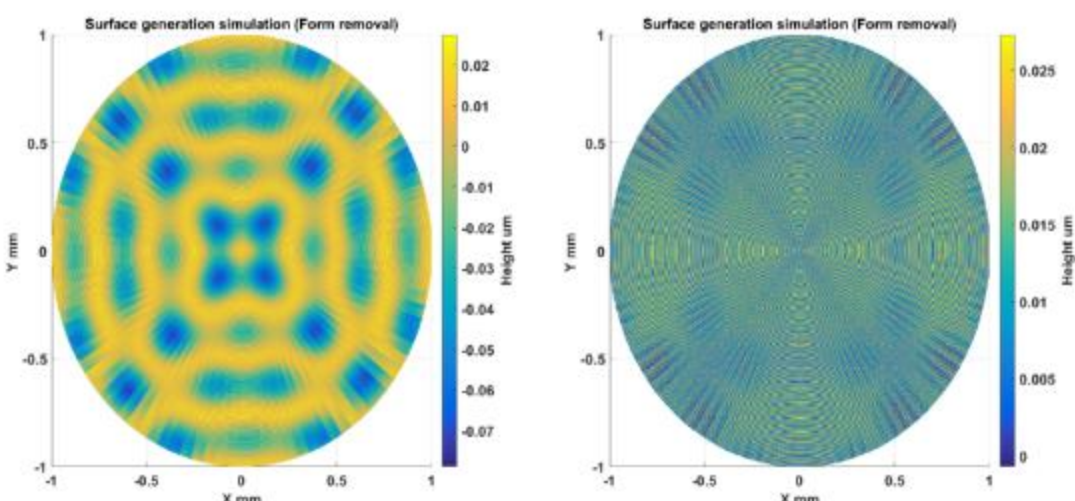
(a) Simulated surface generation



**(b) Extracted radial profile topography**



**(c) Enlarged view of radial profile topography**



**(d) Simulated surface topography residual (after form removal)**

**Figure 4.16 Simulation analysis of overcutting phenomenon and tool radius compensation**

**(left column: without compensation, right column: with compensation)**

## 4.4 Experiments and discussions

In order to show the feasibility and effectiveness of the proposed STS machining methodology, machining experiments of typical freeform surfaces (a sinusoidal grid and MLA surface) are carried out in the section.

### 4.4.1 Experimental setup

The machine tool used in the machining experiment is a Nanoform 250 Ultra Grind [160], which is shown in Figure 4.17.

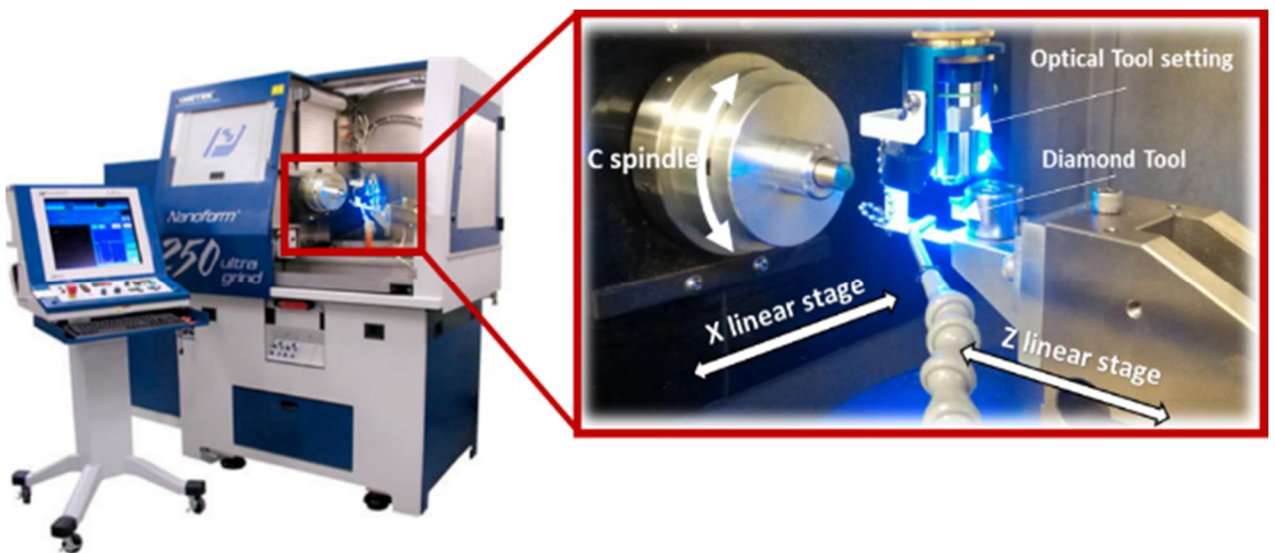


**Figure 4.17 Experimental setup of STS machining**

It can be used for diamond turning and ultra-precision grinding. The machine tool incorporates a finite element analysis (FEA) optimized dual frame for the ultimate environmental isolation. A sealed natural granite base also provides excellent long term stability and vibration damping. Both  $X$  and  $Z$  slides are equipped with hydrostatic oil bearing with symmetrical linear motor placement. The position of the  $X$  and  $Z$  axes is measured with linear laser scale encoders, which are capable of resolving 0.016 nm after signal subdivision. The straightness error for both  $X$  and  $Z$  axis over the full travel is less than 0.2  $\mu\text{m}$  according to the machine tool specification. Under position controlled mode, maximum rotational speed of  $C$  axis can be 1500 rpm with a feedback resolution of 0.01 arc sec, while maintaining axial and radial error motion of less than

15 nm. The high precision and stability of the machine tool is the prerequisite for the ultra-precision machining process. The sample material used in the experiments is an aluminium alloy (Al6082) with a chemical composition of (0.7%Mn, 0.5%Fe, 0.9%Mg, 1%Si, 0.1%Cu, 0.1%Zn and 0.25%Cr). The material is of good machinability and its mechanical properties are listed in Table 4.1.

**Table 4.1 Mechanical properties of the sample material (Al6082)**

Parameters	Value
Density (g/cm <sup>3</sup> )	2.70
Modulus of elasticity (GPa)	70
Tensile strength (MPa)	260
Shear strength (MPa)	170
Thermal conductivity (W/m.K)	180

#### 4.4.2 Sinusoidal grid surface machining

A sinusoidal grid surface can be used for measurement of two-dimensional (2D) planar displacements [161]. The freeform surface is continuous and described mathematically by Equation 4.3. In the experiment, the design parameters were set to be  $A_x = A_y = 2 \mu\text{m}$ ,  $\lambda_x = \lambda_y = 2.5 \text{ mm}$ ,  $\varphi_x = \varphi_y = 0$ . The machining and diamond cutting tool parameters are respectively listed in Table 4.2 and Table 4.3. With the analysis discussed in section 4.2.2, the selected diamond tool can avoid interference with the machined surface. The proposed Z direction tool radius compensation was also performed on the ideal tool path to avoid the overcutting phenomenon. The design and STS tool path of the sinusoidal grid surface are illustrated in Figure 4.18 (a) and Figure 4.18 (b) respectively. The sample was successfully machined, as shown in Figure 4.19.

**Table 4.2 Machining parameters for sinusoidal grid surface**

Parameters	Value
Machining mode	STS
Spindle speed (rpm)	50
Feedrate (mm/min)	0.5

Cutting depth ( $\mu\text{m}$ )	3
---------------------------------	---

**Table 4.3 Diamond tool parameters**

Parameters	Value
Manufacturer	Contour fine tooling
Tool material	Single crystal
Tool tip radius (mm)	0.514
Rake angle (deg)	0
Clearance angle (deg)	10
Included angle (deg)	60

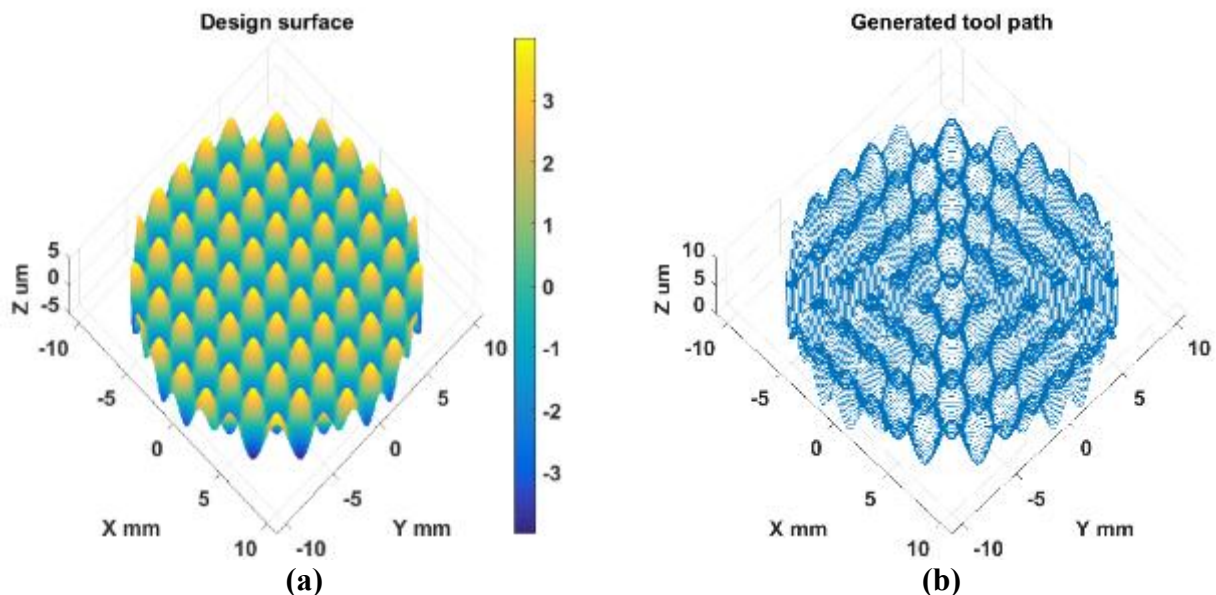


**Figure 4.18 (a) Design and (b) STS tool path of sinusoidal grid surface**

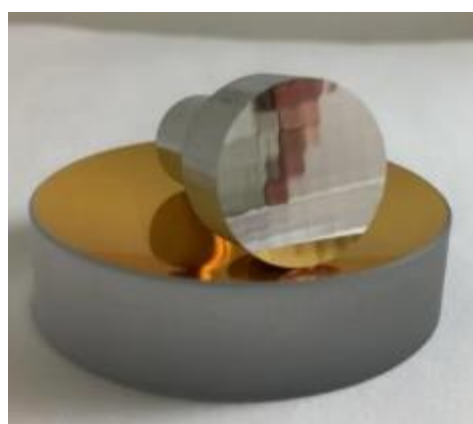


**Figure 4.19 Photo of STS machined sinusoidal grid surface**

To inspect the machining quality, the sample was measured using a Talysurf CCI 3000 [162], equipped with a 20X microscope objective. The original and processed measurement result are shown in Figure 4.20 (a) and Figure 4.20 (b) respectively. After filtering out the form component, the turning marks can be clearly observed from the CCI measurement. The surface topography was characterised by  $S_q$ .

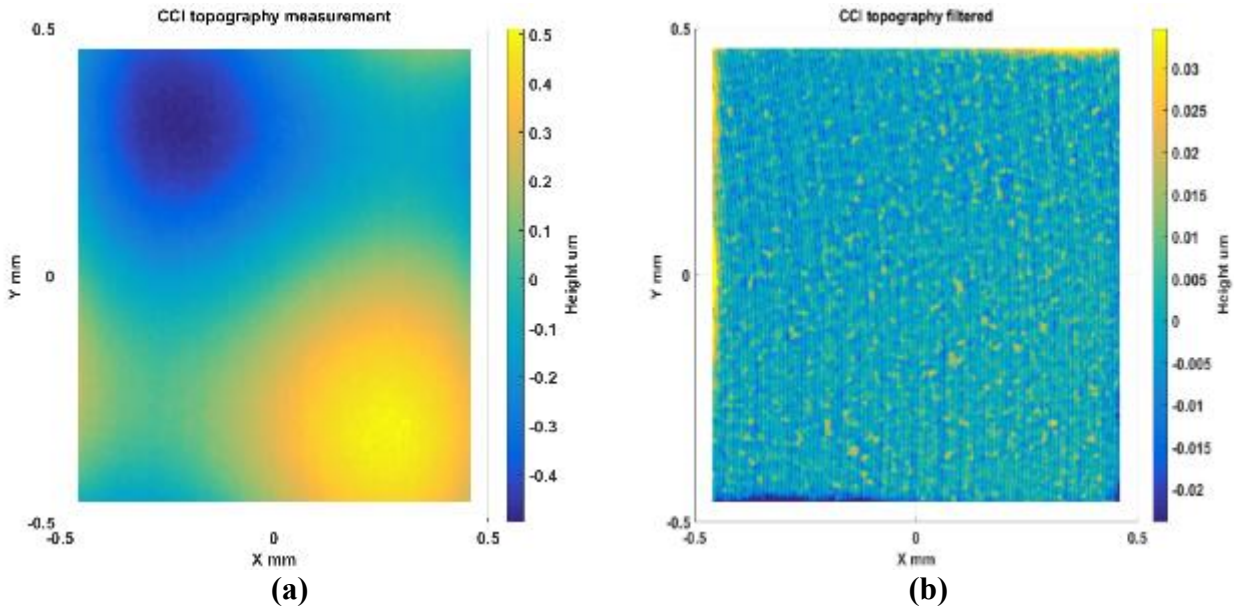


**Figure 4.20** Machined sinusoidal grid surface CCI measurement: (a) original; (b) after form removal

To examine the uniformity of the topography distribution, five areas were measured on the surfaces. The average  $S_q$  is calculated as 7.1 nm and standard deviation is 0.30 nm. The measurement results indicate the machined topography of the continuous freeform surface is uniformly distributed over the surface and less than 10 nm.

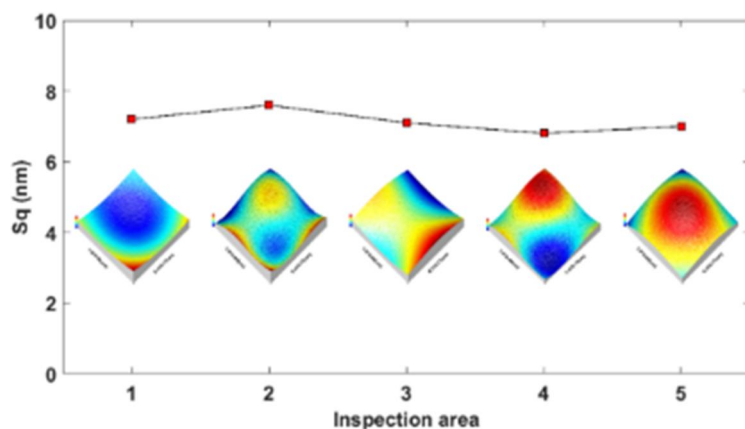


**Figure 4.21** Topography distribution of sinusoid grid surface

#### 4.4.3 MLA surface machining

Micro-lens arrays (MLAs) are playing a key role in highly efficient light transmission [163]. MLA surface is regarded as a type of structured freeform surface. It is composed of multiple elemental lenses, which are distributed in a specific pattern. In this experiment, the design parameters for MLA are listed in Table 4.4.

**Table 4.4 MLA design parameters**

Parameters	Value
Nominal feature shape	Sphere
Pattern	$2 \times 2$
Centre Spacing (mm)	4.243
Aperture radius (mm)	2
Chord height ( $\mu\text{m}$ )	8
Radius of curvature (mm)	250.004

The same machining parameters and tool used for the sinusoidal grid sample are used. The design and STS tool path of the MLA surface are respectively illustrated in Figure 4.22 (a) and Figure 4.22 (b). As shown in Figure 4.23, the MLA sample was successfully machined to prove the effectiveness of STS machining of different type freeform surfaces.

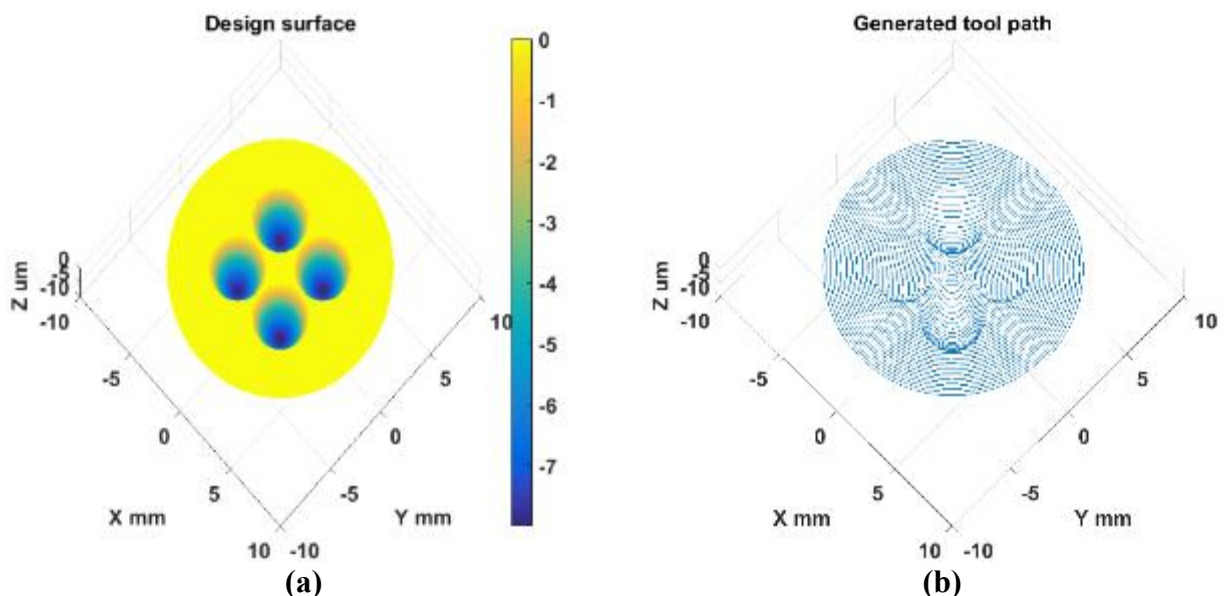


**Figure 4.22 (a) Design and (b) STS tool path of MLA surface**



**Figure 4.23 Photo of STS machined MLA surface**

To inspect the machining quality, five areas in different element lens were measured using a Talysurf CCI 3000. The measurement result is shown in Figure 4.24. The average  $S_q$  is calculated as 7.4 nm and standard deviation is 0.34 nm. The measurement results indicate the machined topography of the structured freeform surface is also less than 10 nm and uniformly distributed.

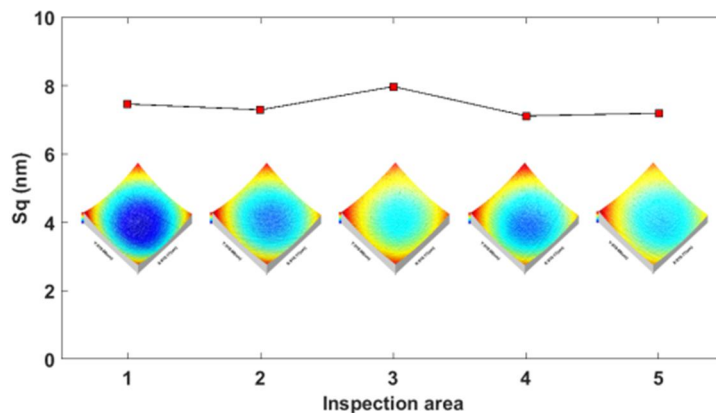


**Figure 4.24 Topography distribution of MLA surface (CCI measurement)**

The measured and simulated results of surface topography are also summarized in Table 4.5.  $S_q$  value of the actual measurement agrees with the simulated value, which proves the feasibility of the surface generation simulation.

**Table 4.5 Surface topography  $S_q$  by actual measurement and simulation**

Sample	Measured average $S_q$ (nm)	Standard deviation $S_q$ (nm)	Simulated $S_q$ (nm)
Sinusoidal grid	7.1	0.30	6.7
MLA	7.4	0.34	6.7

## 4.5 Summary

In this chapter, a theoretical and experiment study has been carried out to investigate STS machining of freeform surfaces. A systematic approach for the tool path generation is firstly presented, including tool path planning, tool geometries selection and tool radius compensation. To avoid the overcut of a rounded tool tip, tool radius compensation was performed only in  $Z$  direction to ensure no high frequency motion is imposed on the dynamic-limited  $X$  axis. Tool path motion analysis validated the  $Z$  direction compensation method and it was shown to be advantageous over conventional normal direction compensation methods. The development of the surface generation simulation allows the prediction of the surface topography under various tool and machining parameters. From the simulation results, it can be concluded that better surface finish (lower  $S_q$  value) can be obtained under a higher spindle speed, a smaller feedrate and larger tool radius. However, other practical issues (such as machining efficiency and tool accessibility) need to be considered to select optimised parameters. The simulation analysis also reveals the surface generation mechanism (such as overcutting phenomenon) without the need for costly trial and error tests. With the proposed tool radius compensation, waviness error components resulting from the overcut are totally eliminated.

Finally, machining experiments of a sinusoidal grid and MLA sample demonstrated the effectiveness of STS machining to fabricate optical freeform surfaces. The surface topography is measured less than 10 nm. The measurement result also shows uniform topography distribution over the entire surface and agrees well with the simulation results. Such knowledge was acquired as a priori information, indicating that the following OMSM should focus on form deviation rather than surface topography.

## **5 Development and systematic calibration of OMSM**

### **5.1 Introduction**

As presented in Chapter 4, ultra-precision STS machining is capable of generating optical freeform surfaces with uniform topography under 10 nm (PV). To ensure the functionality of the components, these surfaces are also required to have form accuracy within the micrometre to sub-micrometre range [11]. However, many factors such as machine structural errors, thermal expansion and tool wear inevitably induce form deviations from the design [164, 165]. Thus the process of metrology is indispensable in the evaluation of surface quality and understanding of the machining process. OMSM can avoid the errors caused by re-positioning workpieces and use the machine axes to extend the measuring range and improve the measuring efficiency.

Due to the relatively harsh environment in the machine tools, the metrology characteristics of OMSM instruments should deviate from those tested in laboratories. The metrology characteristics and calibration of offline measurement instruments have been intensively investigated [166, 167]. However, there is still relatively little research regarding the calibration process of OMSM instruments as applied in ultra-precision machining. Zou et al. [151] evaluated the linearity precision of a confocal probe by measuring a 50  $\mu\text{m}$  quartz step height standard. Additionally, the combined standard uncertainty of the OMSM system was estimated to result from the flatness uncertainty of the scanning hydrostatic slide. To facilitate the reliable quantification of the demanding specifications, Zhu et al. [138] investigated modelling and analysis of OMSM (STM type) uncertainty in the characterisation of form error of structured surfaces. Quinsat and Tournier [168] evaluated the effects of thermal and positioning repeatability for confocal OMSM on a five-axis machining centre. Compensation strategies were presented to improve the sensor performance. Most studies have focused on the development and evaluation of measurement sensors characteristics. However, less attention has been paid to evaluate comprehensive performance of OMSM system. This chapter will firstly describe the

configuration of the proposed OMSM system. A coordinate alignment method and various scanning strategies are also presented. In order to improve the accuracy of OMSM, it is necessary to calibrate the OMSM system and compensate the systematic errors. Experimental investigation is conducted which proves the validity of proposed calibration methodology and the effectiveness of OMSM.

## 5.2 Overview of the developed OMSM system

### 5.2.1 Working principle and system configuration

The schematic of the OMSM platform is illustrated in Figure 5.1. As discussed in chapter 4, the ultra-precision machine tool used in this study is equipped with two linear hydrostatic stages ( $X$  and  $Z$  axis) and an air bearing spindle ( $C$  axis). A robust single point interferometer probe, termed Dispersed Reference Interferometry (DRI) [94], was designed in-house and integrated onto the machine tool.

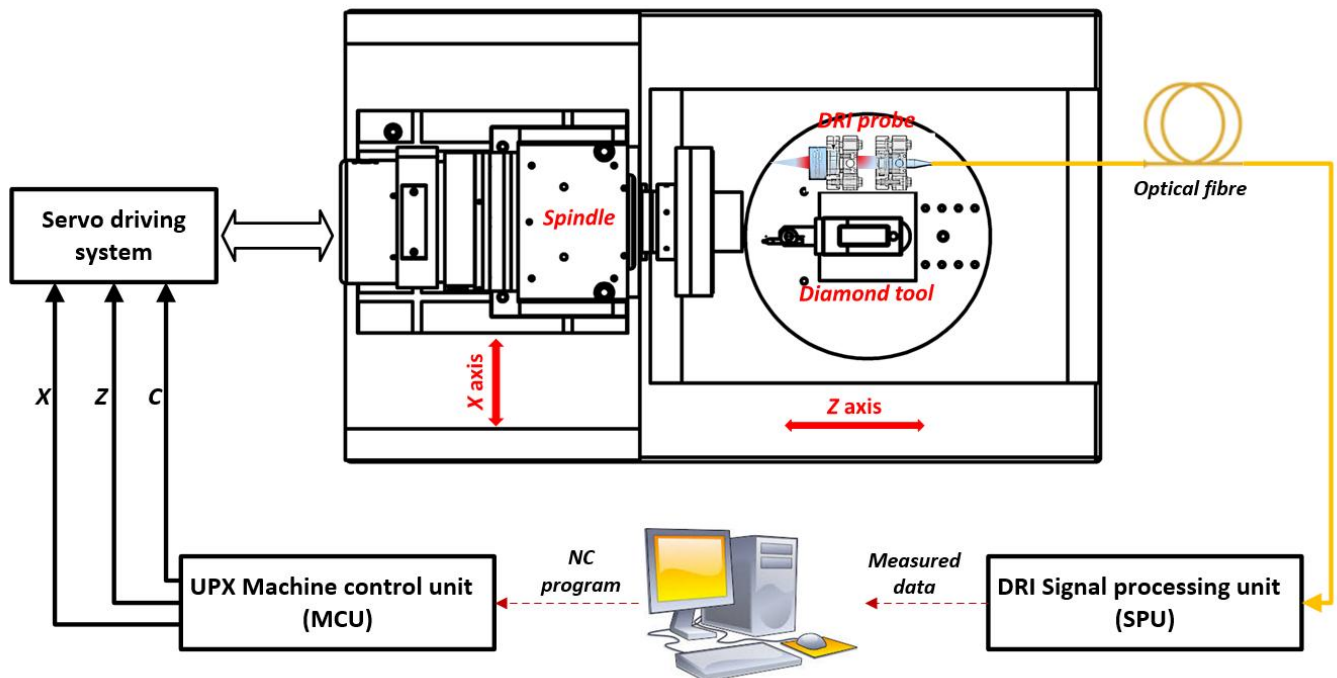


**Figure 5.1 Schematic of the OMSM platform**

DRI works on the principle of a modified Michelson interferometer with chromatic dispersion purposefully added to the reference arm, resulting in a wavelength dependent optical

path length [169]. As shown in Figure 5.2, one light beam emitted by a superluminescent diode (SLD) source goes into the measurement arm and focuses on the sample mirror M1 through an objective lens L1. In the reference arm, two transmission gratings G1 and G2 are used for chromatic dispersion to the reference light. Two beams are then recombined at the beam splitter BS and decomposed by a spectrometer, which includes a reflective grating, spherical mirror and a line detector. The resulting spectral interferogram is shown in Figure 5.3.

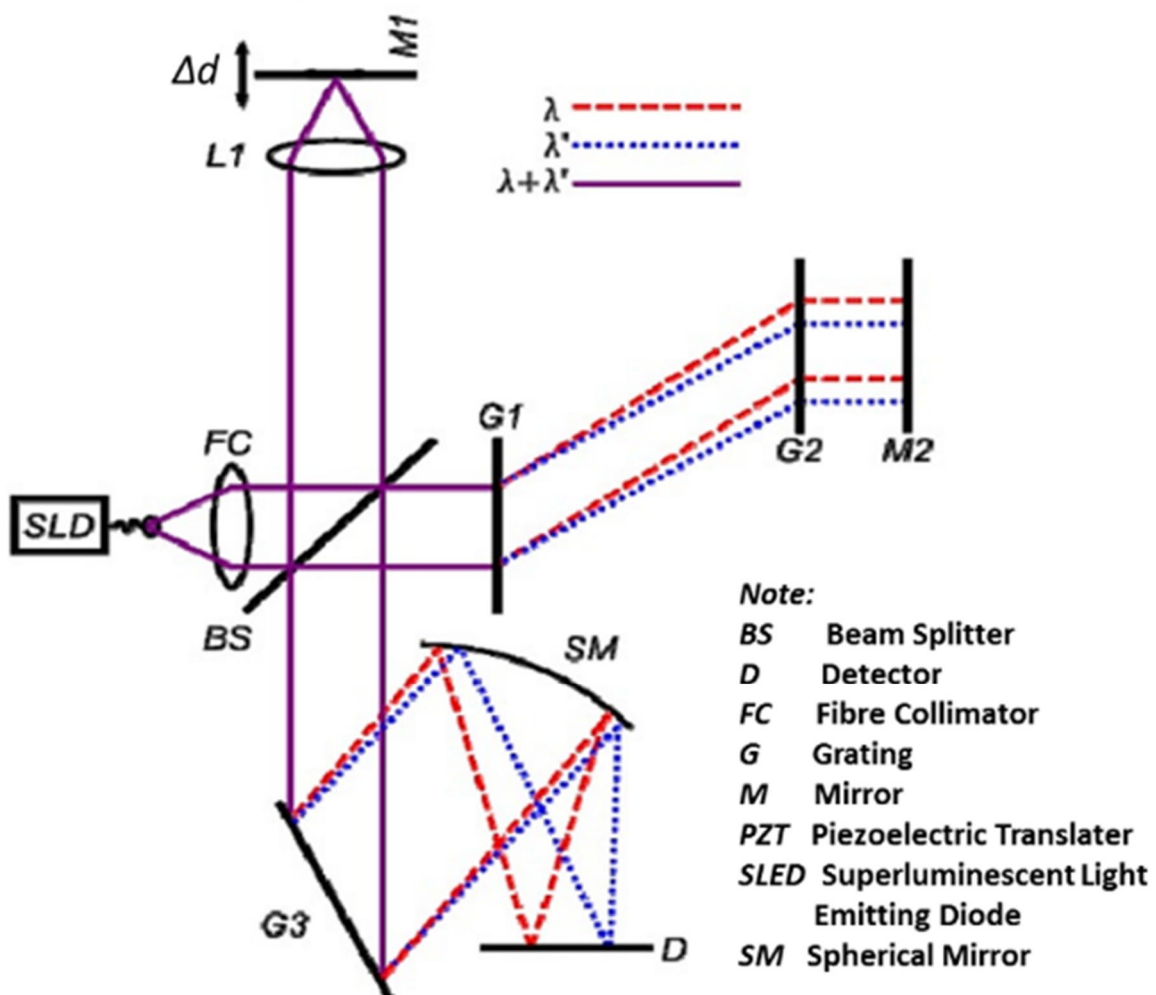
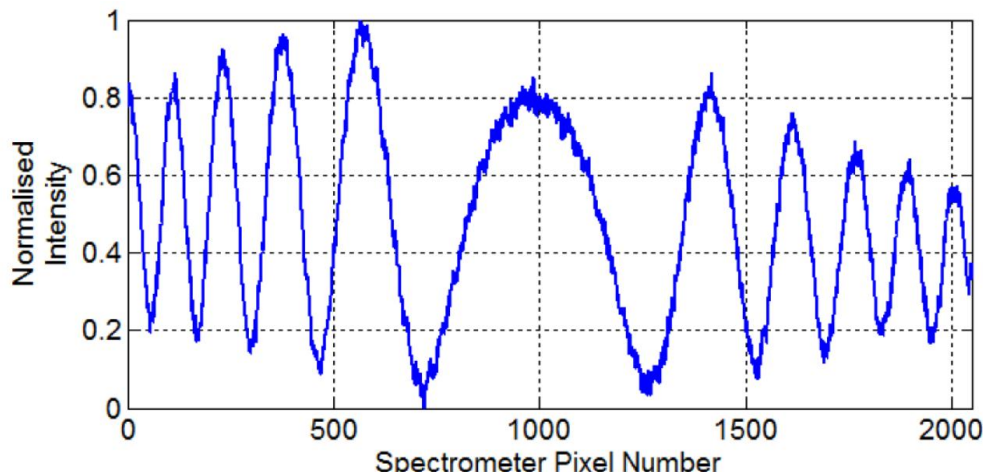
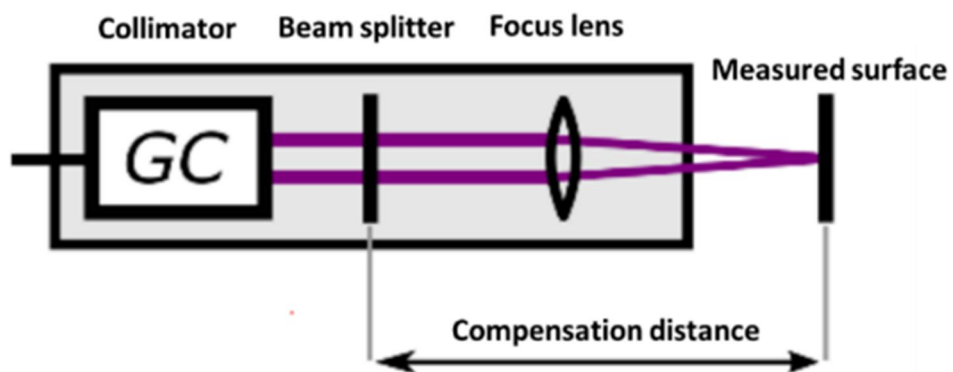


Figure 5.2 Schematic diagram of DRI bulk optics interferometer [169]



**Figure 5.3 DRI spectral interferogram [94]**

The absolute distance from the measured surface can be determined by deducing the wavelength of the stationary phase point, while template matching can provide high axial resolution (nanometre) measurement through extraction of relative phase information [94]. The nanometre resolution (down to 0.6 nm) and millimetre vertical range (up to 800  $\mu\text{m}$ ) makes this robust single point sensor dynamic enough to measure complex surface features. Moreover, the low coherence source lends the method to an optical fibre based implementation, which adds the potential for remote configuration and miniaturization. The remote DRI probing kit (shown in Figure 5.4) is connected to its bulk optics apparatus (signal processing unit illustrated in Figure 5.1) with an optical fibre. The sampled surface data is then transferred into a computer for further processing.



**Figure 5.4 Remote DRI probe setup [170]**

### 5.2.2 Measurement coordinate alignment

The first issue to integrate metrology on the machine is the determination of its position in the machine tool coordinate system. In this case, the DRI probe needs to be aligned coaxially to the spindle axis. The schematic diagram and experimental setup of DRI alignment process is respectively shown in Figure 5.5 (a) and Figure 5.5 (b).

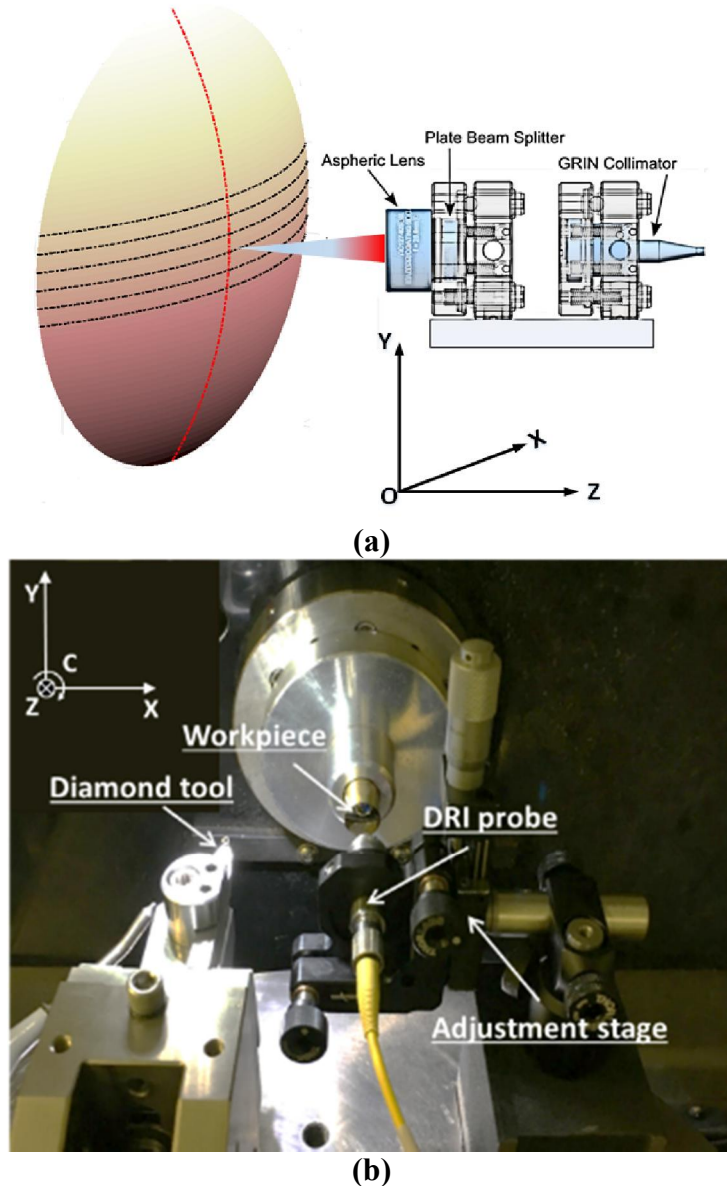


**Figure 5.5 (a) Schematic diagram and (b) experiment setup of OMSM probing alignment**

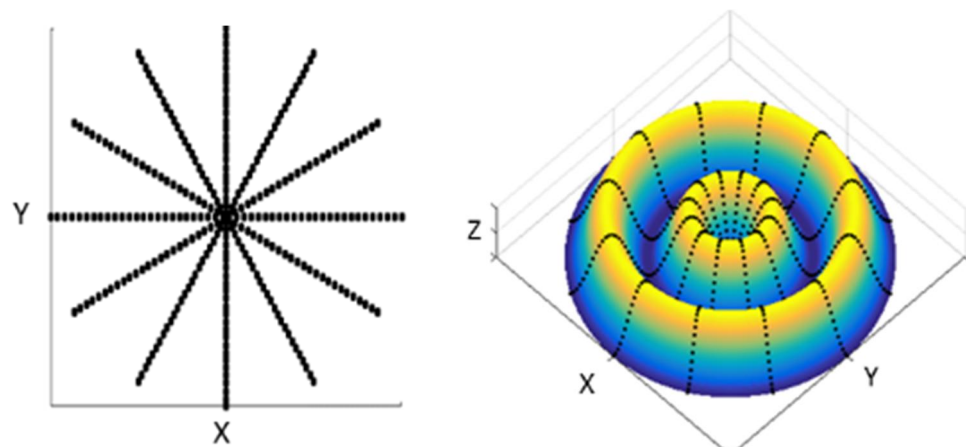
A two-step alignment method is proposed. In the first step, a flat surface is turned on the machine and the DRI is oriented perpendicular to the surface by adjusting the angularity of the kinematic mount according to the detected reflectivity strength. In the second step, a convex

spherical surface needs to be turned on the machine for DRI positional alignment in two directions. Alignment in the  $X$  direction is achieved by the machine  $X$  axis motion, while alignment in the  $Y$  direction is performed by adjusting the manual linear stage. As shown in Figure 5.5, multiple parallel scanning over the turned sphere surface along  $X$  axis can be consequently performed after the manual stage is adjusted in the  $Y$  direction, and the fitted symmetric point of measurement profiles is regarded as the zero position of DRI, where it is coincident with the spindle axis.

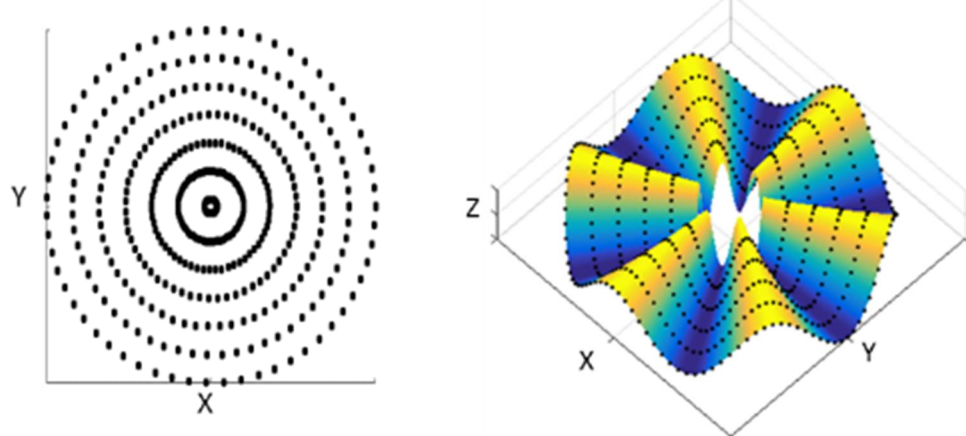
The position of the DRI was recorded in the machine tool table for later use. Compared with conventional methods using additional calibrated standard balls [151], the proposed alignment method using a self-turned surface is capable of avoiding artefact alignment error. Because the convex sphere sample is directly cut on the machine, its symmetric centre is automatically aligned with the rotational axis of the spindle.

### 5.2.3 On-machine scanning strategies

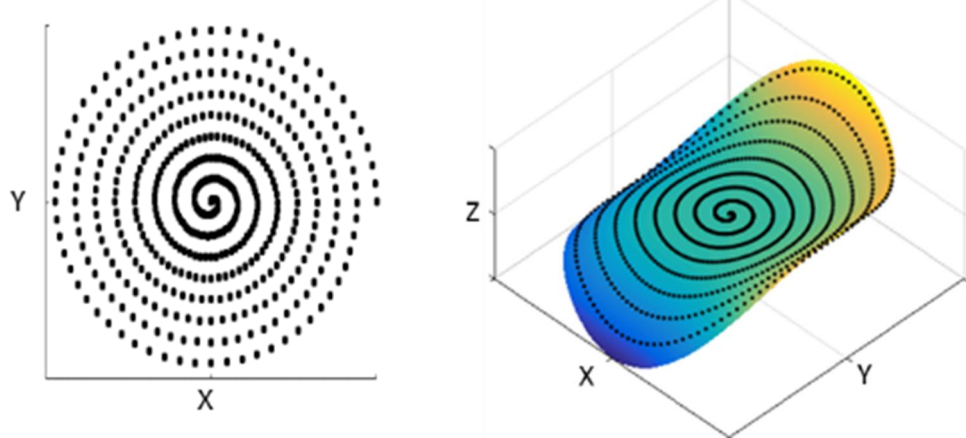
The DRI probe is scanned over the sample surface by the machine's 3 axes' motion while the  $C$  axis is enabled as a position controlled axis. In this system, multiple radial, multiple circular, and spiral paths can be employed for on-machine surface inspection. The selection of measurement paths primarily depends on the measurement tasks and surface feature distribution. Among them, multiple radial paths are mainly applicable to measurement of radial surface features; multiple circular paths are applicable to measurement of circumferential surface features; a spiral path is a continuous trajectory and an efficient way to measure the overall surface form. However, the reconstruction of surfaces from the spiral measurement points needs additional interpolation and fitting processes. The measurement paths and corresponding applicable surfaces are displayed in Figure 5.6.



(a)



(b)



(c)

**Figure 5.6 (a) Multiple radial, (b) multiple circular, (c) spiral measurement paths and their applicable surfaces**

## 5.3 Calibration of OMSM system

### 5.3.1 OMSM calibration scheme

Measuring conditions vary with machine configuration, probing system setup and measurement task. Calibration of the OMSM system is thus considered to be a task specific process [171]. According to the configuration and measurement task of the OMSM system for the diamond turning process, the calibration process is performed in the sensitive direction (Z direction shown in Figure 5.21). The measurement accuracy in the radial scanning direction ( $X$  direction) is guaranteed by the ultra-precision linear scale feedback (with 8.6 nm resolution), which compares positively with micrometre-level lateral resolution achievable in common optical instruments. The structure diagram of the OMSM calibration process is illustrated in Figure 5.7.

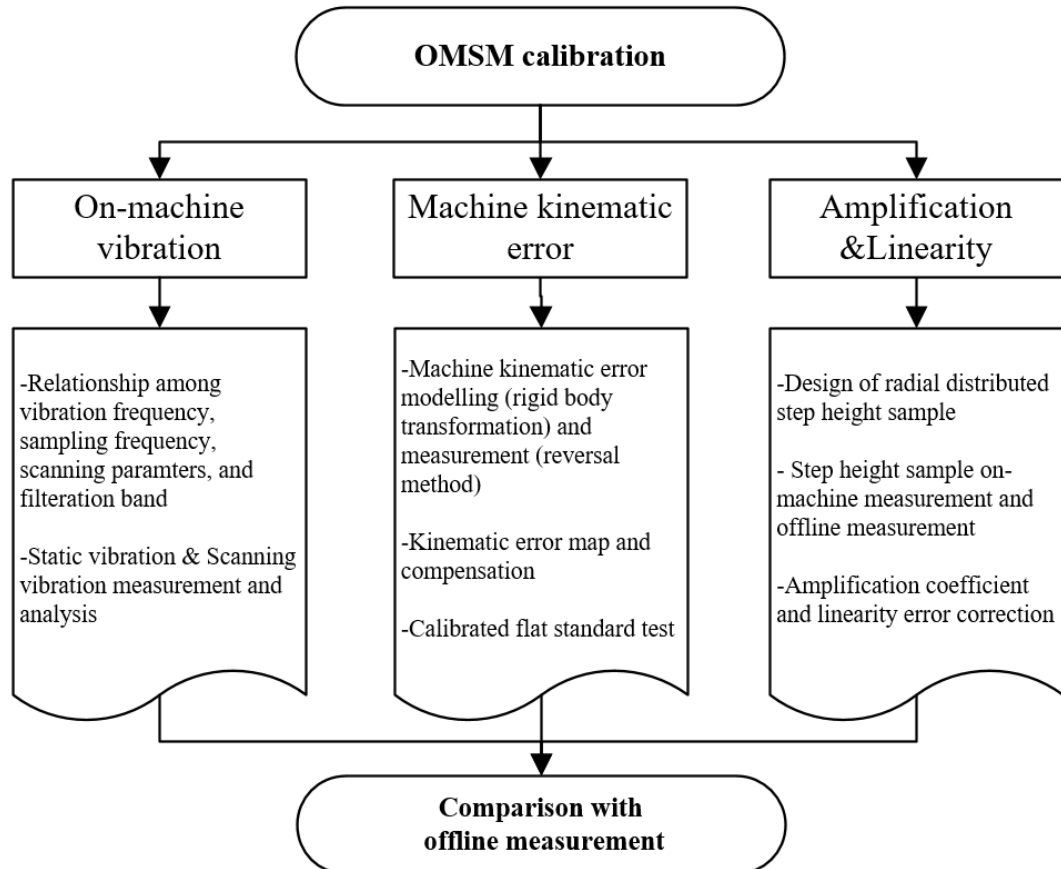


Figure 5.7 Structure diagram of OMSM calibration

Three aspects of calibration are taken into consideration and discussed in the following sections: on-machine vibration test, machine kinematic error mapping and compensation, amplification coefficient and linearity error correction.

### 5.3.2 On-machine vibration analysis

Aspects of the machine tool environment will inevitably influence the performance of OMSM systems. Vibration from machine tool axes, such as the air bearing spindle and linear stages will degrade measurement results. Probe internal electrical noise may also be magnified due to the electromagnetic disturbance. Therefore, it is necessary to conduct on-machine vibration testing and analysis to assess its relationship with the sampling frequency, scanning parameters and filtration operations in post processing. On-machine vibration in the measurement process is a combination of the internal noise of the instrument, machine tool static vibration and vibration induced by the machine motion. The induced vibration components onto the OMSM result should be filtered out for accurate characterisation of the surface form and topography.

According to Nyquist sampling theorem [172], the sampling frequency  $F_s$  is required to be at least 2 times the on-machine vibration frequency  $F_{vibration}$  to avoid aliasing effects. Also, to separate the vibration frequency component from the frequency associated with the topography features of interest  $F_{topo}$ , the upper limit of  $F_{topo}$  is recommended to be lower than the  $F_{vibration}$ . The relationship between  $\lambda_{topo}$  and  $F_{topo}$  is described as follows:

$$\lambda_{topo} = \frac{Feedrate}{F_{Topo}} \quad (5.1)$$

where  $\lambda_{topo}$  is the wavelength of the surface topography of interest and  $F_{topo}$  is the corresponding frequency.

According to the topography band of interest and vibration test results, a frequency decision graph is plotted in Figure 5.8, providing guidance in selection of the proper scanning

parameters and sampling frequency. For a given scanning feedrate, the topography frequency of interest should be lower than the vibration frequency shown in the hatched region. To meet the requirement for avoiding signal aliasing, lower scanning speed and higher sampling frequency are preferable from the perspective of filtering out induced vibration components from the topography band of interest. However, other issues have to be carefully considered, such as computation cost and measurement efficiency.

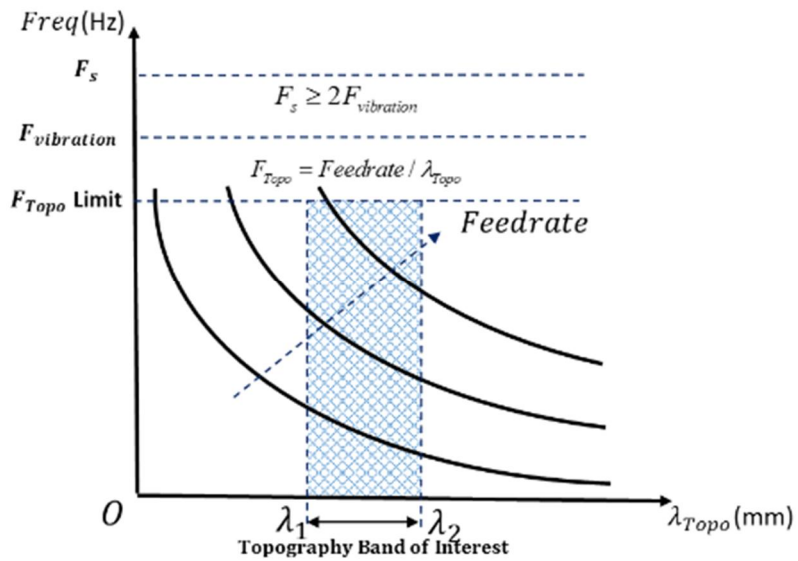


**Figure 5.8 Sampling frequency decision graph**

A calibrated flat standard from NPL Bento Box [173] was employed for static and scanning vibration testing. The vibration measurement results under different test modes are summarized in Table 5.1. The vibration level is characterised as the RMS value of the signal. The static vibration test was performed when the machine is in static condition, while the scanning vibration test was performed when the machine axes moves simultaneously to measure the sample surface. As presented in Table 5.1, static vibration on the machine is nearly 4 times the DRI internal noise in the laboratory environment, indicating the machine tool environmental effect on the measurement. Furthermore, scanning vibration amplitude is higher than static vibration due to additional vibration arising from the drive units of machine stages. To reduce the influence of machine kinematic error on the vibration test, six profiles were scanned at a

feedrate of 5 mm/min along the radial direction at equally spaced intervals of 30°. The scanning vibration results and frequency analysis are shown respectively in Figure 5.9 (a) and Figure 5.9 (b).

**Table 5.1 Vibration test results**

Probe status	Test Mode	Root mean square RMS /nm
Fixed	Lab [94]	0.63
	Static on-machine	2.2
Scanning on-machine	Multiple radial	3.5
	Multiple circular	4.4
	Spiral	3.7

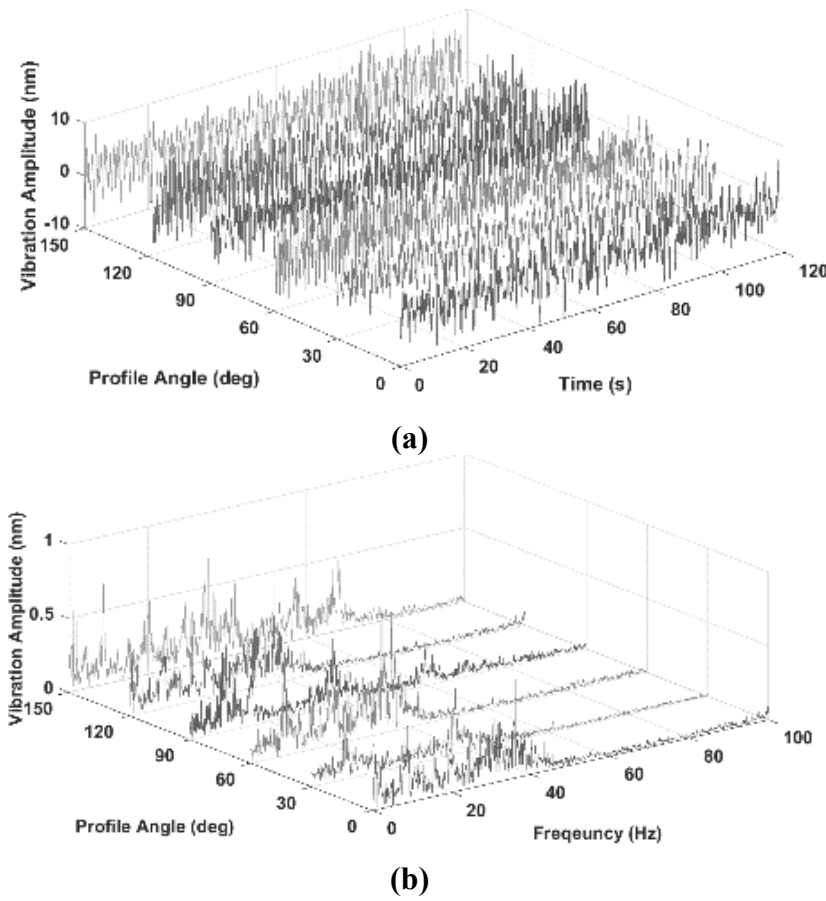


**Figure 5.9 Scanning vibration test: (a) time domain vibration signal and (b) spectrum analysis of vibration signal**

The camera height parameter is used to adjust the sampling frequency of the measurement system. The spectrum analysis in Figure 5.9 (b) indicates the primary vibration components are less than 100 Hz and the sampling frequency of DRI probe is consequently set to be 200 Hz.

### 5.3.3 Machine tool kinematic error mapping

For on-machine metrology, the DRI probe is carried by the machine tool axes to cover the inspection area. Due to mechanical imperfections, wear of machine tool elements, and stage misalignments, the deviation from the programmed scanning path will induce additional measurement errors [164]. Therefore, the influence of machine tool kinematic errors on measurement results needs to be modelled, measured and compensated. The flow chart of the proposed methodology is illustrated in Figure 5.10. According to the measurement task and machine tool configuration, a selective kinematic error modelling and measurement process will be carried out. The machine tool kinematic error in the scanning region is consequently mapped in order to compensate the OMSM result.

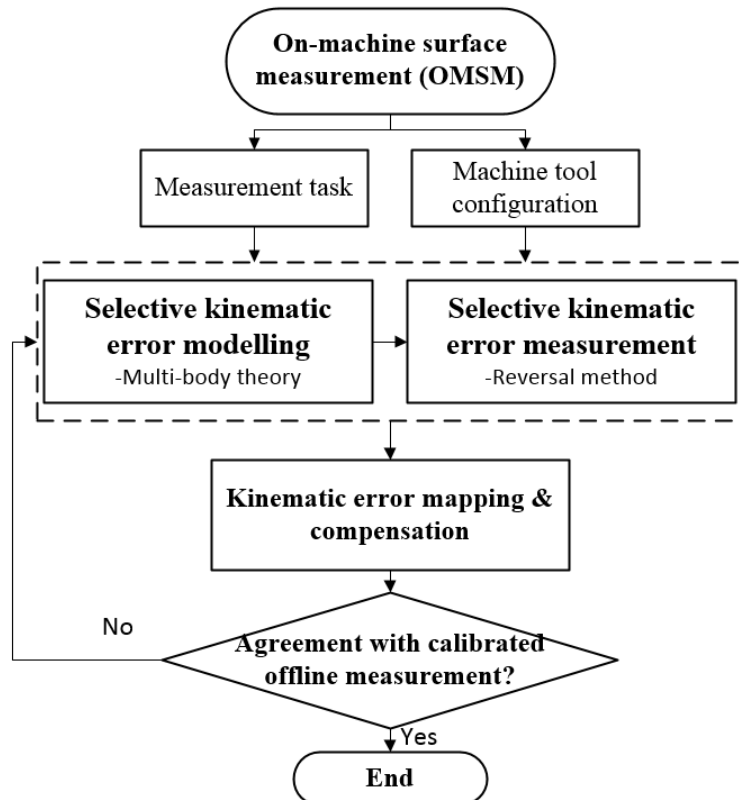


**Figure 5.10 Flow chart of kinematic error mapping**

Kinematic error modelling in machine tools is based on rigid body kinematics [174] and multi-body system theory [175]. Multi-body system theory offers a comprehensive description of general mechanical systems utilizing a lower order body topological structure. Using a homogeneous transformation matrix (HTM), spatially distributed single error components can be synthesized as a volumetric error model. For the 3-axis turning configuration in the current work, there are two kinematic error chains shown in Figure 5.11. One is from machine base to the workpiece surface, and the other is from the machine base to the interferometric probe.

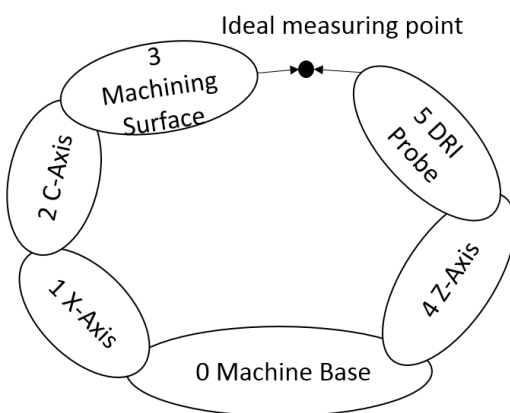


**Figure 5.11 Kinematic error chain for on-machine surface measurement system**

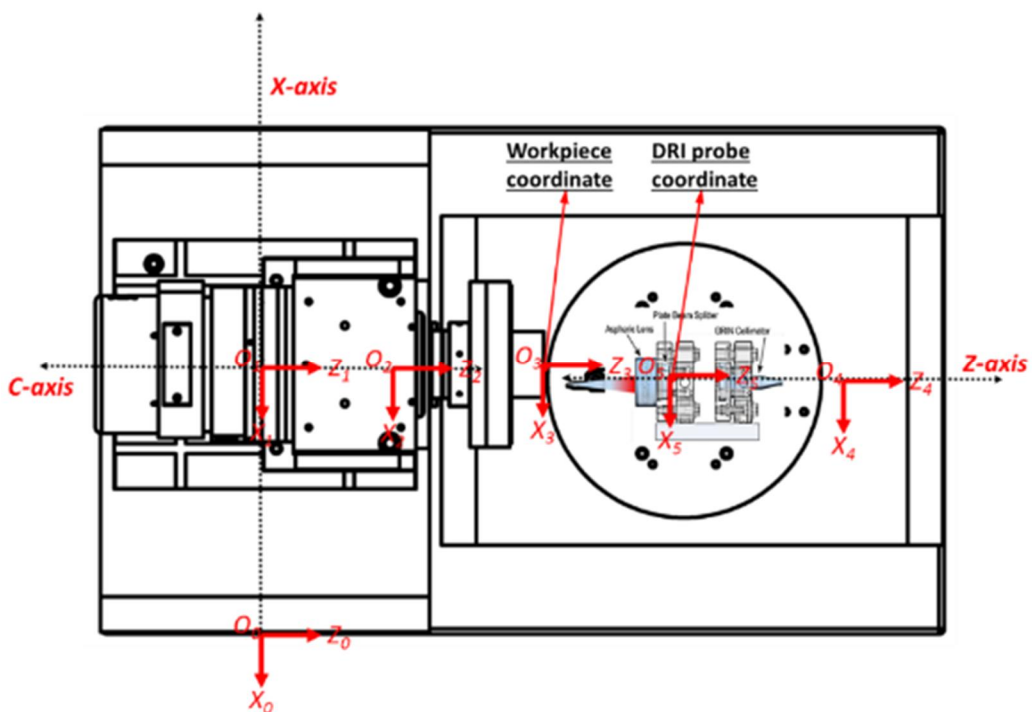


**Figure 5.12 Configuration of the machine tool coordinate systems**

The overall configuration of the machine tool coordinate systems is shown in Figure 5.12.

The spatial relationship between adjacent coordinate systems can be mathematically described using the homogeneous transformation matrix.

Based on rigid body kinematics, the transformation matrix  ${}^j_k T$  describes the coordinate transformation from coordinate  $k$  to coordinate  $j$ , which comprises four component matrices and can be formulated as:

$${}^j_k T = {}^j_k T_l {}^j_k T_{le} {}^j_k T_m {}^j_k T_{me} \quad (5.2)$$

where  ${}^j_k T_l$  is the location transformation matrix,  ${}^j_k T_{le}$  is the location error transformation matrix,  ${}^j_k T_m$  is the motion (translation or rotation) transformation matrix, and  ${}^j_k T_{me}$  is the motion (translation or rotation) error transformation matrix. These matrices are expressed as follows:

$${}^j_k T_l = \begin{bmatrix} 1 & 0 & 0 & p_{kx} \\ 0 & 1 & 0 & p_{ky} \\ 0 & 0 & 1 & p_{kz} \\ 0 & 0 & 0 & 1 \end{bmatrix} \quad (5.3)$$

where  $[p_{kx}, p_{ky}, p_{kz}]$  are the location vectors from coordinate  $k$  to coordinate  $j$ .

$${}^0_1 T_m = \begin{bmatrix} 1 & 0 & 0 & x \\ 0 & 1 & 0 & 0 \\ 0 & 0 & 1 & 0 \\ 0 & 0 & 0 & 1 \end{bmatrix} \quad (5.4)$$

$${}^0_4 T_m = \begin{bmatrix} 1 & 0 & 0 & 0 \\ 0 & 1 & 0 & 0 \\ 0 & 0 & 1 & z \\ 0 & 0 & 0 & 1 \end{bmatrix} \quad (5.5)$$

$${}^1T_m = \begin{bmatrix} \cos(c) & -\sin(c) & 0 & 0 \\ \sin(c) & \cos(c) & 0 & 0 \\ 0 & 0 & 1 & 0 \\ 0 & 0 & 0 & 1 \end{bmatrix} \quad (5.6)$$

$${}^j_k T_{me} = \begin{bmatrix} 1 & -E_{Ck} & E_{Bk} & E_{Xk} \\ E_{Ck} & 1 & -E_{Ak} & E_{Yk} \\ -E_{Bk} & E_{Ak} & 1 & E_{Zk} \\ 0 & 0 & 0 & 1 \end{bmatrix} \quad (5.7)$$

According to the kinematic chain structure, all transformation matrices between adjacent coordinate systems can be derived as follows:

$${}^0_1 T = \begin{bmatrix} 1 & 0 & 0 & p_{1x} \\ 0 & 1 & 0 & p_{1y} \\ 0 & 0 & 1 & p_{1z} \\ 0 & 0 & 0 & 1 \end{bmatrix} \begin{bmatrix} 1 & 0 & 0 & 0 \\ 0 & 1 & 0 & 0 \\ 0 & 0 & 1 & 0 \\ 0 & 0 & 0 & 1 \end{bmatrix} \begin{bmatrix} 1 & 0 & 0 & x \\ 0 & 1 & 0 & 0 \\ 0 & 0 & 1 & 0 \\ 0 & 0 & 0 & 1 \end{bmatrix} \begin{bmatrix} 1 & -E_{CX} & E_{BX} & E_{XX} \\ E_{CX} & 1 & -E_{AX} & E_{YX} \\ -E_{BX} & E_{AX} & 1 & E_{ZX} \\ 0 & 0 & 0 & 1 \end{bmatrix} \quad (5.8)$$

$${}^1_2 T = \begin{bmatrix} 1 & 0 & 0 & p_{2x} \\ 0 & 1 & 0 & p_{2y} \\ 0 & 0 & 1 & p_{2z} \\ 0 & 0 & 0 & 1 \end{bmatrix} \begin{bmatrix} 1 & 0 & E_{BOC} & 0 \\ 0 & 1 & -E_{AOC} & 0 \\ -E_{BOC} & E_{AOC} & 1 & 0 \\ 0 & 0 & 0 & 1 \end{bmatrix} \begin{bmatrix} \cos(c) & -\sin(c) & 0 & 0 \\ \sin(c) & \cos(c) & 0 & 0 \\ 0 & 0 & 1 & 0 \\ 0 & 0 & 0 & 1 \end{bmatrix}$$

$$\begin{bmatrix} 1 & -E_{CC} & E_{BC} & E_{XC} \\ E_{CC} & 1 & -E_{AC} & E_{YC} \\ -E_{BC} & E_{AC} & 1 & E_{ZC} \\ 0 & 0 & 0 & 1 \end{bmatrix} \quad (5.9)$$

$${}^2_3 T = \begin{bmatrix} 1 & 0 & 0 & p_{3x} \\ 0 & 1 & 0 & p_{3y} \\ 0 & 0 & 1 & p_{3z} \\ 0 & 0 & 0 & 1 \end{bmatrix} \quad (5.10)$$

$${}^0_4 T = \begin{bmatrix} 1 & 0 & 0 & p_{4x} \\ 0 & 1 & 0 & p_{4y} \\ 0 & 0 & 1 & p_{4z} \\ 0 & 0 & 0 & 1 \end{bmatrix} \begin{bmatrix} 1 & 0 & E_{BOZ} & 0 \\ 0 & 1 & 0 & 0 \\ -E_{BOZ} & 0 & 1 & 0 \\ 0 & 0 & 0 & 1 \end{bmatrix} \begin{bmatrix} 1 & 0 & 0 & 0 \\ 0 & 1 & 0 & 0 \\ 0 & 0 & 1 & z \\ 0 & 0 & 0 & 1 \end{bmatrix} \begin{bmatrix} 1 & -E_{CZ} & E_{BZ} & E_{XZ} \\ E_{CZ} & 1 & -E_{AZ} & E_{YZ} \\ -E_{BZ} & E_{AZ} & 1 & E_{ZZ} \\ 0 & 0 & 0 & 1 \end{bmatrix} \quad (5.11)$$

$${}^2T = \begin{bmatrix} 1 & 0 & 0 & p_{3x} \\ 0 & 1 & 0 & p_{3y} \\ 0 & 0 & 1 & p_{3z} \\ 0 & 0 & 0 & 1 \end{bmatrix} \quad (5.12)$$

By transferring to a common machine base coordinate system from two chains, we have:

$$T = \prod {}_k^j T_l {}_k^j T_{le} {}_k^j T_m {}_k^j T_{me} \quad (5.13)$$

$${}^0_3 T = {}^0_1 T {}^1_2 T {}^2_3 T \quad (5.14)$$

$${}^0_5 T = {}^0_4 T {}^4_5 T \quad (5.15)$$

The volumetric error vector, which describes the relative displacement between the DRI probe and the workpiece surface, is defined as the following:

$$\begin{bmatrix} E_x \\ E_y \\ E_z \\ 1 \end{bmatrix} = {}^0_3 T \begin{bmatrix} p_{3x} \\ p_{3y} \\ p_{3z} \\ 1 \end{bmatrix} - {}^0_5 T \begin{bmatrix} p_{5x} \\ p_{5y} \\ p_{5z} \\ 1 \end{bmatrix} \quad (5.16)$$

All the error variables above follow the convention according to the ISO 230-1 [176]. It is time-consuming and unnecessary to measure and model all the error components. More attention should be paid to the influential error components in the sensitive direction because they directly influence the workpiece surface accuracy. In the current work, according to the OMM scanning characteristics and measurement tasks, four selected error components are considered as primary factors affecting the on-machine measurement results in the sensitive Z direction. They are X axis straightness in the Z direction  $E_{ZX}$ , squareness error between X axis and C axis  $E_{BOC}$ , C axis axial error  $E_{ZC}$  and C axis tilt error  $E_{BC}$  respectively. These four error components are measured, synthesized and employed to generate the kinematic error map. With the derived selective kinematic error model, the individual and combined effect of these errors on OMSM results are numerically simulated and illustrated as 3D error maps in Figure 5.13. X axis straightness error in the Z direction  $E_{ZX}$  will cause the wavy pattern along the radial direction while the squareness

error  $E_{BOC}$  between the  $C$  axis and  $X$  axis in the  $X-Z$  plane results in the cone shape surface.  $C$  axis motion errors, including axial motion  $E_{ZC}$  and tilt error  $E_{BC}$ , will induce several circumferential ripples, whose number depends on the spindle motion error characteristics. It can also be inferred that the squareness error and  $C$  axis tilt error tends to exaggerate the motion error in the  $Z$  direction with increasing sample radius. Compensation of the error components  $E_{BOC}$  and  $E_{BC}$  should receive more attention for on-machine measurement of large scale surfaces.

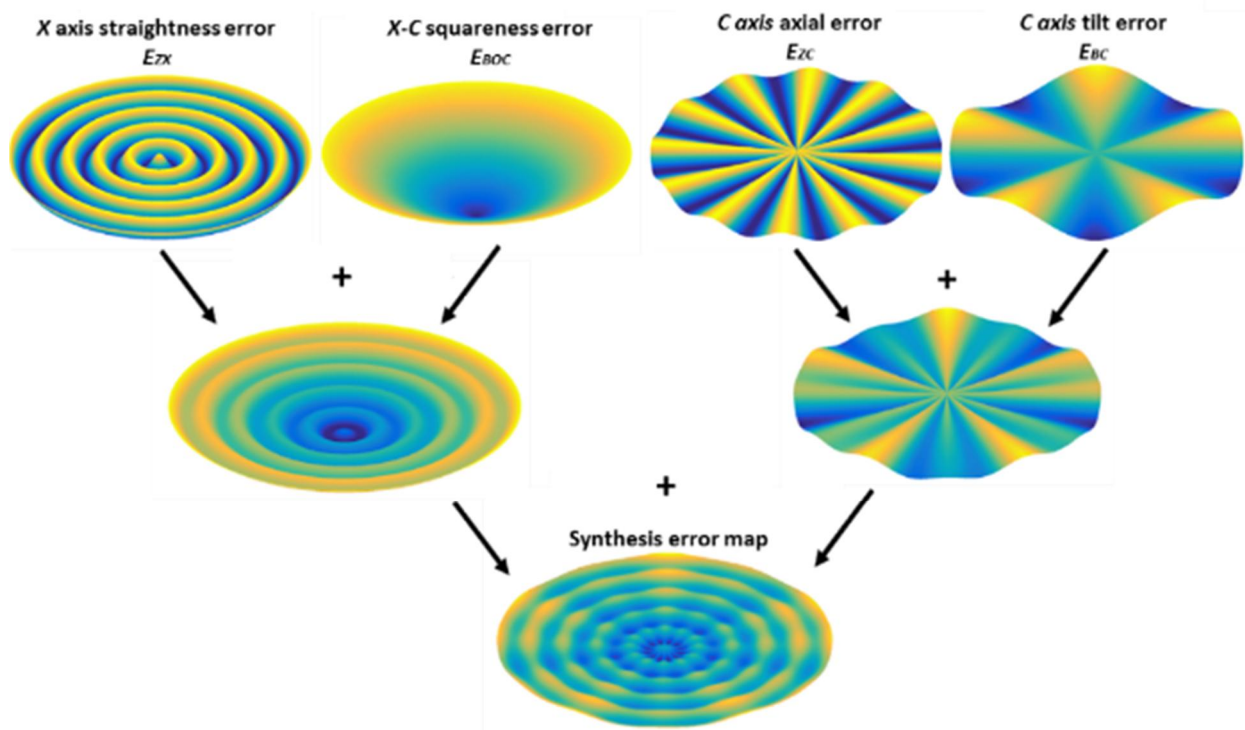


**Figure 5.13 Simulation of kinematic error effect on OMSM results**

Reversal method has been developed for accurate measurement of part features without reference to an externally calibrated artefact and is widely used in ultra-precision machine kinematic error measurement [71, 177]. Four primary error components, were respectively measured using the reversal method, including  $X$  axis straightness in the  $Z$  direction  $E_{ZX}$ , squareness error between  $X$  axis and  $C$  axis  $E_{BOC}$ ,  $C$  axis axial error  $E_{ZC}$  and  $C$  axis tilt error  $E_{BC}$ . The kinematic error measurement is presented in detail in Appendix A.

Based on the established kinematic error model and error measurement results presented above, the machine tool kinematic error was mapped, as shown in Figure 5.14. The kinematic error can be stored as a look-up table for further compensation of on-machine measurement results. It can be observed that the kinematic error map is dominated by 2 UPR (undulations per revolution) component along the circumferential direction, which mainly results from the  $C$  axis tilt error motion  $E_{BC}$ , corresponding to the measurement result shown in Figure A.10 (b).

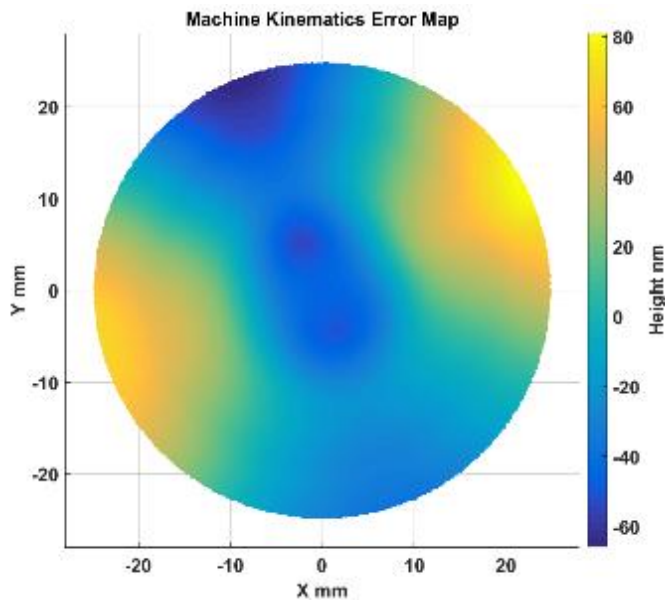


**Figure 5.14 Machine kinematic error map**

To validate the generated machine kinematic error map, a commercial optical flat (Edmund optics) was measured on the machine. Use of a flat surface in the experiment aimed to minimize the effect of linearity error from the DRI probe. The probe was scanned over the sample in a spiral path with  $C$  axis rotational speed of 1 rpm and  $X$  axis feedrate of 2 mm/min. The flat was also measured offline on a calibrated Twyman–Green interferometer (Fisba FS10) and this offline result was regarded as the accurate representation of the flat surface form. The measurement results and scanning error map are shown in Figure 5.15. The scanning error model plot was interpolated from the machine kinematic error map in Figure 5.14.

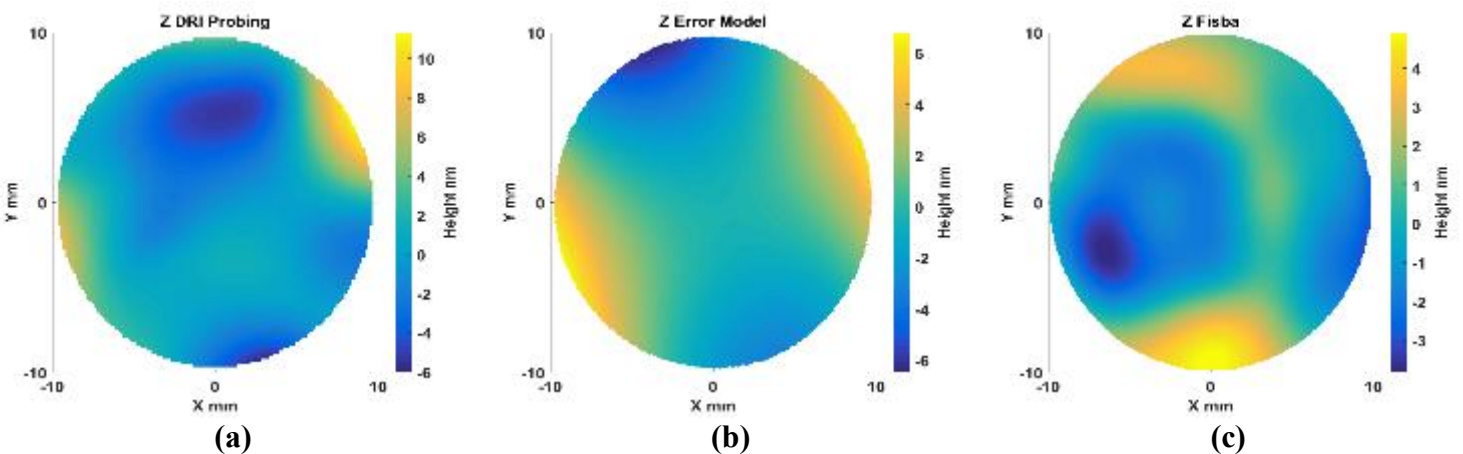


**Figure 5.15 (a) DRI measurement, (b) scanning error map and (c) Fisba measurement of optical flat**

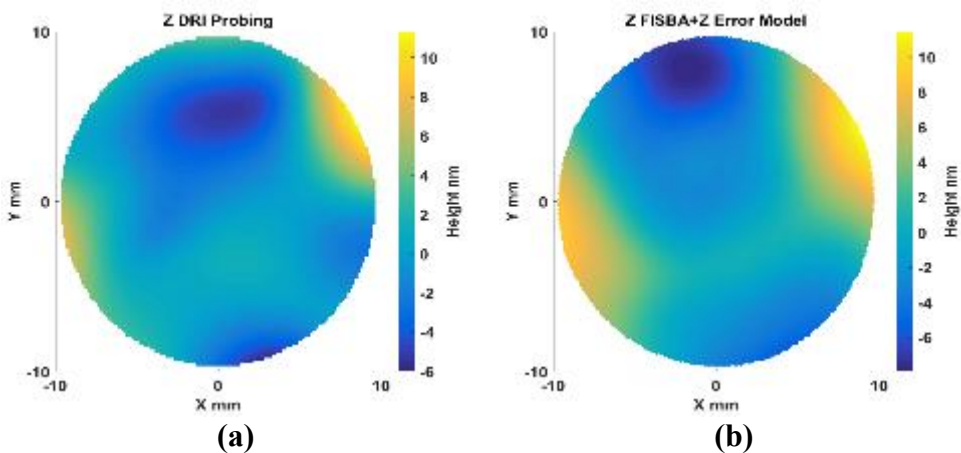


**Figure 5.16 (a) DRI measurement versus (b) combination of scanning error and Fisba measurement**

The similarity of two results in Figure 5.16 (a) and Figure 5.16 (b) indicates that DRI on-machine measurement is the superposition of machine kinematic error and flat form error. With the aid of the machine kinematic error mapping established above, it is possible to compensate for the kinematic errors in the on-machine probing data. Using this approach the characterised flatness error from on-machine measurement reduced from 17.3 nm to 11.4 nm, compared with results of the calibrated offline measurement of 8.7 nm. It is noted that the offline measurement needs to be aligned to conduct the comparison and the alignment process would inevitably result in some deviation between the two measurements.

### 5.3.4 Amplification coefficient and linearity error correction

Due to uncontrolled temperature and humidity in machine tools, environmental variations would cause the response characteristics of high-precision interferometric probe to deviate from a laboratory test. To further analyse and improve the on-machine measurement performance it is necessary to calibrate the response curve of the instrument in the machine tool environment. The linearity error is defined as the maximum deviation of the instrument response curve from the linear fitted curve where the slope is the amplification coefficient [178]. It is advantageous to employ a multiple step artefact to calibrate the amplification and linearity error of measurement system for the reason that it accounts for the  $X$ - $Z$  squareness error, which behaves as a part of amplification error. According to the turning machine configuration, a radial distributed step height sample is designed, machined, and compared with a calibrated offline instrument. The artefact is designed with four nominal step heights ( $1\text{ }\mu\text{m}$ ,  $2\text{ }\mu\text{m}$ ,  $4\text{ }\mu\text{m}$  and  $8\text{ }\mu\text{m}$ ) to cover the necessary working range in the  $Z$  direction, as illustrated in Figure 5.17. By fitting a first order polynomial curve to the characterisation results of the different step heights, the linearity errors and amplification coefficient are consequently derived.

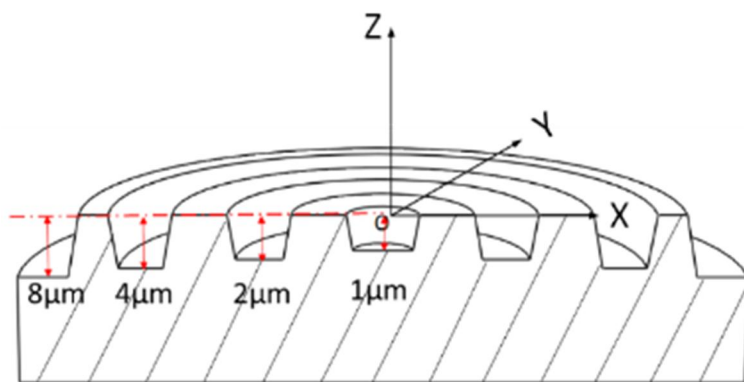


**Figure 5.17 Schematic of radial distributed step artefact**

Calibration of the amplification coefficient and linearity error in the  $Z$  direction includes measuring different step heights to study the relationship between the ideal response curve and the instrument response curve. The artefact with 4 step heights ( $1\text{ }\mu\text{m}$ ,  $2\text{ }\mu\text{m}$ ,  $4\text{ }\mu\text{m}$ , and  $8\text{ }\mu\text{m}$

respectively) shown in Figure 5.17 is used for DRI on-machine calibration of amplification coefficient and linearity error. The step height sample was measured on-machine using multiple radial paths. Six measurement profiles are spaced across the surface at equal angles of (30°), as shown in Figure 5.18. Measurement span was from 10 mm to -10 mm along the radial direction and scanning speed was set at 2 mm/min. The linearity error mainly originates from the DRI single point probing instrument, which is independent of machine tool kinematic error. The pre-mapped machine kinematic error was subtracted from the on-machine measurement data, which was then segmented and mapped onto the workpiece Cartesian coordinate system.

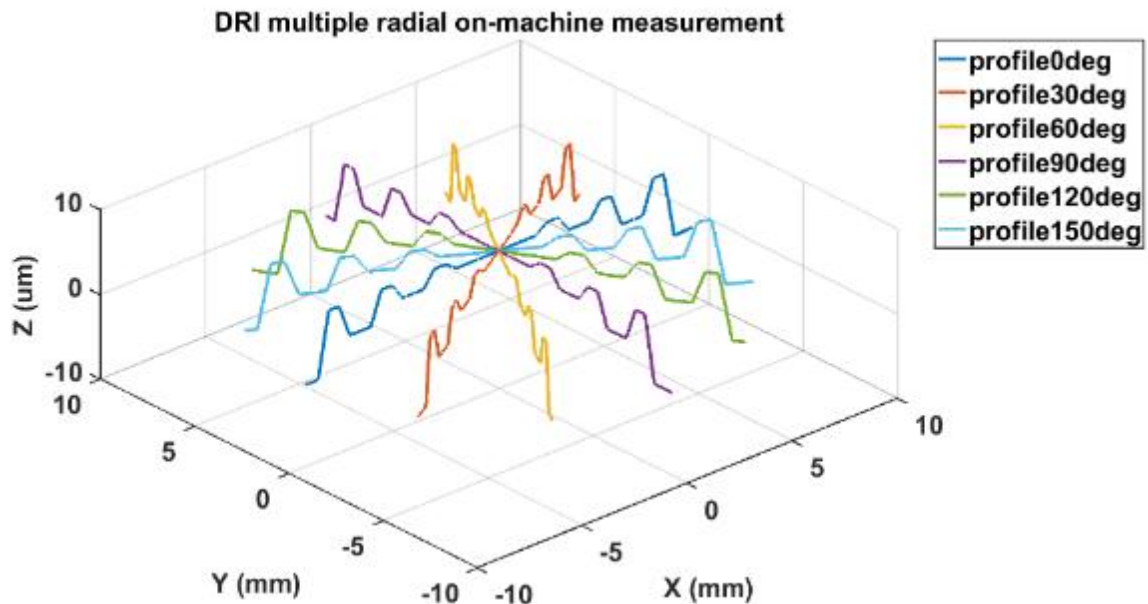


**Figure 5.18 DRI on-machine measurement of the step artefact**

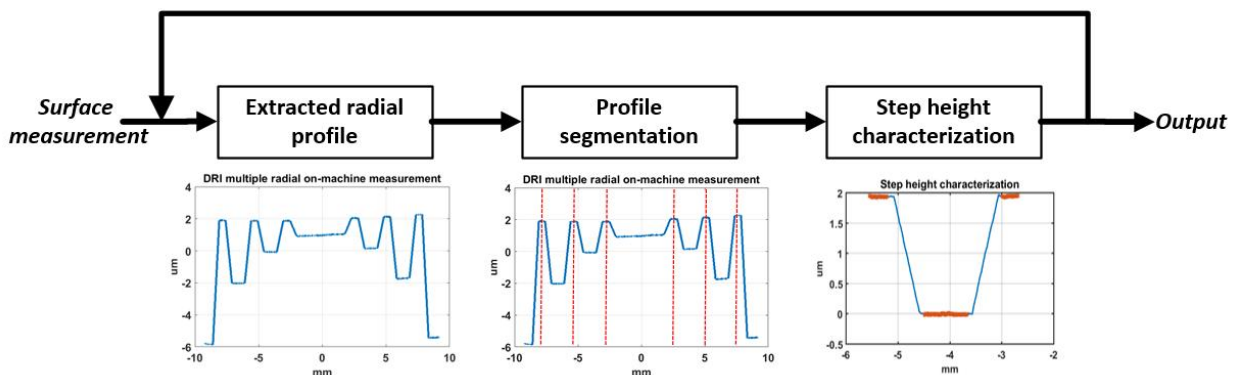


**Figure 5.19 Flow chart of step height characterisation**

The characterisation procedure for the measured step heights is illustrated in Figure 5.19. Each extracted radial profile is separated into 4 different step segments, and for each segment the step height is characterised according to ISO 5436 part 1 [179]. Mean step height and repeatability is reported over all radial profiles with 3 repeated measurements. Measurement error  $\delta_{error}$  is defined as the difference between multiple step height value of on-machine measurement and that of offline calibrated white light interferometer (Talysurf CCI 3000). The CCI result was also employed as the calibrated values to correct the DRI linearity error. The measurement results are summarized in Table 5.2.

**Table 5.2 Step height measurement results**

Design height ( $\mu\text{m}$ )	1	2	4	8
DRI on-machine ( $\mu\text{m}$ )	0.9969	1.9465	3.9115	7.8199
Talysurf CCI ( $\mu\text{m}$ )	1.0011	1.9774	3.9771	7.9128
$\delta_{error}$ ( $\mu\text{m}$ )	-0.0042	-0.0309	-0.0656	-0.0929

Figure 5.20 (a) and Figure 5.20 (b) respectively show the uncorrected and corrected error plot for the step height measurement. The error bars represent the measurement repeatability calculated as the standard deviation of the mean values. After calibration, slope correction coefficient was 1.0123 and the linearity error was reduced from 93 nm to 14 nm.

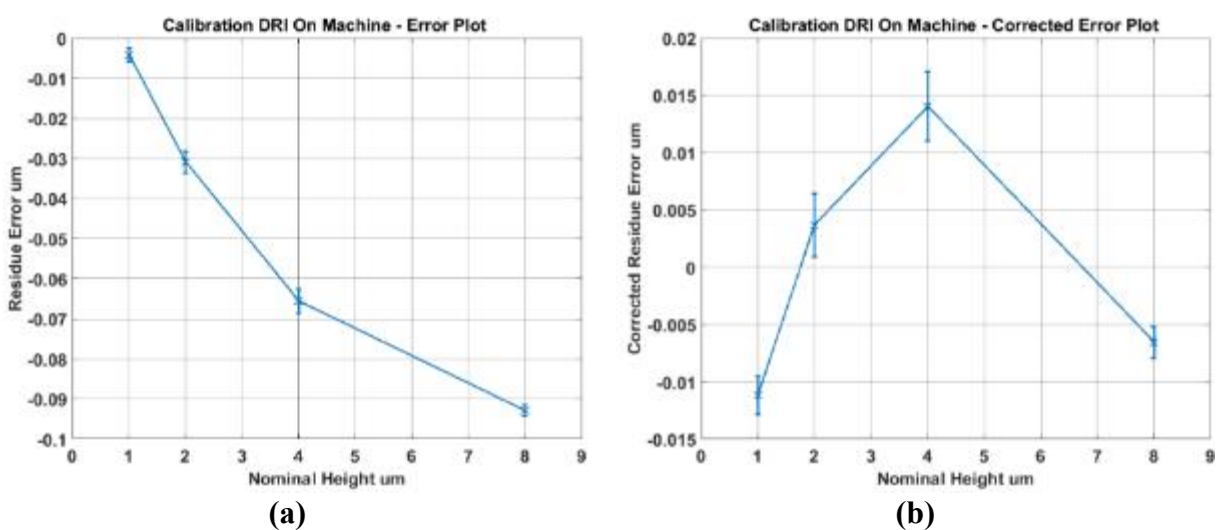


**Figure 5.20 (a) Uncorrected and (b) corrected error plot of the step height measurement**

## 5.4 OMSM experiment

To evaluate the proposed calibration process and the performance of DRI on-machine measurement, experimental work and results are presented and discussed in this section. Figure 5.21 illustrates the experimental setup of the proposed OMSM system. The fibre-linked DRI probe was mounted on a multi-degree-of-freedom adjustment stage for the purpose of alignment.

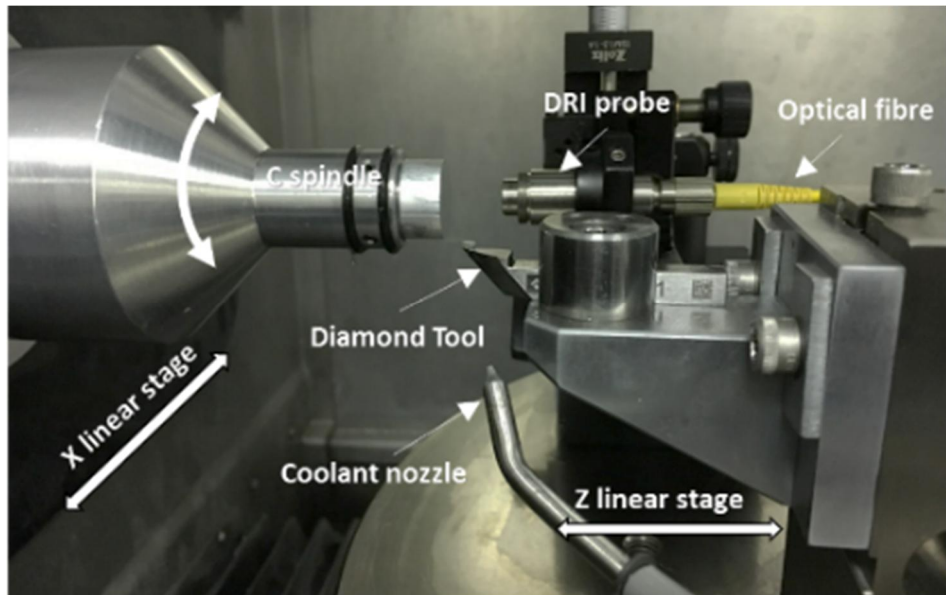


**Figure 5.21 Experimental setup of the proposed OMSM system**

Following the calibration procedure discussed above, two additional samples were measured on the machine. The OMSM results were compared with calibrated offline measurement of the same samples.

A 2D cosine curve ( $Z = A\cos(2\pi/\lambda X)$ ) with  $A = 5 \mu\text{m}$  and  $\lambda = 2.5 \text{ mm}$  was fabricated on an aluminium sample, followed by the DRI on-machine measurement. In this experiment, as the designed surface feature is a cosine curve along the radial direction, multiple radial path measurement scanning was adopted for the surface measurement. Six measurement profiles were spaced across the surface at equal angles ( $30^\circ$ ), as shown in Figure 5.22. The measurement span was 4 mm to -4 mm along the radial direction and the scanning speed was set to be 2 mm/min. After each radial scan, the  $C$ -axis was rotated by  $30^\circ$  and another radial scan was performed.

When all data acquisition process was finished, the measurement points were segmented and mapped onto the workpiece Cartesian coordinate system.

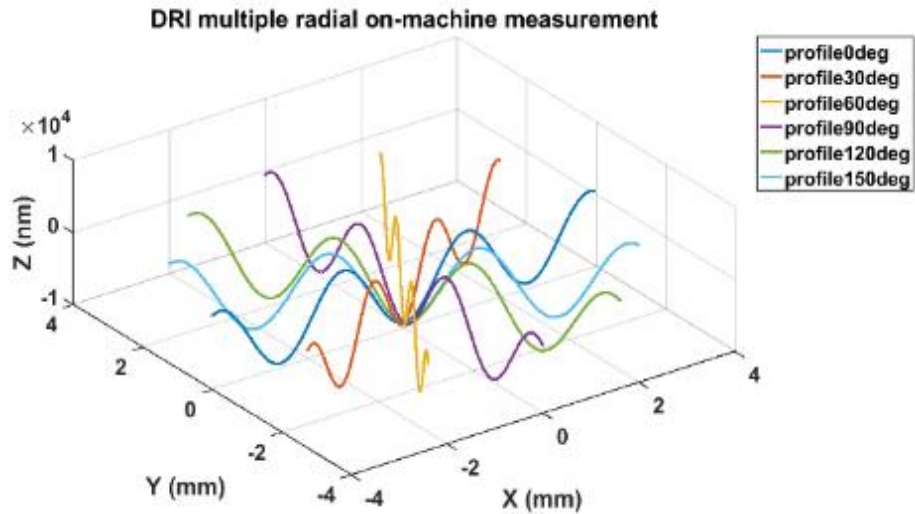


**Figure 5.22 Multiple radial measurement of a cosine curve sample**

In order to find out the correlation between the online and offline measurements, offline measurements of the machined sample were carried out using a calibrated stylus profilometer (Talysurf PGI, Taylor Hobson). For comparison, the  $0^\circ$  profile of DRI on-machine measurement was extracted. With the aid of marked reference points on the workpiece surface, the corresponding  $0^\circ$  profile was measured on Talysurf PGI profilometer. Figure 5.23 (a) and Figure 5.23 (b) show the DRI on-machine and PGI offline measurements respectively.

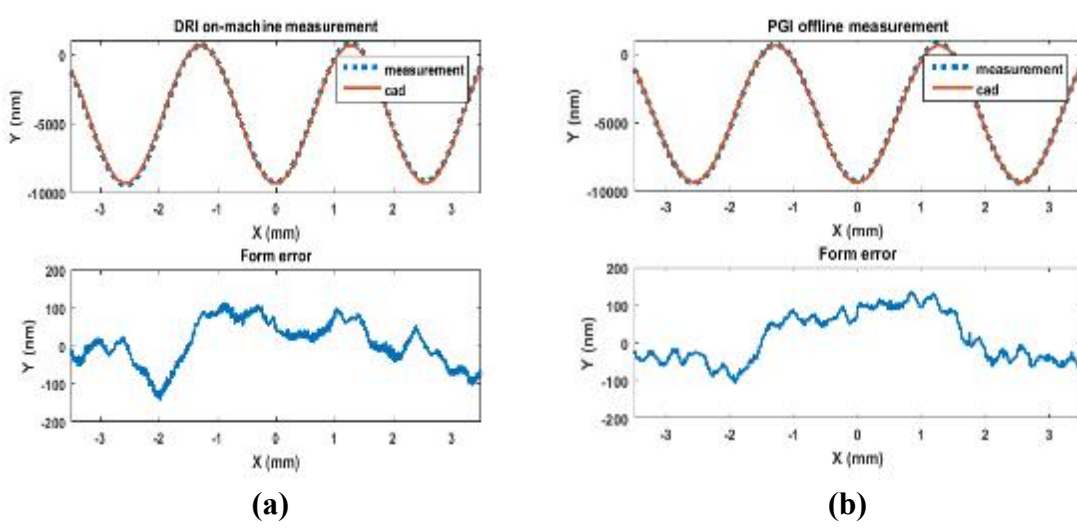


**Figure 5.23 Measurement results and error analysis of (a) DRI on-machine measurement and (b) PGI offline measurement**

It is observed that DRI on-machine measurement agrees well with PGI offline measurement in terms of form evaluation. The derived form error also has similar shape and the characterisation parameters difference is less than 10%. It can be noticed that DRI on-machine measurement acquires more surface components of high frequency, mainly due to the physically filtering effect of PGI stylus tip and the fact that the DRI probe works in a relatively noisy manufacturing environment. For the purpose of similarity quantification, Pearson's correlation coefficient (PCC) was employed as a measure of correlation between the two profiles measurements, which is described as [180]:

$$P(X, Y) = \frac{N(\sum_{i=1}^N X_i Y_i) - (\sum_{i=1}^N X_i)(\sum_{i=1}^N Y_i)}{\sqrt{\left[ N \sum_{i=1}^N X_i^2 - \sum_{i=1}^N X_i \sum_{i=1}^N X_i \right] \left[ N \sum_{i=1}^N Y_i^2 - \sum_{i=1}^N Y_i \sum_{i=1}^N Y_i \right]}} \\ = \frac{1}{N-1} \sum_{i=1}^N \left( \frac{X_i - \bar{X}}{S_x} \right) \left( \frac{Y_i - \bar{Y}}{S_y} \right) \quad (5.17)$$

where  $S_x$  and  $S_y$  are the sample standard deviation. The calculated coefficient between DRI on-machine measurement and PGI offline measurement is  $P=0.991$  (close to 1), which indicates the two measurement signals are strongly correlated.

A high precision convex sphere provided by Precitech was scanned in a spiral tool path with  $C$  axis rotational speed of 1 rpm and  $X$  axis feedrate of 0.3 mm/min. The sphere surface was nickel plated with stated roughness less than 1 nm. Due to high surface slope, the radius of the measurement area was limited to 1.5 mm. For comparison, offline measurement was performed on a calibrated white light interferometer (Talysurf CCI 3000 with 5X objectives). The measurement results are respectively shown in Figure 5.24 (a) and Figure 5.24 (b). The measured surface was characterised by radius of curvature, and form error RMS value, summarized in Table 5.3.

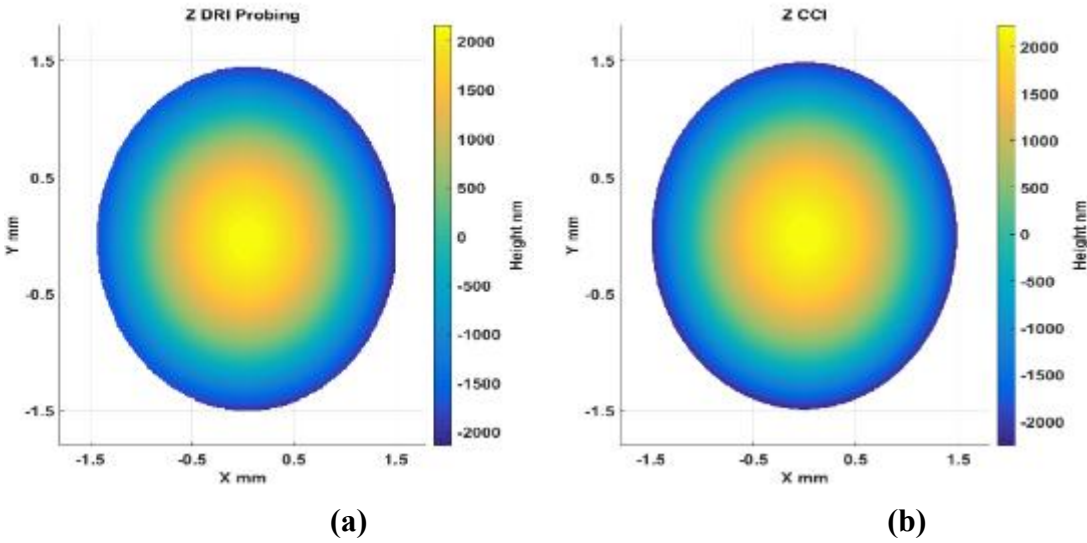


**Figure 5.24 Sphere sample (a) DRI on-machine and (b) CCI measurement**

From the two measurement experiments, it can be seen that the results measured by on-machine measurement system agree well with the calibrated offline measurement results, demonstrating the effectiveness of the calibration process. Although kinematic error compensation and linearity error correction have been conducted to improve the measurement accuracy, higher measurement error were observed for on-machine measurement of complex surfaces, resulting from the surface slope effect and non-linearity characteristics of the DRI probe.

**Table 5.3 Characterisation results of on-machine and offline measurement**

Sample	Characterisation parameter	DRI on-machine (standard deviation)	Offline measurement (standard deviation)	Deviation
Convex sphere	Radius of curvature (mm)	253.8 (std = 0.056)	246.9 ( std < 0.001)	6.9
	Form error RMS (nm)	10.9 (std = 2.52)	3.7 ( std = 0.17)	7.2
Cosine curve	Fitted amplitude ( $\mu\text{m}$ )	4.974 (std = 0.0035)	4.982 (std = 0.002)	0.008
	Fitted frequency ( $\text{mm}^{-1}$ )	0.390 (std = 0.0005)	0.391 (std = 0.0005)	0.001
	Form error RMS (nm)	58.6 (std = 2.25)	65.7 (std = 1.26)	7.1

## 5.5 Summary

In order to establish a metrology-integrated manufacturing platform, a robust interferometric DRI probe was integrated on a 3-axis ultra-precision turning machine.

The measurement coordinate was aligned coaxially to the spindle rotational axis, by means of multiple scanning of a convex sphere sample. The selection of measurement path primarily depends on the measurement tasks and surface feature distribution. Three scanning paths (multiple radial, multiple circular and spiral) were presented with corresponding applicable surfaces.

A systematic calibration methodology was proposed to compensate the measurement errors. Three major error sources, including on-machine vibration, machine tool kinematic errors, and linearity errors were investigated. Vibration test Experimental results have shown machine static and motion vibration tend to induce additional error of measurement results. A theoretical study of the relationship between sampling frequency, scanning parameters, vibration frequency and topography frequencies of interest was presented. The proposed frequency decision graph can be used to select the proper sampling frequency and scanning parameters.

Machine tool kinematic error was mapped for OMSM correction with the proposed kinematic error modelling measurement and compensation method. The optical flat measurement by DRI on-machine and offline Twyman–Green interferometer indicated that the kinematic error compensation effectively increased the OMSM accuracy. Calibration of the response curve and linearity error correction was conducted by measuring a radially distributed step height sample on the machine. The linearity error of DRI probe was reduced from 93 nm to 14 nm after the calibration process. Additionally, the results obtained from DRI on-machine measurement system agreed well with the results of offline measurement when measuring a precision sphere and a diamond turned cosine curve surface. It is considered that the validity of the proposed

calibration methodology and the effectiveness of the OMSM system have been demonstrated by a set of calibration and measurement experiments.

## **6 Process investigation and machining error modelling with OMSM**

### **6.1 Introduction**

The continuing evolution of high-precision manufacture places an increasing need to perform surface measurement in the manufacturing environment. After the establishment of integrated metrology, this chapter together with chapter 7 will explore the potential applications of machine-measurement closed loop processes for accuracy and efficiency improvement of ultra-precision manufacturing.

Although ultra-smooth surfaces can be directly generated by diamond machining without additional processing [38, 181], there are still many factors causing surface form deviations from the design, such as environmental factors, process parameters and tool wear [164, 165]. A valid investigation of process parameters, together with reliable metrology feedback is considered indispensable in order to achieve demanding surface accuracy and functionality [182-185]. Nalbant et al. [186] presented a robust parameter design using the Taguchi method for the optimization of turning processes. The relationship between cutting parameters and surface finish was analysed with the orthogonal array, the signal-to-noise ratio, and analysis of variance. Experimental results indicated that 335% improvement of the surface finish has been achieved when using the optimal cutting parameters. Haq et al. [187] employed grey analysis methodology to investigate the drilling parameters with the considerations of multi responses such as surface roughness, cutting force and torque. Based on the grey relational grade, optimum levels of parameters have been identified and the experiment results satisfied the practical requirements of the drilling operation of Al/SiC metal matrix composites. Kwak et al. [188] developed a response surface model to predict the power consumption and the surface roughness in external cylindrical grinding of hardened SCM440 steel. A Hall sensor was used to monitor the real-time power of the spindle driving motor. According to the established model, proper

grinding parameters were consequently selected to meet the production requirement. Previous studies focused on the parameters investigation and process modelling with intermediate physical quantity sensors, such as vibration, force, and temperature. However, machined surface quality is directly linked to designed functionality and specified in the production process. Few researchers have integrated surface measurement instruments onto the manufacturing platform for the purpose of process investigation.

This chapter attempts to exploit the benefits of OMSM for the process investigation of ultra-precision machining. The consistency between machining and measurement coordinates can be preserved with the integration of metrology on the machine, which fundamentally avoid the errors caused by re-positioning workpieces. Thus, application of OMSM in ultra-precision machining process will help to increase the level of production automation and enhance the performance of process parameters investigation, leading to intelligent manufacturing. In this chapter, the effect of process parameters on the surface form errors in ultra-precision cylindrical turning is investigated by empirical modelling. Experimental work was carried out and analysed to evaluate the validity of the established process model.

## 6.2 Process investigation methodology

Although the diamond turning process is capable of generating surfaces with sub-micrometre form accuracy and nanometre surface roughness, surface form accuracy must be well controlled and optimized, as it is strongly linked to the functional attributes. For a given workpiece material, the factors can be classified into the machining process, the machine tool, the cutting tool and the environment related aspects, shown in Figure 6.1. The controllable factors or the input to the machining systems are processing parameters, such as federate, spindle speed and depth of cut. Selection of proper process parameters is of critical importance to achieve surface design specification. Process investigation with reliable metrology should identify the relationship between cutting parameters and the machined surface quality.

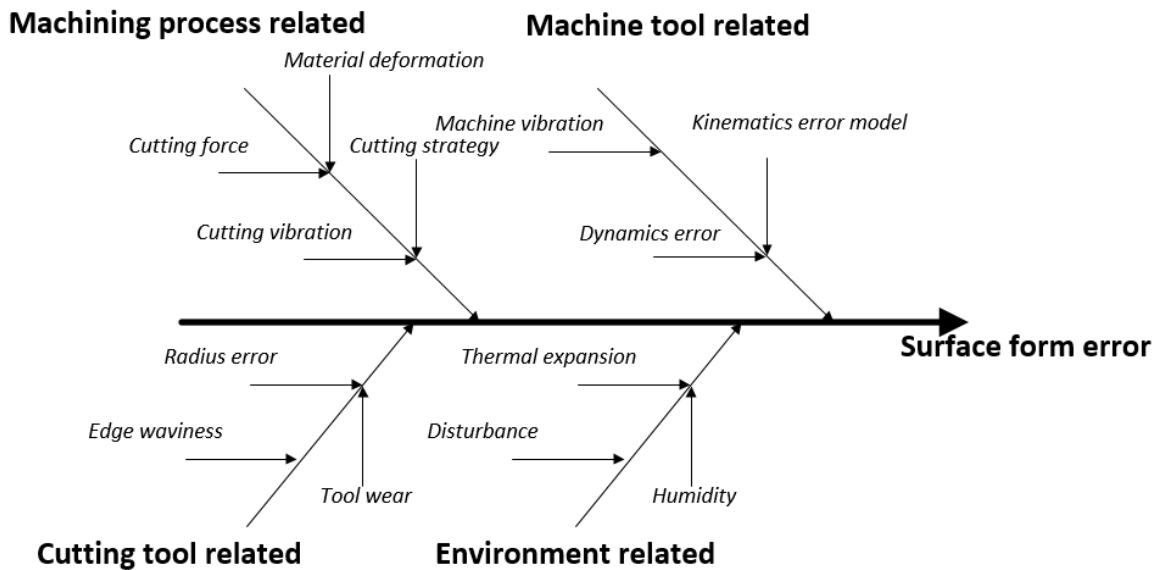


**Figure 6.1 Factors influencing surface form error in ultra-precision turning process**

The flow chart of the proposed process investigation methodology is illustrated in Figure 6.2. The objectives, factors, and constraints need to be set before the experimental investigation. One-factor-at-a-time experimental approach is often time-consuming and has been gradually replaced by the design of experiment approach (DOE) [189], such as factorial design, Taguchi methods and response surface methodology. After the machine-measurement experimental run, the acquired data can be analysed by a variety of statistical methods to test the significance. The empirical relationship between input variables and the response can be modelled. Therefore, proper machining parameters can be selected using the developed model. OMSM plays a key role in the process investigation, as it is able to enhance automation, reduce transfer risk and allow machined surfaces to be inspected in a more deterministic way without misalignment error.

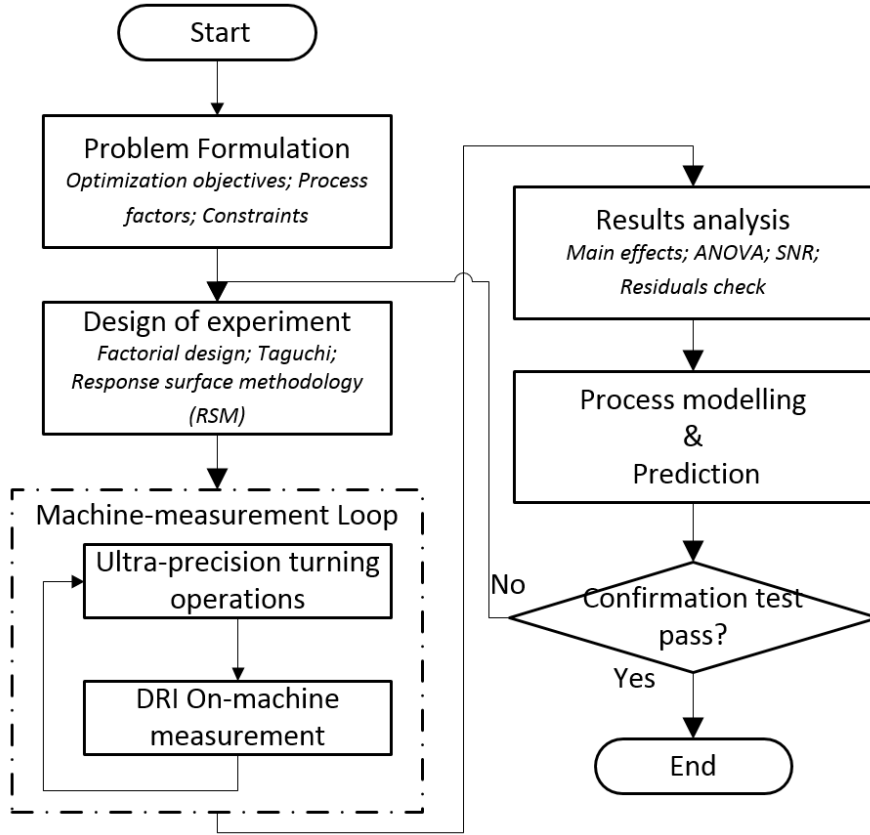


**Figure 6.2 Flow chart of process investigation strategy with the aid of OMSM**

### 6.2.1 Response surface methodology

Compared with theoretical and simulation methods [190, 191], experimental investigation of process parameters is practical and widely used for manufacturing operations. In this study, experimental response surface methodology (RSM) [189] was adopted to develop the statistical relationship between process parameters and generated surface accuracy. RSM design is a powerful tool to investigate the complex effect of input parameters on the response and develop a mathematical model to describe this relationship. The experiment data can be analysed statistically by means of regression based on least squares method. For example, if the full quadratic model is employed, the relationship between the response and input variables can be described as follows:

$$Y = \alpha_0 + \sum_{i=1}^k \alpha_i X_i + \sum_{i=1}^k \alpha_{ii} X_i^2 + \sum_i \sum_j \alpha_{ij} X_i X_j + \varepsilon \quad (6.1)$$

where  $Y$  is the estimated response,  $X_i$  is the input variables and  $\varepsilon$  is the random error.  $\alpha_i$ ,  $\alpha_{ii}$  and  $\alpha_{ij}$ , respectively represent the coefficients of the linear, quadratic and interaction terms. The model coefficients  $\{\alpha\}$  need to be estimated using a regression method and determined from the following equation:

$$\boldsymbol{\alpha} = [\alpha_0, \alpha_1, \dots, \alpha_n]^T = (X^T X)^{-1} X^T \hat{Y} \quad (6.2)$$

where  $X^T$  is the transposed matrix of input variables  $X$  and  $(X^T X)^{-1}$  is the inverse of the matrix  $(X^T X)$ . The test for significance of the regression model and each model coefficient needs to be performed to validate the goodness of fit for the established response surface model. Furthermore, the analysis of variance (ANOVA) is applied to identify the influential factors and eliminate non-significant terms to improve the model adequacy. Finally, confirmation experiments are carried out to determine the model validity and accuracy.

### 6.2.2 Design of experiment

In order to investigate the influence of machining parameters on the surface accuracy, 3 principal process parameters including spindle speed, feed rate and depth of cut, were selected as input variables for the empirical model. The feasible experimental ranges followed conventional practice and recommendations from the machine tool manufacturer. Each factor was assigned three levels, as listed in Table 6.1.

**Table 6.1 Factors and levels of process parameters**

Factors	Symbol	Level		
		1	2	3
Spindle speed (rpm)	$S$	600	900	1200
Feedrate (mm/min)	$f$	2	4	6
Depth of cut ( $\mu\text{m}$ )	$a_p$	3	6	9

Central composite design (CCD) is widely used in empirical RSM to establish a quadratic model for the response variable without the needing of a full factorial experiment [189]. CCD is

a factorial or fractional factorial design with centre points, augmented with a group of star points. It is particularly useful in sequential experiments as previous factorial experiments can be reused by adding axial and centre points. In this study, CCD for 3 factors with 3 levels was adopted. Star points were set at the face of the design cube and 5 central points were added to estimate the measurement variations and check the model curvature. The complete design matrix of 20 runs is shown in Table 6.2. All the experiments were operated in a random sequence to balance the uncontrollable conditions.

**Table 6.2 CCD design of experiment**

Std run	Run order	Block	Factors		
			Feedrate (mm/min)	Spindle speed (rpm)	Depth of cut ( $\mu\text{m}$ )
1	6	1	2	600	3
2	16	1	6	600	3
3	15	1	2	1200	3
4	7	1	6	1200	3
5	3	1	2	600	9
6	19	1	6	600	9
7	13	1	2	1200	9
8	5	1	6	1200	9
9	2	1	2	900	6
10	17	1	6	900	6
11	8	1	4	600	6
12	1	1	4	1200	6
13	18	1	4	900	3
14	11	1	4	900	9
15	12	1	4	900	6
16	9	1	4	900	6
17	14	1	4	900	6
18	10	1	4	900	6

19	20	1	4	900	6
20	4	1	4	900	6

## 6.3 Experiments and discussions

### 6.3.1 Experimental setup

To further evaluate the performance of OMSM and the effectiveness of the proposed process investigation methodology, experimental results are presented and discussed in this section. A cosine curve, mathematically described as  $Z = A\cos(2\pi/\lambda X)$  with  $A = 2 \text{ um}$  and  $\lambda = 1 \text{ mm}$ , was fabricated on a brass rod, followed by on-machine measurement. The measurement length was set as 4 mm along the axial direction and speed scanning speed was set at 2 mm/min. The composition of the brass material was 0.01%Al, 0.1%Ni, 0.2%Fe, 0.2%Sn, 3.3%Pb and 38.4%Zn. Diamond cutting tool parameters are the same as shown in Table 4.3.

The experimental configuration is illustrated in Figure 6.3. Different from the setup in chapter 5, the DRI kit is installed beside the diamond tool holder perpendicular to the cylinder surface. When the probe scans along the Z direction, the axial profile of cylinder workpiece can be acquired.

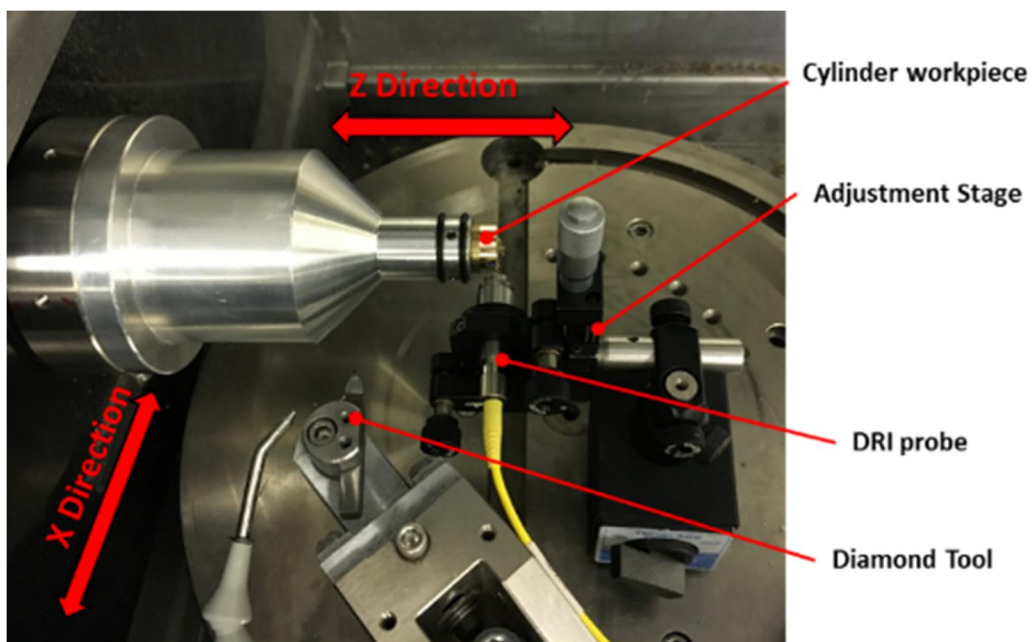
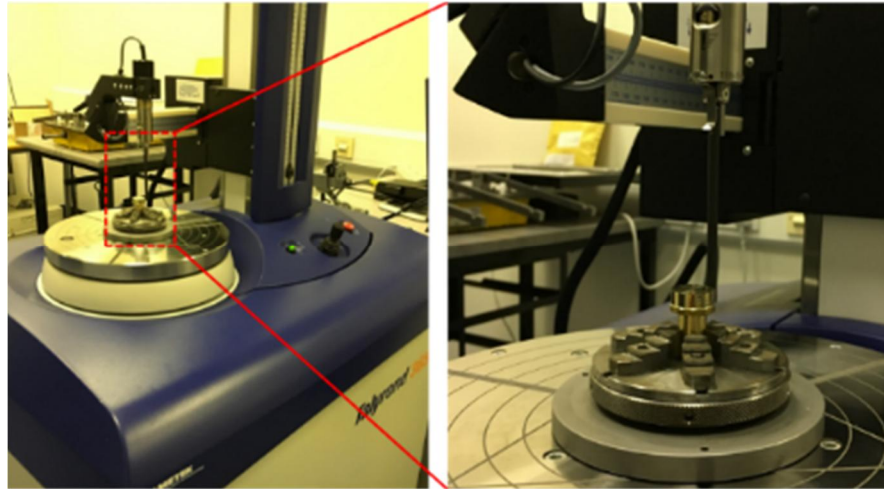


Figure 6.3 Experimental setup for process investigation with OMSM

### 6.3.2 Comparison between OMSM and Talyrond

In order to validate the result of OMSM, offline measurement of the sample surface was carried out on a calibrated profilometer (Talyrond 365 Taylor Hobson) which is shown in Figure 6.4. The machining parameters used were feed rate ( $f = 4 \text{ mm/min}$ ), spindle speed ( $S = 900 \text{ rpm}$ ), and depth of cut ( $a_p = 3 \mu\text{m}$ ).



**Figure 6.4 Talyrond offline measurement**

Figure 6.5 (a) and Figure 6.5 (b) indicate that DRI on-machine measurement along the axial direction agrees well with Talyrond offline measurement in terms of form evaluation. The derived profile error also shows a high degree of similarity over the measurement length and the root mean square (RMS) value is 28.8 nm and 31.2 nm respectively for DRI and Talyrond measurement.

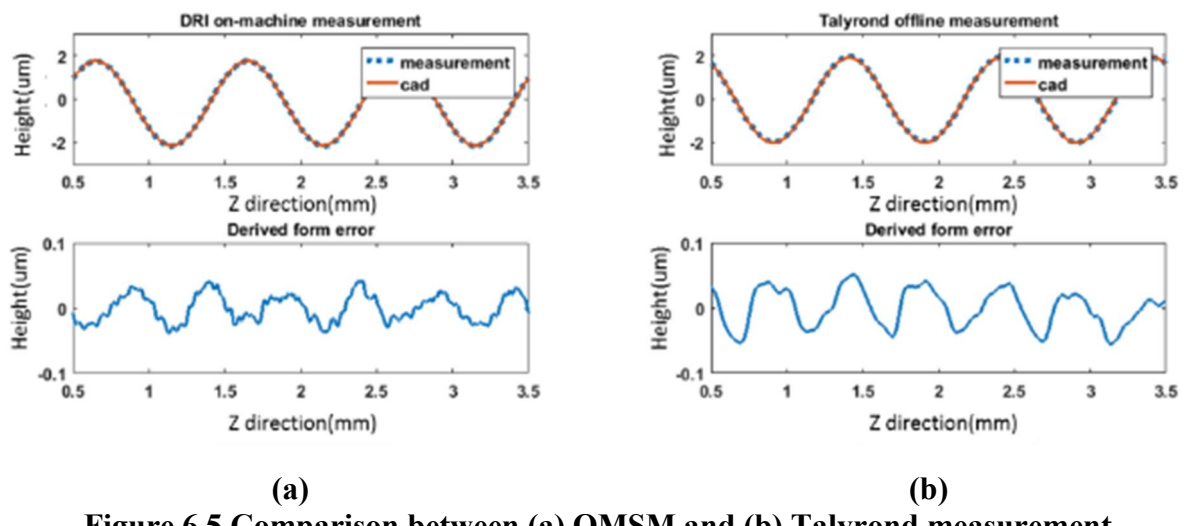


**Figure 6.5 Comparison between (a) OMSM and (b) Talyrond measurement**

The deviation between DRI and Talyrond measurement might result from their different sensor types (optical and mechanical respectively). Also, the machine tool kinematic error ( $Z$  axis straightness error in  $X$  direction  $E_{XZ}$ ) will induce into on-machine measurement results. However, as the measurement length is fixed, the kinematic error is repeatable for each experimental run. This is applicable for the process investigation and find out the proper parameters in the design table.

It is noted that there is a certain amount of horizontal shift between two sets of original measurement data, due to the fact that the sample was measured under different measurement coordinates. It can also be inferred that it is impossible to measure the same portion of machined surface after each trial run if the process investigation is carried out with offline measurement, which would inevitably induce more variation in the response variable. After the two sets of measurement data were aligned, the correlation coefficient  $PCC$  between DRI on-machine measurement and Talyrond offline measurement is 0.97 (close to 1), indicating that the two measurement signals are strongly correlated.

### 6.3.3 Response surface analysis

A series of machining operations and on-machine measurements were carried out, following the CCD in section 6.2.2. The process parameters used and the corresponding response are listed in Table 6.3. The response surface form error, was measured on-machine by DRI probe and characterised as RMS value.

**Table 6.3 Experimental results of form error (OMSM)**

Std run	Factors			Response Measured form error RMS (nm)
	Feedrate (mm/min)	Spindle speed (rpm)	Depth of cut ( $\mu\text{m}$ )	
1	2	600	3	21.8
2	6	600	3	27.6
3	2	1200	3	33.9

4	6	1200	3	38.3
5	2	600	9	26.0
6	6	600	9	32.7
7	2	1200	9	38.3
8	6	1200	9	43.3
9	2	900	6	22.2
10	6	900	6	23.8
11	4	600	6	28.4
12	4	1200	6	44.2
13	4	900	3	28.8
14	4	900	9	35.8
15	4	900	6	30.7
16	4	900	6	31.6
17	4	900	6	31.3
18	4	900	6	28.4
19	4	900	6	29.5
20	4	900	6	30.1

These experimental result data were input and analysed in Minitab 17 [192]. The response surface methodology was adopted for modelling the empirical relationship between independent factors and the response. Analysis of variance was performed to test the significance of regression model and the goodness of fit. The statistical significance of the response surface model was evaluated using  $P$ -values. If  $P$ -values are less than 0.05 (95% confidence), the obtained models are considered to be statistically significant, which means the selected variable in the model have a significant effect on the response. A preliminary analysis was tested for a full quadratic response model. By means of removing the insignificant terms, the resulting ANOVA for the reduced quadratic model is summarized in Table 6.4 and Table 6.5.

**Table 6.4 ANOVA table of response surface model for machined surface error**

Source	DF	Seq SS	Adj SS	Adj MS	F-value	P-value
--------	----	--------	--------	--------	---------	---------

Model	6	710.974	710.974	118.496	60.01	<0.0001
Linear	3	499.499	499.499	166.500	84.32	<0.0001
$f$	1	55.225	55.225	55.225	27.97	<0.0001
$S$	1	378.225	378.225	378.225	191.53	<0.0001
$a_p$	1	66.049	66.049	66.049	33.45	<0.0001
Square	3	211.475	211.475	211.475	35.70	<0.0001
$f^2$	1	5.941	121.945	121.945	61.75	<0.0001
$S^2$	1	186.355	121.280	121.280	61.42	<0.0001
$a_p^2$	1	19.180	19.180	19.180	9.71	0.008
Error	13	25.671	25.671	1.975		
Lack of fit	8	18.538	18.538	2.317	1.62	0.308
Pure error	5	7.133	7.133	1.427		
Total	19	736.645				

**Table 6.5 Regression model summary**

	S-value	R <sup>2</sup>	R <sup>2</sup> adjusted	Press
Surface form error RMS	1.40524	96.52%	94.91%	75.5148

The analysis result indicates that the reduced model and all the remaining terms are statistically significant. All linear and corresponding square terms are thus employed in the response surface model. Spindle speed is the most significant factor associated with the surface form error, contributing 51.34% to the total variation. This can be explained by the fact that spindle motion characteristics have a strong relationship with the rotational speed, resulting in the deviation of cutting trajectories in the cylindrical turning process. It is noted that the interaction terms between feedrate, spindle speed and depth of cut are not of statistical significance and are eliminated from the model, thus not shown in the ANOVA table. The lack of fit is insignificant as the  $P$ -value is 0.308, larger than 0.05 (level of significance), implying that the null hypothesis cannot be rejected. Besides, the determination coefficient  $R^2$ , defined as

the proportion of the explained variation to the total variation, is close to 1, indicating the measured response data is well fitted.

**Table 6.6 Coded coefficients of regression model**

Model term	Coded regression coefficient	Contribution
Constant	30.024	
$f$	2.350	7.50%
$S$	6.150	51.34%
$a_p$	-2.66	8.97%
$f^2$	-6.659	0.81%
$S^2$	6.641	25.30%
$a_p^2$	2.641	2.60%

In addition, the plot of the fitted residuals in the observation order and the normal probability plot of the residuals are respectively drawn in Figure 6.6 and Figure 6.8. As shown in the normal probability plot, the residuals approximately fall on a straight line, indicating that the errors are distributed normally. A good agreement between the predicted and on-machine measured response value is also observed.

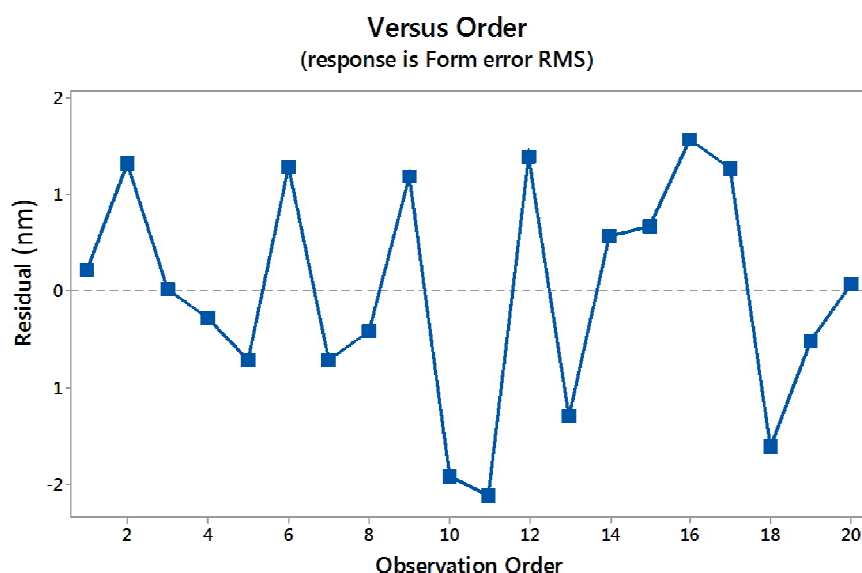


**Figure 6.6 Fitted residual plot in the observation order**

Moreover, the response residual plots (versus input factors) are shown in Figure 6.7. No obvious distribution pattern exists in fitted residuals plot. To sum up, the fitted quadratic model is statistically significant and adequate for further analysis.

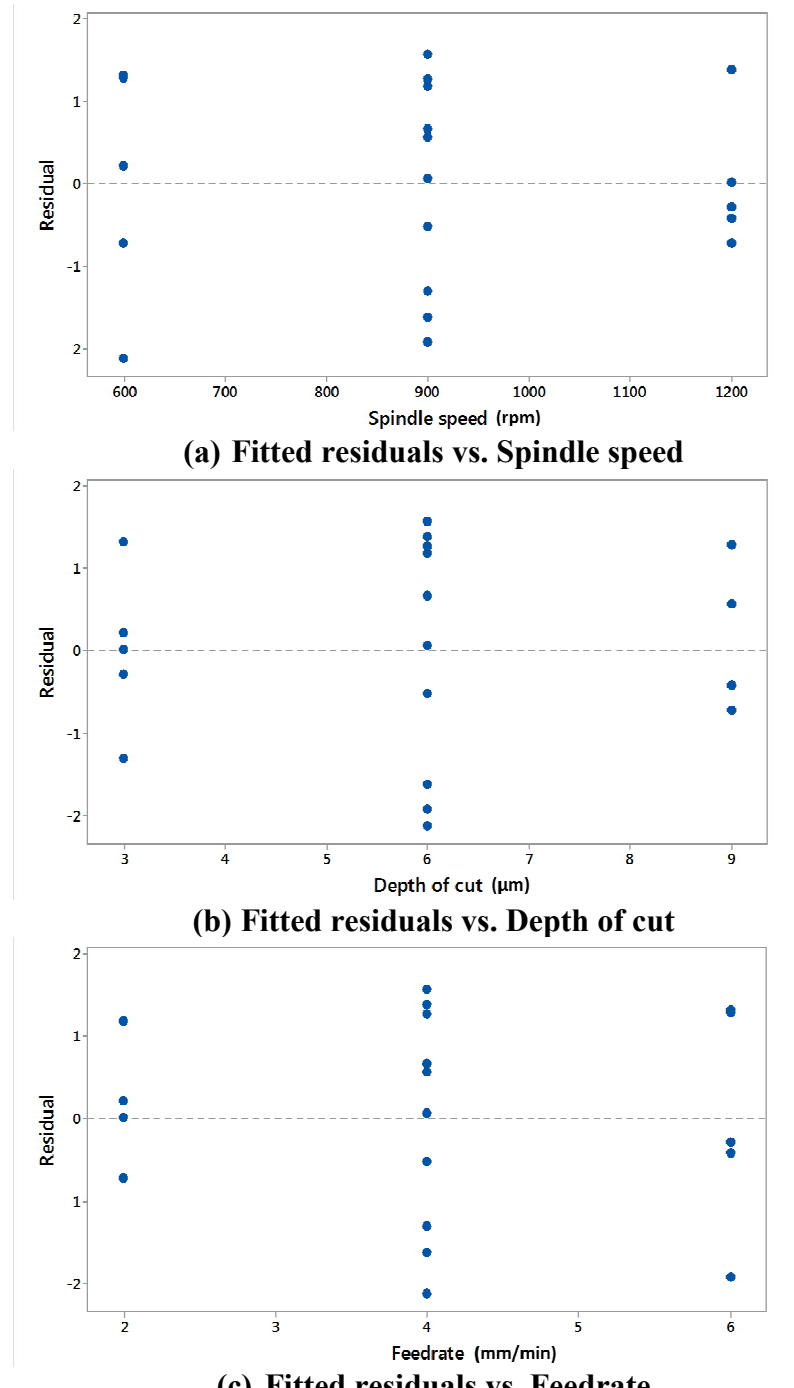
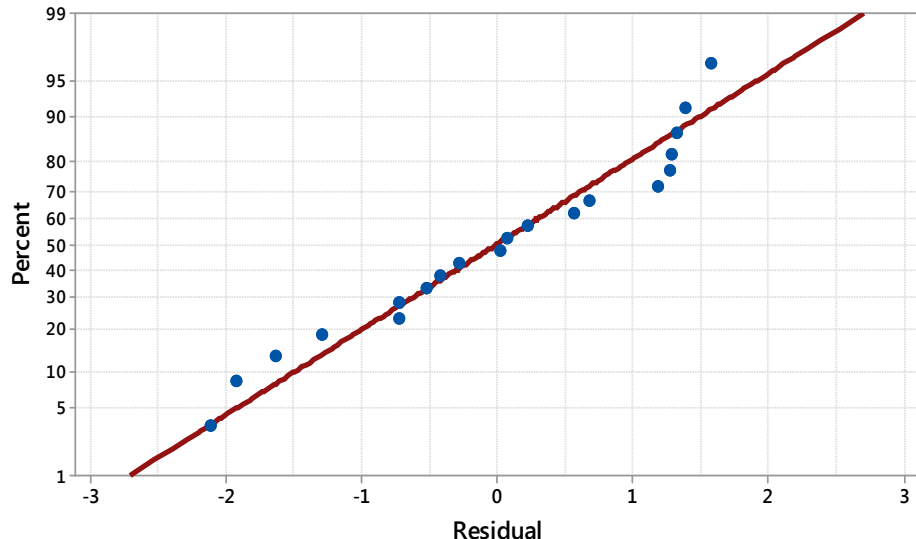


Figure 6.7 Fitted residual plot (versus factors)

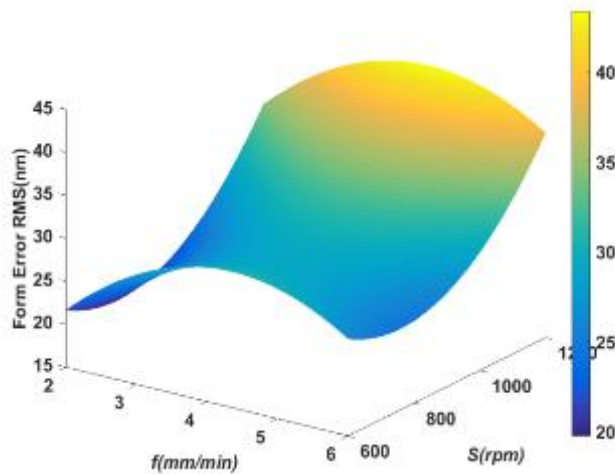


**Figure 6.8 Normal probability plot of residuals**

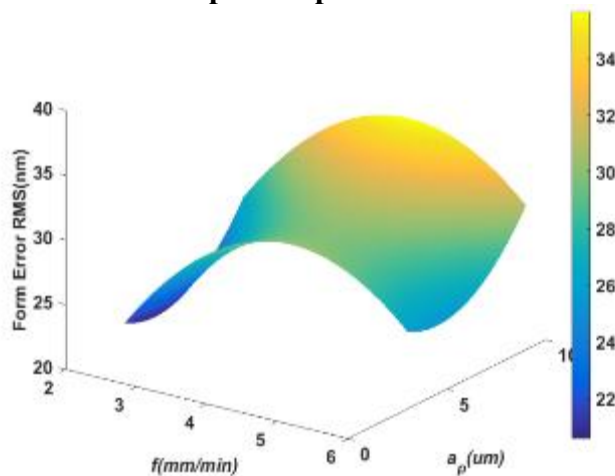
With estimated regression coefficients for individual variable listed in Table 6.6, the reduced quadratic response surface model can be expressed as a mathematical function of machining parameters. This empirical equation can be also employed to predict the machined surface form error as follows:

$$Y = 45.43 + 14.49 f - 0.1123 S - 2.66 a_p - 1.665 f^2 + 0.000074 S^2 + 0.2934 a_p^2 \quad (6.3)$$

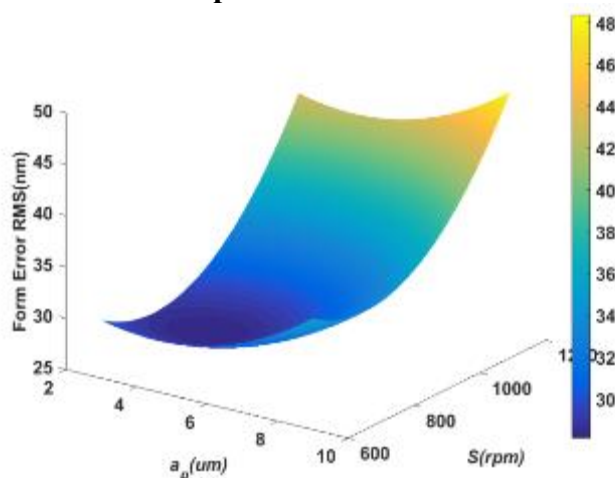
In order to visualize the interaction effect among the machining parameters, the 3D response graphs for the surface form error RMS values are plotted in Figure 6.9 (a), Figure 6.9 (b) and Figure 6.9 (c). In each plot, there are two independent variables and the third factor is held constant at the middle level. The graphs illustrate that the form error of machined surface decreases with the lower level of feedrate and represents a concave form with depth of cut and spindle speed.



**(a) Feedrate and spindle speed vs. form error RMS value**



**(b) Feedrate and depth of cut vs. form error RMS value**



**(c) Depth of cut and spindle speed vs. form error RMS value**

**Figure 6.9 3D response surface graphs**

#### 6.3.4 Confirmation test

In order to validate the established model and evaluate the prediction accuracy, three confirmation tests were performed. The experiment condition and measurement results are

shown in Table 6.7. The first confirmation trial was performed under the cutting conditions used previously while the other two experiments were carried out under new conditions but within the range of the levels defined. The model predicted values and the experimental values were compared and the difference lies within 4%. As discussed above, the developed response surface model can be used to model and predict the machined surface error within 95% confidence intervals ranges of parameters studied.

**Table 6.7 Confirmation tests**

Confirmation run	Factors			Response		
	$f$ (mm/min)	$S$ (rpm)	$a_p$ ( $\mu\text{m}$ )	Measured (nm)	Predicted (nm)	Error %
1	4	900	6	28.9	30.0	-3.81
2	6	600	6	26.7	26.2	1.87
3	2	1200	6	34.6	33.8	2.31

## 6.4 Summary

This chapter has described the experimental investigation of the effect of machining parameters on the surface form error. An empirical model to predict the form error in ultra-precision cylindrical turning process has been developed with the aid of OMSM. DRI measurement along Z axis was verified by means of correlation with the result of calibrated offline measurement. Due to the lack of alignment error between machining and measurement coordinates, OMSM is capable of giving more accurate feedback and improve the performance of the investigation strategy. The statistical relationship between the process parameters and the machined surface form error was established by means of response surface methodology. The reduced quadratic model obtained was verified by the test for significance of the regression model and goodness of fit. The determination coefficient  $R^2$  is 96.52% and lack of fit is

insignificant ( $P$ -value =  $0.308 > 0.05$ ), indicating the model is adequate. For the process conditions considered, the ANOVA results indicate that spindle speed is the most significant factor influencing machined surface form error, with 51.34% contribution to the total variability. The linear and quadratic terms of the chosen process parameters (feedrate, spindle speed and depth of cut) are all of statistical significance and are included in the response surface model. The confirmation tests show the model predicted value conformed to the experimental value, with a difference less than 4%. The empirical response surface model allows prediction of machined surface form error with a 95% confident interval. Therefore, the approach presented can be regarded as an effective empirical tool for modelling the ultra-precision turning processes.

## **7 Corrective machining with OMSM**

### **7.1 Introduction**

The process of measurement, characterisation and compensation are considered indispensable in further improvement of the machining accuracy. Particularly in ultra-precision machining processes, the transportation of workpiece between machine tools and metrology platform is problematic [20]. As the critical requirements for surface quality become more demanding, OMSM can fundamentally avoid the errors induced by the removal and remounting process. Rahman et al. [193] developed an on-machine profile measurement system based on contact CMM principle to check the profile radius of the ground surface. A software compensation method was also applied in ELID grinding of an aspheric surface to overcome several machine kinematic errors and compensate the wheel wear in the grinding cycles. Yu et al. [194] analysed the main sources of machine component errors and their effect on the profile accuracy of the fast tool servo machined micro-structured surfaces. A compensation method was proposed to modify the tool path for each component error to pre-compensate the induced profile errors. Kim et al. [195] employed a novel long-stroke FTS mechanism on a diamond turning machine for corrective figuring of non-rotationally symmetric components. A special on-machine measurement device was added to measure the optical parameters of the machined surface and to compensate for the residual form of errors that were commonly produced in the diamond turning process. Although most studies mainly focused on the improvement of machining accuracy by compensating the machine tool component errors, there is a lack of systematic research on the corrective machining based on the information from surface measurement and characterisation.

This chapter will utilize the benefits of OMSM and explore the corrective machining strategy for ultra-precision turning to further improve surface accuracy. OMSM enables the in-situ inspection and characterisation of surface features, for better understanding of machining

process behaviour. Furthermore, as the consistency between the machining and measurement coordinate is preserved without rechucking the workpiece, corrective machining can be carried out in a more deterministic manner. The profile/surface corrective machining strategy and dedicated surface error characterisation are presented in this chapter in detail. Experimental studies are carried out to prove the effectiveness of the proposed characterisation and corrective machining methodology.

## 7.2 Corrective machining methodology

Corrective machining in the ultra-precision level requires not only the highly accurate dynamics axes but the determined measurement datum as well. A framework of corrective machining with the aid of OMSM is proposed, as illustrated in Figure 7.1. According to the surface design and specification, proper machining and OMSM parameters are firstly selected. Following the machining process, the sample surface can be directly measured on-machine without removing and remounting operations. Data from on-machine measurement, often represented as point clouds, is then compared with the design model. The overall surface error is obtained by subtracting the design surface from the measurement along Z direction. If the characterised surface error is larger than the pre-defined threshold, a corrective machining cycle is necessitated. As the coordinate datum for machining and measurement is preserved with the aid of OMSM, the derived surface error map can be directly used to generate a compensation tool path for corrective machining. The new tool path for corrective machining process is generated by superposing the processed surface error on the original tool path. If the new tool path meets the dynamics capacity of the machine tool, corrective machining process will be carried out. The proposed corrective machining is software-based, which is considered as an economical method for achieving higher surface accuracy rather than using a more accurate machine tool.

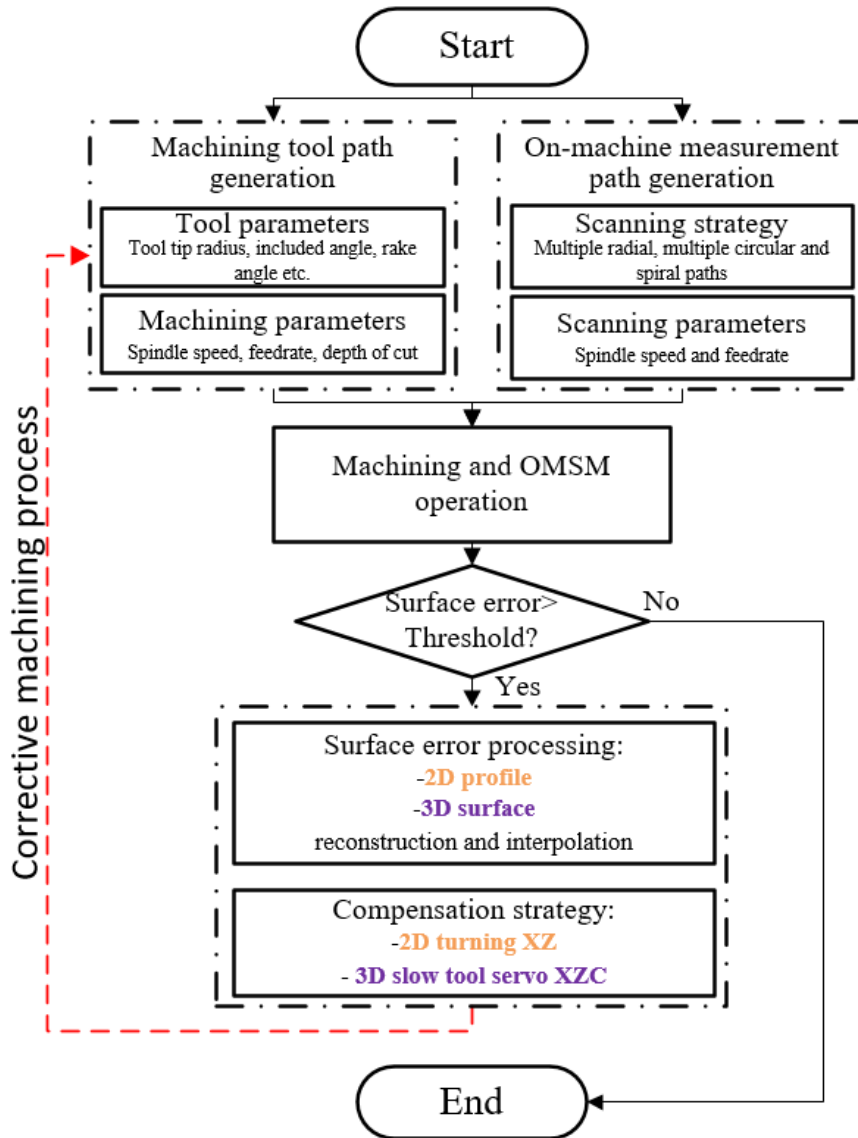


**Figure 7.1 Framework of corrective machining with the aid of OMSM**

As discussed in section 5.2.3, the selection of measurement path primarily depends on the measurement and corrective machining tasks. Multiple radial paths are suitable for measurement of rotationally symmetric features and employed for further profile correction under the conventional turning mode; continuous spiral scanning is considered as an efficient way to measure the overall form of freeform surface and employed for surface correction under the STS machining mode.

## 7.3 OMSM processing for corrective machining

In order to conduct the corrective machining, profile and surface error have to be derived from OMSM results and subsequently processed to generate the compensation tool path. Different scanning strategies are adopted according to measurement and correction tasks. Therefore, OMSM data processing methods are different for profile and surface corrective machining.

### 7.3.1 2D profile processing

OMSM data processing for profile correction is shown in Figure 7.2. Multiple radial paths are adopted to extract the height data from rotationally symmetric surfaces. The processed profile is compared with the design model or a mathematical function. If the characterised error is larger than the specification, the profile correction needs to be performed. In the conventional 2D turning process, the cutting tool path is often programmed from the sample border to the rotational centre. As the multiple radial scanning paths move across the sample diameter, averaging and symmetric folding of the profile data should be carried out. Before the corrective tool path is generated, low-pass filtration can be also performed on the profile error to accommodate to dynamic capability of machine tools. The detailed process will be described in the experiment section below.

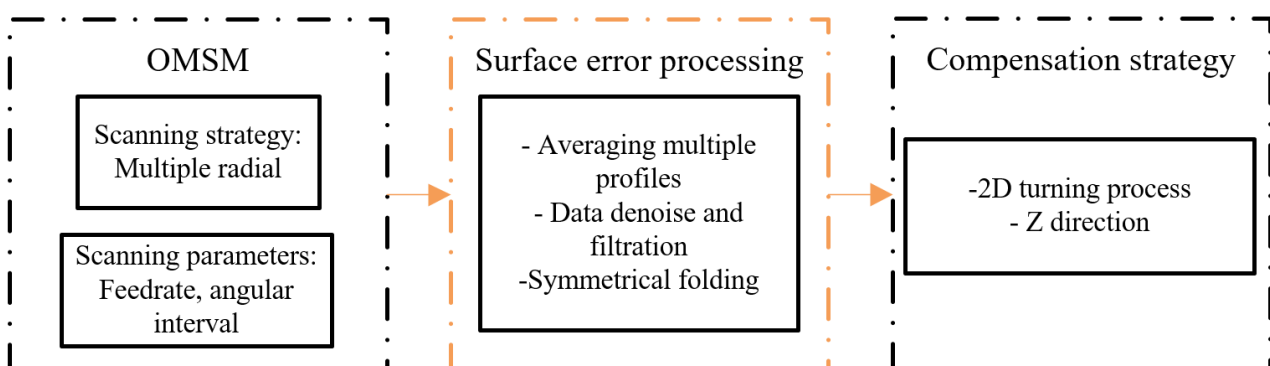


Figure 7.2 Data processing for profile corrective machining

### 7.3.2 Surface processing

For on-machine measurement of general freeform surfaces, spiral scanning is often applied. Surface processing of OMSM data is the core part of the surface corrective machining process, which is aimed at the surface error characterisation and compensating tool path generation. Error characterisation for continuous freeform surfaces has been widely investigated [114, 116, 196]. For on-machine metrology, the complex registration process can be avoided due to the coordinate consistency [20]. However, characterisation for structured freeform surfaces receives less attention, particularly for the purpose of corrective machining.

Structured surface error includes holistic surface error and individual feature error. The proposed OMSM surface data processing is illustrated in Figure 7.3. Holistic surface error characterisation is aimed at assessment of the machined freeform surface as a whole. This is useful for the investigation and correction of the machining errors. The holistic surface error is obtained by subtracting the design model from the OMSM results. As the coordinate datum for machining and measurement is preserved, the derived surface error map can be directly used to generate a compensating tool path.

Individual feature evaluation emphasizes the analysis of the surface quality of each element, such as form and dimensional accuracy. Individual feature quality often directly correlates with the designed functionality [197] and thus specified in the feature design stage. The characterised values of individual feature error determine if the corrective machining cycle is necessitated. To evaluate the individual feature, each individual element needs to be firstly segmented from the arrays. Geometric properties of the segmented elements are then characterised and compared with the specification. The statistics analysis can be additionally carried out to observe the uniformity of machined surface quality.

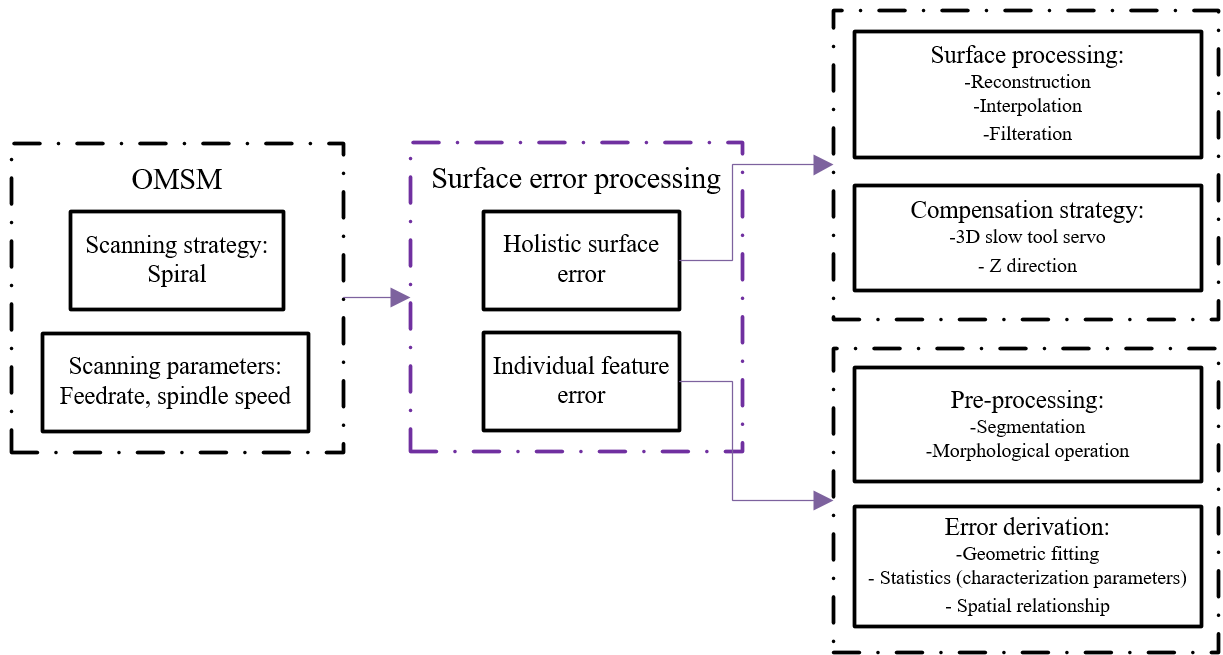


**Figure 7.3 Data processing for surface corrective machining**

MLA is a typical structured freeform surface with individual features arranged in a specific pattern. To demonstrate the proposed processing method, individual feature analysis of a MLA surface is carried out. A  $3 \times 3$  micro-lens array height map is simulated without surface error, as shown in Figure 7.4. The processing procedure is presented as follows and illustrated in Figure 7.5.

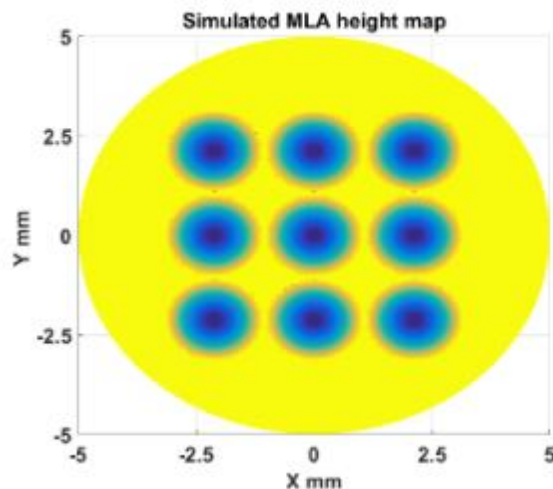


**Figure 7.4 Simulated MLA measurement map**

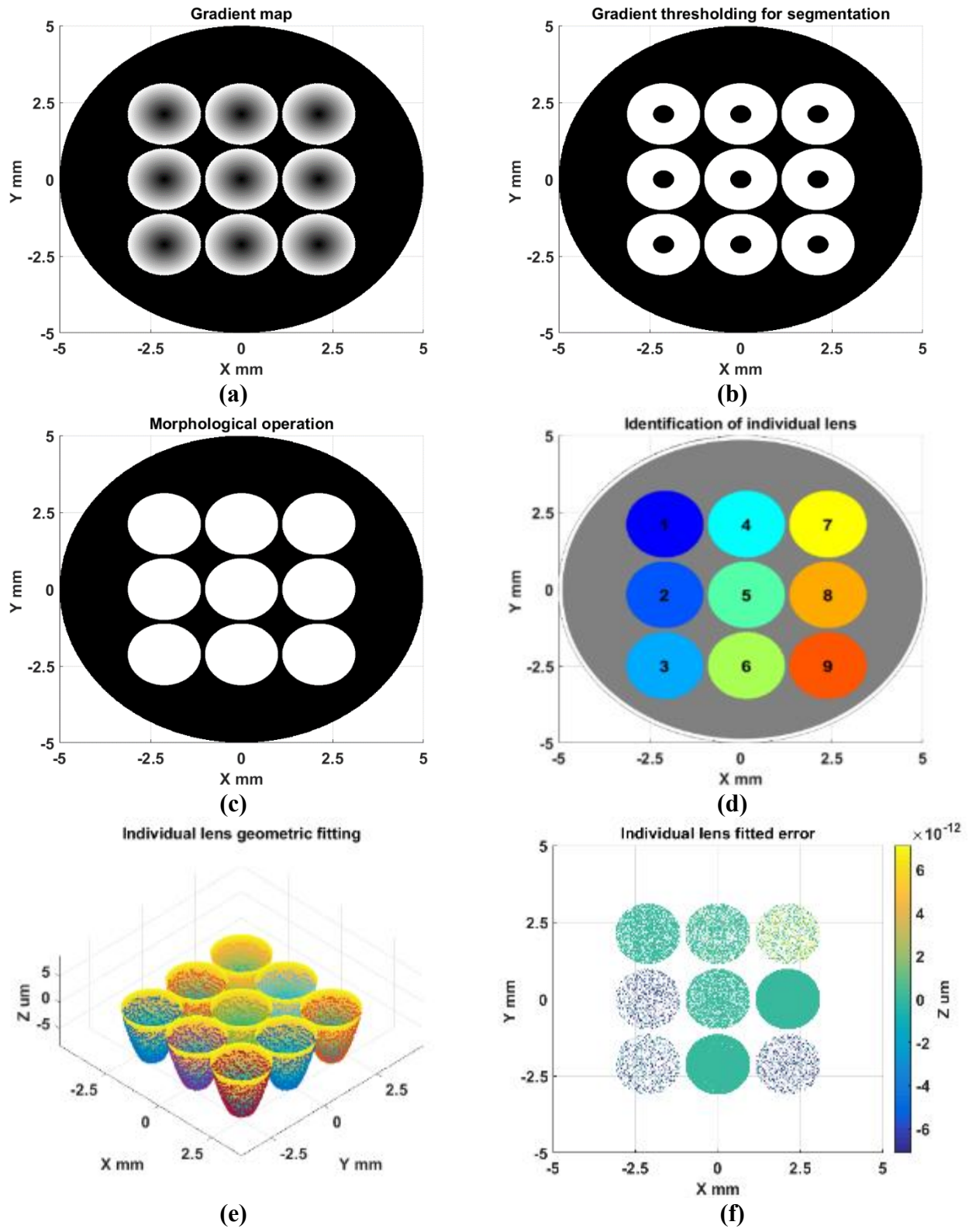


**Figure 7.5 Process of MLA individual feature analysis**

- Gradient map generation: The height map was transformed into a local gradient map by a Sobel operator [198] for subsequent segmentation. The Sobel operator employed two  $3 \times 3$  kernels and convolved with the height map to calculate approximations of

the derivatives in the horizontal and vertical direction. The gradient magnitude map was then generated by combination of the gradient approximations in the two directions. The resulting map is shown in Figure 7.5 (a). Individual lens regions, particularly close to the boundary, were identified with high gradient (white colour regions).

- Threshold segmentation: A thresholding operation on the derived gradient map was carried out to segment the MLA surface. Otsu's method [199] was applied to determine the global threshold value. The algorithm assumes that the histogram of the processed map is bimodal and the optimum threshold is calculated to separate the two classes to minimize the intra-class variance. Consequently, a binary classification map was obtained as shown in Figure 7.5 (b).
- Morphological operation: It is noted that due to low gradient, the middle area of each individual lens was wrongly segmented as the background class (black colour regions). In this step, a morphological operation, termed flood fill [200], was performed on the binary classification map to fill in the low gradient area of individual lens. The resulting binary map is illustrated as Figure 7.5 (c).
- Identification of individual lens: After segmentation of featured arrays from the background class, each individual lens object was identified by boundary tracing. Moore-Neighbour tracing algorithm modified by Jacob's stopping criteria [198] was implemented for each given object. It can be seen from Figure 7.5 (d) that the 9 individual lenses were successfully identified and labelled for later characterisation.
- Geometry fitting: The nominal shape of the simulated MLA is a sphere. Therefore, spherical fitting was conducted on each identified individual lens to determine the geometric properties. Least squares approach was adopted in the fitting process to minimize the sum of the squared distances from the measurement points to the

reference sphere. Figure 7.5 (e) shows the fitted results together with the individual lens surface data.

- Characterisation parameters: Feature attributes of each individual lens, such as form error, were derived as the deviation between the measured data and the nominal surface. As illustrated in Figure 7.5 (f), the residual error can be neglected due to the fact that the surface data of MLA was simulated without error. From another perspective, the resulting negligible error validates the accuracy of the processing algorithm and effectiveness of the MLA characterisation process.

With this processing method, surface corrective machining of a MLA surface will be investigated in the experimental section.

## 7.4 Experiments and discussions

To evaluate the proposed profile and surface corrective machining methodology, experimental work was carried out and the results were discussed in this section.

### 7.4.1 Profile corrective machining

As shown in Figure 5.23, the results from both DRI on-machine measurement and PGI offline measurement indicate the presence of certain amount of form error on the diamond turned cosine curve surface ( $(Z = A\cos(2\pi/\lambda X))$  with  $A = 5 \mu\text{m}$  and  $\lambda = 2.5 \text{ mm}$ ).

A profile error correction experiment of the cosine curve sample was performed. The machining parameters are listed in Table 7.1. Profile corrective machining is performed under the conventional  $X$ - $Z$  turning mode.

**Table 7.1 Machining parameters**

Parameters	Value
Spindle Speed (rpm)	1000
Feedrate (mm/min)	0.5
Cutting depth ( $\mu\text{m}$ )	5

According to the proposed corrective machining and data processing method above, the scanned multiple radial profiles were averaged and compared with the design model to derive the profile error. For corrective machining, symmetric folding operation was carried out on the derived error due to the characteristic of the 2D turning process. The symmetric folding result is shown in Figure 7.6. A new tool path for profile correction was subsequently generated by superposing the processed error on the original tool path. The workflow of profile corrective machining experiment is illustrated in Figure 7.7.

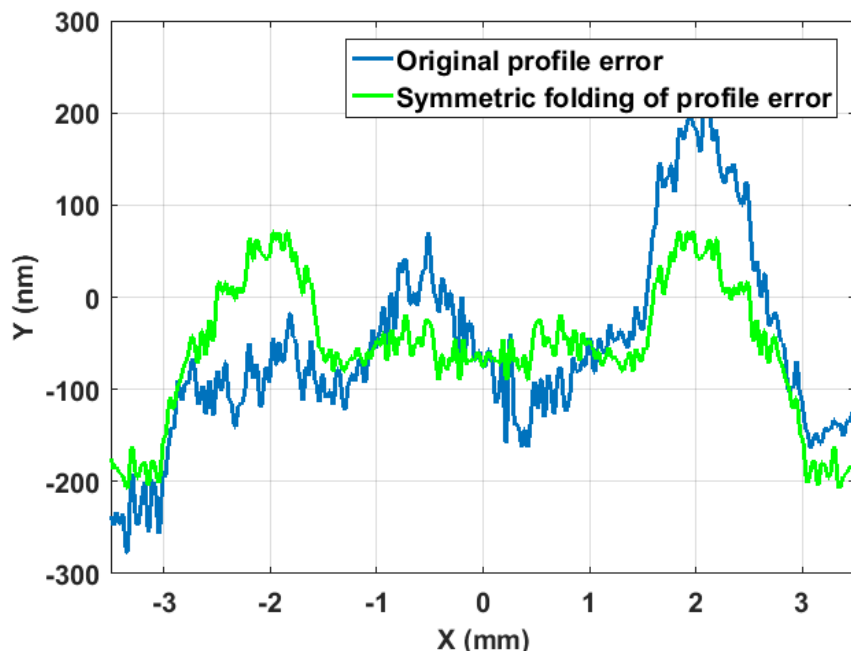


**Figure 7.6 Symmetric folding of profile error derived from OMSM**

The corrective machining was then executed and the sample was measured on-machine again. Profile errors before and after the correction process were compared, as illustrated in Figure 7.8.

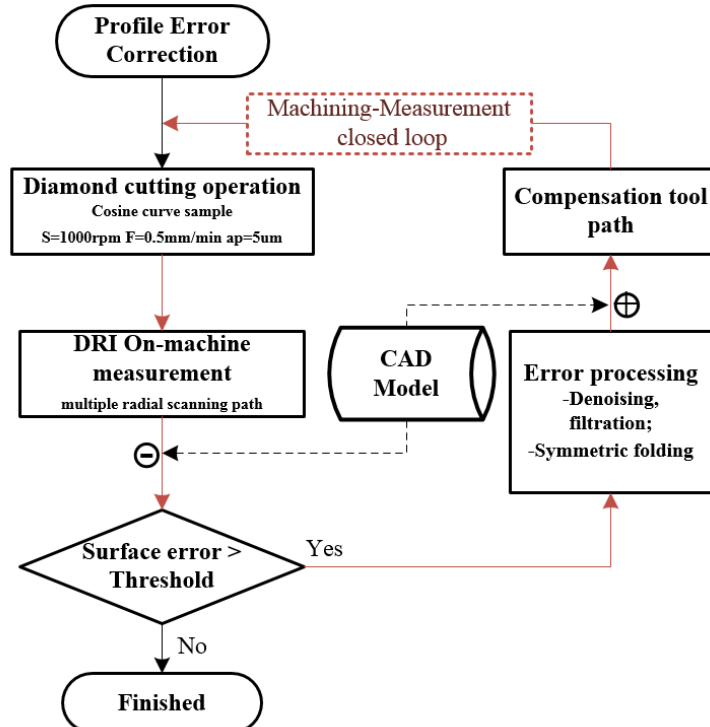


**Figure 7.7 Workflow of profile corrective machining experiment**

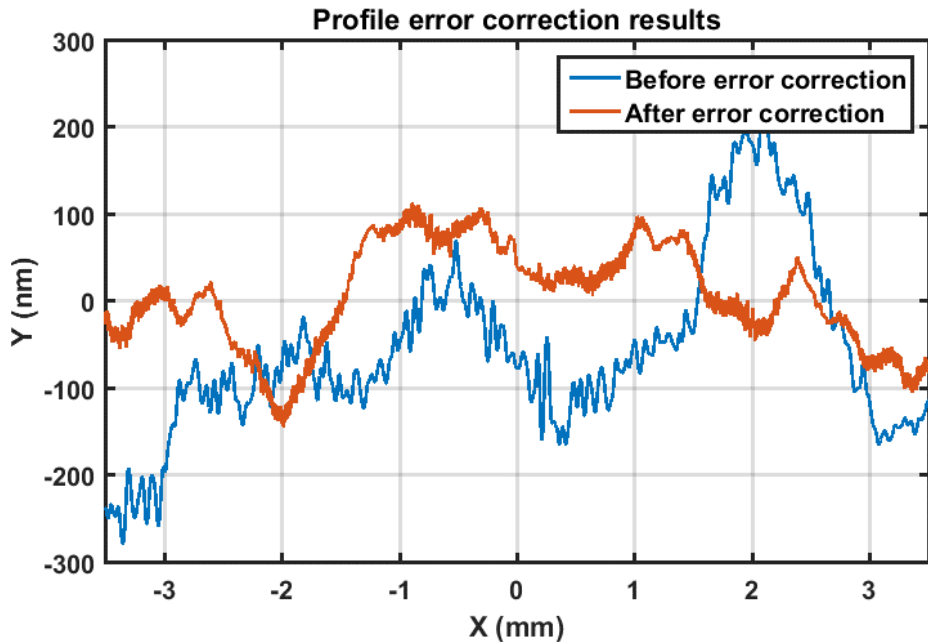


**Figure 7.8 Profile error correction results**

The characterisation results in Table 7.2 show that the profile accuracy was improved from 104.7 nm (RMS) and 495.2 nm (PV), to 58.6 nm (RMS) and 257.6 nm (PV). The profile correction experiment result has validated the effectiveness of proposed corrective machining to improve profile accuracy.

**Table 7.2 Profile error correction results**

Parameters	Before correction	After correction	Improvement
Error PV (nm)	495.2	257.6	47.9%
Error RMS (nm)	104.7	58.6	44.1%

#### 7.4.2 Surface corrective machining

STS machining enables the fabrication and corrective machining of non-rotationally symmetric surfaces by oscillating the cutting tool in and out relative to the workpiece surfaces with synchronization to the rotational axes and linear axes. Following the machining operation described in section 4.4, the machined surface was measured on-machine by DRI probe. According to the surface feature distribution and the machine tool configuration, corrective machining experiment was carried out on the MLA sample and a spiral scanning path was applied. The scanning parameters are listed in Table 7.3.

**Table 7.3 OMSM scanning parameters**

Parameters	Value
Scanning mode	Spiral path
Spindle speed (rpm)	6
Feedrate (mm/min)	2

As the spiral scanning resulted in a non-regular lattice of distributed sample points, the Delaunay triangulation-based method [201] was used for surface reconstruction in the work. Neighbourhood connections among the measurement data points are established with the Delaunay triangulation algorithm and all the non-neighbouring points in the Voronoi diagram of the given points are neglected, which avoids poorly shaped triangles. Compared with tensor product method, Delaunay triangulation-based methods have the advantages of computational efficiency and numerical stability [121]. The acquired point clouds and the corresponding reconstructed surface are respectively plotted in Figure 7.9 (a) and Figure 7.9 (b).

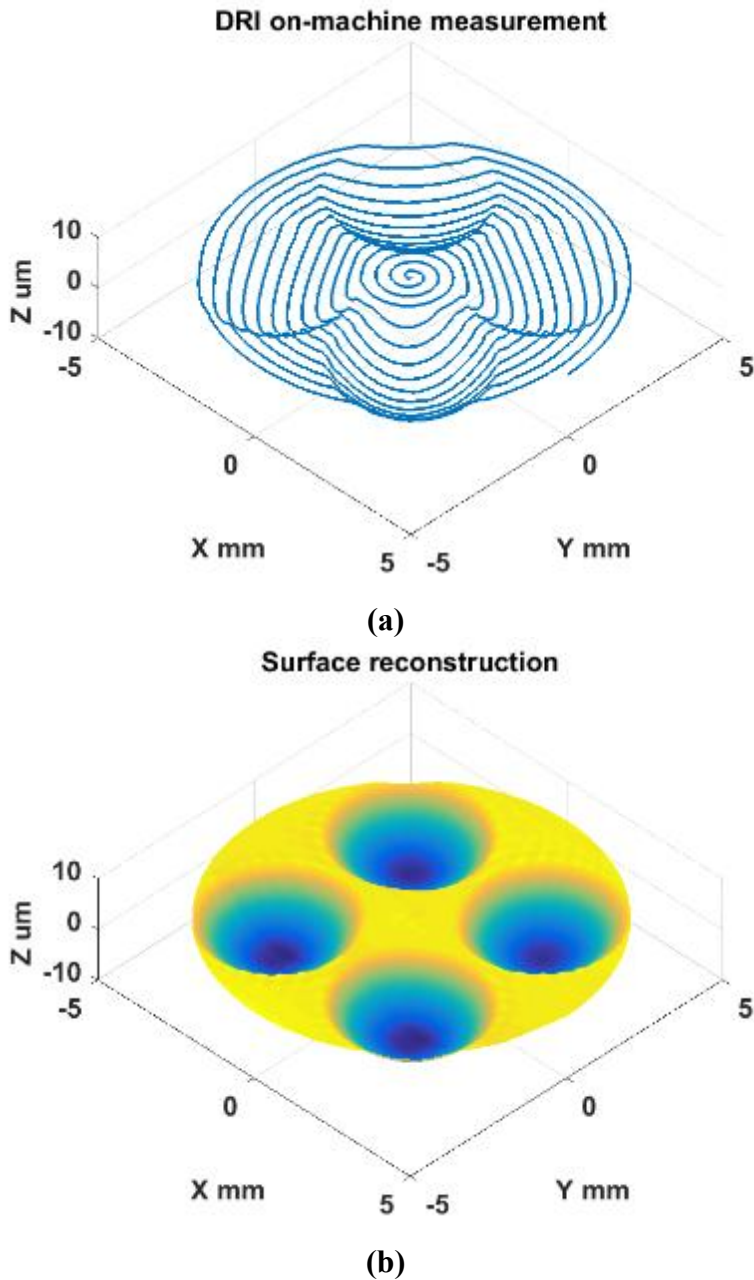


**Figure 7.9 (a) OMSM point clouds and (b) the corresponding reconstructed surface**

According to the discussion in section 7.3.2, MLA surface error consists of holistic surface error and individual feature error. As the consistency between the machining and measurement coordinate is preserved, the holistic surface error was obtained by directly subtracting the design model from the measurement data along the Z direction. As illustrated in Figure 7.10 and Figure 7.11 (a), the derived surface error represented a rotationally distorted four petals pattern, mainly resulting from the tool setting error [202, 203]. A new spiral tool path for corrective machining was accordingly generated by superposing the processed surface error onto the original tool path

(shown in Figure 7.10). Corrective machining was carried out under the STS machining mode. The same machining and tool parameters were used as in section 4.4.3.

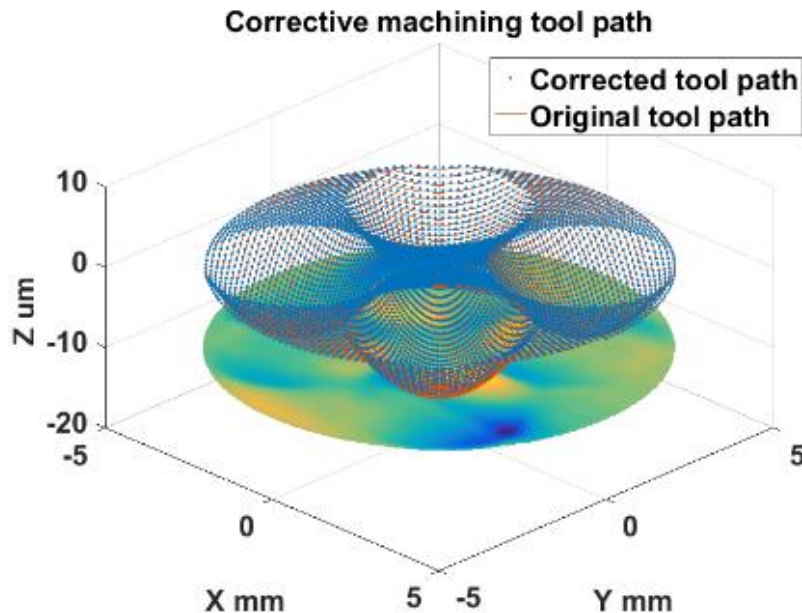


**Figure 7.10 Corrective machining tool path generation**

Another OMSM operation was performed afterwards. Derived surface error before and after the correction process was respectively plotted in Figure 7.11 (a) and Figure 7.11 (b). It can be seen that after the correction process, the error distribution was more axially symmetric, indicating that the error component resulting from tool setting has been corrected. The residual error pattern was considered to result from the hysteretic phenomenon of the tool servo [204].

In addition, individual lens error was analysed to evaluate the surface quality of each lens in the arrays. Following the analysis procedure discussed in section 7.3, individual lens was firstly segmented from each other. Due to the existence of measurement noise, opening and closing morphological operators [198] were additionally applied to remove small misclassified objects and clear the boundaries for individual lens identification. Spherical fitting was then conducted on each identified individual lens to determine their geometric properties. Form error was derived as the deviation between the measured data and the nominal surface. In this study, the form error was characterised as RMS and PV values.

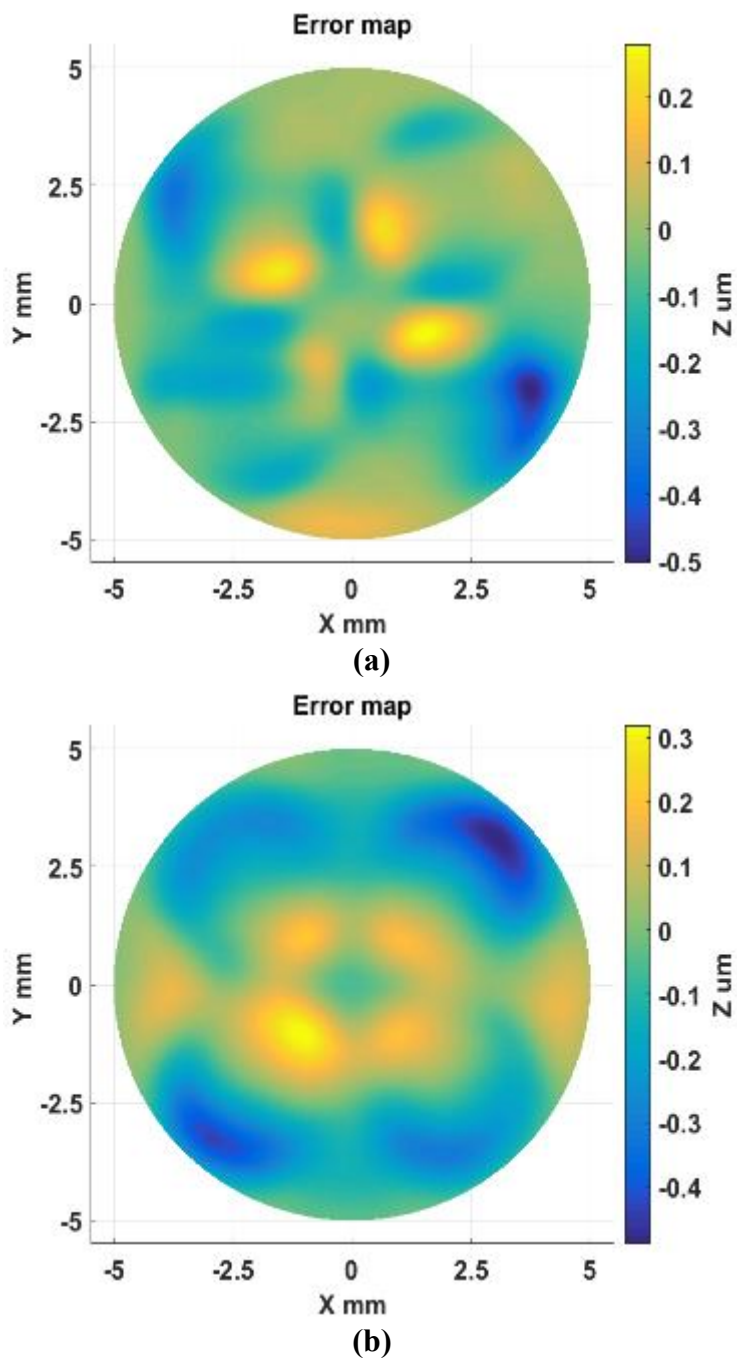
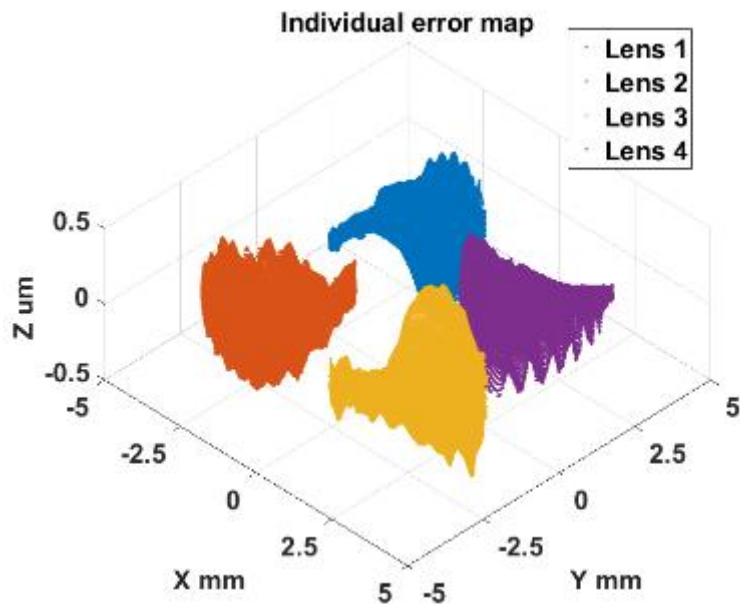
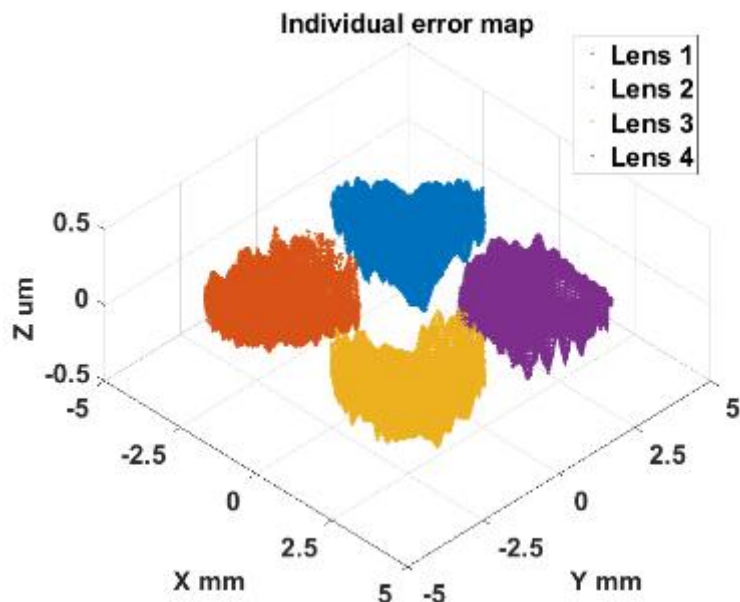


**Figure 7.11 Holistic error (a) before and (b) after corrective machining**

Individual lens error topography before and after the corrective machining was respectively shown in Figure 7.12 (a) and Figure 7.12 (b). It can be clearly seen that the amplitude of the derived form error was largely decreased for each individual lens and the error distribution was more uniform after the corrective machining.



(a)



(b)

**Figure 7.12 Individual error distribution (a) before and (b) after corrective machining**

The characterisation results were summarized in Table 7.4 and the corresponding bar graph was illustrated in Figure 7.13. After the correction process, the average form accuracy of individual lens has been increased from 113.7 nm (RMS) and 349.1 nm (PV), to 64.0 nm (RMS) and 205.4 nm (PV). The average improvement was respectively 40.4% for PV value and 42.8% for RMS value. The experiment result has validated the improvement of surface accuracy through surface corrective machining.

**Table 7.4 Individual surface error characterisation**

Characterisation parameters	Before correction	After correction	Average improvement
Individual lens (1,2,3,4) form error PV (nm)	341.1	174.3	40.4%
	301.7	239.5	
	435.7	237.6	
	317.8	170.3	
Individual lens (1,2,3,4) form error RMS (nm)	111.6	51.8	42.8%
	99.8	78.3	
	141.2	71.1	
	102.2	54.8	

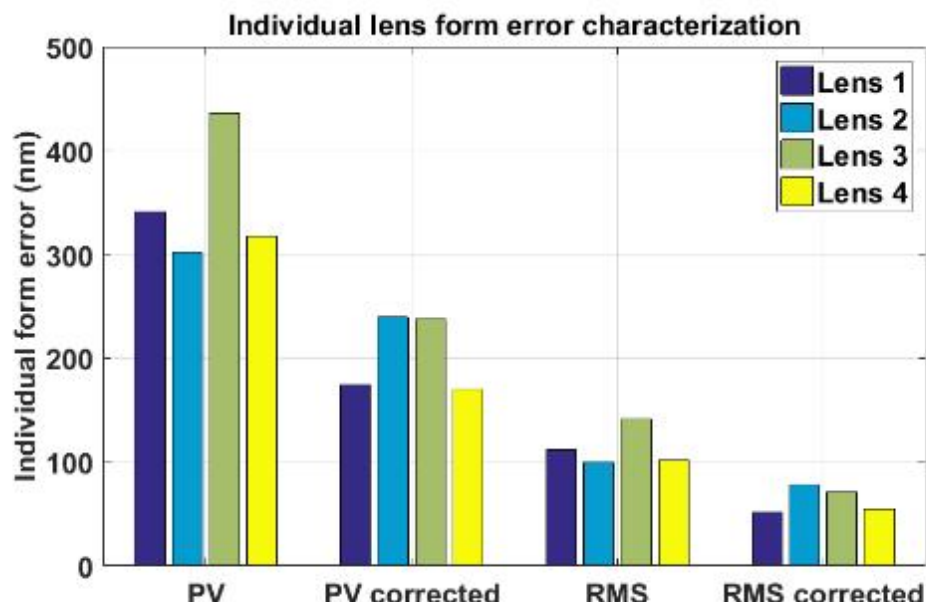


**Figure 7.13 Bar graph of MLA form error**

## 7.5 Summary

After the establishment of the metrology-integrated machining platform, this chapter investigated the corrective machining with the aid of OMSM to further improve the ultra-precision turning accuracy.

Different scanning strategies were adopted according to measurement and correction tasks. The corresponding data processing methods were discussed for profile and surface OMSM

respectively. Multiple radial paths scanning is suitable for measurement of rotationally symmetric features and the results were employed for further profile correction under the conventional turning mode. Because the cutting tool moves from the border to centre rather than across the diameter, averaging and symmetric folding need to be performed on the on-machine measured profile data to generate the compensating tool path. Continuous spiral scanning is considered as an efficient way to measure the overall shape of freeform surfaces. With the consistency between the machining and measurement coordinate, the holistic surface error is obtained by directly subtracting the design model from the OMSM data and used for surface correction under the STS machining mode. For structured type of freeform surfaces, individual feature error evaluation was applied to analyse the form accuracy of individual features specified in the design. To demonstrate the proposed processing method, individual feature analysis of a MLA surface was carried out.

The experiment results have validated the effectiveness of the proposed corrective machining methodology. The profile accuracy of a cosine curve sample was improved approximately 44.1%, from 495.2 nm (PV) and 104.7 nm (RMS), to 257.6 nm (PV) and 58.6 nm (RMS). In surface corrective machining experiment of a MLA surface, the distorted error component caused by tool setting was corrected. The residue error pattern was considered to result from the hysteretic phenomenon of the tool servo. The individual feature form accuracy of a MLA surface was improved by an average of 40.4% (PV) and 42.8% (RMS). As the consistency between the machining and measurement coordinate is preserved with OMSM, corrective machining can be carried out in a more deterministic manner.

## **8 Conclusions and Future work**

### **8.1 Overall conclusions**

High precision optical freeform surfaces, featured with high functional performance, are playing an increasingly important role in modern imaging and illumination systems. To ensure the functionality of the components, these freeform surfaces are required to have sub-micrometre form accuracy and nanometre surface topography. However, the geometrical complexity and high precision demand place considerable challenges on the existing machining and measurement technologies. For the future intelligent and autonomous manufacturing, a technical shift in the approach of metrology from offline lab-based solutions towards the use of metrology upon manufacturing platforms is needed. OMSM can avoid the errors caused by re-positioning workpieces and utilize the machine axes to extend the measuring range. The aim of the thesis is to improve the efficiency and accuracy of ultra-precision manufacturing of optical freeform surfaces with the integration of on-machine metrology. The research conclusions completed in the thesis are listed below.

- The theoretical and experimental investigation of surface generation in STS freeform machining processes

Ultra-precision STS machining, differing from the conventional SPDT process, is an enabling manufacturing technology for fabrication of freeform optics. To achieve the targeted surface quality, an approach for the tool path generation has been investigated, including tool path planning, tool geometries selection and tool radius compensation. The tool radius compensation is performed only in  $Z$  direction to ensure no high frequency motion is imposed on the non-dynamic  $X$  axis. The development of the surface generation simulation allows the prediction of the surface topography under various tool and machining parameters. It also provides an important means for better understanding surface generation mechanism (such as overcutting phenomenon) without the need for costly trial and error tests.

Machining experiments of a sinusoidal grid sample and MLA sample validated the proposed tool path generation and demonstrated the effectiveness of slow tool machining process to fabricate optical freeform surfaces with nanometric topography. The measurement results show uniform topography distribution over the entire surface and agree well with the simulated results. Such knowledge was acquired as a priori information, indicating that form deviation rather than surface topography should be the measurands for the subsequent OMSM.

- The development and systematic calibration of OMSM

The review of OMSM for ultra-precision machining applications reveals that single point interferometric method is preferred over other methods for its unbeatable measurement resolution and the ability of miniature fibre connection to relay surface information to remote interrogation apparatus. In this study, a robust single-point interferometric probe DRI was thus adopted on a 3-axis ultra-precision turning machine to establish a metrology-integrated manufacturing platform. The DRI probe was aligned coaxially to the spindle rotational axis, by means of multiple scanning of a convex sphere sample. The selection of OMSM scanning path primarily depends on the measurement tasks and surface feature distribution. Three scanning paths (multiple radial, multiple circular and spiral) were presented with corresponding applicable surfaces.

Since operating in the manufacturing environment, the effects of machine tools on the OMSM have been comprehensively evaluated and the systematic errors have been compensated. Three major error sources, including on-machine vibration, machine tool kinematic errors, and linearity errors were investigated. Vibration test results have shown machine static and motion vibration tend to induce additional error of measurement results. A theoretical study of the relationship between sampling frequency, scanning parameters, vibration frequency and topography frequencies of interest was presented. The proposed frequency decision graph was proposed to select the proper sampling frequency and scanning parameters. Machine tool

kinematic error was mapped for OMSM correction with the proposed kinematic error modelling measurement and compensation method. The optical flat measurement by DRI and offline Twyman–Green interferometer indicated that the kinematic error compensation effectively increased the OMSM accuracy. Calibration of the response curve and linearity error correction was conducted by measuring a radially distributed step height sample on the machine. The linearity error of DRI probe was reduced from 93 nm to 14 nm.

Additionally, the results obtained from DRI measurement agreed well with the results of offline measurement when measuring a standard precision sphere and a diamond turned cosine curve surface. In summary, a set of calibration and measurement experiments is considered to have proved the validity of the proposed calibration methodology and the effectiveness of the established OMSM system.

- The development and validation of a deterministic process investigation with the assistance of OMSM

With the aid of the established OMSM, this study investigated the effect of machining parameters on the surface form error in the ultra-precision cylindrical turning process. Due to the lack of alignment error between machining and measurement coordinates, OMSM is capable of giving more accurate feedback and improve the performance of the empirical process investigation. DRI measurement along Z axis was verified by means of correlation with the result of calibrated offline measurement.

The statistical relationship between the process parameters and the machined surface form error was established by means of response surface methodology (RSM). The reduced quadratic model obtained was verified by the test for significance of the regression model and goodness of fit. The linear and quadratic terms of the chosen process parameters (feedrate, spindle speed and depth of cut) are all of statistical significance and are included in the response surface model. For the process conditions considered, the ANOVA results indicate that spindle speed is the most

significant factor influencing machined surface form error, with 51.34% contribution to the total variability. The confirmation tests show the model predicted value conformed to the experimental value, with a difference less than 4%. The empirical response surface model allows prediction of machined surface form error with a 95% confident interval. Therefore, the approach presented can be regarded as an effective tool for modelling the ultra-precision turning processes.

- The investigation of profile/surface corrective machining with the assistance of OMSM

To further improve the ultra-precision machining accuracy, corrective machining strategy was investigated with the assistance of OMSM. As the consistency between the machining and measurement coordinate is preserved, OMSM enables corrective machining to be carried out in a more deterministic manner. Different scanning strategies are adopted according to measurement and correction tasks. Multiple radial paths are suitable for measurement of rotationally symmetric features and employed for further profile correction under the conventional turning mode. Continuous spiral scanning is applicable to measure non-rotationally symmetric freeform surfaces. Due to the datum consistency, the holistic surface error can be obtained by directly subtracting the design model from the OMSM data and used for surface correction under the STS machining mode. For structured type of freeform surfaces, individual feature error evaluation needs to be applied to analyse the geometrical accuracy of individual features.

The experimental results have validated the effectiveness of the proposed corrective machining methodology. After the correction process, the profile accuracy of a cosine curve sample was improved approximately 44%, from 495.2 nm (PV) and 104.7 nm (RMS), to 257.6 nm (PV) and 58.6 nm (RMS). In surface corrective machining experiment, the individual feature form accuracy of a MLA surface was improved by an average of 40.4% (RMS) and 42.8% (PV).

## 8.2 Future work

In this thesis, an interferometric OMSM system has been investigated and applied in ultra-precision machining process to further improve the manufacturing efficiency and accuracy.

However, still many factors need to be considered to establish a metrology-oriented ultra-precision manufacturing system. Some suggestions for further research are pointed out as follows:

- The surface generation simulation provides an important means for better understanding and improvement of the STS machining process. In the current work, the simulation is based on the geometrical interaction between the tool shape and machining surface. A more comprehensive model (including cutting forces, material properties) will contribute to further understanding the cutting mechanism as well as more accurate prediction of surface generation. Moreover, the knowledge acquired through the modelling of machining process provides valuable information to the subsequent measurement process which is potential to increase the inspection efficiency and intelligence.
- The selection of scanning paths primarily depends on the measurement tasks and surface feature distribution. In the study, three OMSM scanning strategy (multiple radial, multiple circular and spiral) were presented to meet the inspection demand for different types of surfaces. However, the uniform sampling strategy may lead to undesirable results, including over-sampling data points on low curvature regions of the surface, or under-sampling on strong features and high curvature regions. Adaptive and efficient sampling techniques are of promise in the further improvement of OMSM efficiency while ensuring the accuracy as well.
- A set of experiments in chapter 5 demonstrated the machine tools' effects on OMSM results and calibration methodology was proposed to compensate the systematic

errors. The presented calibration method is considered comprehensive but complex, particularly in the kinematic error compensation part. For ease of use in practice and promotion of OMSM, a simple and fast calibration process needs to be investigated in the future work. For example, it is preferred that three influential factors (on-machine vibration, machine tool kinematic errors, and linearity errors) are calibrated all together rather than separately. Furthermore, the proposed OMSM calibration is limited to the 3-axis turning machine configuration. A general calibration methodology needs to be developed for multi-axis machine tools with different configurations.

- The statistical model between the process parameters and the machined surface form error was established by means of empirical process investigation with the aid of OMSM. Due to the potentials to deal with the highly nonlinear, multidimensional, and ill-behaved complex engineering problems, artificial intelligence methods (such as fuzzy logic and neural network) and advanced optimization methods (such as Genetic Algorithm, Particle Swarm Optimization and Ant Colony Optimization) should be investigated to model and understand the ultra-precision machining processes. Artificial intelligence models take into consideration the particularities of the equipment used and the real machining phenomena. Artificial intelligence together with OMSM is considered as the key to achieving smart manufacturing of high precision freeform surfaces.
- Profile and surface corrective machining has successfully improved the accuracy of ultra-precision machined surfaces. As discussed in chapter 7, it is suggested that dynamics capability of the machine tools limits the ultimate achievable surface accuracy. A potential way to reduce the motion complexity of the dynamic axis is the decomposition of the measured surface error and only the selected component is used

to generate the compensating tool path. In addition, research work is suggested to study the relationship between the functional performance and geometrical accuracy, which provides an important means for the optimization of corrective machining processes.

## **Publications and Awards**

### **Refereed Journal Papers**

- Li, D., Tong, Z., Jiang, X., Blunt, L., & Gao, F. (2018). Calibration of an interferometric on-machine probing system on an ultra-precision turning machine. *Measurement*, 118, 96-104.
- Li, D., Jiang, X., Tong, Z., Blunt, L. (2018). Kinematics error compensation for a surface measurement probe on an ultra-precision turning machine. *Micromachines*, 9(7), 334;
- LI D, Jiang X, Tong Z, Blunt L. (2018). Development and application of interferometric on-machine surface measurement for ultra-precision turning process. ASME. *Journal of Manufacturing Science and Engineering*

### **Refereed Conference Papers**

- Li, D., Qiao, Z., Jiang, X., Tong, Z., Blunt, L. (2018) Application of interferometric probing on process investigation of diamond cylindrical turning. In: 14th China-Japan International Conference on Ultra-Precision Machining Process, CJUMP2018, Harbin, China
- Li, D., Tong, Z., Blunt, L., Jiang, X. (2018) 'Investigation of kinematics error influence on on-machine measurement for ultra-precision turning'. In: Euspen's 18th International Conference, 4th – 8th June 2018, Venice, Italy
- Li, D., Jiang, X., Blunt, L., Tong, Z. (2018). Intelligent investigation for ultra-precision turning with on-machine surface measurement and neural network. In: 6th International Conference on Nanomanufacturing, NANOMAN 2018, Brunel University, UK.
- Li, D., Jiang, X. (2018) Process investigation of diamond cylindrical turning with embedded measurement. In: Industrial Doctorate Centre Machining Conference, Advanced Manufacturing Research Centre (AMRC), Sheffield, UK
- Li, D., Blunt, L., Jiang, X. (2018) Calibration of an interferometric on-machine measurement on a diamond turning lathe. In: 14th National Academic Forum for Doctoral Researchers in Mechanical Engineering, Wuhu, China
- Li, D., Blunt, L., Tong, Z. and Jiang, X. (2017) Application of on-machine surface measurement in ultra-precision machining. In: Special Interest Group Meeting: Micro/Nano Manufacturing 8th – 9th November 2017, University of Strathclyde, UK
- Li, D., Jiang, X. (2017) A selective kinematics error model for on-machine measurement compensation. In: University of Huddersfield PGR Conference, 17 Nov 2017, University of Huddersfield.
- Li, D., Jiang, X., Blunt, L., Tong, Z., Williamson, J. and Young, C. (2017) 'Development of on-machine measurement for ultra-precision machining'. In: Euspen's 17th International Conference, 29 May - 2 June 2017, Hannover, Germany
- Mohamed, Z., Blunt, L., Young, C., Tong, Z. and Li, D. (2017) 'Development of precision polishing machine based on a hexapod'. In: Euspen's 17th International Conference, 29 May - 2 June 2017, Hannover, Germany
- Li, D., Ding, F., Jiang, X., Blunt, L. and Tong, Z. (2017) 'Calibration of an interferometric surface measurement system on an ultra-precision turning lathe'. In: Lamdamap 12th International Conference & Exhibition, 15-16th March 2017, Renishaw Innovation Centre, UK
- Li, D., Wang, B., Jiang, X. (2015). The design of inductively coupled plasma jet processing system for high power laser optics. In: Laser Metrology and Machine Performance XI, LAMDAMAP 2015. Huddersfield, UK (pp. 31-39). EUSPEN.

### **Book Chapter**

Jiang, X., Gao, F., Martin, H., Williamson, J., Li, D. (2017). On-machine metrology for hybrid machining. In: Xichun Luo, Yi Qin (eds). *Hybrid Machining: Theory, Methods, and Case Studies*. Elsevier, Amsterdam.

Jiang, X., Tong, Z., Li, D. (2018). On-machine measurement system and its application in ultra precision manufacturing. In: Shuming Yang, Zhuangde Jiang (eds). *Precision Manufacturing. Precision Machines*. Springer, Berlin.

### Awards

Li, D., HEIDENHAIN GmbH scholarship, Lamdamap 12th International Conference & Exhibition, Renishaw Innovation Centre, UK

## References

- [1] J.M. Rodgers, K.P. Thompson, Benefits of freeform mirror surfaces in optical design, in: Proceedings of the American Society of Precision Engineering 2004 Winter Topical Meeting on Freeform Optics, 2004, pp. 73-78.
- [2] F. Duerr, Y. Nie, H. Thienpont, Potential Benefits of Freeform Optics in On-Axis Imaging Applications, in: Imaging and Applied Optics 2015, Optical Society of America, Arlington, Virginia, 2015, pp. FW2B.2.
- [3] K.P. Thompson, J.P. Rolland, Freeform optical surfaces: a revolution in imaging optical design, *Optics and Photonics News*, 23 (2012) 30-35.
- [4] Z. Xin, Z. Ligong, H. Xin, Design and fabrication of imaging optical systems with freeform surfaces, in: SPIE, 2012, pp. 848607.
- [5] X. Jiang, P. Scott, D. Whitehouse, Freeform surface characterisation-a fresh strategy, *CIRP Annals-Manufacturing Technology*, 56 (2007) 553-556.
- [6] K. Fuse, T. Okada, K. Ebata, Diffractive/refractive hybrid F-theta lens for laser drilling of multilayer printed circuit boards, in: Proceedings of the SPIE, 2003, pp. 95-100.
- [7] D. Cheng, Y. Wang, H. Hua, M. Talha, Design of an optical see-through head-mounted display with a low f-number and large field of view using a freeform prism, *Applied optics*, 48 (2009) 2655-2668.
- [8] J. Wang, F. Santosa, A numerical method for progressive lens design, *Mathematical models and methods in applied sciences*, 14 (2004) 619-640.
- [9] O. Dross, R. Mohedano, M. Hernandez, A. Cvetkovic, P. Benitez, J.C. Miñano, Illumination optics: Köhler integration optics improve illumination homogeneity, *Laser Focus World*, 45 (2009) 135-150.
- [10] X.J. Jiang, D.J. Whitehouse, Technological shifts in surface metrology, *CIRP Annals-Manufacturing Technology*, 61 (2012) 815-836.
- [11] F.Z. Fang, X.D. Zhang, A. Weckenmann, G.X. Zhang, C. Evans, Manufacturing and measurement of freeform optics, *CIRP Annals - Manufacturing Technology*, 62 (2013) 823-846.
- [12] A. Yi, L. Li, Design and fabrication of a microlens array by use of a slow tool servo, *Optics letters*, 30 (2005) 1707-1709.
- [13] E. Brinksmeier, Y. Mutlugünes, F. Klocke, J. Aurich, P. Shore, H. Ohmori, Ultra-precision grinding, *CIRP Annals-Manufacturing Technology*, 59 (2010) 652-671.
- [14] F. Klocke, C. Brecher, E. Brinksmeier, B. Behrens, O. Dambon, O. Riemer, H. Schulte, R. Tuecks, D. Waechter, C. Wenzel, Deterministic Polishing of Smooth and Structured Molds, in: *Fabrication of Complex Optical Components*, Springer, 2013, pp. 99-117.
- [15] X. Jiang, Precision surface measurement, *Philosophical Transactions of the Royal Society of London A: Mathematical, Physical and Engineering Sciences*, 370 (2012) 4089-4114.
- [16] X. Jiang, P.J. Scott, D.J. Whitehouse, L. Blunt, Paradigm shifts in surface metrology. Part I. Historical philosophy, in: *Proceedings of the Royal Society of London A: Mathematical, Physical and Engineering Sciences*, The Royal Society, 2007, pp. 2049-2070.
- [17] X. Jiang, P.J. Scott, D.J. Whitehouse, L. Blunt, Paradigm shifts in surface metrology. Part II. The current shift, in: *Proceedings of the Royal Society of London A: Mathematical, Physical and Engineering Sciences*, The Royal Society, 2007, pp. 2071-2099.
- [18] D. Walker, A. Beaucamp, V. Doubrovski, C. Dunn, R. Evans, R. Freeman, J. Kelchner, G. McCavana, R. Mortonb, D. Riley, Automated optical fabrications: first results from the new Precessions 1.2 m CNC polishing machine, in: *Proc. SPIE*, 2006, pp. 627309.
- [19] M. Elrawemi, L. Blunt, H. Muhamedsalih, F. Gao, L. Fleming, Implementation of in process surface metrology for R2R flexible PV barrier films, *International Journal of Automation Technology*, 9 (2015) 312-321.

- [20] X. Zhang, Z. Zeng, X. Liu, F. Fang, Compensation strategy for machining optical freeform surfaces by the combined on-and off-machine measurement, *Optics Express*, 23 (2015) 24800-24810.
- [21] N. Clayor, D.M. Combs, O.M. Lechuga, J.J. Mader, J. Udayasankaran, An overview of freeform optics production, in: *Proceedings of the SPIE*, 2004.
- [22] D. Cheng, Y. Wang, H. Hua, Free form optical system design with differential equations, in: *Photonics Asia 2010*, International Society for Optics and Photonics, 2010, pp. 78490Q-78490Q-78498.
- [23] L. Dick, High Precision Freeform Polymer Optics, *Optik & Photonik*, 7 (2012) 33-37.
- [24] G.S. Wright, G.H. Rieke, L. Colina, E. van Dishoech, G. Goodson, T. Greene, P.-O. Lagage, A. Karnik, S.D. Lambros, D. Lemke, The JWST MIRI instrument concept, in: *SPIE*, 2004.
- [25] S. Sinzinger, J. Jahns, *Microoptics*, John Wiley & Sons, 2006.
- [26] W.T. Plummer, Free-form optical components in some early commercial products, in: *Proc. SPIE*, 2005, pp. 67-73.
- [27] D.R. Pope, Progressive addition lenses: history, design, wearer satisfaction and trends, in: *Vision Science and Its Applications*, Optical Society of America, 2000, pp. NW9.
- [28] H. Hoshi, N. Taniguchi, H. Morishima, T. Akiyama, S. Yamazaki, A. Okuyama, Off-axial HMD optical system consisting of aspherical surfaces without rotational symmetry, in: *Electronic Imaging: Science & Technology*, International Society for Optics and Photonics, 1996, pp. 234-242.
- [29] R. Wu, H. Li, Z. Zheng, X. Liu, Freeform lens arrays for off-axis illumination in an optical lithography system, *Applied optics*, 50 (2011) 725-732.
- [30] I. Moreno, C.-C. Sun, Modeling the radiation pattern of LEDs, *Opt. Express*, 16 (2008) 1808-1819.
- [31] L. Sun, S. Jin, S. Cen, Free-form microlens for illumination applications, *Applied optics*, 48 (2009) 5520-5527.
- [32] J.C. Miñano, P. Benítez, A. Santamaría, Free-form optics for illumination, *Optical review*, 16 (2009) 99-102.
- [33] D. Dornfeld, S. Min, Y. Takeuchi, Recent advances in mechanical micromachining, *CIRP Annals-Manufacturing Technology*, 55 (2006) 745-768.
- [34] O. Riemer, Advances in ultra precision manufacturing, *Proc. Jpn. Soc. Precis. Eng.* (2011).
- [35] C. Brecher, S. Lange, M. Merz, F. Niehaus, C. Wenzel, M. Winterschladen, M. Weck, NURBS based ultra-precision free-form machining, *CIRP Annals-Manufacturing Technology*, 55 (2006) 547-550.
- [36] W. Chiu, W. Lee, Development of ultra-precision machining technology, (1997).
- [37] C. Cheung, W. Lee, A theoretical and experimental investigation of surface roughness formation in ultra-precision diamond turning, *International Journal of Machine Tools and Manufacture*, 40 (2000) 979-1002.
- [38] C. Cheung, W. Lee, Characterisation of nanosurface generation in single-point diamond turning, *International Journal of Machine Tools and Manufacture*, 41 (2001) 851-875.
- [39] J.L. Allsop, A. Mateboer, P. Shore, Optimising efficiency in diamond turned Fresnel mould masters, in: *SPIE Eco-Photonics 2011: Sustainable Design, Manufacturing, and Engineering Workforce Education for a Green Future*, International Society for Optics and Photonics, 2011, pp. 806509.
- [40] Y. Tohme, Trends in ultra-precision machining of freeform optical surfaces, in: *Optical fabrication and testing*, Optical Society of America, 2008, pp. OThC6.
- [41] S. Scheiding, Y.Y. Allen, A. Gebhardt, L. Li, S. Risse, R. Eberhardt, A. Tünnermann, Freeform manufacturing of a microoptical lens array on a steep curved substrate by use of a voice coil fast tool servo, *Opt. Express*, 19 (2011) 23938-23951.

- [42] Y. Tohme, R. Murray, E. Allaire, Principles and applications of the slow slide servo, Moore Nanotechnology Systems White Paper, (2005).
- [43] H. Lu, D. Lee, J. Kim, S. Kim, Modeling and machining evaluation of microstructure fabrication by fast tool servo-based diamond machining, *Precision Engineering*, 38 (2014) 212-216.
- [44] M. Zhou, H. Zhang, S. Chen, Study on diamond cutting of nonrationally symmetric microstructured surfaces with fast tool servo, *Materials and Manufacturing Processes*, 25 (2010) 488-494.
- [45] S. Rakuff, J.F. Cuttino, Design and testing of a long-range, precision fast tool servo system for diamond turning, *Precision Engineering*, 33 (2009) 18-25.
- [46] Moore Nanotechnology and Systems, <http://www.nanotechsys.com/accessories/nanotech-250uplv2-factory-options/>, (2017).
- [47] M. Cheng, C. Cheung, W. Lee, S. To, L. Kong, Theoretical and experimental analysis of nano-surface generation in ultra-precision raster milling, *International Journal of Machine Tools and Manufacture*, 48 (2008) 1090-1102.
- [48] L. Kong, C. Cheung, Prediction of surface generation in ultra-precision raster milling of optical freeform surfaces using an integrated kinematics error model, *Advances in Engineering Software*, 45 (2012) 124-136.
- [49] S. Zhang, S. To, A theoretical and experimental study of surface generation under spindle vibration in ultra-precision raster milling, *International Journal of Machine Tools and Manufacture*, 75 (2013) 36-45.
- [50] G. Zhang, S. To, G. Xiao, Novel tool wear monitoring method in ultra-precision raster milling using cutting chips, *Precision Engineering*, 38 (2014) 555-560.
- [51] M. Chen, Q. Zhao, S. Dong, D. Li, The critical conditions of brittle–ductile transition and the factors influencing the surface quality of brittle materials in ultra-precision grinding, *Journal of materials processing technology*, 168 (2005) 75-82.
- [52] Y.E. Tohme, Grinding aspheric and freeform micro-optical molds, in: Proc. SPIE, 2007, pp. 64620K.
- [53] H. Ohmori, T. Nakagawa, Analysis of mirror surface generation of hard and brittle materials by ELID (electronic in-process dressing) grinding with superfine grain metallic bond wheels, *CIRP Annals-Manufacturing Technology*, 44 (1995) 287-290.
- [54] H. Lim, K. Fathima, A.S. Kumar, M. Rahman, A fundamental study on the mechanism of electrolytic in-process dressing (ELID) grinding, *International Journal of Machine Tools and Manufacture*, 42 (2002) 935-943.
- [55] S. Yin, H. Ohmori, Y. Dai, Y. Uehara, F. Chen, H. Tang, ELID grinding characteristics of glass-ceramic materials, *International Journal of Machine Tools and Manufacture*, 49 (2009) 333-338.
- [56] D. Stephenson, X. Sun, C. Zervos, A study on ELID ultra precision grinding of optical glass with acoustic emission, *International Journal of Machine Tools and Manufacture*, 46 (2006) 1053-1063.
- [57] D.D. Walker, R. Freeman, G. McCavana, R. Morton, D. Riley, J. Simms, D. Brooks, E. Kim, A. King, The Zeeko/UCL process for polishing large lenses and prisms, in: Proc. SPIE, 2002, pp. 106-111.
- [58] H. Fang, P. Guo, J. Yu, Surface roughness and material removal in fluid jet polishing, *Applied optics*, 45 (2006) 4012-4019.
- [59] A. Beaucamp, Y. Namba, R. Freeman, Dynamic multiphase modeling and optimization of fluid jet polishing process, *CIRP Annals-Manufacturing Technology*, 61 (2012) 315-318.
- [60] P. Dumas, D. Golini, M. Tricard, Improve figure and finish of diamond turned surfaces with magneto-rheological finishing (MRF), in: Proc. of SPIE Vol, 2005, pp. 297.

- [61] S. Jha, V. Jain, Design and development of the magnetorheological abrasive flow finishing (MRAFF) process, *International Journal of Machine Tools and Manufacture*, 44 (2004) 1019-1029.
- [62] C. Cheung, L. Ho, P. Charlton, L. Kong, S. To, W. Lee, Analysis of surface generation in the ultraprecision polishing of freeform surfaces, *Proceedings of the Institution of Mechanical Engineers, Part B: Journal of Engineering Manufacture*, 224 (2010) 59-73.
- [63] D. Walker, A. Beaucamp, V. Doubrovski, C. Dunn, R. Freeman, G. McCavana, R. Morton, D. Riley, J. Simms, X. Wei, New results extending the Precessions process to smoothing ground aspheres and producing freeform parts, in: *Proc. SPIE*, 2005, pp. 58690E.
- [64] D.D. Walker, D. Brooks, R. Freeman, A. King, G. McCavana, R. Morton, D. Riley, J. Simms, The first aspheric form and texture results from a production machine embodying the precession process, in: *Proc. SPIE*, 2001, pp. 267-276.
- [65] S. Zeng, L. Blunt, Experimental investigation and analytical modelling of the effects of process parameters on material removal rate for bonnet polishing of cobalt chrome alloy, *Precision Engineering*, 38 (2014) 348-355.
- [66] F. Shiou, C. Cheng, Ultra-precision surface finish of NAK80 mould tool steel using sequential ball burnishing and ball polishing processes, *Journal of materials processing technology*, 201 (2008) 554-559.
- [67] E. Brinksmeier, L. Schönenmann, Generation of discontinuous microstructures by diamond micro chiseling, *CIRP Annals-Manufacturing Technology*, 63 (2014) 49-52.
- [68] D. Huo, K. Cheng, F. Wardle, Design of a five-axis ultra-precision micro-milling machine—UltraMill. Part 1: holistic design approach, design considerations and specifications, *The International Journal of Advanced Manufacturing Technology*, 47 (2010) 867-877.
- [69] D. Brehl, T. Dow, Review of vibration-assisted machining, *Precision engineering*, 32 (2008) 153-172.
- [70] G. Chen, Y. Liang, Y. Sun, W. Chen, B. Wang, Volumetric error modeling and sensitivity analysis for designing a five-axis ultra-precision machine tool, *The International Journal of Advanced Manufacturing Technology*, 68 (2013) 2525-2534.
- [71] W. Gao, M. Tano, T. Araki, S. Kiyono, C.H. Park, Measurement and compensation of error motions of a diamond turning machine, *Precision Engineering*, 31 (2007) 310-316.
- [72] W. Lee, C. Cheung, W. Chiu, T. Leung, An investigation of residual form error compensation in the ultra-precision machining of aspheric surfaces, *Journal of Materials Processing Technology*, 99 (2000) 129-134.
- [73] T. Moriwaki, Thermal deformation and its on-line compensation of hydrostatically supported precision spindle, *CIRP Annals-Manufacturing Technology*, 37 (1988) 393-396.
- [74] E. Savio, L. De Chiffre, R. Schmitt, Metrology of freeform shaped parts, *CIRP Annals-Manufacturing Technology*, 56 (2007) 810-835.
- [75] R. Leach, The measurement of surface texture using stylus instruments, National Physical Laboratory, 2001.
- [76] I.K. Buehring, D. Mansfield, Probe measurement apparatus using a curved grating displacement interferometer, in, Google Patents, 1996.
- [77] X. Jiang, Theory and method for measurement of curved surface topography, in, PhD dissertation, Huazhong University of Science and Technology, Wuhan, China, 1995.
- [78] Taylor Hobson, PGI series Profilometer, <http://www.taylor-hobson.com/products/surfaceprofilers.html>, (2017).
- [79] A. Weckenmann, T. Estler, G. Peggs, D. McMurtry, Probing systems in dimensional metrology, *CIRP Annals-Manufacturing Technology*, 53 (2004) 657-684.
- [80] G. Peggs, A. Lewis, S. Oldfield, Design for a compact high-accuracy CMM, *CIRP Annals-Manufacturing Technology*, 48 (1999) 417-420.

- [81] IBS, IBS Isara ULTRA PRECISION COORDINATE MEASURING MACHINE, <http://www.ibspe.com/category/isara-400-3d-cmm.htm>, (2017).
- [82] F. Meli, A. Kueng, R. Thalmann, Ultra precision micro-CMM using a low force 3 D touch probe, in: Proc. SPIE, 2005, pp. 265-272.
- [83] I. Widdershoven, R. Donker, H. Spaan, Realization and calibration of the "Isara 400" ultra-precision CMM, in: Journal of Physics: Conference Series, IOP Publishing, 2011, pp. 012002.
- [84] R. Hocken, N. Chakraborty, C. Brown, Optical metrology of surfaces, CIRP Annals-Manufacturing Technology, 54 (2005) 169-183.
- [85] D. Malacara, Optical shop testing, John Wiley & Sons, 2007.
- [86] P. de Groot, Phase shifting interferometry, Optical Measurement of Surface Topography, 8 (2011) 167-186.
- [87] T. Kim, J.H. Burge, Y. Lee, S. Kim, Null test for a highly paraboloidal mirror, Applied optics, 43 (2004) 3614-3618.
- [88] S. Reichelt, C. Pruss, H.J. Tiziani, Absolute interferometric test of aspheres by use of twin computer-generated holograms, Applied optics, 42 (2003) 4468-4479.
- [89] P. Zhou, J.H. Burge, Fabrication error analysis and experimental demonstration for computer-generated holograms, Applied optics, 46 (2007) 657-663.
- [90] J. Petter, G. Berger, Non-contact profiling for high precision fast asphere topology measurement, in: Proc. SPIE, 2013, pp. 878819.
- [91] J.C. Wyant, White light interferometry, in: Proc. SPIE, 2002, pp. 98-107.
- [92] F. Gao, R.K. Leach, J. Petzing, J.M. Coupland, Surface measurement errors using commercial scanning white light interferometers, Measurement Science and Technology, 19 (2007) 015303.
- [93] X. Jiang, K. Wang, F. Gao, H. Muhamedsalih, Fast surface measurement using wavelength scanning interferometry with compensation of environmental noise, Applied optics, 49 (2010) 2903-2909.
- [94] J. Williamson, H. Martin, X. Jiang, High resolution position measurement from dispersed reference interferometry using template matching, Optics express, 24 (2016) 10103-10114.
- [95] D. Tang, F. Gao, X. Jiang, On-line surface inspection using cylindrical lens-based spectral domain low-coherence interferometry, Applied optics, 53 (2014) 5510-5516.
- [96] R. Leach, L. Brown, X. Jiang, R. Blunt, M. Conroy, D. Mauger, Guide to the measurement of smooth surface topography using coherence scanning interferometry, Measurement good practice guide, 108 (2008) 17.
- [97] P.J. De Groot, Vibration in phase-shifting interferometry, JOSA A, 12 (1995) 354-365.
- [98] C. Faber, E. Olesch, R. Krobot, G. Häusler, Deflectometry challenges interferometry: the competition gets tougher!, in: Proc. SPIE, 2012, pp. 84930R.
- [99] M.C. Knauer, J. Kaminski, G. Hausler, Phase measuring deflectometry: a new approach to measure specular free- form surfaces, in: Proceedings of SPIE, 2004, pp. 366-376.
- [100] Y. Tang, X. Su, Y. Liu, H. Jing, 3D shape measurement of the aspheric mirror by advanced phase measuring deflectometry, Optics express, 16 (2008) 15090-15096.
- [101] H. Ren, F. Gao, X. Jiang, Least-squares method for data reconstruction from gradient data in deflectometry, Applied optics, 55 (2016) 6052-6059.
- [102] H. Ren, F. Gao, X. Jiang, Iterative optimization calibration method for stereo deflectometry, Optics express, 23 (2015) 22060-22068.
- [103] M.C. Knauer, J. Kaminski, G. Hausler, Phase measuring deflectometry: a new approach to measure specular free-form surfaces, in: Photonics Europe, International Society for Optics and Photonics, 2004, pp. 366-376.
- [104] Z. Sárosi, Detection of surface defects on sheet metal parts by using one-shot deflectometry in the infrared range, (2010).

- [105] P. Su, M. Khreishi, R. Huang, T. Su, J.H. Burge, Precision aspheric optics testing with SCOTS: a deflectometry approach, in: Proc. SPIE, 2013, pp. 87881E.
- [106] G. Häusler, C. Faber, E. Olesch, S. Ettl, Deflectometry vs. interferometry, in: Proc. of SPIE, 2013, pp. 13-16.
- [107] F. Chen, G.M. Brown, M. Song, Overview of three-dimensional shape measurement using optical methods, *Optical Engineering*, 39 (2000) 10-22.
- [108] L. Blunt, X. Jiang, Advanced techniques for assessment surface topography: development of a basis for 3D surface texture standards" surfstand", Elsevier, 2003.
- [109] H. Muhamedsalih, Investigation of Wavelength Scanning Interferometry for Embedded Metrology, in, University of Huddersfield, 2013.
- [110] R. Leach, Characterisation of areal surface texture, Springer, 2013.
- [111] S. Zeng, Bonnet Polishing of Cobalt Chrome Alloys for Artificial Implants, in, University of Huddersfield, 2014.
- [112] ISO25178-2, Geometrical Product Specification (GPS) - Surface Texture: Areal - Part 2: Terms, Definitions, and Surface Texture Parameters, (2012).
- [113] ISO10110-7, Optics and photonics -- Preparation of drawings for optical elements and systems -- Part 7: Surface imperfections, (2017).
- [114] X. Jiang, X. Zhang, P.J. Scott, Template matching of freeform surfaces based on orthogonal distance fitting for precision metrology, *Measurement Science and Technology*, 21 (2010) 045101.
- [115] X. Zhang, X. Jiang, P.J. Scott, A new free-form surface fitting method for precision coordinate metrology, *Wear*, 266 (2009) 543-547.
- [116] M.J. Ren, C.F. Cheung, L.B. Kong, X. Jiang, Invariant-feature-pattern-based form characterization for the measurement of ultraprecision freeform surfaces, *IEEE Transactions on Instrumentation and Measurement*, 61 (2012) 963-973.
- [117] D. Yu, X. Zhong, Y. Wong, G. Hong, W. Lu, H. Cheng, An automatic form error evaluation method for characterizing micro-structured surfaces, *Measurement Science and Technology*, 22 (2010) 015105.
- [118] P.J. Besl, N.D. McKay, A method for registration of 3-D shapes, *IEEE Transactions on pattern analysis and machine intelligence*, 14 (1992) 239-256.
- [119] A.W. Fitzgibbon, Robust registration of 2D and 3D point sets, *Image and Vision Computing*, 21 (2003) 1145-1153.
- [120] Y. Li, P. Gu, Free-form surface inspection techniques state of the art review, *Computer-Aided Design*, 36 (2004) 1395-1417.
- [121] J. Wang, R.K. Leach, X. Jiang, Review of the mathematical foundations of data fusion techniques in surface metrology, *Surface Topography: Metrology and Properties*, 3 (2015) 023001.
- [122] P. Shore, P. Parr-Burman, Manufacture of large mirrors for ELTs: a fresh perspective, in: *Optical Systems Design*, International Society for Optics and Photonics, 2004, pp. 55-62.
- [123] H.N. Hansen, K. Carneiro, H. Haitjema, L. De Chiffre, Dimensional micro and nano metrology, *CIRP Annals-Manufacturing Technology*, 55 (2006) 721-743.
- [124] K. Vacharanukul, S. Mekid, In-process dimensional inspection sensors, *Measurement*, 38 (2005) 204-218.
- [125] E. Novak, Advanced defect and metrology solutions, in: *SPIE Sensing Technology+ Applications*, International Society for Optics and Photonics, 2014, pp. 91100G-91100G-91108.
- [126] J.-H. Jung, J.-P. Choi, S.-J. Lee, Machining accuracy enhancement by compensating for volumetric errors of a machine tool and on-machine measurement, *Journal of Materials Processing Technology*, 174 (2006) 56-66.

- [127] M.-W. Cho, T.-I. Seo, Inspection planning strategy for the on-machine measurement process based on CAD/CAM/CAI integration, *The International Journal of Advanced Manufacturing Technology*, 19 (2002) 607-617.
- [128] Y. Arai, W. Gao, H. Shimizu, S. Kiyono, T. Kuriyagawa, On-Machine Measurement of Aspherical Surface Profile [J], *Nanotehnology and Precision Engineering*, 3 (2004) 008.
- [129] B. Li, F. Li, H. Liu, H. Cai, X. Mao, F. Peng, A measurement strategy and an error-compensation model for the on-machine laser measurement of large-scale free-form surfaces, *Measurement Science and Technology*, 25 (2013) 015204.
- [130] X.-Q. Li, Z. Wang, L.-H. Fu, A Fast and in-Situ Measuring Method Using Laser Triangulation Sensors for the Parameters of the Connecting Rod, *Sensors*, 16 (2016) 1679.
- [131] F. Da, S. Gai, Flexible three-dimensional measurement technique based on a digital light processing projector, *Applied optics*, 47 (2008) 377-385.
- [132] T. Ha, Y. Takaya, T. Miyoshi, S. Ishizuka, T. Suzuki, High-precision on-machine 3D shape measurement using hypersurface calibration method, in: *Machine Vision and its Optomechatronic Applications*, International Society for Optics and Photonics, 2004, pp. 40-51.
- [133] H. Suzuki, T. Onishi, T. Moriwaki, M. Fukuta, J. Sugawara, Development of a 45° tilted on-machine measuring system for small optical parts, *CIRP Annals-Manufacturing Technology*, 57 (2008) 411-414.
- [134] F. Chen, S. Yin, H. Huang, H. Ohmori, Y. Wang, Y. Fan, Y. Zhu, Profile error compensation in ultra-precision grinding of aspheric surfaces with on-machine measurement, *International Journal of Machine Tools and Manufacture*, 50 (2010) 480-486.
- [135] Moore Nanotechnology and Systems, <http://www.nanotechsys.com/accessories/nanotech-250uplv2-additional-accessories/>, (2017).
- [136] W. Gao, J. Aoki, B.-F. Ju, S. Kiyono, Surface profile measurement of a sinusoidal grid using an atomic force microscope on a diamond turning machine, *Precision Engineering*, 31 (2007) 304-309.
- [137] B.-F. Ju, Y.-L. Chen, Y. Ge, The art of electrochemical etching for preparing tungsten probes with controllable tip profile and characteristic parameters, *Review of Scientific Instruments*, 82 (2011) 013707.
- [138] W.-L. Zhu, S. Yang, B.-F. Ju, J. Jiang, A. Sun, Scanning tunneling microscopy-based on-machine measurement for diamond fly cutting of micro-structured surfaces, *Precision Engineering*, 43 (2016) 308-314.
- [139] W.-L. Zhu, S. Yang, B.-F. Ju, J. Jiang, A. Sun, On-machine measurement of a slow slide servo diamond-machined 3D microstructure with a curved substrate, *Measurement Science and Technology*, 26 (2015) 075003.
- [140] Y.J. Noh, Y. Arai, W. Gao, Improvement of a fast tool control unit for cutting force measurement in diamond turning of micro-lens array, *International Journal of Surface Science and Engineering*, 3 (2009) 227-241.
- [141] K. Lee, Y. Noh, Y. Arai, Y. Shimizu, W. Gao, Precision measurement of micro-lens profile by using a force-controlled diamond cutting tool on an ultra-precision lathe, *International Journal of Precision Technology*, 2 (2011) 211-225.
- [142] Y.-L. Chen, S. Wang, Y. Shimizu, S. Ito, W. Gao, B.-F. Ju, An in-process measurement method for repair of defective microstructures by using a fast tool servo with a force sensor, *Precision Engineering*, 39 (2015) 134-142.
- [143] Y.-L. Chen, W. Gao, B.-F. Ju, Y. Shimizu, S. Ito, A measurement method of cutting tool position for relay fabrication of microstructured surface, *Measurement Science and Technology*, 25 (2014) 064018.
- [144] F.J. Chen, S.H. Yin, H. Huang, H. Ohmori, Y. Wang, Y.F. Fan, Y.J. Zhu, Profile error compensation in ultra-precision grinding of aspheric surfaces with on-machine measurement, *International Journal of Machine Tools and Manufacture*, 50 (2010) 480-486.

- [145] T. Nomura, K. Kamiya, H. Miyashiro, S. Okuda, H. Tashiro, K. Yoshikawa, Shape measurements of mirror surfaces with a lateral-shearing interferometer during machine running, *Precision Engineering*, 22 (1998) 185-189.
- [146] P. Shore, P. Morantz, D. Lee, P. McKeown, Manufacturing and measurement of the MIRI spectrometer optics for the James Webb space telescope, *CIRP Annals-Manufacturing Technology*, 55 (2006) 543-546.
- [147] J.C. Wyant, Dynamic interferometry, *Optics and photonics news*, 14 (2003) 36-41.
- [148] C.W. King, Integrated On-Machine Metrology Systems, in: International Symposium on Ultraprecision Engineering and Nanotechnology (ISUPEN), Japan Society for Precision Engineering Semestrial Meeting 2010 JSPE Autumn Conference, 2010.
- [149] X. Jiang, In situ real-time measurement for micro-structured surfaces, *CIRP Annals-Manufacturing Technology*, 60 (2011) 563-566.
- [150] C. Röttinger, C. Faber, E. Olesch, G. Häusler, M. Kurz, E. Uhlmann, Deflectometry for Ultra Precision Machining—Measuring without Rechucking, in: Proc. DGaO, 2011, pp. P28.
- [151] X. Zou, X. Zhao, G. Li, Z. Li, T. Sun, Non-contact on-machine measurement using a chromatic confocal probe for an ultra-precision turning machine, *The International Journal of Advanced Manufacturing Technology*, (2016) 1-10.
- [152] W. Gao, M. Tano, S. Sato, S. Kiyono, On-machine measurement of a cylindrical surface with sinusoidal micro-structures by an optical slope sensor, *Precision Engineering*, 30 (2006) 274-279.
- [153] D. Li, C.F. Cheung, M. Ren, D. Whitehouse, X. Zhao, Disparity pattern-based autostereoscopic 3D metrology system for in situ measurement of microstructured surfaces, *Optics letters*, 40 (2015) 5271-5274.
- [154] Z. Yin, Y. Dai, S. Li, C. Guan, G. Tie, Fabrication of off-axis aspheric surfaces using a slow tool servo, *International Journal of Machine Tools and Manufacture*, 51 (2011) 404-410.
- [155] L. Kong, C. Cheung, S. To, B. Wang, L. Ho, A theoretical and experimental investigation of design and slow tool servo machining of freeform progressive addition lenses (PALs) for optometric applications, *The International Journal of Advanced Manufacturing Technology*, 72 (2014) 33-40.
- [156] L. Li, Y.Y. Allen, C. Huang, D.A. Grewell, A. Benatar, Y. Chen, Fabrication of diffractive optics by use of slow tool servo diamond turning process, *Optical Engineering*, 45 (2006) 113401-113401-113409.
- [157] S. Agarwal, P.V. Rao, A probabilistic approach to predict surface roughness in ceramic grinding, *International Journal of Machine Tools and Manufacture*, 45 (2005) 609-616.
- [158] L. Kong, C. Cheung, T. Kwok, Theoretical and experimental analysis of the effect of error motions on surface generation in fast tool servo machining, *Precision Engineering*, 38 (2014) 428-438.
- [159] P. Venkataraman, Applied optimization with MATLAB programming, John Wiley & Sons, 2009.
- [160] Precitech, Nanoform 250 ultra grinding machine, [http://www.precitech.com/products/nanoform250ultragrind/nanoform\\_250\\_ultragrind.html](http://www.precitech.com/products/nanoform250ultragrind/nanoform_250_ultragrind.html), (2017).
- [161] W. Gao, S. Dejima, Y. Shimizu, S. Kiyono, H. Yoshikawa, Precision measurement of two-axis positions and tilt motions using a surface encoder, *CIRP Annals-Manufacturing Technology*, 52 (2003) 435-438.
- [162] Taylor Hobson, CCI Non-contact 3D Optical Profilers, <http://www.taylor-hobson.com/products/non-contact-3d-optical-profilers.html>, (2017).
- [163] S.-I. Chang, J.-B. Yoon, H. Kim, J.-J. Kim, B.-K. Lee, D.H. Shin, Microlens array diffuser for a light-emitting diode backlight system, *Optics letters*, 31 (2006) 3016-3018.

- [164] R. Ramesh, M. Mannan, A. Poo, Error compensation in machine tools—a review: part I: geometric, cutting-force induced and fixture-dependent errors, *International Journal of Machine Tools and Manufacture*, 40 (2000) 1235-1256.
- [165] H. Schwenke, W. Knapp, H. Haitjema, A. Weckenmann, R. Schmitt, F. Delbressine, Geometric error measurement and compensation of machines—an update, *CIRP Annals-Manufacturing Technology*, 57 (2008) 660-675.
- [166] R. Leach, C. Giusca, H. Haitjema, C. Evans, X. Jiang, Calibration and verification of areal surface texture measuring instruments, *CIRP Annals-Manufacturing Technology*, 64 (2015) 797-813.
- [167] P.J. de Groot, Progress in the specification of optical instruments for the measurement of surface form and texture, in: SPIE Sensing Technology+ Applications, International Society for Optics and Photonics, 2014, pp. 91100M-91100M-91112.
- [168] Y. Quinsat, C. Tournier, In situ non-contact measurements of surface roughness, *Precision Engineering*, 36 (2012) 97-103.
- [169] H. Martin, X. Jiang, Dispersed reference interferometry, *CIRP Annals-Manufacturing Technology*, 62 (2013) 551-554.
- [170] J. Williamson, Dispersed reference interferometry for on-machine metrology, in, University of Huddersfield, 2016.
- [171] R. Wilhelm, R. Hocken, H. Schwenke, Task specific uncertainty in coordinate measurement, *CIRP Annals-Manufacturing Technology*, 50 (2001) 553-563.
- [172] S. Haykin, B. Van Veen, *Signals and systems*, John Wiley & Sons, 2007.
- [173] R.K. Leach, C.L. Giusca, P. Rubert, A single set of material measures for the calibration of areal surface topography measuring instruments: the NPL Areal Bento Box, *Proc. Met. & Props*, (2013) 406-413.
- [174] A. Okafor, Y.M. Ertekin, Derivation of machine tool error models and error compensation procedure for three axes vertical machining center using rigid body kinematics, *International Journal of Machine Tools and Manufacture*, 40 (2000) 1199-1213.
- [175] C. Raksiri, M. Parnichkun, Geometric and force errors compensation in a 3-axis CNC milling machine, *International Journal of Machine Tools and Manufacture*, 44 (2004) 1283-1291.
- [176] ISO230-1, Test code for machine tools Part 1: Geometric accuracy of machines operating under no-load or quasi-static conditions, (2012).
- [177] C.J. Evans, R.J. Hocken, W.T. Estler, Self-Calibration: Reversal, Redundancy, Error Separation, and ‘Absolute Testing’, *CIRP Annals - Manufacturing Technology*, 45 (1996) 617-634.
- [178] C.L. Giusca, R.K. Leach, F. Helery, Calibration of the scales of areal surface topography measuring instruments: part 2. Amplification, linearity and squareness, *Measurement Science and Technology*, 23 (2012) 065005.
- [179] ISO5436-1, Geometrical product specifications (GPS)—surface texture: profile method; measurement standards—part 1. Material measures (2000).
- [180] W.L. Martinez, A.R. Martinez, Computational statistics handbook with MATLAB, CRC press, 2007.
- [181] E. Brinksmeier, R. Gläbe, L. Schönemann, Review on diamond-machining processes for the generation of functional surface structures, *CIRP Journal of Manufacturing Science and Technology*, 5 (2012) 1-7.
- [182] J.A. Ghani, I. Choudhury, H. Hassan, Application of Taguchi method in the optimization of end milling parameters, *Journal of materials processing technology*, 145 (2004) 84-92.
- [183] N. Alagumurthi, K. Palaniradja, V. Soundararajan, Optimization of grinding process through design of experiment (DOE)—A comparative study, *Materials and Manufacturing Processes*, 21 (2006) 19-21.

- [184] R.Q. Sardinas, M.R. Santana, E.A. Brindis, Genetic algorithm-based multi-objective optimization of cutting parameters in turning processes, *Engineering Applications of Artificial Intelligence*, 19 (2006) 127-133.
- [185] N. Tosun, Determination of optimum parameters for multi-performance characteristics in drilling by using grey relational analysis, *The International Journal of Advanced Manufacturing Technology*, 28 (2006) 450-455.
- [186] M. Nalbant, H. Gökkaya, G. Sur, Application of Taguchi method in the optimization of cutting parameters for surface roughness in turning, *Materials & design*, 28 (2007) 1379-1385.
- [187] A.N. Haq, P. Marimuthu, R. Jeyapaul, Multi response optimization of machining parameters of drilling Al/SiC metal matrix composite using grey relational analysis in the Taguchi method, *The International Journal of Advanced Manufacturing Technology*, 37 (2008) 250-255.
- [188] J.-S. Kwak, S.-B. Sim, Y.-D. Jeong, An analysis of grinding power and surface roughness in external cylindrical grinding of hardened SCM440 steel using the response surface method, *International Journal of Machine Tools and Manufacture*, 46 (2006) 304-312.
- [189] D.C. Montgomery, *Design and analysis of experiments*, John Wiley & Sons, 2008.
- [190] C. Cheung, W. Lee, Modelling and simulation of surface topography in ultra-precision diamond turning, *Proceedings of the Institution of Mechanical Engineers, Part B: Journal of Engineering Manufacture*, 214 (2000) 463-480.
- [191] W. Grzesik, A revised model for predicting surface roughness in turning, *Wear*, 194 (1996) 143-148.
- [192] I. Minitab, MINITAB release 17: statistical software for windows, Minitab Inc, USA, (2014).
- [193] M.S. Rahman, T. Saleh, H. Lim, S. Son, M. Rahman, Development of an on-machine profile measurement system in ELID grinding for machining aspheric surface with software compensation, *International Journal of Machine Tools and Manufacture*, 48 (2008) 887-895.
- [194] D.P. Yu, G.S. Hong, Y. San Wong, Profile error compensation in fast tool servo diamond turning of micro-structured surfaces, *International Journal of Machine Tools and Manufacture*, 52 (2012) 13-23.
- [195] H.-S. Kim, K.-I. Lee, K.-M. Lee, Y.-B. Bang, Fabrication of free-form surfaces using a long-stroke fast tool servo and corrective figuring with on-machine measurement, *International Journal of Machine Tools and Manufacture*, 49 (2009) 991-997.
- [196] G. Forbes, Characterizing the shape of freeform optics, *Opt. Express*, 20 (2012) 2483-2499.
- [197] S. Reichelt, A. Bieber, B. Aatz, H. Zappe, Micro-optics metrology using advanced interferometry, in: Proc. SPIE, 2005, pp. 437-446.
- [198] R.C.E. Gonzalez, S.L. Woods, R.E.R.E.R.C. Gonzalez, R.E. Woods, S.L. Eddins, *Digital image processing using MATLAB*, 2004.
- [199] N. Otsu, A threshold selection method from gray-level histograms, *IEEE transactions on systems, man, and cybernetics*, 9 (1979) 62-66.
- [200] P. Soille, *Morphological image analysis: principles and applications*, Springer Science & Business Media, 2013.
- [201] F. Cazals, J. Giesen, Delaunay triangulation based surface reconstruction, *Effective computational geometry for curves and surfaces*, (2006) 231-276.
- [202] Y.-f. Dai, C. Guan, Z.-q. Yin, G.-p. Tie, H.-f. Chen, J.-m. Wang, Tool decentration effect in slow tool servo diamond turning off-axis conic aspheric surface, in: 5th International Symposium on Advanced Optical Manufacturing and Testing Technologies, International Society for Optics and Photonics, 2010, pp. 76550P-76550P-76556.

- [203] X. Liu, X. Zhang, F. Fang, Z. Zeng, H. Gao, X. Hu, Influence of machining errors on form errors of microlens arrays in ultra-precision turning, International Journal of Machine Tools and Manufacture, 96 (2015) 80-93.
- [204] L. Kong, C. Cheung, Modeling and characterization of surface generation in fast tool servo machining of microlens arrays, Computers & Industrial Engineering, 63 (2012) 957-970.
- [205] Y. Qin, A. Brockett, Y. Ma, A. Razali, J. Zhao, C. Harrison, W. Pan, X. Dai, D. Loziak, Micro-manufacturing: research, technology outcomes and development issues, The International Journal of Advanced Manufacturing Technology, 47 (2010) 821-837.
- [206] D. Huo, K. Cheng, F. Wardle, Design of a five-axis ultra-precision micro-milling machine—UltraMill. Part 2: integrated dynamic modelling, design optimisation and analysis, The International Journal of Advanced Manufacturing Technology, 47 (2010) 879-890.
- [207] X. Luo, K. Cheng, D. Webb, F. Wardle, Design of ultraprecision machine tools with applications to manufacture of miniature and micro components, Journal of Materials Processing Technology, 167 (2005) 515-528.
- [208] R. Grejda, E. Marsh, R. Vallance, Techniques for calibrating spindles with nanometer error motion, Precision engineering, 29 (2005) 113-123.
- [209] D. Chen, J. Fan, F. Zhang, Dynamic and static characteristics of a hydrostatic spindle for machine tools, Journal of Manufacturing Systems, 31 (2012) 26-33.
- [210] Z.-q. Yin, S.-y. Li, High accuracy error separation technique for on-machine measuring straightness, Precision engineering, 30 (2006) 192-200.
- [211] Lion Precision, Capacitive Sensor Operation and Optimization, <http://www.lionprecision.com/tech-library/technotes/cap-0020-sensor-theory.html>, (2017).
- [212] Lion Precision, High-Performance Capacitive Sensor, <http://www.lionprecision.com/capacitive-sensors/cap-products.html>, (2017).
- [213] Measurement Computing, Data acquisition (DAQ) USB-1608HS Series, <https://www.mccdaq.com/usb-data-acquisition/USB-1608HS-Series.aspx>, (2017).
- [214] E.R. Marsh, Precision spindle metrology, DEStech Publications, Inc, 2010.

## **Appendix A Machine tool kinematic error measurement**

### **A.1 Introduction**

Kinematic errors are fundamental errors, which exist in machine tools due to imperfect machine parts, misalignment between axes and configuration of structural loop [165]. Kinematic errors have a variety of components, including linear displacement error, straightness and flatness of movement of the axis, spindle inclination angle, squareness error, etc. Ultra-precision machine tools are often equipped with high precision linear hydrostatic guideways and air-bearing spindles. The motion errors of the linear and rotational axes often lie in the sub-micrometre, even in the nanometre range [205-207].

Without the influence of the inherent surface form error on the artefact, error separation techniques have been widely adopted for precision measurement of error motions on the ultra-precision machine tools [208-210]. Among them, the reversal method is considered simple and accurate for measurement of part features without reference to an externally calibrated artefact [177]. This appendix proposes a simple scheme for machine tool kinematic error measurement in nanometric level, with capacitance probes and a flat mirror artefact.

When two conductive surfaces are near each other, there is an electrical property called capacitance that exists between them. The amount of capacitance depends on the distance and material between the two conductors, as shown in Figure A.1. A capacitive sensor uses an electric field to measure changes of capacitance between the probe surface and a conductive target surface. The sensing principle is illustrated in Figure A.2. The advantage of such type probe is the high vertical resolution in relative wide bandwidth compared with other displacement probes.

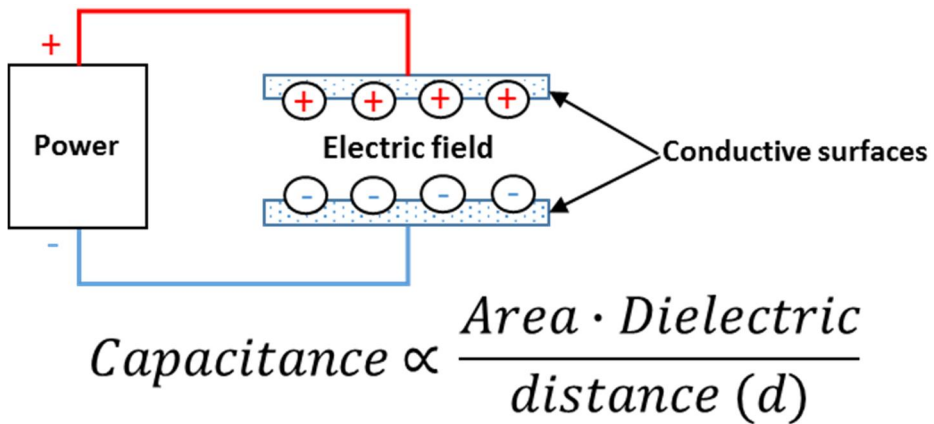


**Figure A.1 Schematic of capacitive theory [211]**

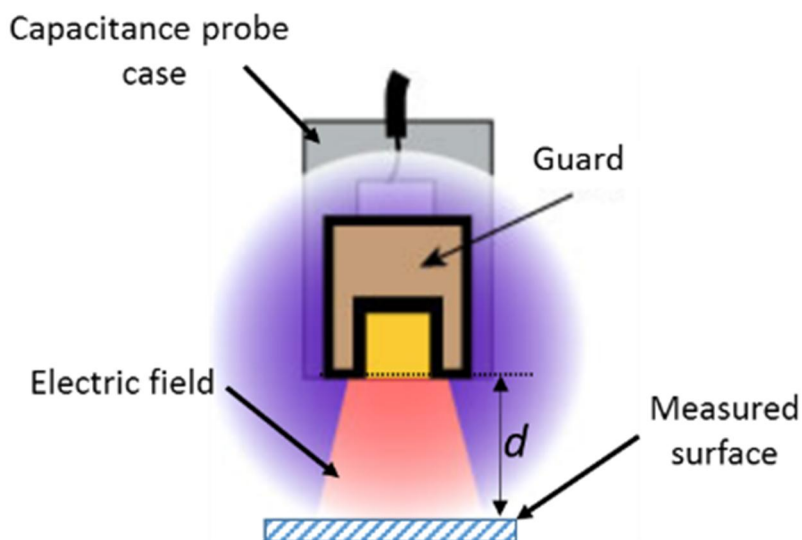


**Figure A.2 Schematic of capacitance probe working principle [211]**

The capacitance probes used in this experiment are provided by Lion Precision [212]. The probe model is C8 and its sensor driver is CL190. The maximum sampling frequency of used can be up to 1 kHz and the displacement measurement resolution is 0.08 nm. Furthermore, the 2 mm spot size also automatically filters out short wavelength errors on the target surface so that the artefact surface finish will not affect the measurement. The output of the sensor is analog voltage. Therefore, a data acquisition board (DAQ device) is additionally used. Its primary function is to digitize incoming analog signals so that a computer can interpret them. The DAQ device used in this work is USB-1608HS, provided by Measurement Computing with 16-bit resolution and 250

k/s acquisition speed per channel [213]. The photo of capacitance probes and DAQ card is shown in Figure A.3.



**Figure A.3 Photo of the capacitance probing system and DAQ card**

In the following part, the measurement principle and process will be respectively described for  $X$  axis straightness in the  $Z$  direction  $E_{ZX}$ ,  $C$  axis axial error  $E_{ZC}$ ,  $C$  axis tilt error  $E_{BC}$ , and squareness error between  $X$  axis and  $C$  axis  $E_{BOC}$ .

## A.2 $X$ axis straightness error

The schematic diagram and experimental setup of  $E_{ZX}$  measurement using the reversal method are respectively shown in Figure A.4 and Figure A.5. A metal flat mirror was mounted on the  $Z$  axis stage and kept stationary. The capacitance probe was carried on the  $X$  slide and scanned over the mirror. Subsequently, the mirror was rotated 180° using a manual rotational stage and the mirror was scanned again after the reversal operation.

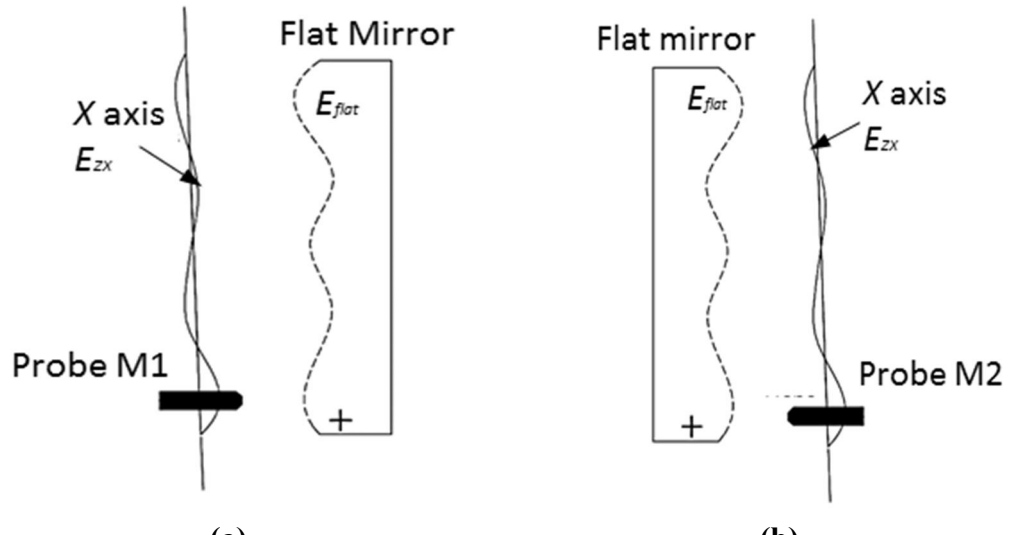


**Figure A.4 Schematic diagram of  $E_{ZX}$  measurement before (a) and after (b) reversal operation**

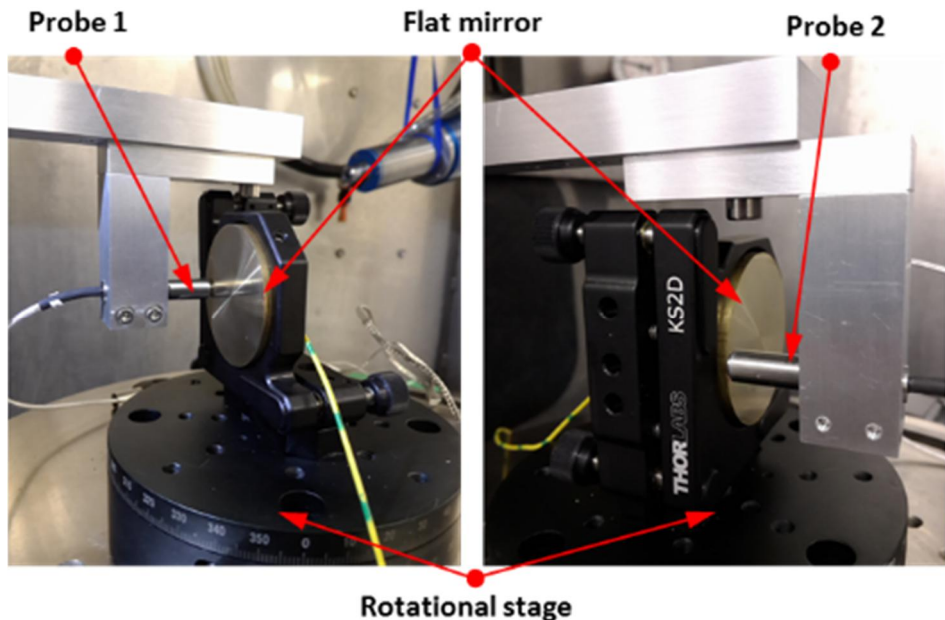


**Figure A.5 Experimental setup of  $E_{ZX}$  measurement using reversal method**

The two measurements are respectively denoted as  $M_1$  and  $M_2$ . According to the reversal principle, the straightness error  $E_{ZX}$  can be separated from the surface error of flat mirror  $E_{flat}$  and calculated as the following:

$$\begin{cases} M_1 = E_{flat} - E_{ZX} \\ M_2 = E_{flat} + E_{ZX} \end{cases} \quad (\text{A.1})$$

$$E_{ZX} = \frac{1}{2}(M_2 - M_1) \quad (\text{A.2})$$

Multiple measurements were carried out and the average value was used. The error separation results are shown in Figure A.6. As shown in the upper plot, the straightness error of  $X$  axis  $E_{ZX}$  is 52.6 nm over 38 mm measurement range, in accordance with the machine tool specification (50 nm over 25 mm range).

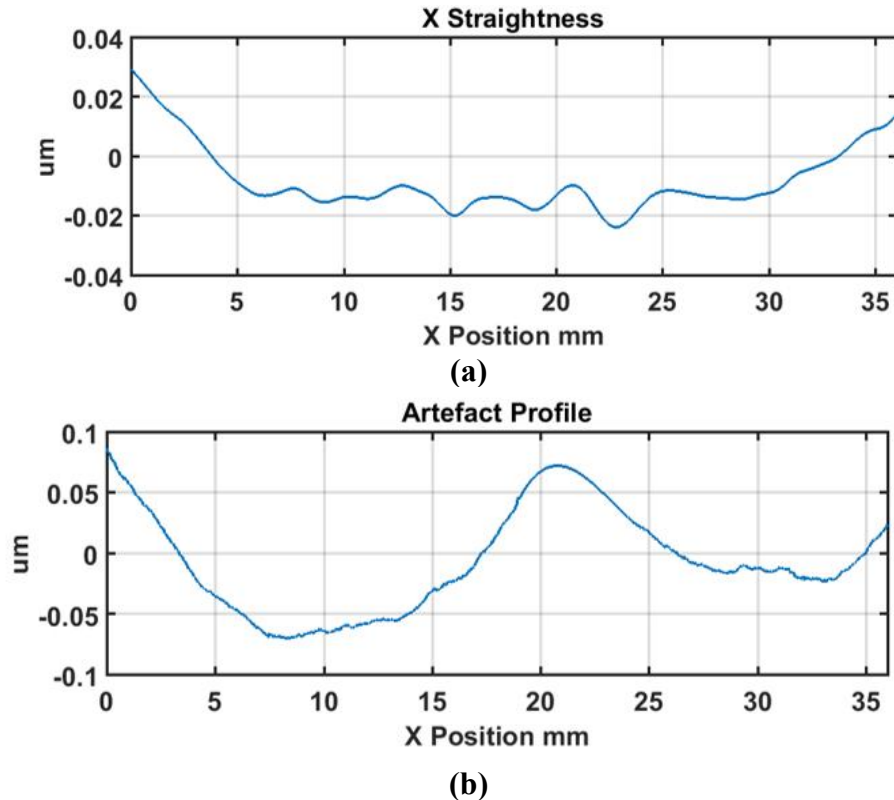


**Figure A.6 Error separation of straightness error  $E_{ZX}$  (a) and artefact profile error  $E_{flat}$  (b)**

### A.3 C axis axial and tilt errors

For  $C$  axis error measurement, the facial reversal method is utilized to measure the axial and tilt motion error [214]. Facial error motion, which is parallel to the rotational axis, is the superposition of the axial error and the tilt error. The schematic diagram and experimental setup of facial reversal measurement is respectively illustrated in Figure A.7 and Figure A.8. Two capacitance probes were set separately at the distance  $L$ . After the forward measurement (output  $M_1$  and  $M_2$ ), the flat mirror was rotated 180° relative to  $C$  axis and the two probes were moved

according to Figure A.7 (b). Next, the reversal measurement (output  $M_3$  and  $M_4$ ) was performed. It is noted that the measurement outputs  $M_1$  and  $M_4$  are the combination of the flat form error  $E_{flat}$ , the tilt error  $E_{BC}$  and the axial error  $E_{ZC}$ .

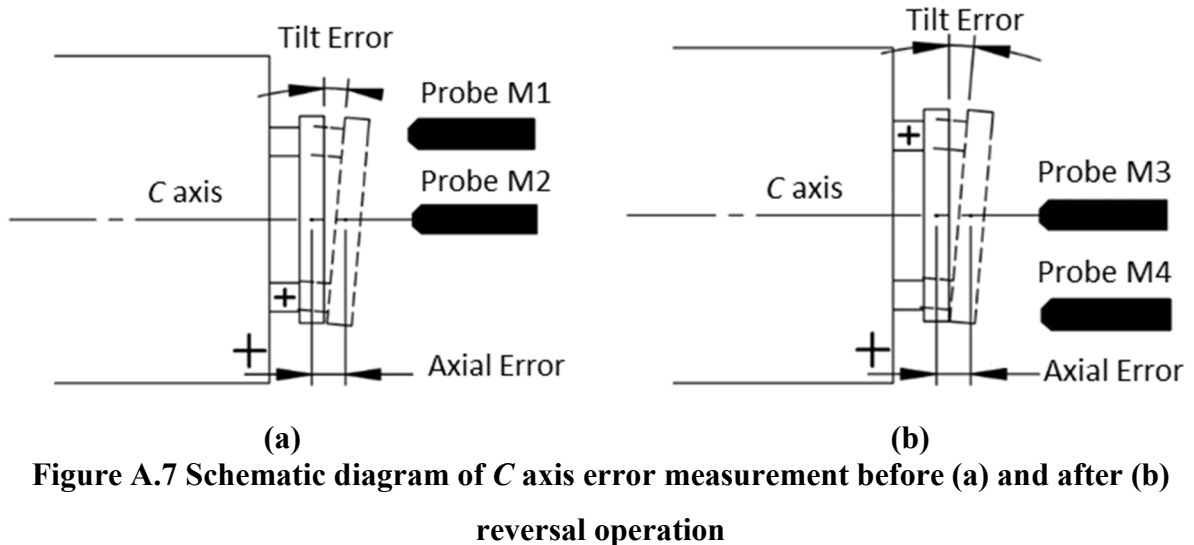


**Figure A.7 Schematic diagram of C axis error measurement before (a) and after (b) reversal operation**

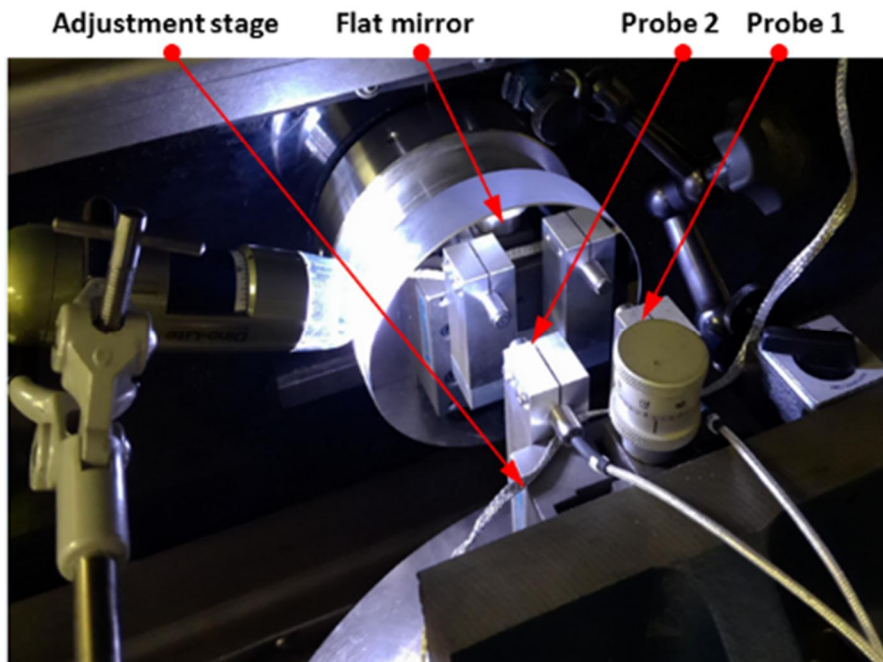


**Figure A.8 Experiment setup of C axis error measurement before (a) and after (b) reversal operation**

According to the facial reversal principle, the form error  $E_{flat}$ , the tilt error  $E_{BC}$  and the axial error  $E_{ZC}$  can be separated as the following:

$$\begin{cases} M_1 = E_{Flat} + L \times E_{BC} + E_{ZC} \\ M_4 = E_{Flat} - L \times E_{BC} + E_{ZC} \\ M_2 = M_3 = E_{ZC} \end{cases} \quad (\text{A.3})$$

$$\begin{cases} E_{ZC} = \frac{(M_2 + M_3)}{2} \\ E_{BC} = \frac{(M_1 - M_4)}{2L} \\ E_{Flat} = \frac{(M_1 + M_4)}{2} - E_{ZC} \end{cases} \quad (\text{A.4})$$

In practice, the measurement signal from the edge probe is dominated by the fundamental frequency (rotational frequency) due to the unavoidable tilt setup of optical flat on the spindle chuck. Additional signal processing is carried out to remove the fundamental frequency. The pre-processing includes noise filtering, signal truncation, and subdivision. It can be seen that the polar curve of motion error is centred after removal of the fundamental frequency. Synchronous error component can be acquired by averaging the polar curves over revolutions. Alternatively, it can be filtered out by keeping the integer multiple of foundation frequency. The reason to extract the synchronous error is that they are repeatable and applicable for machine tool error modelling.

Figure A.9 illustrates the error separation results of the *C* axis measurement. Axial error  $E_{ZC}$  is measured to be 4.4 nm, which is within the range of machine tool specification (less than 15 nm). Tilt error  $E_{BC}$  shows a two-lobe pattern as shown in the polar plot Figure A.9 (b). This measurement result indicates that the *C* axis tilt error motion  $E_{BC}$  contributes most to the kinematic error.

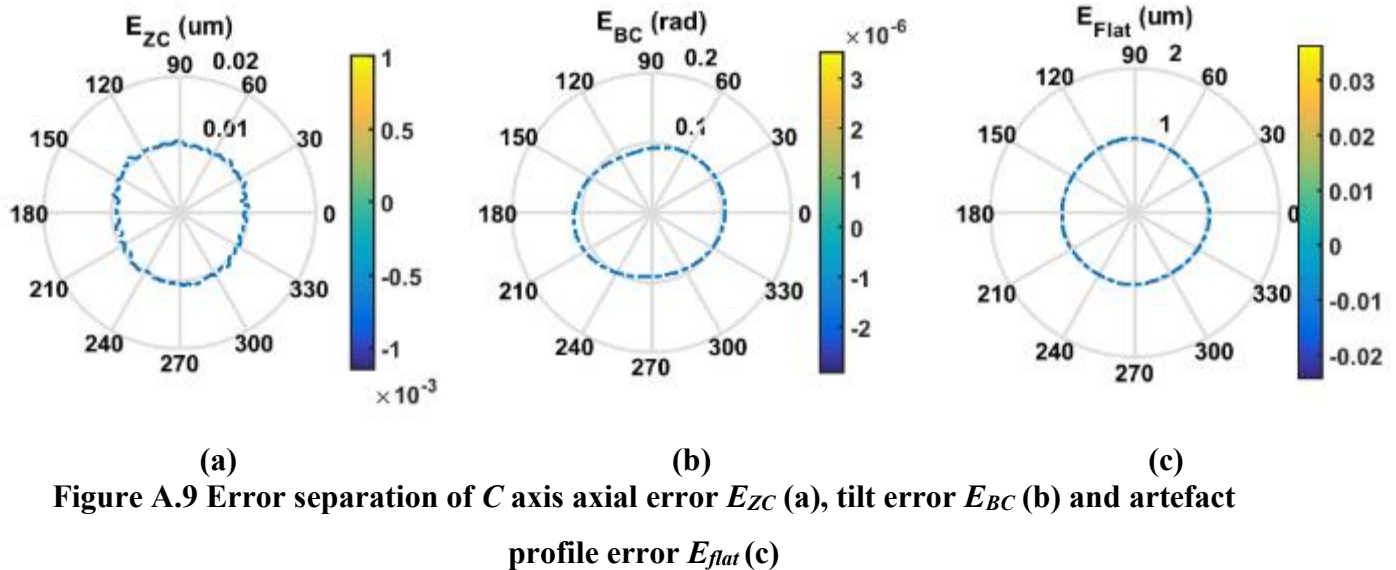


**Figure A.9** Error separation of  $C$  axis axial error  $E_{zc}$  (a), tilt error  $E_{BC}$  (b) and artefact profile error  $E_{flat}$  (c)

#### A.4 Squareness error between $X$ and $C$ axis

The squareness error  $E_{BOC}$  tends to induce a linear trend deviation on the surface measurement results. The schematic diagram and experimental setup of the squareness error  $E_{BOC}$  measurement are respectively illustrated in Figure A.10 and Figure A.11. The same flat mirror was mounted on the  $C$  axis and the measurement using a capacitance probe was performed by  $X$  directional scanning over the mirror surface. Linear slope  $\beta$  can be calculated by linear fitting of the acquisition data, which describes the angle between the linear  $X$  axis motion and the flat mirror. Then, the  $C$  axis was rotated 180° and the scanning along the  $X$  axis was performed again.

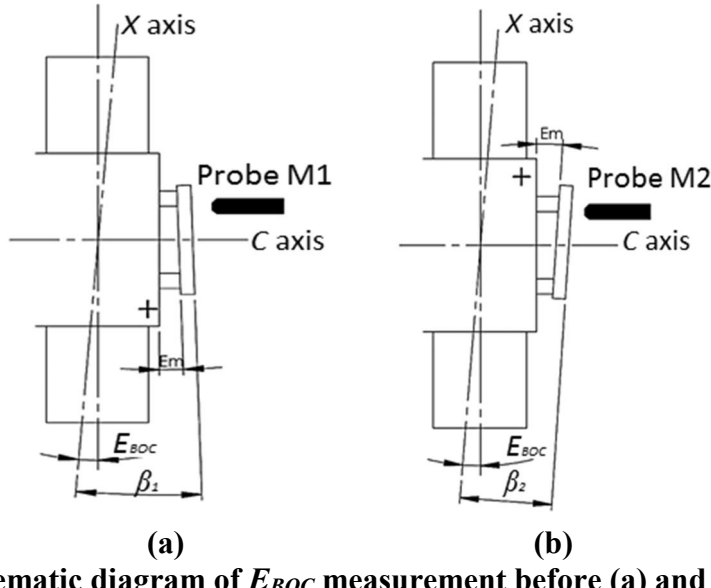


**Figure A.10 Schematic diagram of  $E_{BOC}$  measurement before (a) and after (b) reversal operation**

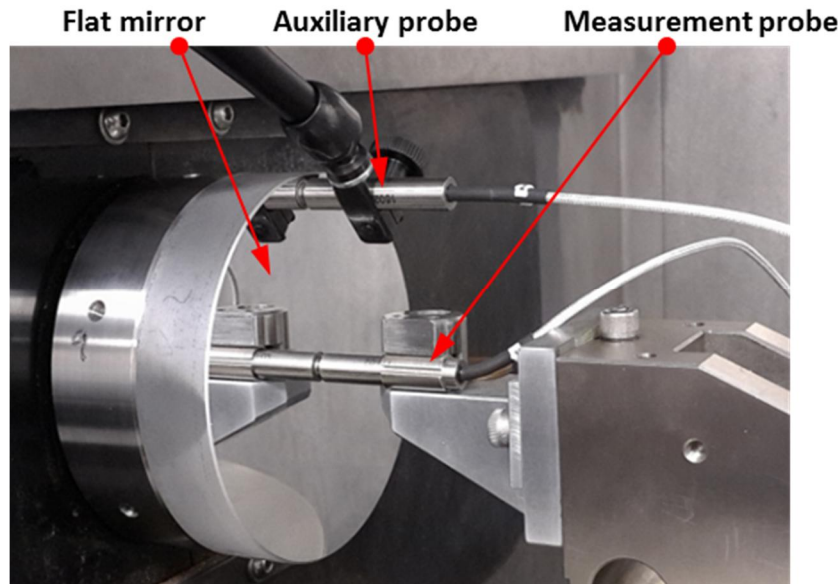


**Figure A.11 Experimental setup of  $E_{BOC}$  measurement**

The measurement results are shown in Figure A.12. The squareness error between  $X$  axis and  $C$  axis  $E_{BOC}$  can be derived as the following:

$$E_{BOC} = \frac{1}{2} \times (\beta_1 + \beta_2) - E_{tilt} \quad (A.5)$$

where  $\beta_1$  and  $\beta_2$  are the angles derived respectively from the fitting of the two measurement data sets. The squareness error  $E_{BOC}$  is calculated to be 0.08 arc sec.

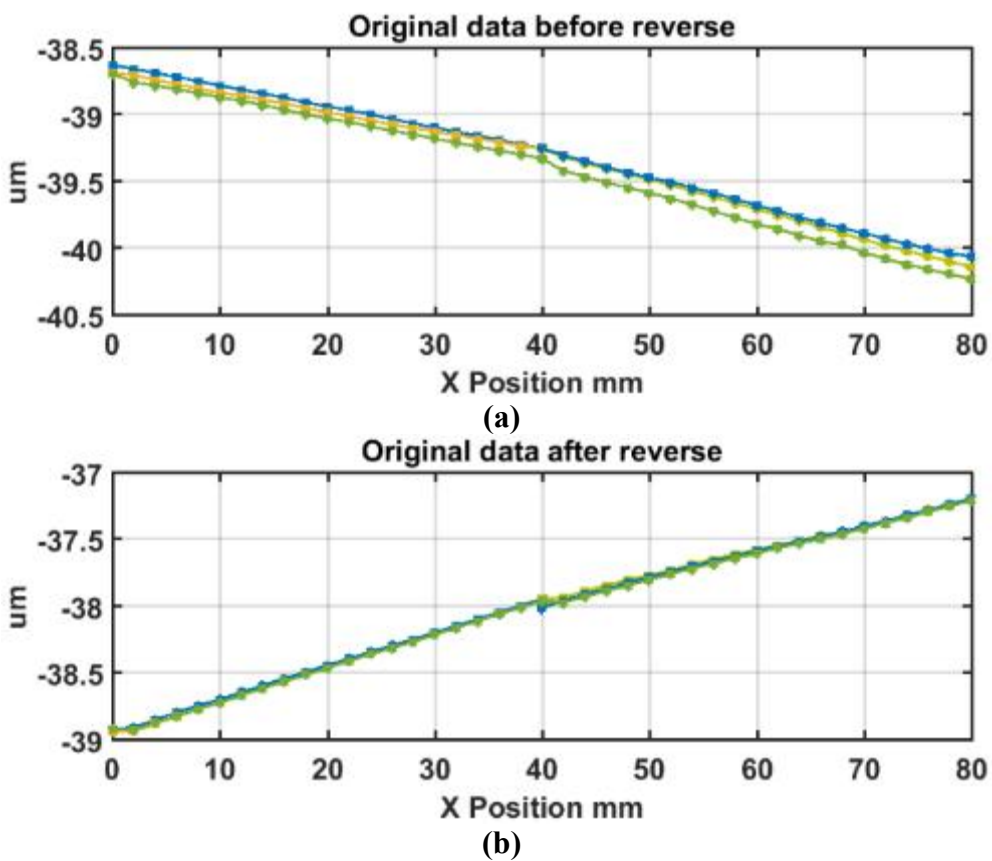


Figure A.12 Squareness error  $E_{BOC}$  measurement result before (a) and after (b) reversal operation